A CHEMICAL ODYSSEY ON THE MARTIAN SURFACE

A Dissertation

Presented to the Faculty of the Graduate School

of Cornell University

in Partial Fulfillment of the Requirements for the Degree of

Doctor of Philosophy

by

Suniti Kumara Karunatillake Walimuni Devage

January 2009

A CHEMICAL ODYSSEY ON THE MARTIAN SURFACE

Suniti Kumara Karunatillake Walimuni Devage, Ph.D.

Cornell University 2009

The Mars Odyssey Gamma Subsystem (GS) underpins most of this narrative, sensing the planetary subsurface γ photons. Midlatitudinal maps of Ca, Cl, Fe, K, H_2O, Si, and Th mass fractions have been generated with the GS. We first determine whether GS estimates represent chemical composition on the ground by computing representative in situ compositions for Pathfinder, Spirit, Opportunity, and Viking 1 landing sites. GS estimates compare favorably with the in situ estimates for Cl and K. However, the GS-determined Fe content at each landing site is consistently higher than the in situ value. Nevertheless, these comparisons reassure us that the GS data are indeed representative of the actual surface of Mars.

Next, we describe statistical analysis methods with particular emphasis on comparing distributions, computing multivariate correlations, and modeling optimal predictor sets hierarchically. Examples of their application using the GS data set clarify their use in the geochemically oriented chapters that follow. Multivariate analyses indicate a remarkable correlation among K, Th, and the areal fraction of the mineralogically distinct surface type 2 (ST2).

With our chemical insight into ST2, we consider the likelihood of different genetic scenarios that have been proposed previously. Consistent with the multivariate results, we observe significant enrichment of both K and Th in regions representative of ST2. In addition, Si does not appear to be significantly enriched in ST2. These results are more consistent with ST2 originating from a

compositionally distinct mantle source than the aqueous alteration of basalts.

Lastly, we delineate chemically striking regions to be analyzed with data from other missions. We also examine a Tharsis region marked by the enrichment of Cl and depletion of Fe and Si, and find it to overlap significantly with a radar stealth region. Surface dust observed at the two rover sites mixed with and indurated by Ca-bearing sulfate salts would be a reasonable chemical and physical analog to meter-scale depths. The sulfates may have been produced by regional-scale activity of ground-ice driven brines.

BIOGRAPHICAL SKETCH

Suniti Karunatillake was born in Colombo, Sri Lanka on 05 March 1975. Most of his primary and secondary education was completed at Sri Lankan schools Ashoka and Royal College, with one-year stints at the Beverly J. Martin Elementary and Ithaca High School in NY. Suniti's interest in planetary exploration began with childhood curiosity in lunar exploration stemming from the library collection at the B. J. Martin Elementary School. It evolved into a resilient dream of seeking life beyond Earth thanks to the documentaries by Carl Sagan identifying us as "children of the stars," and science fiction work - especially the 2001: A Space Odyssey series and Rendezvous with Rama series - by Arthur C. Clarke.

The dream had to wait while Suniti dabbled in engineering at the University of Moratuwa, Sri Lanka during 1995 - 1996, which taught him the grave folly of surrendering one's dreams for the sake of a profession. He subsequently attended Wabash College, IN, in the liberal arts tradition of exploration to satisfy curiosity and to find one's niche in life. Suniti graduated Summa Cum Laude in 2001 with induction into Phi Beta Kappa, a major in physics, and a minor in math. Along the way, he attempted numerical simulations involving the quark-gluon plasma with advisers Cheuk Yin Wong and Ted Barnes at the Oak Ridge National Laboratory, TN; and modeled gravitational interactions at ultrashort distances under the guidance of Dennis Krause at Wabash College. Such diverse experiences at Wabash gave him a sense of where to head in life.

Suniti took a decisive step toward his dreams by accepting the offer to follow graduate studies in physics at Cornell University, NY. He then found his dream adviser - Steven W. Squyres - while browsing faculty home pages in 2002. With that began six years of a Martian Odyssey during which Suniti mastered the

fundamental tools of planetary exploration. He also learned the synergy of different perspectives with the aid of 2001 Mars Odyssey, Mars Exploration Rover, Mars Global Surveyor, and several other missions. It befits his *Odyssey* that he found his niche by returning to the dreams of childhood in the city - Ithaca - where they had formed and at the university where he had first set foot as a seven year-old clinging to his father's hand. Suniti shared two National Recognition for Excellence in Space Research group awards by NASA in the process - one for the Mars Odyssey mission in 2005 and the other for the Mars Exploration Rover mission in 2008.

Suniti intends to pursue his dream knowing that while the first contact with communicative aliens may not be realized in his lifetime, he is assured a lifetime of wonder at the vanguard of human exploration. Having learned the lesson of ignoring one's calling in life the hard way, he also seeks to preserve the flame of curiosity by sharing his planetary adventures with young inquiring minds. To that end, he has contributed to Cornell's Ask an Astronomer website, Expanding Your Horizons workshops, the 4-H Focus For Teens workshops, and a Space Explorers online discussion. His mentoring experience with Nicole E. Button in particular reinforced his faith that the next generation of astronomers will reach beyond what is now the limits of imagination for humanity. For him, curiosity and exploratory urge are the keys to an amazing future for humans as travelers on what would otherwise be a mediocre planet orbiting a mediocre star in the remote reaches of a mediocre galaxy.

I dedicate my work firstly to those who love me so unconditionally that they never hesitate to criticize me. In particular, my soulmate Maheshi Dassanayake for being my anchor in reality as I head far afield in dreams; my parents W. Sisil and R. Kalyani Karunatillake for allowing me to challenge even their deepest held beliefs; Reverend Naravalpita Dhammaratana for showing my parents the strength of love; my uncle James Gair for sharing the path to knowledge by disputation with me and for showing my father the path to Cornell and beyond; my aunt Barbara Lust for demonstrating the strength of humility as a scientist; and my elementary school teacher Cynthia Lambert for developing my ethical foundations.

I dedicate my work secondly to the citizens of Sri Lanka and the USA. If not for their cultures and financial support, my dreams would not have become reality.

ACKNOWLEDGEMENTS

It is my strong belief and experience that none of what I have achieved - that I now narrate as my personal Odyssey on Mars - would have been possible without the collaborative support of my mentors who became my colleagues and friends over the life of the 2001 Mars Odyssey mission. In recognition of their contributions, I name my fellow explorers of each chapter. Much of the credit goes to them, while I alone am responsible for any errors.

John M. Keller, Steven W. Squyres, William V. Boynton (Bill), Johannes Brückner, Daniel M. Janes (Buck), Olivier Gasnault, and Horton E. Newsom collaborated on Chapter 2; Steve, Olivier, John, Buck, Bill, and Michael J. Finch on Chapter 3; Steve, Olivier, John, Buck, and Bill on Chapter 4; Steve, G. Jeffrey Taylor (Jeff), John, Olivier, Larry G. Evans, Robert C. Reedy, Richard Starr, Bill, Buck, Kristopher E. Kerry, James M. Dohm, Ann L. Sprague, Brian C. Hahn, and Dave Hamara on Chapter 5; and Steve, James J. Wray, Jeff, Olivier, Scott M. McLennan, Bill, and M. R. El Maarry on Chapter 6.

In addition to my immediate collaborators, Jason Marshall, Gregory Russell Stiesberg, Patrick Alan Taylor, Harold Y. McSween, Ralf Gellert, Robert J. Sullivan, Thomas Roledo, and Saul A. Teukolsky helped to improve the clarity and accuracy of several chapters. I am especially grateful to my friends Jason and Gregg for listening patiently to my ramblings about Mars and statistics. The extensive feedback I received from Maheshi Dassanayake, John M. Cheeseman, James J. Wray, Shoshanna B. Cole, Briony Horgan, Ryan Shannon, and Ryan Anderson enabled me to defend my dissertation with clarity and brevity.

I thank the American public for financing the NASA Mars Odyssey and Mars Exploration Rover missions that kept me sheltered and fed in addition to providing scientific insight into Mars. Mary Mulvanerton, Diane Bollen, Heather

Enos, Pamela Smith, and Danielle O'Conner worked so effectively and tirelessly that funding issues never burdened me as a graduate student.

My graduation became a reality thanks to a patient and supportive special committee consisting of Jeevak Parpia, Steve, Veit Elser, and Robert W. Kay. I am also thankful to all my mentors at Wabash College, especially Dennis Krause and Steve Bever for having more faith in me than I during my first year of graduate school. I would not have reached Wabash College if not for the sound education I received from dedicated teachers at Royal College, Sri Lanka, among whom Hemachandra, Y. M. Jayasuriya, and R. H. B. Sirisena figure prominently. One of my high school mentors, Rohini Perera, both improved my analytical skills and epitomized the selfless dedication of educators: I can only hope to pass it forward. I am also fortunate to have been taught to think analytically and communicate clearly by Cassendra Loomis, Pauline Halpern, and Helen Spanswick at Ithaca High School; and by Mohan Lal Grero in Sri Lanka.

TABLE OF CONTENTS

LIST OF TABLES

LIST OF FIGURES

CHAPTER 1

INTRODUCTION

Until recent human history, the exploration of Mars has been fueled more by imagination, hope, and fear than information and reason. Around twelve hundred years ago, Mars was a beneficent god of war to the Roman civilization (http://www.britannica.com/eb/article-9106271) and the ruddy, malefic god Angaraka to the even more ancient Indus civilization (*Kieffer et al.*, 1992, p. 2). Traces of such hopes and fears of our ancients survive to this day even in contexts as commonplace as naming of the days. Mars marks one day of the week in diverse languages - indirectly Tuesday in English ("Tuesday" Etymology *Durkin*, 2008), Mardi in French ("Tuesday" Etymology *Durkin*, 2008), Angaharuvada in Sinhala, and Sevvaai-kizhamai in Tamil.

Even as recently as a century ago, Giovanni Schiaparelli's map of Mars that helped ignite scientific exploration of the planet was misunderstood by English-speakers to show canals. The pioneering American planetary explorer, Percival Lowell, subsequently succumbed to the difficulties of optically observing Martian features across our planetary atmosphere and claimed that the canals on Mars were sustaining a tool-using civilization. Ironically, if not for the publicity he brought upon his imagined discovery, Mars may not have captured the imagination of the public as it does to this day.

Thanks in part to the seed of exploratory urge that Lowell instilled, a virtual armada of satellites and landers have explored Mars over the last forty years. Nevertheless, a clear first order sense of the planet's bulk properties were not established until as recently as the early 90's - thanks in great part to the Mariner and Viking missions. While the bulk planet may be known, the surface

of Mars remains an enigma. Even the most basic surficial material that we take for granted on Earth, soil, remains a source of lively discussion among Martian explorers (*Banin*, 2005).

My participation in this great journey of attempting to understand the upper few meters of Mars at local and regional scales has been supported primarily by the Gamma Subsystem (GS) of the Mars Odyssey Gamma Ray Spectrometer (GRS) instrument suite. With its sensitivity to γ photons emanating with characteristic energies from nuclear reactions, the GS has been able to identify and map the mass fractions of several key elements - Cl, Fe, H (as stoichiometrically equivalent H_2O), K, Si, and Th with reasonable uncertainties (*Boynton et al.*, 2007). Ca was finalized recently, while work is currently underway to finalize the maps of Al and S as well. The GS is in fact the first instrument to generate maps of elemental mass fractions throughout the midlatitudes of Mars, and also helped to confirm the presence of significant mass fractions of $H_2O_{(s)}$ at both poles.

As with the earlier missions, we have been able to interpret surficial processes on this planet only by utilizing the synergy of the GS with many others. The missions that have aided me greatly in a synergistic manner include the now defunct Viking orbiters (and the thermally-derived attribute maps that they helped to generate), Mars Pathfinder, and Mars Global Surveyor (MGS) as well as the currently active Mars Express, Mars Exploration Rover (MER), and Mars Reconnaissance Orbiter (MRO). Each has had a large suite of instruments aboard, and the chapters that follow illustrate how combinations of particular instruments are particularly insightful in the characterization of specific chemical properties and potential processes in the Martian surface.

Since the GS is a primary source of data and a key motivator of questions in the succeeding chapters, we begin by summarizing the operational details of the GS in Chapter 2. We then compare the GS data with in situ observations, analogous in some sense to a "calibration" of the GS. Such comparisons, or normalizing the GS data to in situ compositional data is difficult due to issues such as dramatic differences in spatial resolution; difficulties in convolving densities, abundances, and compositions of different regolith components; and a limited number of elements observed in common. We address these concerns in the context of the GS, using Si at Pathfinder to normalize remote data. In addition, we determine representative in situ compositions for Spirit (both with and without Columbia Hills rocks), Opportunity, and Viking 1 landing sites using GS-derived H content to hydrate the soil component. The estimate of the Si mass fraction at Pathfinder, with 13 % areal fraction of rocks, is 21 %. The composition of major elements, such as Si and Fe, is similar across the four landing sites, while minor elements show significant variability. Areal dominance of soil at all four landing sites causes representative compositions to be driven by the soil component, while proportionally large uncertainties of bulk densities dominate the net uncertainties. GS compositional determinations compare favorably with the in situ estimates for Cl and K, and for Si by virtue of the normalization. However, the GS-determined Fe content at each landing site is consistently higher than the in situ value. Nevertheless, these comparisons enable us to explore the planetary surface with some reassurance that the GS data are indeed representative of the actual surface of Mars.

Following the "grounding" of the GS data "in truth," we proceed to lay the statistical foundation - in the form of recipes of established statistical analysis methods - that is required to substantiate the inferences made in subse-

quent chapters. The statistical framework consists of two chapters. Chapter 3 is mostly an overview of exploratory statistical techniques to compare one region of Mars with another and also includes a summary of data processing specific to the GS. Specifically, instruments such as the GS typically assign the value of a continuous-valued geospatial attribute to a uniform latitude-longitude grid of bins that covers the surface without overlap. Typical attributes include elemental-mass fraction, areal fraction of a mineral type, altitude, areal fraction of rocks, thermal inertia, albedo, etc. The fineness of the grid is chosen according to the spatial resolution of the orbiter and concomitant data processing. The bins act as locational indices, yielding insight on spatial variation. In addition, the Mars Odyssey mission also estimates compositions within spherical polygonal regions on Mars independent of the bin data. We describe methods to maximize the information extracted from both bin and regional data. Rigorous use of statistical parameters and related methods for inter- and intra-regional comparisons are also discussed. While the Mars Odyssey mission provides the exploratory context, the techniques we discuss are applicable in any situation where continuous-valued attributes of a planet's surface are characterized with bins and regions. The treatment also highlights the applicability of economic, environmental, and social spatial data analysis methods in planetary exploration. Our goal is to distill the simplest statistical methods for regional comparisons, from the extensive field of Exploratory Spatial Data Analysis (ESDA), that would be intuitively accessible to planetary geologists.

The second discussion of statistical methods in Chapter 4 is essentially an algorithm - albeit one needing human judgment calls - to identify sets of attributes that show the most meaningful covariability at global scales and to quantify the strengths of the interdependencies, without ignoring numerical and spatial un-

certainties. We also describe how to address the effects of spatial smoothing and variability of uncertainties, assign statistical confidence to regression and correlation coefficients, and implement method/fit diagnostics. Spatial autocorrelation is a key concern when analyzing most types of spatial data due to the mutual dependence of adjacent data from smoothing, while heteroscedasticity is an issue when numerical uncertainties vary with location and observational duration. The Mars Odyssey and MGS missions provide the exploratory context in the discussion, but the techniques we discuss are applicable whenever the interrelationships of spatially binned data of continuous-valued planetary attributes are sought. The treatment also extends the applicability of economic, environmental, and social spatial data analysis methods to planetary exploration. Our goal is to provide an intuitively accessible and application-oriented summary of the simplest multivariate regression and correlation analyses methods from the extensive field of Explanatory Spatial Data Analysis (ESDA). The discussion is structured to enable the direct implementation of a corresponding algorithm in mathematical array-handling software such as IDL©, Mathematica©, MatLab©, and R©. It should also enable users of commercial multivariate analysis software to decipher underlying algorithms and realize associated limitations.

The methods outlined in Chapter 4 are utilized directly in Chapter 5 to explore the chemical underpinnings of mineralogically interesting regions in the northern lowlands of Mars, evident even from Earth on account of low albedo. Specifically, analysis of data acquired by the MGS Thermal Emission Spectrometer (TES) instrument led to the identification of two distinct surface types."Surface type 1," lying mostly within southern low albedo terrain, is likely to be composed of basalt. However, there are several competing mineralogical models for "surface type 2," which is found primarily in northern

low albedo terrain. We attempt to identify which models better agree with element concentrations determined through the GS. We have binned GS data over threshold regions derived from maps of surface types 1 and 2, and examined the spatial correlation of element concentrations with surface type 2. The results show that K concentration, Th concentration, and the areal abundance of surface type 2 are strongly correlated, with significant enrichment of both K and Th in regions representative of surface type 2. In addition, Si does not appear to be significantly enriched in surface type 2. These results are more consistent with surface type 2 originating from a compositionally distinct mantle source, than the aqueous alteration of basalts.

Lastly, we turn the methodology of Chapter 6 on its head by using the GS to delineate regions of interest to be explored by other instruments. The delineation method and chemical comparisons rely extensively on the statistical foundation established in Chapters 3 and 4. In this work, we establish regions of unusual chemical composition relative to average Mars primarily on the basis of Cl, Fe, H_2O, K, Si, and Th, along with the recently finalized Ca. Al is considered a candidate for future study. As a case study demonstrating the synergy of independent observation methods - Mars Odyssey, Mars Exploration Rover, Mars Reconnaissance Orbiter imaging, and radar observations from Earth in particular - we examine a chemically striking $\approx 2. \times 10^6$ km^2 region and find it to overlap significantly with a radar stealth region on Mars. It is remarkably enriched in Cl and depleted in Fe and Si - along with minor variations in H, K, and Th - relative to average Mars. Surface dust observed at the two rover sites mixed with and indurated by Ca-bearing sulfate salts would be a reasonable chemical and physical analog to meter-scale depths. We describe potential scenarios that may have contributed to the unique properties of this region. Hydrothermal

acid fog reactions on the flanks of nearby volcanoes may have generated sulfates with subsequent deflation and transport. Alternatively, the sulfates may have been produced by low temperature regional scale activity of ground-ice driven brines and/or regional scale deposition of acidified H_2O snowfall.

In Chapter 7, I summarize the current phase of my Martian Odyssey in the context of the preceding chapters, and consider future investigations that would proceed directly from the present work. The surface of Mars may always remain an enigma for humanity, but that will only sharpen the collective human mind with the challenge of the unknown.

CHAPTER 2

GROUNDED IN TRUTH*

2.1 Of Goals and Instruments

The Mars Odyssey GRS is the first to provide global data of elemental concentrations as mass fractions in the Martian subsurface to several tens of centimeter depths. In addition to the GS, this suite consists of a High Energy Neutron Detector (HEND) and Neutron Spectrometer (NS). The three instruments, particularly the NS and GS, are complimentary in their determination of H, with different sensitivities to variability as a function of mass fraction as well as different sampling depths (*Boynton et al.*, 2004). While the NS is capable of indirectly estimating the mass fractions of elements such as H that affect the neutron energy spectrum, only the GS provides direct estimates for multiple elements. Therefore, we exclusively employ GS data.

The sensor of the GS is an n-type-ultrahigh-purity Ge crystal (HPGe) at 3 kV reverse bias and passive cooling to 85 K (*Boynton et al.*, 2004). The low operating temperature minimizes loss in energy resolution and alteration of the recorded γ spectrum from exposure to high fluxes of energetic particles (*Brückner et al.*, 1991) under normal galactic-cosmic ray (GCR) fluxes as well as coronal-mass ejections (CMEs). In spite of the low operating temperature, several anneals, where the HPGe was heated to $\approx$ 345 K, were needed over the course of the mission to recover from radiation damage during CMEs and sun pointing "safe

*Originally published by Karunatillake, S., J. M. Keller, S. W. Squyres, W. V. Boynton, J. Brückner, D. M. Janes, O. Gasnault, and H. E. Newsom (2007), Chemical compositions at Mars landing sites subject to Mars Odyssey Gamma Ray Spectrometer constraints, *J. Geophys. Res. Planets*, 112, E08S90, doi:10.1029/2006JE002859.

mode" orientations of the spacecraft (*Boynton et al.*, 2007). Since annealing doesn't fully restore the original energy resolution, data collected after anneals postdating Apr 2005 have been treated as separate epochs. The signal-to-noise ratio is also maximized by cumulating spectra over the duration of each epoch. Except where noted otherwise, we restrict the GS examples to the primary mapping period from 08 Jun 2002 (00:00 UTC) to 02 Apr 2005 (20:20 UTC), treated as the first epoch (*Boynton et al.*, 2007, Para. 6).

In analyzing the GS data, a model composition is used to predict expected γ spectral peak intensities for each element subject to atmospheric corrections. The ratio of expected to observed intensities enables scaling of the model composition to represent the actual surface composition. Intermediate steps and assumptions therein introduce the potential for systematic errors, the presence or absence of which may be verified by comparing remotely determined elemental mass fractions with corresponding in situ values. Instruments similar to the Mars Odyssey GS (i.e., Ge based) are already en route to orbit Mercury (e.g., *McNutt et al.*, 2006) and planned for the Moon (*Kobayashi et al.*, 2005). The future may hold similar missions to other solar system bodies and surface missions as well. Consequently, an effective approach to compare and normalize remote data with in situ estimates of a representative regolith composition could be useful even beyond Mars. In essence, such comparisons act as "reality checks" for remote observations, making the computation of representative in situ compositions a primary goal of our discussion.

As described below, the effective instrumental spatial resolution of the GS is $\approx 3.7°(\approx 220\,\text{km})$ arc radius. In situ measurements at landing sites, on the other hand, involve samples of only centimeter and tens of centimeter spatial

extent. Furthermore, lateral spacing of samples is only on the order of kilometers even for the Mars Exploration Rover (MER) mission, the most mobile mission to date. Additional concerns include dramatic differences in the sampling depths between remote instruments (the GS, for example) and surface instruments (the Pathfinder Alpha Proton X-ray Spectrometer, for example), a limited set of elements observed in common between them, and difficulties in convolving bulk densities and areal fractions of different regolith components with their compositions.

Given the underlying issues, is it reasonable to compare the GS data with in situ data? In spite of all the caveats, there is a correspondence between these data sets in that the γ photons are produced in the upper few tens of centimeters of the Martian surface, which includes the surficial materials investigated by the landers and rovers. Furthermore, the nature of surficial material at the landing sites can be extrapolated to the GS spatial resolution scales with remote sensing data such as thermal inertia – sensitive to thermophysical properties of the upper surface such as thermal conductivity, bulk density, and heat capacity – mineralogic information (e.g., *Bibring et al.*, 2006b), and future visual observations at fine spatial resolution (cf., *Mustard and Cooper*, 2005; *Bibring et al.*, 2006a; *Shkuratov et al.*, 2005). However, the massive difference in spatial resolution implicitly applies representative in situ compositions over GS footprint spatial scales whenever the GS data are compared or normalized with in situ values. We address this issue by using a weighted mean of rock and soil component compositions at landing sites, considered the "ground truth" composition.

Elemental mass fractions determined with the GS are spatially binned on a uniform latitude-longitude grid, typically at $5^\circ \times 5^\circ$ resolution. Since the compo-

sition is estimated with the relative intensities of spectral peaks, only mass fractions, not absolute masses, of elements and oxides are estimated directly. This is different from wet chemical analysis of terrestrial rocks, for example, where ideally the total mass of all elements present must equal the known mass of the sample. In this case the oxidation states of important elements such as Fe may be determined directly. Other types of analyses, such as electron induced X-ray microanalysis (e.g., electron microprobe analysis at the micron scale), and remote and in situ spectral observations do not allow such rigor, and generally require reasonable oxidation states and absence of X-Ray invisible elements/minerals to be assumed for mass fraction normalization, as done by missions involving Alpha Particle X-Ray Spectrometers (APXS) of the MERs (*Gellert et al.*, 2006), Alpha Proton X-Ray Spectrometer (APXS) of the Mars Pathfinder Sojourner rover (*Rieder et al.*, 1997), and X-Ray Fluorescence Spectrometers (XRFS) of the Viking Landers (*Clark et al.*, 1977). Nevertheless, Mössbauer spectrometers enable the MER mission to determine Fe oxidation states.

Where systematic differences between in situ and remote compositions are evident it is possible to normalize the remote data with in situ values. Insufficient information, on the galactic cosmic ray (GCR) flux, neutron energy distribution, and γ photon production factors (*Evans et al.*, 2006; *Masarik and Reedy*, 1996) to rigorously model all nonlinear relationships between composition and γ photon production necessitates this normalization for the GS. Abundances of radioactive elements such as K and Th are unaffected by such issues and do not require normalization with in situ measurements.

Normalization with in situ data would be reasonable only for elements that do not show much variability in mass fractions across landing sites. As such, Si,

the most abundant element that is in situ and GS detectable, is the best choice for the GS normalization. An additional benefit of normalizing Si is that it has both capture and scatter derived γ peaks (refer to the work of *Evans et al.* (2006) for identification of individual peaks), while Cl, Fe, and H are primarily estimated with capture peaks. As discussed in Section 2.3, the relationship between the normalized scatter-derived Si concentration and that derived via capture can indirectly resolve issues with capture-derived elemental concentrations. Given the importance of normalization to an in situ result, selecting a suitable value for the Si normalization is also a key goal of our work.

We calculate representative in situ compositions at the Pathfinder Sojourner (at Ares Vallis), Spirit (at Gusev crater), Opportunity (at Meridiani Planum), and Viking 1 (at Chryse Planitia) landing sites. The Viking 2 landing site is excluded, given its proximity to the extreme latitude regions with elevated H and consequent exclusion from reported GS results (Section 2.3.4).

2.2 General Processing and Terminology

The GS records γ photon interactions as counts assigned to 2^{14} discrete-energy bins in the range $0.1\,\mathrm{MeV} - -10\,\mathrm{MeV}$, with each spectrum generated in $\approx 20\,\mathrm{s}$ called a "pixel." Calibrated energies of spectral peaks help to identify elements on the basis of known nuclear processes (typically natural radioactivity, neutron inelastic scatter, and neutron capture) and the counts above the continuum within peaks correlate with the concentration of elements (*Evans et al.*, 2006). Several factors necessitate the spatial and temporal summing of pixel spectra to limit relative uncertainties of peak areas above the continuum to $\approx 10\,\%$. Key

among them are: detection efficiencies, interferences among neighboring peaks, photons from the continuum, and photons from the spacecraft material. The latter is minimized by deploying the GS at the end of a 6 m boom. Cumulative spectra are typically obtained over uniform latitude-longitude grids at $2^\circ \times 2^\circ$ and coarser resolution, called "bins."

An additional $0.5^\circ \times 0.5^\circ$ grid with each areal unit termed a "cell" serves three functions. One is to identify pixels over spherical polygonal regions of Mars with which to generate cumulative spectra. These summed spectra are processed to directly estimate mean elemental mass fractions representative of a region. The second use is to assign the elemental concentration at each bin to each cell within it and subsequently process the grid of cells with a constant arc radius mean filter. The mean filter reduces significant random fluctuations (i.e., noise) present in the bin data, consequently reducing the dynamic range of mass fractions while retaining geospatially meaningful variations. The filtered mass fractions at the cells are subsequently rebinned to coarser bins, typically at $5^\circ \times 5^\circ$ resolution. This bin size, though finer than the spacecraft footprint, is a qualitative compromise between maximizing the data available for intraregional and correlation analyses, and minimizing spurious spatial effects of the mean filter.

Lastly, the cells are used in the forward model. The forward model is a key component in the processing of spectra to generate elemental-mass fractions. It accounts for atmospheric attenuation, subsurface attenuation, neutron-nuclear interaction cross sections for nonradioactive elements, the omnidirectional sensitivity of the GS to γ photons, etc. While involving many steps and stochastic simulations, the forward model is summarized in Section 2.3.1.

2.3 Key GS Data Processing Steps

There are numerous intermediate steps to generating mass fractions with the GS, which are discussed in detail by *Boynton et al.* (2007), *Evans et al.* (2006), and *Kim et al.* (2006b). We focus only on those immediately relevant for the comparison between remote and in situ compositions. Key among them, in the general order in which they are applied, are: model composition grid, scatter corrections, spatial filter, normalization of Si mass fractions (w(Si)) to an in situ value, and capture corrections.

2.3.1 Model Composition Grid and Instrumental Spatial Resolution

The model composition grid is the starting point for GS determination of the Martian regolith composition. The grid consists of $0.5^\circ \times 0.5^\circ$ cells, with each assumed to be compositionally homogeneous at the few tens of centimeter sampling depth scale of the GS (the model composition is described by *Boynton et al.* (2007)). The γ photon count rates in orbit due to each cell and a given nuclear reaction may be predicted with neutron production simulations, stochastic parameters, regolith attenuation coefficients, and atmospheric attenuation coefficients (*Boynton et al.*, 2007; *Evans et al.*, 2006; *Kim et al.*, 2006b). Even though the Martian atmosphere acts as a weak collimator, since the GS is an uncollimated instrument, it receives γ photons from limb to limb at the nominal 400 km altitude mapping orbit (e.g., *Boynton et al.*, 2004). Therefore, the set of cells within which > 99 % of the signal originates is used for predictive model-

ing, corresponding to a nadir-centered signal contribution region (SCR) of $\approx 17^\circ$ (i.e., 1000 km) arc radius (*Kim et al.*, 2006b).

For a given nuclear reaction of each element, the ratio of predicted γ photon counts to the observed is computed within the SCR. This ratio scales the model composition, yielding an estimate of the actual composition. The estimated composition is assigned to the cell at nadir, and the process repeated for each cell of the $0.5^\circ \times 0.5^\circ$ grid. Such a fine grid is appropriate for data processing and display, but does not represent the actual footprint of the GS, which is defined by the set of cells that contribute more than 50 % of the signal. While dependent on photon energies, the typical footprint is ≈ 440 km, corresponding to $\approx 7.4^\circ$ arc diameter (e.g., *Boynton et al.*, 2004; *Boynton et al.*, 2007).

When photons of differing energies are emitted by a single element, a weighted mean of corresponding mass fractions is generally used to represent the true composition of the element (*Boynton et al.*, 2007). The large number of cells within each SCR and the use of epochal γ spectra yield statistically rigorous uncertainties that are primarily functions of counting statistics and smaller than model composition uncertainties (*Boynton et al.*, 2007; *Evans et al.*, 2006).

The regolith model may introduce systematic errors for all elements, while the model composition may do so for elements determined with capture or scatter processes. The GS regolith model for the midlatitudes assumes compositional homogeneity at GS sampling depths. It also assumes lateral compositional homogeneity within each cell. Significant deviations from lateral homogeneity have the potential of seriously weakening the accuracy of GS compositional estimates, as would the presence of compositional layering (e.g., *Squyres and Evans*, 1992). We consider such deviations and explain what we classify as

rocks and other material in Section 2.4.

2.3.2 Scatter Corrections, Spatial Filter, and Effective Spatial Resolution

Scatter corrections constitute another important step in the reduction of GS data. Si mass fractions derived from the 1779 k eV γ flux are subject to the scatter corrections, increasing the initial Si estimates by $\approx \times 3$ on average. These correction factors, which account for variations in the fast neutron flux driven mainly by Fe and H content in the regolith, precede the spatial filter application, Si normalization to an in situ value, and capture correction determination (*Boynton et al.*, 2007).

The third processing step, spatial filter application, is important in the context of instrument detection efficiency and resolution. The choice of a gamma ray spectrometer type is a trade off between the high efficiency of scintillators and the high energy resolution of solid state detectors (*Metzger and Drake*, 1990; *Pirard et al.*, 2005). The latter option was appropriate for the Mars Odyssey GS, where the ability to resolve and identify many of the lines that characterize the Martian spectrum optimized the science return (*Boynton et al.*, 2004; *Boynton et al.*, 2007). Nevertheless, GS data have low signal-to-noise ratios at fine spatial scale. This concern is addressed by first smoothing with a constant arc radius mean filter. The mean filter is applied simultaneously, not iteratively, on a $0.5^\circ \times 0.5^\circ$ grid with the arithmetic mean of values within the filter window assigned to the central cell. *Boynton et al.* (2007) discuss and illustrate the scatter of values before and after the smoothing.

To first order, the filter radius is greater for elements with smaller signal-to-noise ratios. For nonradioactive elements in particular, the spatial filter is applied at several processing steps (*Boynton et al.*, 2007). The filter arc radii for different elements at the final processing steps are: 5° for K; 10° for Ca, Cl, Fe, H, and Th; and 15° for Al and Si. An unfortunate outcome of filtering is the increase in spatial uncertainty in the form of spatial autocorrelation as discussed in Chapters 3 and 4. Subsequent to the filter application, the data are binned on fairly coarse latitude-longitude grids, typically at $5^\circ \times 5^\circ$. Rebinning further increases the signal-to-noise ratio and provides the necessary oversampling to account for the difference in shape between the response function of the GS, which is circular, and of cells, which are rectangular. However, since the filter window is much larger than an individual $5^\circ \times 5^\circ$ spatial bin, spatial autocorrelation is aggravated in the GS data. Nevertheless, the filter enables a significant increase in numerical precision as evident in relative root-mean-square uncertainties of 10 % for Cl, 8 % for Fe, 11 % for H, 7 % for K, 2 % for Si, and 10 % for Th.

A combined effect of the spacecraft footprint, the SCR, and the spatial filter is a dramatic difference in spatial resolution between the GS and in situ instruments. This difference necessitates careful selection of compositional attributes from in situ missions for comparison with and normalization of the GS data. It is particularly important as the GS is insensitive to the substantial variability at small lateral spatial scales, in composition, density, and texture as seen by the Viking, Pathfinder, and MER missions.

2.3.3 Si Normalization, Capture corrections, and Feedback Effects

As described earlier, we select only one element, Si, for the normalization of GS data. The normalization is achieved in several steps. First, the scatter-derived 1779 k eV γ photons from Si are used to estimate w(Si) subject to the scatter corrections. These mass fractions are then smoothed with the mean filter. Next, the filtered values are scaled by a constant so that the GS-derived w(Si) at the coordinates of a chosen landing site equals the representative in situ w(Si). For reasons discussed in Section 2.7.4, we chose the Pathfinder landing site for the Si normalization.

Capture corrections are subsequently determined as the ratio of the capture-derived w(Si) to the 1779 k eV scatter-derived (also scatter corrected and normalized) w(Si) at each cell (e.g., *Boynton et al.*, 2007). These ratios act as scaling factors for mass fractions of all capture-derived elements (Cl, Fe, and H) (*Boynton et al.*, 2007), increasing initial estimates by $\approx \times 4$ on average. Such scaling is necessary to account for variations of the thermal neutron flux in the regolith due to the presence of neutron moderators, such as H, even at low concentrations (*Boynton et al.*, 2007).

A slight feedback effect exists between the scatter and capture correction steps, since Fe and H content, which are subject to the capture correction, affect the scatter correction. Furthermore, as described in Section 2.6, we renormalize the calculated in situ composition to allow for the presence of GS-determined H, which in turn affects the Si normalization. However, these feedback effects among the scatter correction, capture correction, and Si normalization are so

subtle that the relative variation in estimated elemental mass fractions during iterative processing was < 0.1 %.

2.3.4 Effects of H and Spatial Extent

As discussed in Sections 2.3.3 and 2.3.2, neutron moderation by H in particular introduces an additional complexity to the forward model by affecting the γ photon production via neutron capture and inelastic scatter in other elements. Radioactive elements, Th and ^{40}K, are not subject to the consequent scatter (Section 2.3.2) and capture (Section 2.3.3) corrections.

An additional concern in estimating elemental mass fractions is the presence of large amounts of $H_2O_{(s)}$ toward the high latitudes. This dilutes other elements in the regolith, increases the likelihood of significant layering at depth, and severely alters the neutron energy spectrum. The latter makes both scatter and capture corrections unreliable, while the forward modeling also becomes flawed with the violation of homogeneity assumptions at depth.

To avoid such issues, reported GS data on nonradioactive elements are currently constrained by an "Hmask." The Hmask excludes poleward areas on Mars that are dominated by $H_2O_{(s)}$ on the basis of the 2.223 MeV H line of the γ spectrum (*Boynton et al.*, 2007, Para. 38 and Figure 2a). Though spherical polygonal, not rectangular, in shape, the mask typically constrains global data for all nonradioactive elements to within ±45° latitude. Since dilution severely reduces count rates leading to relatively higher uncertainties, reliable global data for even the radioactive elements are limited to within ±75° latitude (e.g., *Taylor et al.*, 2006a,b; *Boynton et al.*, 2007, Boynton para. 38).

2.4 Summary of the Technique

As outlined in Section 2.1, since we compute a weighted mean of in situ rock and soil compositions, it is important to classify regolith components into these two categories. Throughout our discussion, "rocks" generally refer to 10 cm scale and larger materials (e.g., fragments, breccia, and exposed outcrops) that have high thermal inertia, have areal fractions consistent with the Viking Infrared Thermal Mapper (IRTM) data (e.g., *Christensen*, 1986; *Golombek et al.*, 2005), and are immobile under current eolian conditions. The mean free path of neutrons is $\approx$ 10 cm (e.g., *Squyres and Evans*, 1992), ensuring that what we consider as rocks appear distinct to the GS. "Soil" refers to all other, typically unconsolidated, material including those sufficiently fine-grained to be mobilized by wind (e.g., *Banin et al.*, 1992; *Jerolmack et al.*, 2006). Soil consequently encompasses a variety of regolith components identified at the five landing sites. Typical examples are: bedform armor, clasts, concretions, drift, dust, rocky fragments, sand, and soil (e.g., *Fergason et al.*, 2006a; *Golombek et al.*, 2005; *Sullivan et al.*, 2005; *Yen et al.*, 2005).

While the classification of the regolith into rocks and soil is very broad, it suits the GS data context, with the $\approx$ 440 km instrument footprint and upper few tens of centimeter sampling depth as described in Section 2.3 (e.g., *Boynton et al.*, 2007). For example, the GS would be insensitive to the variability of rock areal fraction by factors of two to four (e.g., *Squyres et al.*, 2004b) as observed in the km scale traverse of Spirit. Satisfactory agreement between average in situ estimates and IRTM orbital estimates of the areal fraction of rocks further support our simple classification (e.g., *Golombek et al.*, 2005). However, the rock size threshold assigns smaller rock fragments to the soil component, potentially

making the areal fraction we assign to rocks less than their in situ value. In addition, since the daily temperature variations do not penetrate very far into rock, and less into soil, even a thin (> 1 cm) soil layer can conceal rocks from the IRTM and lead to an underestimation of the rock abundance.

For a regolith with two key components, rock and soil materials, distributed as a homogeneous mixture within a sample volume, we may compute the representative mass fraction of an element or oxide as

$$C_{\mathrm{m}} = \frac{c_{\mathrm{r}} A_{\mathrm{r}} \rho_{\mathrm{r}} + c_{\mathrm{s}}(1 - A_{\mathrm{r}})\rho_{\mathrm{s}}}{A_{\mathrm{r}} \rho_{\mathrm{r}} + (1 - A_{\mathrm{r}})\rho_{\mathrm{s}}} \tag{2.1}$$

with C_{m} the representative in situ concentration of the element (or oxide) as a mass fraction, A_{r} the areal fraction of rocks, ρ_{r} the density of rocks, ρ_{s} the density of soil, c_{r} the mass fraction of the element (or oxide) in rocks, and c_{s} the mass fraction of the element (or oxide) in soil. Uncertainties are propagated for C_{m} and all other computed values with the standard formula (e.g., *Young*, 1962, pp. 96–101):

$$s_{\mathrm{m}} = \sqrt{\sum_i \left| \frac{\partial f}{\partial x_i} \right|^2 s_{m,x_i}^2} \tag{2.2}$$

where x_i is the i^{th} variable of the function f, s_{m,x_i} the standard error (i.e., net uncertainty defining 68 % statistical confidence under normality assumptions) of x_i, and s_{m} the standard error of the function. Therefore, under gaussian assumptions, f would be 68 % probable to be within $1 s_{\mathrm{m}}$. Following the notation within companion papers of the Mars Odyssey Special Issue (e.g., *Boynton et al.*, 2007; *Keller et al.*, 2006b; *Taylor et al.*, 2006a), we state uncertainties to $1 s_{\mathrm{m}}$ as also discussed in Chapter 5. In contrast, the MER team reports APXS data uncertainties to $2 s_{\mathrm{m}}$ (e.g., *Gellert et al.*, 2006; *Rieder et al.*, 2004).

For a given soil type at each MER site, we estimate c_s in Equation 2.1 as the arithmetic mean ($\hat{\mu}$) of several samples identified in Sections 2.7.2 and 2.7.3. The corresponding standard error ($s_{m,x_i} = s_{m,c_s}$) for use in Equation 2.2 is derived from the standard deviation $s = \sqrt{\frac{\sum_i (c_{s,i} - \hat{\mu})^2}{N-1}}$ as $s_{m,c_s} = \frac{s}{\sqrt{N}}$, where N is the number of samples and $c_{s,i}$ is the concentration in the i^{th} sample (e.g., *Mandel*, 1964, pp. 35–41, 62–63, 106–110). The alternative of computing the maximum likelihood mean and corresponding s_{m,c_s} using the reported uncertainties is less defensible in the rover context, since such samples generally present statistically inconsistent (e.g., *Taylor*, 1982, pp. 147–152) data even though they are spatially indistinct from the GS perspective. We similarly utilize the standard error of the arithmetic mean along with calibration uncertainties for Viking 1 data. In all other cases, we use the reported standard error as s_{m,x_i}, which is primarily driven by counting statistics for the GS data. In summary, the standard error of C_m is mostly a function of the following: (1) statistical uncertainties in rock and soil densities as described in Section 2.5, (2) reported uncertainty in rock areal fraction (Table 2.1), (3) reported uncertainties of in situ element/oxide mass fractions (with the exception of MER soil data as described above), and (4) the standard error of GS-derived $w(H_2O)$ (Section 2.6).

A difficulty with Equation 2.1 is that density, areal fraction, and element concentration measurements are not simultaneously available for a given landing site. In addition, Equation 2.1 is valid only where the regolith is a homogenous mixture of rocks and soil across the γ photon sampling depth, which, as discussed in Section 2.3, is also a primary assumption of all GS datasets. While this assumption may be roughly true for the Gusev, Pathfinder, and Viking landing ellipses (e.g., *Moore et al.*, 1977; *Golombek et al.*, 2005), Meridiani is a clear exception as noted in Section 2.7.3. The effect of rock/soil mixing geometries on mass

Table 2.1: Areal fractions, as %, of rock (A_r) and soil components at the landing sites as discussed in Section 2.5. The reported relative areal fractions of "drift" (A_d) and "soil"(A_s) are used in Equation 2.3. Note that the calculated composition at Opportunity assumes a rock-free surface as described in Section 2.7.3.

Lander/Rover	s_m	Rock areal fraction	Soil areal fraction	
			A_d	A_s
Opportunity		9	91	
Pathfinder		13	87	
Spirit	5	6	94	
Viking 1		13	18. ± 4.	66. ± 13.
Viking 2		16	30. ± 6.	54. ± 11.

fraction estimation has been modeled before (e.g., *Squyres and Evans*, 1992). Additional studies are underway to quantify these effects for rocks embedded in a soil matrix (e.g., *Kim et al.*, 2006a).

2.5 Bulk Densities and Areal Fractions

An estimate of rock and soil bulk densities is key to evaluating Equation 2.1. However, none of the in situ missions have been equipped with instruments to directly determine bulk densities. Consequently, the most reliable density estimates to date are from reasonable terrestrial analogues that utilize thermophysical, textural, and compositional information of the Martian regolith (e.g., *Fergason et al.*, 2006a; *Grant et al.*, 2004). While bulk densities of Martian rocks would be consistent with those of Shergottite-Nakhlite-Chassignite (SNC) meteorites, it is important to note that SNC meteorites may not be petrologically

representative of the general Martian regolith (e.g., *McSween*, 1994, 2002).

In the case of the MER, Rock Abration Tool (RAT) currents and Mössbauer contact plate forces provide additional estimates of rock and soil properties, respectively (e.g., *Arvidson et al.*, 2004a,b; *Squyres et al.*, 2006a). In addition, the Panoramic Cameras (Pancams) (e.g., *Farrand et al.*, 2006; *Bell et al.*, 2004) and Microscopic Imager (MI) (e.g., *Sullivan et al.*, 2005; *Cabrol et al.*, 2006; *Herkenhoff et al.*, 2006) yield detailed textural information. Overall, the MER mission has provided evidence of much greater variability in bulk properties than recognized on earlier missions (e.g., *Fergason et al.*, 2006a). Nevertheless, in the context of remote missions sensitive only to average physical properties at coarse spatial resolution, detailed modeling of in situ bulk densities is unlikely to yield useful insight. Therefore, we utilize the Viking regolith property observations and corresponding terrestrial analogs as our primary sources of density information, supplemented with evidence for heterogeneity as observed by the MER mission.

The density of "average" Martian rocks, considered physically analogous to terrestrial dense basalts (e.g., *Fergason et al.*, 2006a; *McSween et al.*, 2004), is taken to be $(2.6 \pm 0.5) \times 10^3\,\mathrm{kg\,m^{-3}}$ (*Moore et al.*, 1977; *Moore and Jakosky*, 1989; *Olhoeft and Johnson*, 1989). To account for significant variability in rock bulk densities, we quote and substitute the standard deviation (s) instead of the standard error of ρ_r in $s_{\mathrm{m},x_i} = s_{\mathrm{m},\rho_\mathrm{r}}$ of Equation 2.2. Two soil components were identified at the Viking 1 site: "drift" with a density of $(1.15 \pm 0.15) \times 10^3\,\mathrm{kg\,m^{-3}}$ and "blocky soil" with a density of $(1.6 \pm 0.4) \times 10^3\,\mathrm{kg\,m^{-3}}$ (*Moore and Jakosky*, 1989). While the near-field analysis by *Moore and Jakosky* (1989) identified only a "crusty to cloddy soil" with a density of $(1.4 \pm 0.2) \times 10^3\,\mathrm{kg\,m^{-3}}$ at the Viking 2 site, the far-

field analysis by *Moore and Keller* (1991) verified the presence of "drift" as well. Since soil densities at each site overlap within the uncertainties, we use their far-field areal fraction weighted mean as the density of the soil in Equation 2.1. The mean density of the soil, ρ_s, may then be expressed as:

$$\rho_s = \frac{A_d \rho_d + A_s \rho_s}{A_d + A_s} \tag{2.3}$$

where d represents "drift" and s represents "soil" ("blocky" type at Viking 1 and "crusty to cloddy" type at Viking 2). The remaining symbols are analogous to those of Equation 2.1, with the standard error of ρ_s obtained by substituting $f = \rho_s$ in Equation 2.2.

Since Viking 1 and 2 reported different relative areal fractions (Table 2.1) and densities for the "drift" and "soil" components, ρ_s differs slightly between the two soil proxies. For the Pathfinder and MER landing sites where density estimates have not been reported, the maximum-likelihood mean (e.g., *Mandel*, 1964, pp. 131–135) of the two, $(1.34 \pm 0.13) \times 10^3\,\mathrm{kg\,m^{-3}}$, was used as the mean density, ρ_s, of the soil component. This approximation is further justified by the favorable comparison of soil properties across Viking, Pathfinder, and MER landing sites (e.g., *Arvidson et al.*, 2004a). On the other hand, ρ_s at the Viking 1 landing site was computed directly from Equation 2.3 to be $(1.5 \pm 0.3) \times 10^3\,\mathrm{kg\,m^{-3}}$.

In addition to the densities of the rock and soil components, Equation 2.1 requires the areal fraction of rocks, A_r. As explained in Section 2.4, we rely on the global rock areal fraction map at $1^\circ \times 1^\circ$ resolution generated with thermal inertia data from the IRTM (*Christensen*, 1986). We compute the mean of rock areal fractions within a 15° arc radius circle, representative of the GS spatial filter and centered at the coordinates of each landing site: Viking 1 (22.27° latitude, -47.94°

east longitude) (*Mayo et al.*, 1977), Pathfinder (19.13°, −33.22°) (*Golombek et al.*, 1999), Spirit (−14.57°, 175.47°) (*Squyres et al.*, 2004b), and Opportunity (−1.95°, −5.53°) (*Squyres et al.*, 2004a). The absolute, not relative, uncertainty of each mean rock areal fraction is taken to be 5 % (e.g., *Christensen*, 1986). These are summarized in Table 2.1.

2.6 Oxidation and Hydration

we compare compositions across landing sites while conforming with wet chemical analysis normalization of mass fractions at each site to unity. This requires the oxidation state of a given element to be the same across all landing sites for both rock and soil. Reported values satisfy this condition for most elements, with the exception of Fe and S. We adjust the oxidation states of these two elements in three steps. First, we stoichiometrically (atomic masses by *Loss* (2003)) convert reported oxide mass fractions of all elements into the unoxidized (i.e., elemental) mass fractions. Second, we convert the elemental mass fractions back into oxide mass fractions assigning the same oxidation state to a given element across all regolith components and landing sites. Third, we separately renormalize these mass fractions to unity for rock and soil.

Only Pathfinder data needed the oxidation state adjustment for S, by converting rock composition from S to S^{6+}. The adjustment for Fe is much more complicated. To date, the MER Mössbauer spectrometer is the only instrument to measure in situ Fe oxidation states. While the MER data demonstrate significant variability in the molar fraction of Fe^{3+}, once the outcrop and hematitic soils in Meridiani and the Columbia Hills rocks in Gusev are excluded, the mo-

lar fractions are in rough agreement between the two sites (*Klingelhöfer et al.*, 2004; *Morris et al.*, 2004). It is important to note however, that the Fe oxidation states observed in the Columbia Hills indicate much variability, with the molar fraction of Fe^{3+}, $\frac{Fe^{3+}}{Fe_{total}}$, varying from approximately 0.2 to 0.9 (*Morris et al.*, 2006). Columbia Hills rocks are also older than the plains rocks (e.g., *Squyres et al.*, 2006a), and may be comparable in age to the bedrock beyond the crater rim. While these concerns indicate that using a mean of Fe oxidation states observed across landing sites may be simplistic, as explained in Section 2.8, its effect on the computed in situ composition is negligible due to the normalization of oxides. In contrast, a major systematic error could occur if Fe and/or S existed in sulfide or elemental form instead of as oxides.

Since Fe oxidation states vary significantly between and within the only two sites where such data are available, we use the Gusev plains material to estimate a mean molar fraction of Fe^{3+} solely as a formalism. The arithmetic mean and standard deviation of the Fe^{3+} molar fraction of all measurements in the Gusev plains is 0.28 ± 0.01 (*Morris et al.*, 2004). Consequently, we use a mean Fe oxidation state of +2.28 as the standard in all representative in situ estimates. The renormalizations of reported compositions to $FeO_{1.14}$ and SO_3 preceded all other calculations.

While GS measurements include $w(H)$ (reported as stoichiometrically equivalent $w(H_2O)$), H content has not been directly determined in situ (*Rieder et al.*, 2003; *Gellert et al.*, 2006), with the exception of the Viking landers (e.g., *Anderson and Tice*, 1979). We model the rock component to be devoid of H_2O, and propagate the GS-derived $w(H_2O)$ into the soil component. This is achieved by inverting Equation 2.1:

$$c_s = \frac{C_{GS}\{A_r\rho_r + (1 - A_r)\rho_s\}}{(1 - A_r)\rho_s} \tag{2.4}$$

where c_s is the estimated in situ $w(H_2O)$ in soil, and C_{GS} the GS-derived $w(H_2O)$ at the landing site coordinates. C_{GS} values and corresponding standard errors are listed in Table 2.2, and we compute the standard error of c_s by substituting $f = c_s$ in Equation 2.2. The in situ oxide and elemental mass fractions in soil are renormalized to $1 - c_s$ to allow for the presence of H_2O. In spite of exceptions (e.g., *Clark et al.*, 2005) discussed in Section 2.7.3, assuming the rock component to be free of H_2O remains a reasonable approximation for the majority of landing sites. As a concluding step, we convert the representative in situ compositions, renormalized for both uniform oxidation states and the presence of H, into stoichiometrically equivalent elemental mass fractions.

In general, C_{GS} values (Table 2.2) are consistent with in situ estimates of $w(H_2O)$ at Pathfinder, Spirit, and Viking 1. At pathfinder, the stoichiometric $w(H_2O)$ is $\approx 2\,\%$ in soils and $0.1\,\% - -4.3\,\%$ in rocks as calculated via mass balance and subject to Fe and S oxidation state assumptions (*Foley et al.*, 2003). The re-analysis of Viking 1 data indicated that the soil at Viking 1 may contain $w(H_2O)$ in the range $1.1\,\% - -3.0\,\%$ (*Anderson and Tice*, 1979). Mineralogic modeling of H_2O content at Spirit is difficult due to the large mineralogic variability of regolith components that contain H. Nevertheless, current modeling tentatively suggests $w(H_2O) \approx 0.7\,\%$ as Goethite (α – FeOOH) in the most altered Gusev rocks (*Morris et al.*, 2006) and $w(H_2O) < 11\,\%$ as hydrated sulfates in subsurface soils (*Wang et al.*, 2006). Furthermore, recently analyzed salt deposits in the Columbia Hills, such as Paso Robles, may contain much higher amounts of bound H_2O (e.g., *Johnson et al.*, 2007; *Lane et al.*, 2007; *Wang et al.*, 2007; *Yen et al.*, 2008).

Table 2.2: Representative in situ mass fractions and their GS-derived (*Boynton et al.*, 2007) counterparts (as %). Net uncertainty of each mass fraction is given parenthetically to one standard error ($1s_m$). Equation 2.2 and related text describe the uncertainty estimation for calculated in situ mass fractions, while *Boynton et al.* (2007) describe that for GS-derived concentrations. SpiritHW uses an area-weighted mean of Humphrey and Wishstone compositions, while SpiritH only uses the composition of Humphrey. Only four of the elements have both representative in situ and GS-derived concentrations. Continued in Table 2.4.

Element	Opportunity	Pathfinder	SpiritH	SpiritHW	Viking 1
Al	4.69(0.23)	4.5(0.3)	4.38(0.17)	4.6(0.3)	4.4(1.1)
Ca	4.53(0.03)	4.8(0.4)	3.99(0.16)	4.07(0.22)	4.6(0.6)
Cl	0.466(0.006)	0.49(0.07)	0.71(0.08)	0.72(0.07)	0.71(0.17)
GS-derived Cl	0.59(0.06)	0.37(0.04)	0.68(0.06)		0.37(0.04)
Cr	0.303(0.007)	0.16(0.08)	0.26(0.02)	0.23(0.02)	-
Fe	13.8(0.7)	14.6(0.9)	12.3(0.3)	11.8(0.3)	13.2(1.3)
GS-derived Fe	15.4(1.3)	17.3(1.3)	15.7(1.2)		15.4(1.2)
GS-derived H_2O	5.4(0.6)	2.9(0.5)	7.4(0.6)		2.6(0.4)
K	0.336(0.016)	0.63(0.07)	0.25(0.02)	0.284(0.014)	0.22(0.13)
GS-derived K	0.316(0.023)	0.43(0.03)	0.328(0.020)		0.31(0.03)
Mg	4.18(0.13)	4.2(0.6)	5.36(0.18)	5.02(0.24)	3.3(0.6)

2.7 In Situ Specifics

In spite of the generally similar methodology to estimate representative in situ compositions, some differences arise in the calculation details at different landing sites. These differences reflect the compositional diversity on Mars and differences in instrumental capabilities. For example, the elemental composition of the Viking 1 landing site is not as well characterized as the others, since the XRFS had more limited elemental detection capabilities than the APXS used in subsequent missions. Moreover, the MER mission provides additional information due to a comprehensive suite of instruments and mobility.

MER instruments are sensitive to geochemical variations at spatial scales vastly exceeding the sensitivities of remote (e.g., the GS) missions. For example, the MERs have revealed striking morphological, textural, and compositional variations (e.g., *Arvidson et al.*, 2006; *Cabrol et al.*, 2006; *Grotzinger et al.*, 2005) at centimeter to tens of centimeter scales with elemental and mineral detection instruments – the APXS (e.g., *Gellert et al.*, 2006), Miniature Thermal Emission Spectrometer (Mini-TES) (*Fergason et al.*, 2006a), and Miniature Mössbauer Spectrometer (MIMOS II) (*Morris et al.*, 2006) – and at sub-millimeter scales with the MI (e.g., *Herkenhoff et al.*, 2006). As an additional complexity, Spirit has observed chronological variability, including the removal of a thin dust cover by dust devils (e.g., *Arvidson et al.*, 2006; *Greeley et al.*, 2005). Consequently, while we use all the samples of earlier in situ missions, only a carefully selected subset of the MER data is used for remote comparisons.

2.7.1 Viking 1

All Viking data may be used in representative in situ estimations since major compositional heterogeneities were inevident due to instrumental limitations and lack of mobility. The absence of rock compositional data poses a challenge at the Viking site. Given the general geological similarities and spatial proximity of the regolith at Viking 1 and Pathfinder, we address this by using the Pathfinder mean soil-free rock composition (*Wänke et al.*, 2001) as a proxy for the rock composition at Viking 1. However, the apparent geological similarities may conceal significant compositional differences, with the potential to invalidate our choice of a proxy rock composition. Nevertheless, relative to Pathfinder, rock compositions at either MER site are likely to be even more inappropriate as proxies to rock at Viking (see below).

Besides the lack of rock analyses, the Viking 1 XRFS was also incapable of detecting Cr, Mn, Na, and P. Consistent with the approach by *McSween and Keil* (2000), for example, we account for this issue by normalizing Viking 1 rock and soil compositions to 97 %, the net mass fraction of Pathfinder soil-free rock attributable to elements and oxides other than Na_2O, Cr_2O_3, MnO, and P_2O_5. Furthermore, the mean K content based on the work of *Clark et al.* (1982) is below the XRFS detection limit. We use the arithmetic mean of values reported by *Clark et al.* (1982) to estimate the Viking 1 soil composition.

2.7.2 Spirit

we utilize the reported APXS data for Spirit (*Gellert et al.*, 2006). The choice of a suitable rock composition in the context of the GS footprint is somewhat com-

Table 2.3: Identification information of APXS samples at both MER locations extracted from the work of *Gellert et al.* (2006) for Spirit and the Planetary Data System online for Opportunity. "R" refers to abrasion with the RAT, while "T" refers to excavation with the wheels. Sols are subsequent to landing at each site.

Rover	Sol	Sample type	Integration time (h)	Target name
Opportunity	81	T soil	4.0	BeagleBurrow_Trench
Opportunity	368	T soil	3.0	Left_of_peanut_TrenchFloor
Spirit	49	T hollows soil	6.5	Road Cut_Floor3_
Spirit	50	T hollows soil	7.6	Road Cut_WallMIonl
Spirit	60	R unaltered rock	5.0	Humphrey_RAT2
Spirit	114	T typical soil	9.9	Bighole_RS2
Spirit	115	T typical soil	4.0	Bighole_Trico
Spirit	140	T typical soil	8.3	Boroughs_Mills_bottom
Spirit	141	T typical soil	4.0	Boroughs_Hellskitchen_ side
Spirit	335	R altered rock	3.3	Wishstone_chisel_RAT

plicated at Gusev. The uncontaminated composition of rocks in the Gusev crater floor could be represented effectively by the APXS measurements following the second RAT application (RAT 2) on the plains rock "Humphrey" (Table 2.3) (*Gellert et al.*, 2004). Figure 2.1 includes a true color image of Humphrey courtesy of NASA/JPL/Cornell as posted at `http://marswatch.astro.cornell.edu/pancam_instrument/true_color.html`, along with other samples used in this work as posted at `http://marswatch.astro.cornell.edu/pancam_instrument/mosaics.html`. *Bell et al.* (2003), *Bell et al.* (2006a), and *Bell et al.* (2006b) describe the image processing techniques and Pancam instrumentation in detail. Locational information shown in Figure 2.1 as labeled tra-

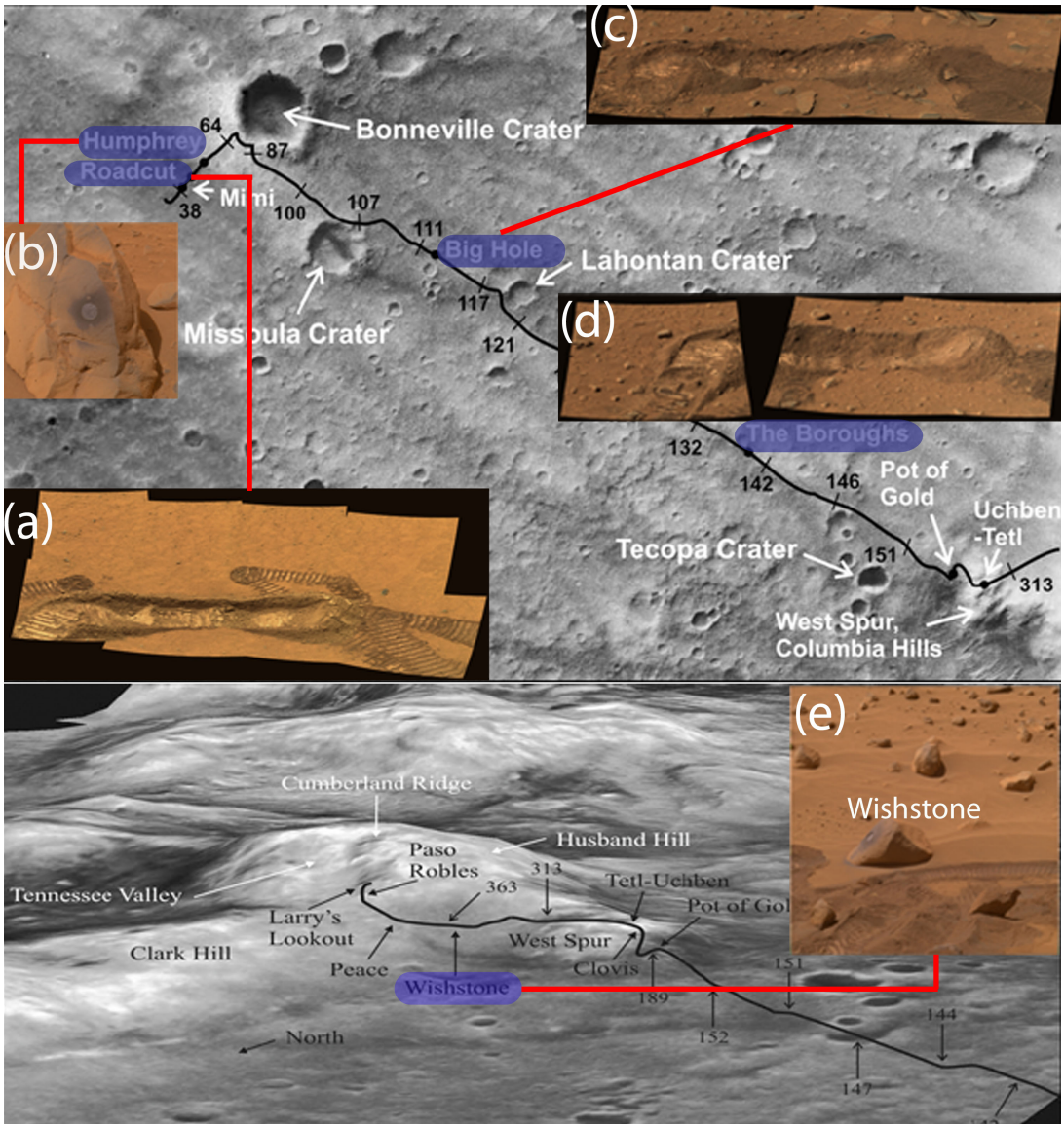

Figure 2.1: Images of rocks and trenches at Gusev that were used to obtain APXS data for our study as traverse map insets. Trenches and wheel tracks are ≈ 20 cm wide and RAT holes ≈ 5 cm across. The images are (sols parenthetical; ATCI: Approximate True Color image, TCI: True Color image):(a)ATCI mosaic of the "Road Cut" trench (47);(b)TCI of RATted "Humphrey"(60 sequence P2597). Humphrey is ≈ 60 cm tall;(c)ATCI mosaic of the "Big Hole" trench (116);(d)ATCI mosaic of the "Boroughs" trench (142). Boroughs is ≈ 11 cm deep;(e)TCI of "Wishstone" (342 sequence P2571). Note wheel tracks for scale. Additional image information available in Section 2.7.2 and APXS sample identification in Table 2.3.

verse maps was adapted from *Arvidson et al.* (2006).

Unlike Humphrey, rocks in the "Columbia" Hills are chemically altered, vary significantly in composition leading to at least five compositionally distinct classes, and are inferred to be geologically older (possibly Noachian) than the potentially Hesperian plains rocks (e.g., *Arvidson et al.*, 2006; *Cabrol et al.*, 2006; *Squyres et al.*, 2006a). While the Columbia Hills constitute < 5% of the area within Gusev crater, the crater itself, with a diameter of ≈ 160 km (*Squyres et al.*, 2004b), accounts for only ≈ 13 % of the GS footprint. The bedrock beyond the crater is more likely to be of a geological age comparable to the Columbia Hills than the Gusev plains. Consequently, using only Humphrey RAT 2 data to represent the rocks of Gusev may be more inappropriate than an areally weighted mean of Gusev plains and Columbia Hills rock compositions. We consider both options, as they reflect the complexity of Martian surface composition and the difficulty of selecting a particular composition to represent even a single location at the spatial scale of a GS footprint. Though found only as float, the composition of "Wishstone" class brushed and abraded rock (Figure 2.1 and Table 2.3) is used to represent the Columbia Hills rock composition as it has been fairly common in the Columbia Hills, and is similar in elemental composition to the "Watchtower" class of outcrop (*Squyres et al.*, 2006a; *Gellert et al.*, 2006).

Compositional differences between the typical crater floor soils (sampled with the "Boroughs" and "Big Hole" trenches, Figure 2.1 and Table 2.3) and "hollows" (sampled with the "Road Cut" trench, Figure 2.1 and Table 2.3) complicate the choice of a representative soil composition at Gusev. As discussed for Equations 2.1 and 2.2, we use four samples from Boroughs and Big Hole trenches to represent the typical soil, and two samples from the Road Cut trench

to represent hollows soil. Hollows appear to be relatively young eolian infill of small impact craters, while the surrounding plains contain mature soil material (e.g., *Haskin et al.*, 2005; *Wang et al.*, 2006). Furthermore, in spite of the ubiquity of hollows (*Golombek et al.*, 2006), plains soils are areally dominant along the rover traverse (*Arvidson et al.*, 2004a; *Grant et al.*, 2004). In light of these issues, we compute a 9 to 1 ratio mean of plains to hollows as the representative composition of soil at Gusev, which is supported in part by areal evidence presented by *Golombek et al.* (2006).

In spite of compositional complexities, trench data sampling up to $\approx 11\,\mathrm{cm}$ deep in the making of Boroughs are much more relevant at GS sampling depth scales than any surface soil measurement. The MER trench campaigns were motivated primarily by this consideration (*Wang et al.*, 2006), and have revealed the presence of significant compositional layering at tens of centimeter depths (e.g., *Haskin et al.*, 2005; *Soderblom et al.*, 2004; *Wang et al.*, 2006). This observation is not contradicted by the lack of evidence in GS data for Cl layering at large lateral spatial scales (*Keller et al.*, 2006a), since Br and Cl in particular have shown highly localized vertical variations at both Gusev (e.g., *Wang et al.*, 2006) and Meridiani (e.g., *Rieder et al.*, 2004).

2.7.3 Opportunity

In contrast to Gusev and other landing sites, the surface at Meridiani consists of a layer of soil with variable thickness locally exceeding $\approx 1\,\mathrm{m}$ (*Soderblom et al.*, 2004), overlying sulfate-rich sedimentary bedrock (e.g., *Grotzinger et al.*, 2005; *Jolliff and McLennan*, 2006; *McLennan et al.*, 2005; *Squyres et al.*, 2006b). There-

fore, the soil and bedrock can each be deeper than the tens of centimeter GS sampling depths, sometimes acting as a semi-infinite layer and sometimes not, complicating the analysis. However, bedrock exposures are sparse along the rover traverse and limited largely to craters (e.g., Victoria) and fractures (e.g., Anatolia) (*Squyres et al.*, 2004a, 2006c).

With the exception of a lag deposit of hematite spherules derived mostly from the bedrock, the soil is predominantly basaltic sand of potentially external origin (*Squyres et al.*, 2004a; *Weitz et al.*, 2006; *Soderblom et al.*, 2004). Furthermore, $w(H_2O)$ may be elevated in Meridiani outcrops (with a modeled maximum of $\approx 22\,\%$) due to hydrated sulfate minerals, while it is probably less than $4\,\%$ in the soil (*Clark et al.*, 2005). If applicable at GS footprint scales, this would attribute much of the GS-derived H content to the outcrop rather than the soil. Furthermore, with the exception of basaltic sands, the unique minerals at Meridiani may make the densities of its regolith components differ significantly from density estimates based on Viking observations (Sullivan, personal communication, 2005).

Such issues considerably weaken the relevance of Equations 2.1 and 2.4 in estimating a representative composition at Meridiani. However, as a first-order approximation to the representative Meridiani composition, we use Equation 2.1 assuming a rock-free surface (i.e., $A_r = 0$) dominated by the (hematite-free) basaltic component of the soil material. Even though the areal fraction of soil as determined with IRTM data is not $100\,\%$ (Table 2.1), it is sufficiently close to unity for our first-order approximation. As at Gusev, the areally dominant soil component – in the context of the GS sampling depths – was sampled by trenching experiments which also revealed the presence

of finer grains at depth in addition to the volumetrically abundant basaltic grains (*Weitz et al.*, 2006; *Sullivan et al.*, 2005). We represent this soil with the arithmetic mean (refer Equation 2.2 and related text for uncertainty estimation) composition at depth in two trenches, "BeagleBurrow_Trench" and "Left_of_peanut_TrenchFloor" (Table 2.3). The two trenches, inset in a traverse map courtesy of NASA/JPL/OSU as posted at `http://marsrovers.nasa.gov/mission/tm-opportunity/images/MERB_481_br2.jpg`, are shown in Figure 2.2. As evident in the low areal fractions of hematite and jarosite (*Klingelhöfer et al.*, 2004; *Morris et al.*, 2006), these two trenches effectively exclude the lag deposit and other contributions from the outcrop unlike those from sols 25 ("Trench_floor") and 26 ("Trench_sidewall"). We use the recalibrated APXS-derived mass fractions available in the Planetary Data System (PDS) at `http://pds-geosciences.wustl.edu/mer/mer1_mer2-m-apxs-5-oxide-sci-v1/merap_2xxx/data/apxs_oxides_mer1.csv`) as an update to those given by *Rieder et al.* (2004).

Complicating matters further, outcrop sampled in the current km scale traverse of Opportunity may not be representative of bedrock in the greater Sinus Meridiani region (e.g., *Edgett*, 2005) and by extension, within the GS's $\approx 440\,\mathrm{km}$ instrumental and $\approx 1\,800\,\mathrm{km}$ filter footprints. In addition, accurately modeling the compositional effect from rocks would require a checkerboard surface model, given the distinctly layered nature to the regolith at Meridiani. Such a model would consist strictly of weighting by the areal fractions of outcrop and soil without the use of bulk densities, since each layer would usually appear infinitely thick to the GS. However, a checkerboard model is unlikely to significantly improve the accuracy or precision of the calculated composition in the context of GS comparisons, particularly since the variability in soil depth is

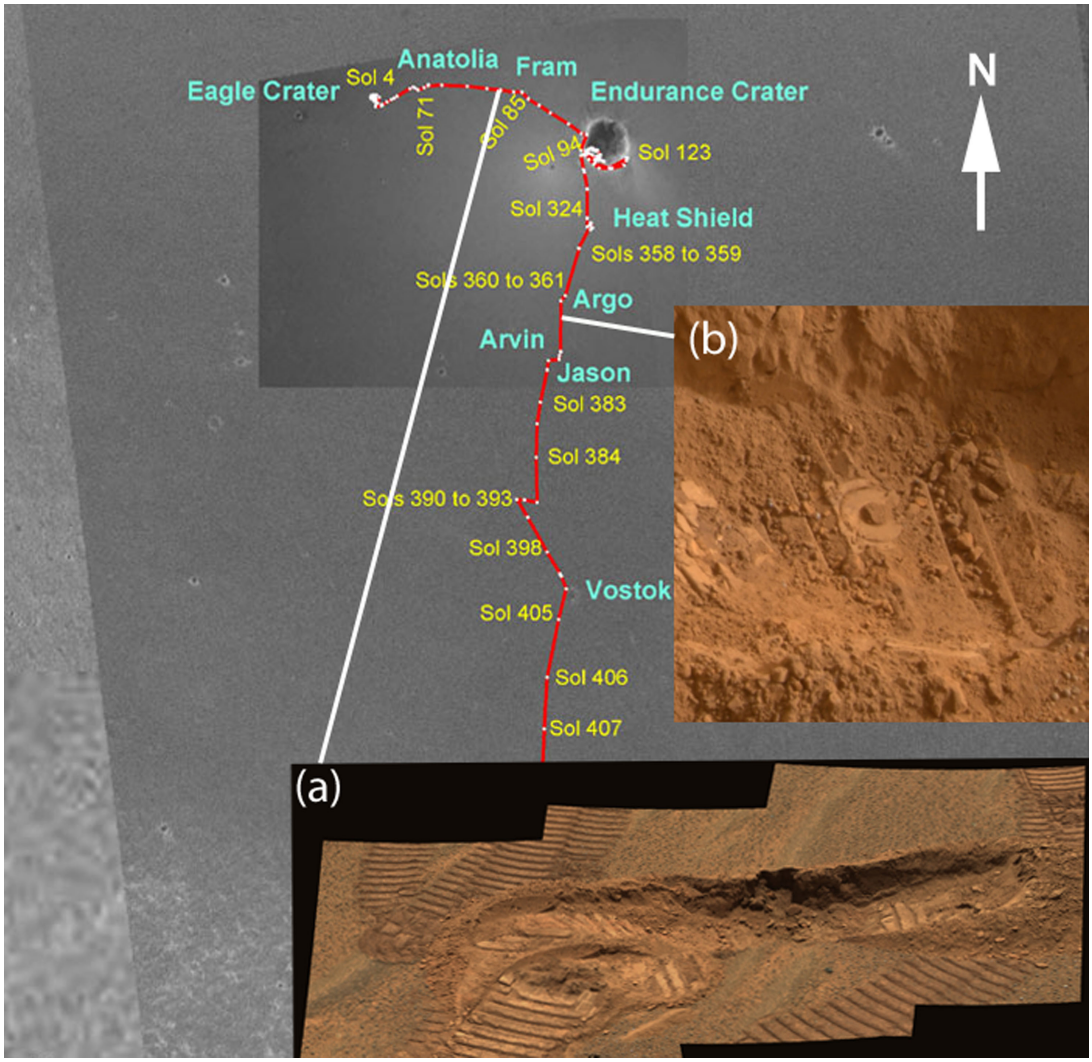

Figure 2.2: Images of trenches at Meridiani that were used to obtain APXS data for our study (Section 2.7.3) as traverse map insets. The width of each trench is ≈ 20 cm.(a)Approximate true color mosaic of the sol 81 "BeagleBurrow_Trench" area. The trench is ≈ 11 cm deep. Image courtesy of NASA/JPL-Caltech as posted at `http://marsrovers.jpl.nasa.gov/gallery/press/opportunity/20040428a/09-SM-02-TrenchPan-B093R1.jpg`;(b)Part of the sol 368 "Left_of_peanut_TrenchFloor" area in true color showing a Mössbauer imprint within. Image courtesy of NASA/JPL/Cornell as posted at `http://marswatch.astro.cornell.edu/pancam_instrument/images/True/Sol373B_P2552_1_True_RAD.jpg`.

poorly known.

2.7.4 Pathfinder and the GS normalization

The reported geochemistry of rock and soil material at Pathfinder shows less heterogeneity than those at either Gusev or Meridiani. In part this may be due to the short Pathfinder traverse of about 100 m (since Sojourner rover remained within $\approx$ 10 m of the lander throughout the mission) (*Golombek et al.*, 1999) relative to MER's km scale traverse. Pathfinder also lacked the capability to brush rock surfaces or abrade them, as the MER rovers have done with the RAT, which may have potentially concealed compositional variations. For example, complex alteration processes have produced both brushable surface accumulations and abradable alteration zones on rocks at both MER sites (e.g., *Hurowitz et al.*, 2006), the compositional effects of which cannot be removed by the S extrapolation method used at Pathfinder (*Wänke et al.*, 2001).

More important, the Pathfinder landing ellipse in Ares Vallis is larger (*Golombek et al.*, 1997) than those of either MER (*Arvidson et al.*, 2003; *Cabrol et al.*, 2003; *Golombek et al.*, 2003). While the landing ellipse is an engineering constraint, missions with smaller landing ellipses are capable of reaching landing sites that are geologically homogeneous over smaller scales. Consequently, the much larger Pathfinder landing ellipse – located in a region less diverse than either MER site – and its immediate neighborhood present a geologically less heterogeneous area that is better suited for comparison with the GS given its coarse spatial resolution. Ironically, the advantage offered by the MER mission with smaller landing ellipses is lost to the GS since both ellipses were chosen to

lie within geologically heterogeneous regions at GS footprint scales. For example – much as Lunokhod-2 was the first rover to traverse a geologic contact on the moon (e.g., *Basilevsky et al.*, 1977; *Basilevsky and Linkin*, 1996) – Spirit is the first rover to traverse a geologic contact on another planet (e.g., *Arvidson et al.*, 2006; *Crumpler et al.*, 2005).

The apparent compositional homogeneity at Pathfinder enables us to use revised values for all samples, as reported by *Wänke et al.* (2001), to estimate the mean compositions of soil and rocks. *Brückner et al.* (2003) provide details of the refined calibration that was used by *Wänke et al.* (2001). Data from both these papers are essentially in agreement. *Foley et al.* (2003) describe Pathfinder APXS data that were derived from an independent calibration and are very similar to those quoted by *Wänke et al.* (2001) and *Brückner et al.* (2003) for the major elements, while discrepancies exist for minor elements.

The representative composition at Pathfinder estimated from the work of *Foley et al.* (2003) is (50 ± 20)% higher for Cl and (30 ± 10)% lower for K than that based on values by *Wänke et al.* (2001). In spite of this, since all three works overlap within net uncertainties for the major elements Fe and Si, we do not anticipate significant changes to GS estimates should the data by *Foley et al.* (2003) be used. The Cr estimate has a minor caveat as well, since soil-free rock has been modeled without Cr (e.g., *Brückner et al.*, 2003; *Foley et al.*, 2003; *Wänke et al.*, 2001). As a result, the estimate of Cr assumes a modeled zero content of Cr in rocks, with only the uncertainty of w(Cr) in soil incorporated into Equation 2.2.

2.8 Sensitivity of Representative Compositions to Unknowns

The accuracy and precision of representative compositions are important considerations given the limited spatial sampling of in situ instruments, IRTM modeling of rock areal fractions, and Viking density estimates. As expected, the content of major elements, such as Si, is consistent across the landing sites and APXS measurements have rigorously quantified uncertainties. Rock areal fraction estimates from rovers and landers have been consistent with IRTM modeling as well. In addition, the density estimates are based upon reasonable parallels with terrestrial material. Collectively, these suggest that the representative compositions are sufficiently accurate for use at GS footprint scales and sampling depths, barring unknown systematic errors in instrument calibrations.

However, there is some variability in rock abundance due to the massive difference in sampling area between the surface instruments and GS. Density uncertainties are poorly constrained, since none of the missions had the means to determine densities. An additional uncertainty is introduced by the oxidation state of Fe, though again, a reasonable value was used in the calculations. A final uncertainty affecting the Gusev representative composition is the areal ratio of typical soil to hollows soil. We estimated the effects of these uncertainties by varying rock abundance, rock density, and soil density values by 50 %; varying the Fe oxidation state as +2, +2.5, and +3; and using a typical soil to hollows soil areal fraction ratio of 3 to 7. The alternative typical soil to hollows soil ratio was selected as a potential value at GS footprint scale, which is much larger than the Gusev crater, as well as to investigate compositional effects if hollows were to be areally dominant.

Table 2.4: Calculated representative in situ mass fractions and their GS-derived (*Boynton et al.*, 2007) counterparts (as %) at four landing sites, continued from Table 2.2

Element	Opportunity	Pathfinder	SpiritH	SpiritHW	Viking 1
Mn	0.273(0.011)	0.40(0.08)	0.252(0.008)	0.238(0.006)	-
Na	1.58(0.05)	1.0(0.3)	1.70(0.03)	1.88(0.16)	-
P	0.32(0.02)	0.42(0.07)	0.295(0.010)	0.49(0.15)	-
S	2.1(0.4)	2.2(0.5)	3.4(0.5)	3.4(0.5)	2.7(0.7)
Si	20.2(0.6)	21.0(1.9)	18.5(0.5)	18.4(0.5)	22.6(1.6)
GS-derived Si	19.8(0.5)	21.0(0.5)	19.6(0.5)		20.9(0.5)
Ti	0.677(0.017)	0.55(0.10)	0.469(0.016)	0.59(0.08)	0.41(0.05)

The effect of the Fe oxidation state was minimal, changing the representative composition by less than 1 %. Rock areal fraction and density variations caused representative compositions to vary by less than 7 % at most. While affecting only the Gusev representative composition the last issue, areal fraction ratio of typical soil to hollows soil, altered the S content by as much as 26 %, even though Si varied by only 6 %. This was a consequence of the elevated S levels at mid-depth in the Boroughs trench wall (e.g., *Wang et al.*, 2006). In summary therefore, with the exception of Gusev, poorly constrained parameters in the representative composition calculation are unlikely to cause more than a 10 % relative uncertainty. While Gusev may be subject to a higher uncertainty, major elements such as Si are still unlikely to vary by more than 15 %. We report standard errors – computed with Equation 2.2 – in Tables 2.2 and 2.4 to one significant figure with the exception of those with 1 or 2 as the leading digit where

we report to two significant figures. We accordingly retain the last significant figure of the result to be of the same order of magnitude as the uncertainty (e.g., *Taylor*, 1982, pp. 15–21).

2.9 Discussion of Results

The representative in situ compositions as computed above are listed in Tables 2.2 and 2.4. As evident in Figure 2.3, the concentrations of major elements vary less and have smaller relative uncertainties than those of many minor elements. Consider for example the difference in variability and uncertainty between K (dynamic range approximately a factor of 3) and Si (dynamic range approximately a factor of 1.2). Furthermore, the variability of K as represented by the standard deviation of the mass fractions is 49 % of the (arithmetic) mean w(K) of all landing sites, while the variability is only 9 % for Si and Fe. The similarity in major elements across the four sites suggests that normalizing w(Si) to Pathfinder is unlikely to introduce systematic errors. On the other hand, normalization of minor elements to in situ values would have been more prone to error, given the variability and associated uncertainties of their mass fractions across the landing sites. The geochemical implications of representative in situ compositions, particularly in terms of their comparison with GS data, are discussed in Chapter 5 as well as by *Boynton et al.* (2007), *Keller et al.* (2006b), *Newsom et al.* (2007), *Taylor et al.* (2006a), and *Taylor et al.* (2006b).

Comparison of the two representative in situ compositions estimated for Gusev, as described in Section 2.7.2, provides insight into the impact on the representative composition from the compositional variability of different rock types

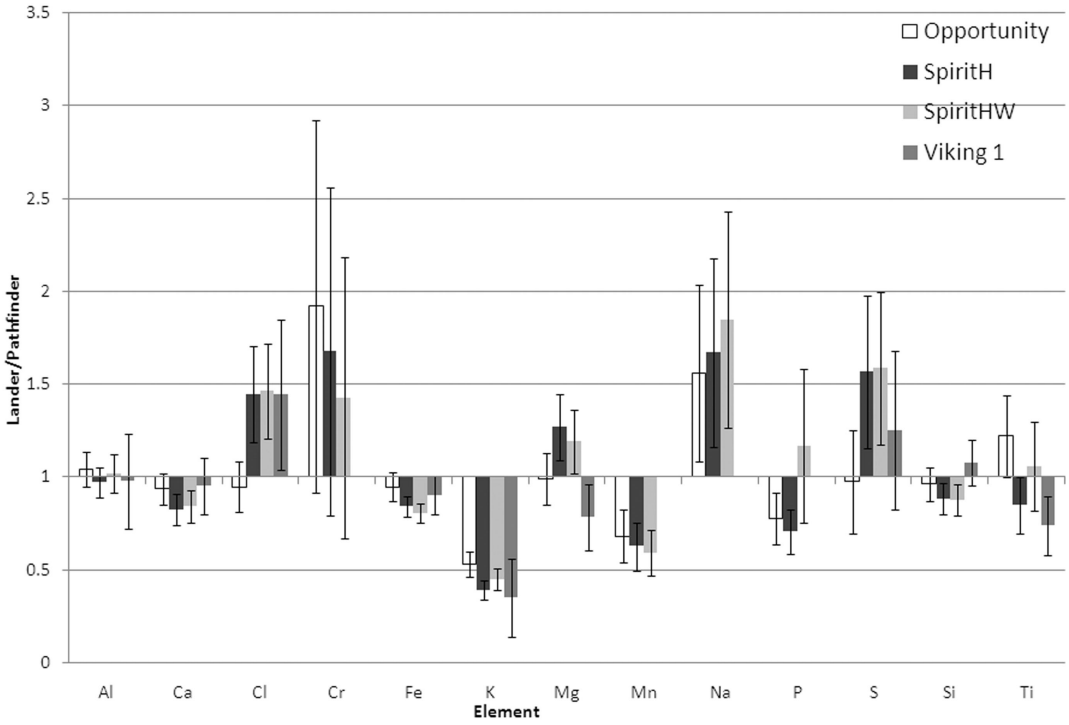

Figure 2.3: The variation in chemistry across the landing sites as the ratio of the chemical composition at each site to that at the Pathfinder site (data from Tables 2.2 and 2.4). Deviation of the ratio from unity reflects differences with the Pathfinder composition. Error bars represent the standard error, $1s_{\mathrm{m}}$, of the ratio as obtained by substituting the ratio for f in Equation 2.2. The text related to Equation 2.2 identifies the uncertainties that have been included in the error propagation. Note that Cr, Mn, Na, and P data are unavailable for Viking 1. SpiritHW uses an area-weighted mean of Humphrey and Wishstone compositions while SpiritH only uses the composition of Humphrey.

at a single landing site. That the impact is minor is evident in Figure 2.3, where the representative concentrations of most elements are similar even though Humphrey and Wishstone are compositionally distinct even with respect to major elements such as Fe (e.g., *Gellert et al.*, 2006). The primary reason for the subdued effect is the areal dominance of the soil component which, due to the general absence of striking differences in soil composition between the plains

and Columbia hills (e.g., *Arvidson et al.*, 2006), was taken to be compositionally uniform both within and beyond Gusev crater. As we mention in Chapter 5, since the soil component is areally dominant across much of Mars (e.g., *Newsom et al.*, 2007), the GS should also be more sensitive to compositional variations of the Martian soils than of rocks. GS data indicate significant chemical variations in soil (*Newsom et al.*, 2007) in spite of evidence for compositionally similar soils across landing sites (e.g., *Yen et al.*, 2005).

The GS-determined K content at Pathfinder is higher at the $1s_{\mathrm{m}}$ level relative to the K content at the other sites, though not at the $2s_{\mathrm{m}}$ level (Tables 2.2 and 2.4). Si does not appear enriched at Pathfinder even at $1s_{\mathrm{m}}$ (Table 2.4), which is consistent with the absence of Si enrichment in surface type 2 material that we discuss in Chapter 5. The GS estimates are compared with the representative in situ estimates in Figure 2.4. In addition to the Si mass fractions, which approximate in situ values by virtue of the normalization, Cl and K also compare favorably. The favorable comparison for Cl (which overlaps with the GS value within $2s_{\mathrm{m}}$) lends additional support for the Si normalization (*Boynton et al.*, 2007). The favorable comparison for K – for which the GS and in situ values overlap within $1s_{\mathrm{m}}$ at Opportunity and Viking – is specially significant, since K is a radioactive element unaffected by capture and scatter processes.

However, the GS estimate of Fe content appears to be consistently higher, even though the relative difference, varying from a low of 10 % at Meridiani to a high of 20 % at Gusev, is always less than $3s_{\mathrm{m}}$. Since the disparity exists across all landing sites in the same direction, it is unlikely to be an effect of the simplifications and sample selections we made in calculating representative in situ compositions at the four sites. *Boynton et al.* (2007) discuss the implications

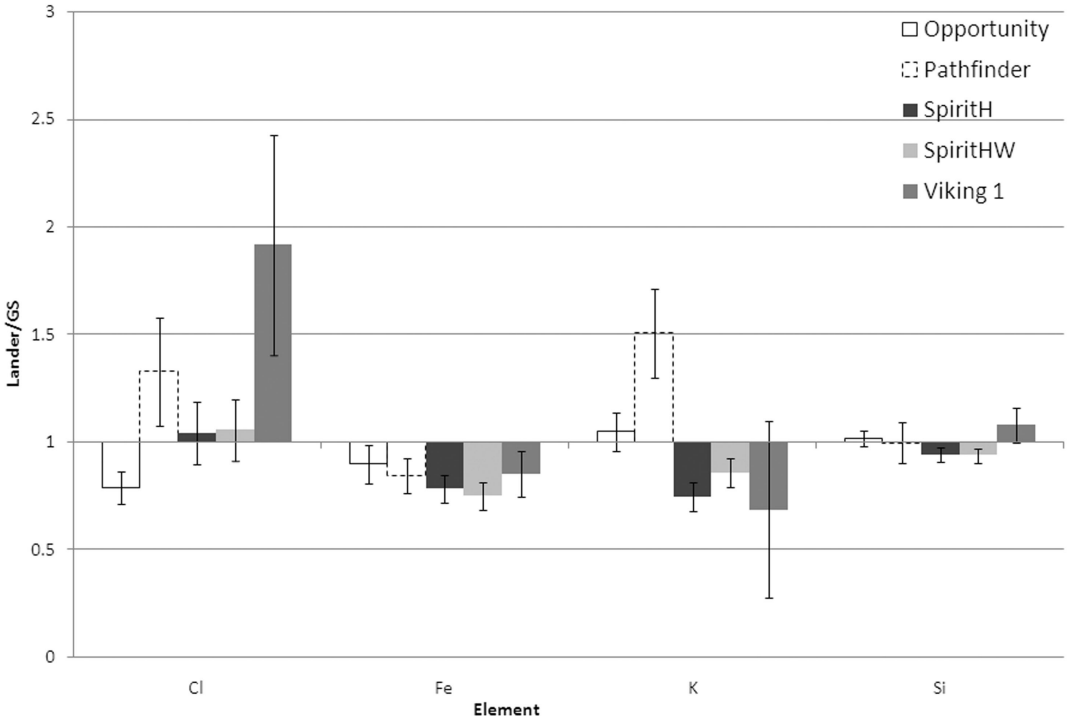

Figure 2.4: Representative in situ compositions compared with corresponding GS estimates for the four elements observed in common (Tables 2.2, 2.2) as the ratio of the calculated in situ value to the GS estimate at each landing site. Interpretation as in Figure 2.3. Note that the Si ratio for Pathfinder is unity by virtue of the GS normalization.

of these comparisons in depth.

2.10 Conclusions

Our study estimating the representative in situ compositions at four landing sites is an example of the synergy between remote sensing and surface missions (cf., *Bibring et al.*, 2006a). For example, the GS determination of H and IRTM determination of rock abundance can be combined with surface data to derive representative in situ chemical compositions across large areas even though

data from surface instruments are inherently local in scope. This method of estimating representative compositions at landing sites is applicable to future remote sensing missions as well. In addition, the representative in situ compositions that we derive (Tables 2.2 and 2.4) may be used in the normalization and "ground truth" comparisons of future remote sensing missions that have depth and lateral spatial resolutions comparable to the GS. As expected at such spatial scales the concentration of major elements tends to be similar across landing sites. However, the compositional diversity evident at the MER sites should be utilized for remote sensing missions with finer lateral spatial resolution.

Future constraints on Martian regolith mechanical properties would help increase the precision of our estimates, since bulk density uncertainties (refer Section 2.5) dominate the standard errors in Tables 2.2 and 2.4. Furthermore, as revealed by the extreme cases in Section 2.8 and given the areal dominance of soil, better constrained densities and areal fractions of regolith components, not elemental oxidation states, would enhance the accuracy of our calculations. In this respect, the future availability of high resolution images and spectral data (such as the Mars Reconnaissance Orbiter data) for the different landing sites would be very useful, since it would greatly enhance the estimates of relative amounts of different regolith components over the entire GS footprint at each landing site. In addition, improved remote sensing data may help reveal and establish the GS footprint most representative of a given landing site, even when it is not centered at the site coordinates. Such improvements would be further enhanced by more realistic modeling of material mixing geometries (e.g., *Kim et al.*, 2006a) by revealing the compositional effect of rocks in spite of their low areal abundance. Better constraints on the surface GCR flux with the Mars Science Laboratory Radiation Assessment Detector (*Hassler et al.*, 2006; *Cucinotta*

et al., 2007) may help refine the GS forward modeling as well.

CHAPTER 3

RECIPES FOR SPATIAL STATISTICS

3.1 Core Concepts

While the processing methods will differ across missions, most global remote sensing missions generate data types analogous to those of the GS discussed in Section 2.2. User level data can be broadly divided into bin data and regional data (Section 2.2). Bin data would necessarily be of global extent for the user to freely select desired subsets. The fineness of a bin would invariably be a compromise among the need to maximize data, to minimize spurious spatial effects of data processing, and to minimize information redundancy.

Information redundancy occurs when the "actual" information content is less than that implied by the amount of data. The most common cause of information redundancy is spatial autocorrelation, the numerical similarity of spatially adjacent values. While this is unavoidable in spatial data, spatial autocorrelation is aggravated whenever convolution filters, such as mean filters (e.g., Section 2.2), are applied to the original data. The effect of spatial autocorrelation on key parameters is discussed in Section 3.2.1, and the implications of spatial autocorrelation on spatial correlations among attributes is discussed in Chapter 4.

In addition to the attribute values, each bin datum must also contain location information (typically as latitude and longitude coordinates) and the numerical uncertainty (i.e., standard error). The numerical uncertainty represents the random statistical fluctuation that may occur in the attribute value at a bin due to

limitations of the measurement technique under normality assumptions. For an attribute, c, we represent the value at the i^{th} bin by c_i and the corresponding numerical uncertainty (standard error) by s_i.

3.1.1 Sample Versus Population

The distinction between the population and sample for remotely sensed data may seem a matter of semantics. That is not so. For both global and regional datasets, be it from the Mars Odyssey or other missions, appropriate statistical analyses cannot be applied until the sample and population (also known as "parent population" or "superpopulation") are distinguished. Typically, the population consists of all possible intrinsic values of the attribute under observation, while the sample consists of either experimental observations or a subset of the dynamic range of the attribute. For example, several measurements of the mass fraction of an element at a given location would constitute a sample. Instrumental uncertainties and sensitivity constraints always prevent exact measurement of such a continuous valued attribute, whether the measurement be made remotely, as with the GS, or locally, as with the MER APXS (*Rieder et al.*, 2003).

Remote-sensing maps of attributes remain estimates, not exact measurements, of the intrinsic values. As a result, global binned datasets are typically samples, not the populations, of the remotely observed attributes (mass fraction of an element in the case of the GS). It is difficult to conjure examples where the observations themselves could constitute the population for a continuous valued geospatial attribute. Such cases are easier to realize for discrete val-

ued attributes such as crater counts for a specified minimum diameter. Even then, the observed may not be the true value or the only possible state (for example, geologic processes subdue crater morphology over time). Consequently, throughout this discussion we consider the observed to be a sample, rather than the population, to ensure better determination of uncertainties in statistical inferences. More general discussions of populations and samples are available in literature (e.g., *Haining*, 2003, pp. 51–54).

3.2 Key Parameters

A population or sample is described primarily in terms of its distribution. The distribution describes the frequency of values in a dataset, consequently enabling probabilistic (i.e., stochastic) estimates. Statistical analyses frequently require the distributional properties of the dataset to be summarized. This is achieved by means of parameters (also called population statistics), which characterize the population, and estimators (also termed sample statistics) of these parameters as determined from the sample. The value of an estimator is called an estimate. In most cases, the parameter values are unknown and their (sample) estimates are used for analysis. This invariably involves a loss in the degrees of freedom, typically negligible for large datasets, with the usual convention a loss of one degree of freedom for each parameter estimated from the sample (e.g., *Young*, 1962, pp. 46–47).

Notational conventions help minimize confusion between references to the population and to the sample. Three popular conventions are to denote population statistics by Greek characters, sample statistics by Roman characters, and

estimate of a population statistic (value of an estimator when used to represent the value of a parameter) by a caret above the Greek symbol. For example, the population mean is given by μ (i.e., a parameter or population statistic), the sample mean by m (i.e., an estimator or sample statistic), and sample mean as an estimate of the population mean by $\hat{\mu}$. Since m and $\hat{\mu}$ are numerically identical, only the first is used throughout this chapter for typographic ease. We use this notation consistently, representing all sample statistics and estimates of the population statistics by roman characters. We adhere to these and other notational conventions in statistical literature (e.g., *Bevington and Robinson*, 2003; *Easton and McColl*, 1997; *Haining*, 2003; *Upton and Fingleton*, 1985; *Rawlings et al.*, 1998) and established stylistic forms such as those by *Mills et al.* (1993, p. 5, 44, 47, 59–62, 77, 83) and *Göbel et al.* (2006, p. 130–135).

Properties of a random normal (i.e., Gaussian or bell-curve) data distribution are frequently understood in terms of the mean, μ, and standard deviation, σ, parameters. The corresponding sample estimators are m and s, respectively. s represents the dispersion as the square root of the variance (i.e., variability of values about the corresponding mean), with the implicit estimation of μ resulting in the loss of a degree of freedom in the calculation. Other measures of dispersion include quartile deviation and median deviation (e.g., *Bevington and Robinson*, 2003). The dispersion is typically due to a combination of actual variation in the attribute and random statistical fluctuations in the measurement. This may be conceptualized as an expression: spatial data = large (macro) scale variability + small (meso) scale variability + error (*Haining*, 2003, p. 185). Macro-scale variability is typically evident at global scales, while meso-scale variability occurs at the scale of the detector's spatial resolution. Error represents the random statistical fluctuations, often due to instrumental lim-

itations.

If the standard deviation, s, is primarily due to the error term, the apparent variability of the attribute across the planetary surface becomes meaningless. This determination requires an independent measure of the contribution to variability from numerical uncertainties. For the usual case, where each bin of a global dataset contains location coordinates, the attribute value, and the standard error of the value, the error term may be estimated directly as the root-mean-square of standard errors (s_{rms}) of all bins. As long as s is satisfactorily greater than s_{rms}, we consider the dispersion of the data to be meaningful, enabling a meaningful characterization of the distribution. Given the importance of the mean, standard deviation, and the root-mean-square of standard errors, we discuss them in detail below.

3.2.1 Mean and Standard Error

When all the data are known to be sampled from distributions that have identical variances, i.e., when data are homoscedastic, the sample mean (m) is simply the arithmetic mean:

$$m = 1/N \sum_{i=1}^{N} c_i \tag{3.1}$$

where N is the number of data and c_i is the value of the i^{th} datum. Homoscedastic data are rare among geospatial attributes, since the standard errors typically vary across the bins leading to heteroscedasticity. It is possible to derive an expression for the mean in the presence of heteroscedasticity by resorting to the notion of maximum likelihood that the observed are the most likely

data (Chapter4). By further assuming that each datum is sampled from a random normal distribution (i.e., Gaussian distribution), which is a reasonable assumption when the datum is based upon a large number of observations of a continuous-valued variable, maximizing the probability for the entire dataset yields:

$$m = \frac{\sum_{i=1}^{N} \frac{c_i}{s_i^2}}{\sum_{i=1}^{N} \frac{1}{s_i^2}} \tag{3.2}$$

where s_i is the standard error of the i^{th} datum (e.g., *Young*, 1962, pp. 107–108). In this context, each datum is regarded as belonging to a gaussian with the probability density function (ρ_i) given by:

$$\rho_i(x) = \frac{1}{s_i \sqrt{2\pi}} \exp\left(-\frac{(x - c_i)^2}{2s_i^2}\right) \tag{3.3}$$

where x is continuous-valued. For example, the 68 % confidence interval of c_i would be given by $c_i \pm s_i$. As such, the standard error (s_i) of the bin value is computed from counting statistics in the case of the GS and represents the precision of each datum. For example, the standard errors of capture-derived elemental mass fractions are computed by propagating the spectral fit uncertainties and the uncertainties of the capture correction factors.

In addition to the issue of heteroscedasticity, the mean of a spatial dataset may also be affected by the disparity between how the instrument observes the planet (which is a nearly-invariant circular footprint for the GS, as discussed in Section 2.2) and the simple cylindrical (i.e., Plate Carée) projection of data onto a grid of bins. Since this projection distorts area by generating a rectangular map on which the bin centroids are latitudinally and longitudinally equispaced, it may be useful to compare the mean values from Equations 3.1 and 3.2 with one

that assigns greater significance to bins that have greater area. The corresponding expression is fairly straightforward for the arithmetic mean (Equation 3.1):

$$m = \sum_{i=1}^{N} c_i \frac{a_i}{A} \tag{3.4}$$

where a_i is the area of the i^{th} bin and,

$$A = \sum_{i=1}^{N} a_i \tag{3.5}$$

By assuming Mars to be spherical, a_i may be computed as directly proportional to a simple expression:

$$a_i = K\Big(sine(\varphi_{i,N}) - sine(\varphi_{i,S})\Big)\Big(\theta_{i,E} - \theta_{i,W}\Big) \tag{3.6}$$

where K is the constant of proportionality, $\varphi_{i,N}$ is the latitude of the northern boundary of the bin, $\varphi_{i,S}$ is the latitude of the southern boundary, $\theta_{i,E}$ is the longitude of the eastern boundary, and $\theta_{i,W}$ the longitude of the western boundary (e.g., *Thornton and Marion*, 2003, p. 610). The area-weighted counterpart of the maximum likelihood mean (Equation 3.2) is given by,

$$m = \frac{\sum_{i=1}^{N} \frac{a_i c_i}{s_i^2}}{\sum_{i=1}^{N} \frac{a_i}{s_i^2}} \tag{3.7}$$

where a_i is as given by Equation 3.6 and the remaining symbols are as previously defined. It is important to note that equations 3.1, 3.2, 3.4, and 3.7 all assume the absence of spatial autocorrelation (Section 3.1). Nevertheless, as the estimation of the mean is generally unbiased by the presence of spatial autocorrelation (e.g., *Haining*, 2003, pp. 273–286), these expressions usually approximate

Table 3.1: Mean percentage mass fraction of Cl in the midlatitudes, subject to the Hmask (Section 2.3.4), as estimated directly by cumulative spectra (*Keller et al.*, 2006b, Table 2), and by the arithmetic mean (Equation 3.1), maximum likelihood mean (Equation 3.2), area-weighted mean (Equation 3.4), and area-and-standard-error-weighted mean (Equation 3.7). Note that the standard error is reported only for the cumulative spectral estimate, as the standard error calculated with bin values would be highly biased due to spatial autocorrelation.

Method	Mean mass fraction
Cumulative spectrum	0.49 ± 0.03
Arithmetic mean	0.48
Maximum likelihood mean	0.47
Area-weighted mean	0.49
Area and standard error weighted mean	0.48

direct regional spectral estimates of the mean for the GS-derived elemental mass fractions (Section 2.2). For example, the midlatitudinal mean mass fraction of Cl as estimated by a direct cumulative spectrum compares favorably with that computed from the preceding equations as evident in Table 3.1. Nevertheless, the direct determination of the regional average of a geospatial attribute would be more robust than the bin-based computation of the same.

The issue of spatial autocorrelation is an important one for data sets that are subject to spatially large filters, such as the mean filter applied to the GS-derived data. While such filters help minimize noise (Section 3.2.3), they also induce significant spatial uncertainty in the data. In essence, bin values that are spatially proximate relative to the scale of the filter become mutually dependent, causing the degrees of freedom of the data set to be less than the apparent number of data. Fortunately, this does not induce a significant bias in the standard devia-

tion or the mean calculated with bin data (e.g., *Haining*, 2003, pp. 273–286).

However, the calculation of the standard error (s_m) (i.e., uncertainty of the mean) becomes difficult, as the standard formula in the absence of heteroscedasticity,

$$s_m = \sqrt{s/N} \tag{3.8}$$

where s is the standard deviation, as well as the maximum likelihood estimate,

$$s_m = 1/\sqrt{\sum_{i=1}^{N} \frac{1}{s_i^2}} \tag{3.9}$$

where s_i is the standard error of the i_{th} bin value, (e.g., *Young*, 1962, pp. 106, 108) both explicitly and implicitly use the number of bins as N. It is possible to adjust N to account for spatial autocorrelation by estimating the degree of spatial autocorrelation with a semi-variogram (Chapter4). However, due to issues with scaling N (e.g., *Dutilleul et al.*, 1993), a more robust approach is to estimate the regional/global mean and the standard error by accumulating data over the entire region/planet in question. For example, the most robust estimate of the midlatitudinal mean mass fraction and corresponding standard error for an element is obtained with the cumulative γ photon spectrum over the midlatitudes. Particularly for the GS, we would discourage the estimation of standard error by means of the bin values or their standard errors as either approach usually underestimates the actual standard error. For example, calculation with bin values/standard errors underestimates the actual standard error of the midlatitudinal mean mass fraction of Cl by a factor of 10.

3.2.2 Standard Deviation

As initially noted, the standard deviation (s) is the key measure of dispersion in the distribution of attribute values. The expression for s is simplest under homoscedastic conditions:

$$s = \sqrt{\frac{1}{N-1}\sum_{i=1}^{N}(m - c_i)^2} \tag{3.10}$$

where m is as determined by any one of the formulas in Section 3.2.1. While not of any practical significance, N is reduced by one due to the use of the estimate m as opposed to the (unknown) population parameter μ (e.g., *Young*, 1962, pp. 46–47). When area weighting is included, the formula is modified to:

$$s = \sqrt{\frac{1}{A(N-1)}\sum_{i=1}^{N}a_i(m - c_i)^2} \tag{3.11}$$

where a_i is the area factor given by Equation 3.6, and A is given by Equation 3.5. The two alternatives for s are often similar valued as long as the region in question does not involve large variations in latitude particularly closer to the poles where a_i decreases most rapidly with latitude (Equation 3.6). For example, the standard deviation of midlatitudinal Cl mass fractions (subject to the Hmask as discussed in Section 2.3.4) from Equation 3.10 is 0.0950 %, while that from Equation 3.11 is 0.0952 %.

Given the difficulty of decoupling the macro-scale variability from mesoscale variability and numerical uncertainties, we do not discuss analogs of Equations 3.2 and 3.7 in the calculation of s. Furthermore, since the mesoscale variability invariably requires bin data, the regional s cannot be estimated directly with the instruments, unlike for the regional average in Table 3.1.

3.2.3 RMS Standard Error

As previously discussed, the primary utility of the root-mean-square of standard errors (s_{rms}) is to determine whether macro-scale variability is significant despite the statistical variability due to numerical uncertainties of attribute values. As in sections 3.2.1 and 3.2.2, the calculation is straightforward when area weighting is not a concern:

$$s_{rms} = \sqrt{\frac{\sum_{i=1}^{N} s_i^2}{N}} \tag{3.12}$$

where the notation is as before. Even though it is also possible to compute the arithmetic mean of the absolute standard errors, the root-mean-square calculation used here is more widely used (e.g., *Young*, 1962, pp. 14–15). It is possible to modify this formula to adjust for area:

$$s_{rms} = \sqrt{\sum_{i=1}^{N} s_i^2 \frac{a_i}{A}} \tag{3.13}$$

where a_i is given by Equation 3.6 and A by Equation 3.5. An important observation across all of Sections 3.2.1 through 3.2.3 is that the area-weighted equations simplify to the unweighted counterparts in the ideal case where $a_i = a_j$ for $i \neq j$, as further reinforced by the similarity of differently computed mean values in Table 3.1.

In essence, s_{rms} represents the numerical uncertainty of a dataset on a per-bin basis and can be used to indicate the precision with which an attribute has been measured globally. For example, stated as a fraction of the corresponding global mean (Section 3.2.1) subject to the Hmask (Section 2.3.4), s_{rms} is 10 % for Cl, 8 % for Fe, 11 % for H, 7 % for K, 2 % for Si, and 10 % for Th. Obviously, the smaller

the fraction, the greater the precision of the data. As discussed before, another essential utility of s_{rms} is to determine whether the apparent spatial variability of the data is meaningful. The greater the value of s relative to s_{rms}, the greater the likelihood that dispersion is not solely due to numerical uncertainties. As evident in Figure 3.1, and consistent with the discussions by *Taylor et al.* (2006a) and *Keller et al.* (2006b), the standard deviation is sufficiently higher than s_{rms} for all elements subject to the mean filter, satisfying this necessary condition for spatial variations in composition to be meaningful. The enhanced variability relative to the numerical uncertainty is a direct benefit of the mean filtering, as s_{rms} generally approximates s prior to filtering.

3.3 What Distribution?

As discussed earlier, m and s are the key estimators that characterize a random normal distribution and are most informative when the underlying distribution is random normal. We describe a few tests that may be used to determine whether a distribution is random normal. The test results are utilized in works that identify chemically distinct regions within the GRS data set (*Karunatillake et al.*, 2007, and Chapter 6). An attribute distribution may be characterized qualitatively with a kernel density plot (e.g., *Sheather and Jones*, 1991), and as shown in Figure 3.2, elemental mass fractions are indeed approximately bell-curves without strong evidence for multimodality and other deviations. The qualitative observation of normality may be complemented by quantitative measures such as kurtosis excess and skewness. Skewness is a measure of asymmetry in the distribution relative to a random normal distribution, and may be computed

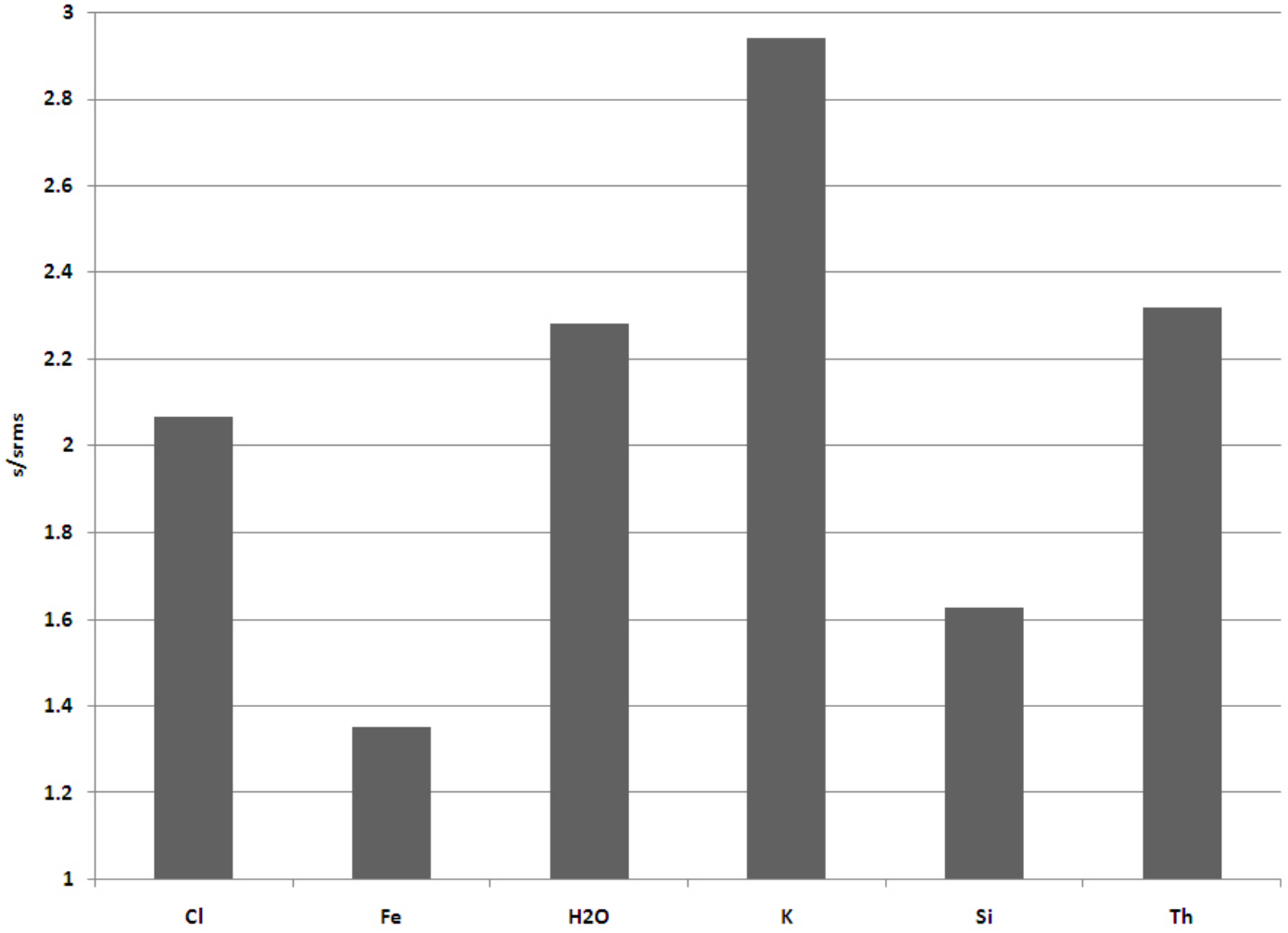

Figure 3.1: Plot of the standard deviation (s) divided by the root-mean-square standard error (s_{rms}) of elemental mass fractions.

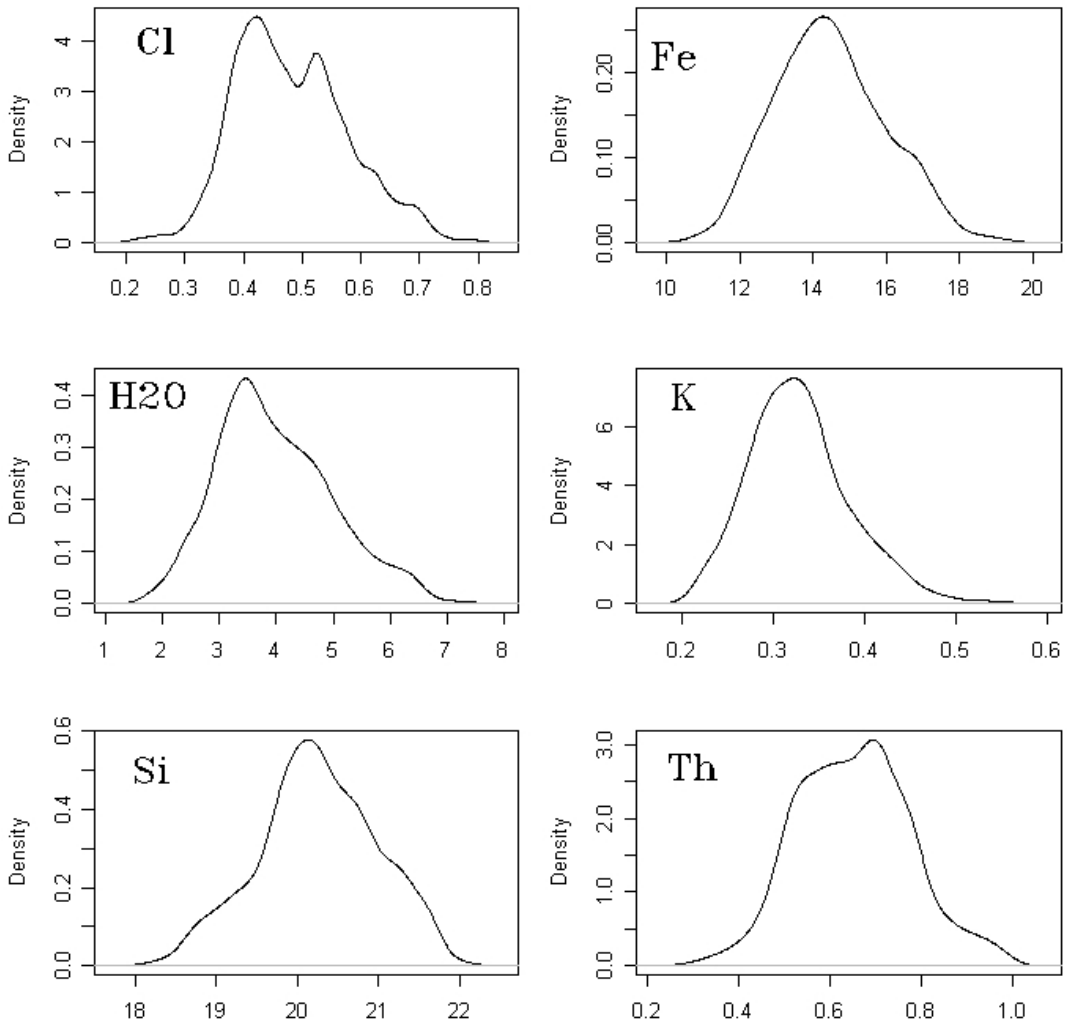

Figure 3.2: Kernel density plots of midlatitudinal distributions of mean-filtered elemental (and for the case of H, stoichiometrically equivalent H_2O) mass fractions. Mass fractions (as % with the exception of Th as mg/kg) are the abscissa, while the probability densities are the ordinate. Note the nearly bell-shaped curves, with only Cl showing a slight hint of bimodality.

as (e.g., *Press et al.*, 2007, pp. 723–724):

$$skewness = \frac{\frac{\sum_{i=1}^{N}(c_i - m)^3}{N}}{\left(\frac{\sum_{i=1}^{N}(c_i - m)^2}{N}\right)^{3/2}} \tag{3.14}$$

where the symbols are as before. A negative skewness indicates that relative to a random normal distribution, the observed distribution has a long tail of values less than the mean (i.e., skewed to the right), while a positive skewness indicates the presence of a long tail of high values (skewed to the left). On the other hand, kurtosis excess (γ_2) indicates the shape of the peak of the distribution relative to that of a random normal distribution, and may be computed as (e.g., *Press et al.*, 2007, p. 724):

$$\gamma_2 = \frac{\frac{\sum_{i=1}^{N}(c_i - m)^4}{N}}{\left(\frac{\sum_{i=1}^{N}(c_i - m)^2}{N}\right)^{2}} - 3 \tag{3.15}$$

where the notation is as before. A positive γ_2 indicates that the distribution is more peaked than a gaussian distribution (i.e., leptokurtic), while a negative γ_2 indicates that the distribution has a flat peak relative to that of a gaussian (i.e., platykurtic) (e.g., *Press et al.*, 2007, p. 724). However, it must be remembered that as skewness (Equation 3.14) and excess kurtosis (Equation 3.15) are functions of the third and fourth central moments, they have greater uncertainties than first central moments such as the mean (e.g., *Press et al.*, 2007, p. 723). In particular, excess kurtosis is a poorly understood parameter (e.g., *Dodge and Rousson*, 1999). Alternatives to Equations 3.14 and 3.15 are available in the literature (e.g., *Joanes and Gill*, 1998).

In our case study with the elemental mass fractions, the skewness and excess kurtosis coefficients do not suggest strong deviations from a random normal distribution, even though some deviation is evident (Table 3.2). Given the dif-

Table 3.2: Skewness and excess kurtosis coefficients for GRS-derived elemental mass fraction distributions in the midlatitudes of Mars. Positive skewness indicates a long tail of values greater than the global mean, while a negative skewness indicates a long tail of values less than the global mean. Positive excess kurtosis suggests a distribution more sharply peaked than a Gaussian, while a negative value would indicate a less sharply peaked distribution.

Element	Skewness	Excess kurtosis
Cl	0.39	-0.14
Fe	0.27	-0.27
H	0.48	-0.093
K	0.64	0.22
Si	-0.12	-0.34
Th	0.18	-0.51

ficulty of making detailed interpretations on the basis of such deviations (e.g., *Balanda and MacGillivray*, 1988), we do not analyze these results further. Nevertheless, the approximation to a random normal distribution is also supported by the Shapiro-Francia test of normality (Chapter4), since scatter plots of ordered elemental mass fractions versus normal order statistics show strong correlations without anomalous shapes to the curve (Figure 3.3).

3.4 Common Questions

Once the distribution of attribute values has been characterized using the techniques outlined in the preceding sections, it is possible to answer several questions that commonly arise when attempting to determine the distinctness of a

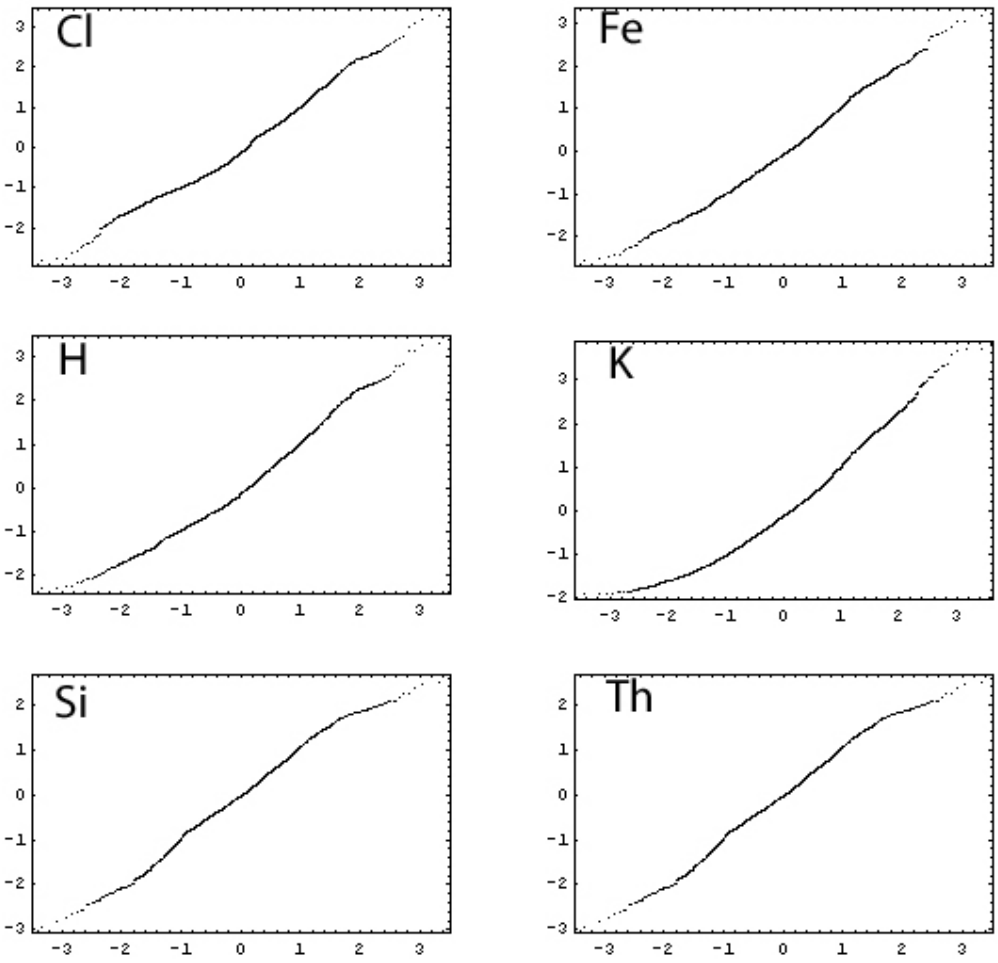

Figure 3.3: Plots of sorted elemental mass fractions versus normal order statistics for the midlatitudes of Mars.

region of interest. These queries are: (1) Can we reject, to a desired degree of confidence, the null hypothesis that the data within region A are from the samedistribution as the data within region B?; (2) How does the distribution of the attribute in region A compare qualitatively with that in region B?; (3) Can we reject, to a desired degree of confidence, the null hypothesis that the mean value of the attribute within region A is identical tothat within region B?; (4) Is the attribute heterogeneous within region A?; and (5) How are the solutions to the preceding questions altered when the ratio of two attributes is being in-

vestigated? In these contexts, "A" would be the region of interest, and "B" the one relative to which it is being evaluated. Obviously, "B" could also be the global distribution, in which case the queries would describe how the regional distribution compares with the global counterpart.

Before we lay out the statistical methods to address these questions, several concepts on the efficacy of statistical tests need to be kept in mind. The first, type 1 error, refers to a statistical test rejecting the null hypothesis even though it happens to be true. Such errors are the gravest, causing the researcher to favor an incorrect model. The second, type 2 error, occurs when the null hypothesis is in fact false but the test fails to to reject it. The power of a test is the probability that it will not cause a type 2 error. These concepts are discussed in detail by *Easton and McColl* (1997, `http://www.stats.gla.ac.uk/steps/glossary/hypothesis_testing.html`) and *Helsel and Hirsch* (2002, `http://pubs.usgs.gov/twri/twri4a3/pdf/chapter4.pdf`).

3.4.1 A versus B: Distributions Compared

The comparison of the distribution of an attribute within one region to that of another responds to questions 1 and 2 that we initially posed. For our case studies with the GS-derived mass fractions we use two regions that were deemed striking on the basis of low thermal inertia, low areal fraction of rocks, Mars Global Surveyor Mars Orbiter Camera (MGS-MOC) imagery, and mapped geologic units: Amazonis and Tharsis (Figure 3.4) (*Newsom et al.*, 2007). As *Newsom et al.* (2007) summarize, we may conclude these two regions to be distinct in Th composition. We now describe the underlying statistical tests that led to that

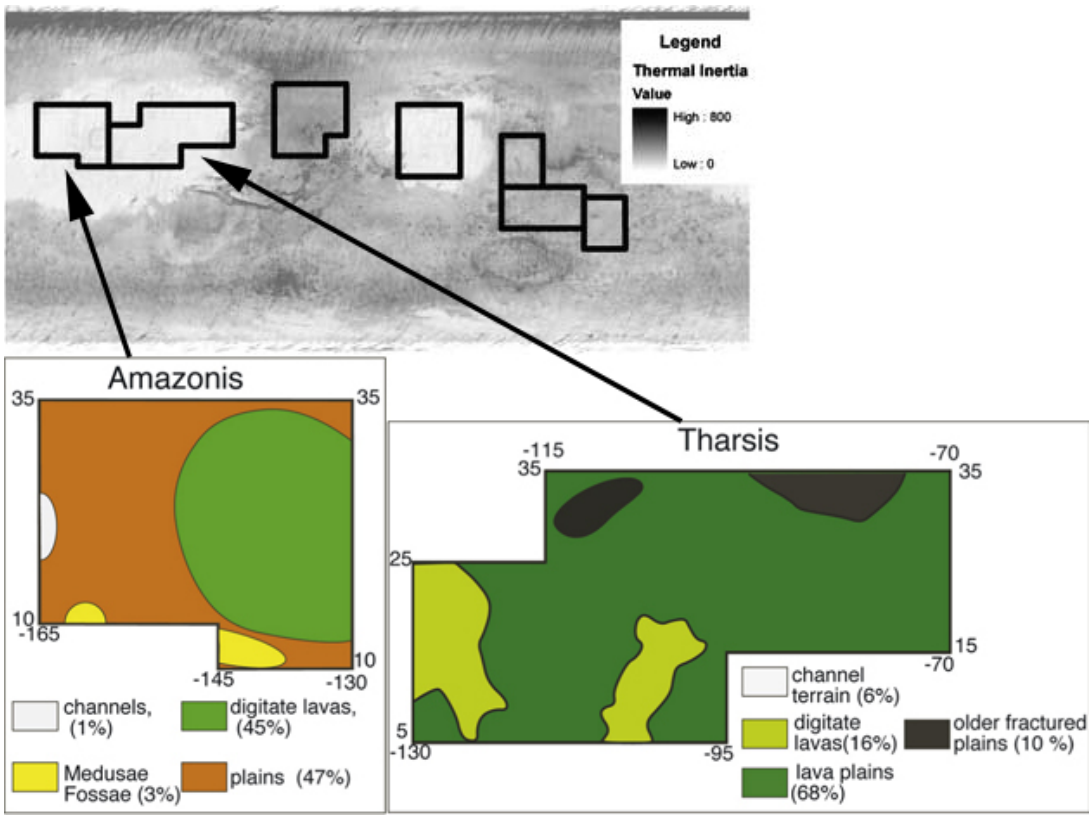

Figure 3.4: Sketches of the Amazonis and Tharsis regions adapted from the work by *Newsom et al.* (2007, Figures 8 and 9). Top image shows their locations on Mars in the context of thermal inertia, while the bottom figures show the surface extent of simplified mapped geologic units within each region as well as the latitude-longitude boundaries.

conclusion. These tests can also be applied to compare the distribution within a region to that of the entire planet, by using the whole planet as the reference region.

Query 1: Is the Distribution in A Identical to that in B?

While several statistical tests are available to answer question 1, one of the simplest is the Kolmogorov-Smirnov (KS) test. This test has the advan-

tages of being non-parametric, robust with satisfactory power, and applicable independent of the underlying attribute distribution as described by *Chakravarti et al.* (1967, pp. 392–394), *DeGroot and Schervish* (2001, Chapter 9), *Press et al.* (2007, pp. 736–740), *Stephens* (1970), and the NIST/SEMATECH e-Handbook of Statistical Methods `http://www.itl.nist.gov/div898/handbook/eda/section3/eda35g.htm`. While the higher power of this test makes type 2 errors less likely (e.g., *Helsel and Hirsch*, 2002, p. 107), it is also highly sensitive to even subtle differences of the centers of the cumulative distribution functions (e.g., *Press et al.*, 2007, p. 738).

The application of the K-S test consists of five key steps (e.g., *Chakravarti et al.*, 1967, pp. 392–394)(e.g., *Press et al.*, 2007, pp. 736–740): (1) Define the cumulative probability as a function of the attribute values, c_i, for each region; (2) Compute the maximum value, D, of the absolute difference between the two cumulative probability distributions (which, in our case study, would be Th mass fraction distributions within Amazonis and Tharsis regions); (3) Determine the degrees of freedom, N_e; (4) Define a test parameter, λ, with a known cumulative probability distribution; and (5) Evaluate the probability (P) that λ is at least as extreme as the observed due to chance alone (For example, if $P < 0.05$, we can reject the null hypothesis with 95 % confidence).

As described by (*Press et al.*, 2007, pp. 736–740), we define the cumulative probability function, $S_N(c)$, for each region as:

$$S_N(c) = \frac{1}{N} \sum_{i=1}^{N} \left\{ c_i \overset{c_i \leq c \Rightarrow 1}{>} c \Rightarrow 0 \right\} \tag{3.16}$$

where N is the number of data within the region in question and c_i the attribute value of the i_{th} datum. D, needed for the second step is computed as:

$$D = Max\left|S_{N,A(c)} - S_{N,B(c)}\right| \tag{3.17}$$

where A denotes the region of interest (e.g., Amazonis), and B the reference region (e.g., Tharsis). Note the use of the same c value, which limits the computation to the dynamic range of c common to both regions A and B. Next, the value of N_e is estimated with $N_e = \frac{N_A N_B}{N_A + N_B}$ where λ is numerically approximated by $\lambda = D(\sqrt{N_e} + 0.12 + 0.11/\sqrt{N_e})$. The final step of evaluating the value of P utilizes the distribution of the λ variable as follows:

$$P = 2\sum_{j=1}^{\infty}(-1)^{j-1}\exp\left(-2j^2\lambda^2\right) \tag{3.18}$$

which, though an infinite series sum, converges. For the GS data we modify this basic test to account for heteroscedasticity by generating 100 simulated datasets for each region where each datum is simulated from a random normal distribution as given by Equation 3.3. A separate cumulative probability function, $S_N(c)$, is generated with Equation 3.16 in each case for each region, and P evaluated accordingly. We take the average of the resulting P values as a more rigorous measure than one from the original dataset alone. We also plot the standard deviation of S_N for each datum as an error bar. For the example of comparing the Th content of Amazonis and Tharsis, the resulting comparative plot of cumulative probability functions is as shown in Figure 3.5. The consequent P for Th is $(8 \pm 3) \times 10^{-5}\%$, which is decisively less 5 %. Consequently, we may reject the null hypothesis that Amazonis and Tharsis have identical distributions of Th at better than 95 % confidence. As expected, the two appear even more distinct under homoscedastic assumptions (Figure 3.6).

A less sensitive way to test whether two distributions are distinct may be

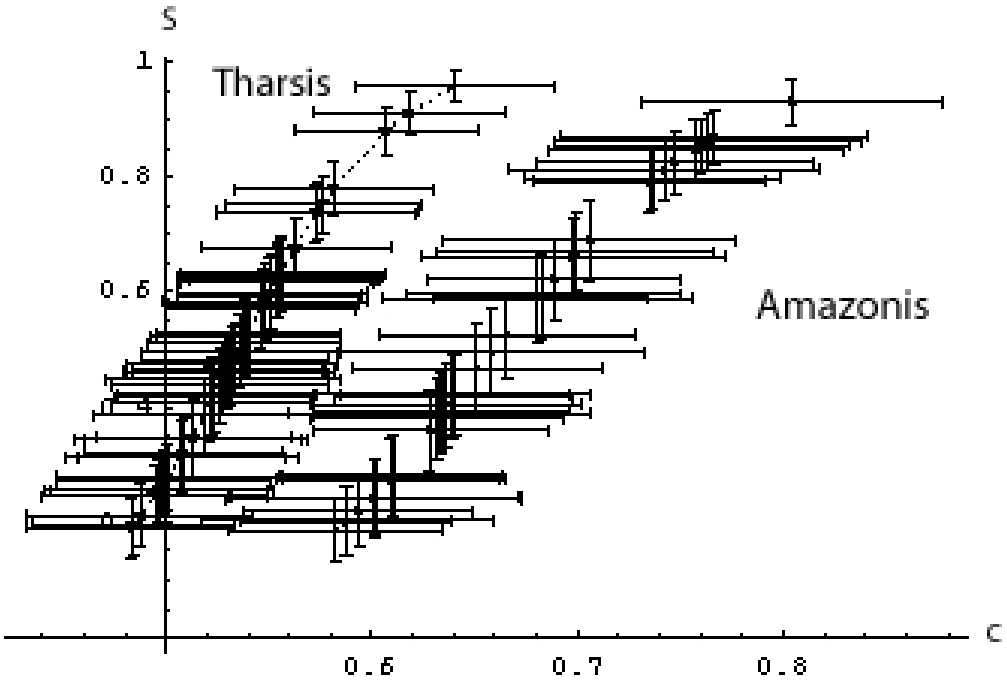

Figure 3.5: Plots of the cumulative probability function (S_N) of the mass fraction of Th (refer to Equation 3.16 and related text) for Amazonis and Tharsis regions. The mass fraction in mg/kg is the abscissa, while the ordinate is S_N. Abscissa error bar is the standard error of the datum, s_i, while the ordinate error bar is the standard deviation of the S_N at each datum. The latter was estimated by simulations involving s_i, as discussed in the text.

devised, although it runs the risk of being simplistic. The fundamental notion for the alternative test is that the mean (m) and standard deviation (s) estimates (Section 3.2) fully characterize an assumed underlying gaussian distribution. We may then compute a test parameter, t, as follows:

$$t = \frac{m_A - m_B}{\sqrt{s_A^2 + s_B^2}} \tag{3.19}$$

where A and B signify the two regions, Amazonis and Tharsis, for example. m and s need to be computed either with Equations 3.1 and 3.10, or with Equa-

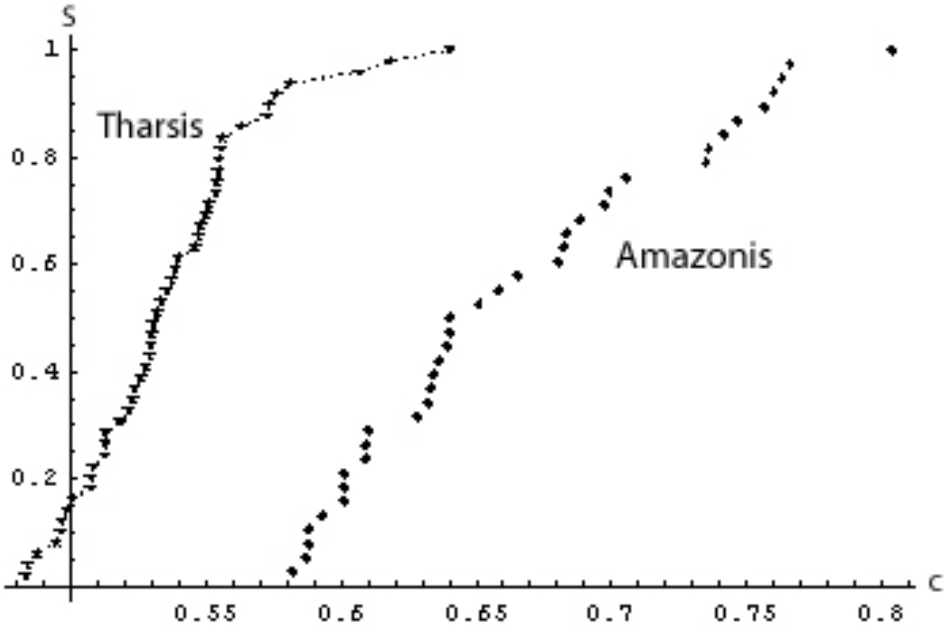

Figure 3.6: Plots of the cumulative probability function of the mass fraction (S_N) of Th (refer to Equation 3.16 and related text) for Amazonis and Tharsis regions without accounting for numerical uncertainties of the data (i.e., under homoscedastic assumptions). The mass fraction in mg/kg is the abscissa, while the ordinate is S_N.

tions 3.4 and 3.11. The latter set incorporates area-weighting. In either case, the distributions are assumed to be random normal and the test parameter t is assumed to follow a Student's-t distribution with degrees of freedom (f) computed as:

$$f = \frac{(s_A^2 + s_B^2)^2}{\frac{s_A^4}{N_A - 1} + \frac{s_B^4}{N_B - 1}} \tag{3.20}$$

where A and B are as before. We then compute the two-tailed probability (P) that t could be as extreme as observed due to chance alone and compare with the desired statistical confidence. For example, if $P < 0.05$, we may reject the null hypothesis that the attribute distributions in regions A and B are identical

at 95 % confidence. As described for the K-S test, it is possible to incorporate the numerical uncertainties (s_i) of the data by simulating new datasets.

For our case study of the Th mass fraction distributions in Amazonis and Tharsis regions, heteroscedastic simulations with Equation 3.19 yield an average $P = (24 \pm 0.5)\%$, while $P = 7\%$ when numerical uncertainties are disregarded. Figure 3.7 shows the Th mass fraction histograms under such homoscedastic assumptions. Clearly, under either heteroscedastic or homoscedastic gaussian assumptions, the null hypothesis cannot be rejected at 95 % confidence. Therefore, while this alternative test may be useful to avoid type-1 errors, the K-S test is recommended where a higher power is desired. Moreover, it is important to note that the alternative test would be invalid when the underlying distributions are not gaussian. It also fails to distinguish distributions that differ greatly in dispersions but not the means. In addition, the test is mostly an intuitive modification of the common mean comparison (Section 3.4.2), and lacks a theoretical basis.

Query 2: A Compared Qualitatively with B

The second question, of how the distribution of the attribute in region A compares qualitatively with that in region B, is best answered with a variant of the box-and-whiskers plot. One method would be to compare the general variability as represented by the 25^{th} and 75^{th} percentiles of the attribute values. Specifically, the ratio of the 25^{th} percentile within region A to the 75^{th} percentile within region B would bound how low the attribute values within A can be relative to those within B. Likewise, the ratio of the 75^{th} percentile within A to the 25^{th} percentile within B would bound how high the values within A can get relative to

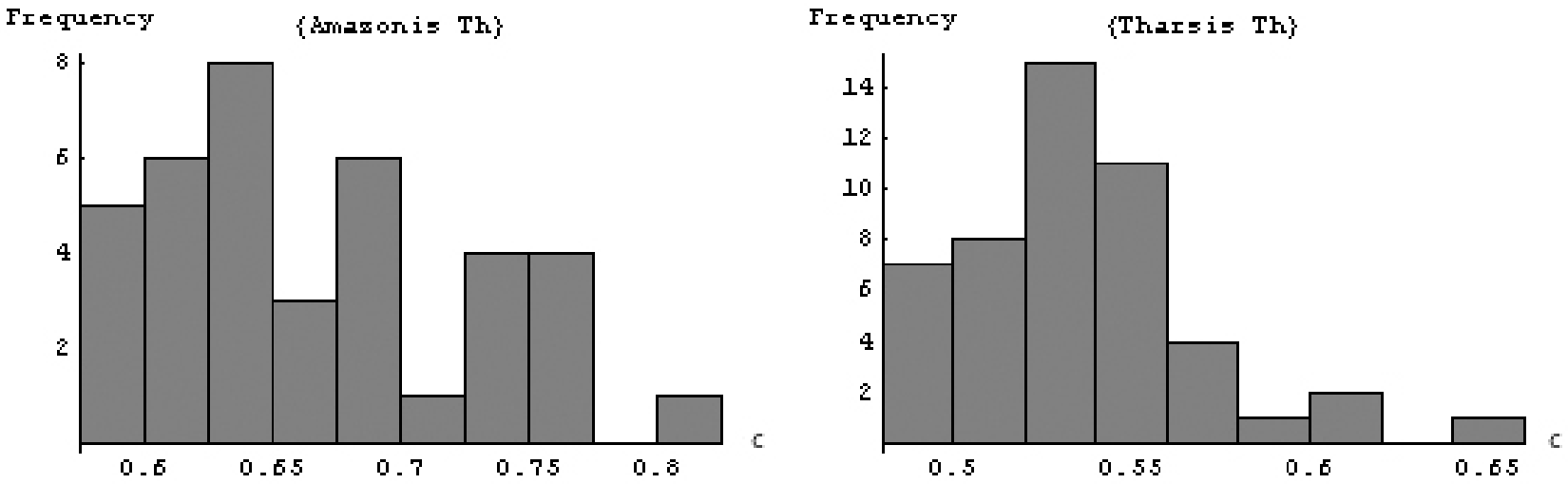

Figure 3.7: Plots of the frequency histograms of Th mass fraction (as mg/kg) within Amazonis and Tharsis regions at a $5° \times 5°$ bin resolution. c denotes the mass fraction.

those within B. Lastly, the ratio of the 50$^{\text{th}}$ percentiles (medians) would indicate how the typical compositions compare to each other. To evaluate qualitatively whether these variabilities are significant in the context of numerical uncertainties (i.e., s_i), we compute each error bar by propagating the s_{rms} (Equation 3.12) as the error term of the ratio:

$$b_e = \frac{m'_{\text{A}}}{m'_{\text{B}}} \sqrt{\left(\frac{s_{\text{rmsA}}}{m'_{\text{A}}}\right)^2 + \left(\frac{s_{\text{rmsB}}}{m'_{\text{B}}}\right)^2} \tag{3.21}$$

where b_e is one error bar, m' denotes the median, "A" denotes region A, "B" denotes region B, and the remaining symbols are as before. For clarity, we center the error bars about the ratio of the medians. The resulting graph for the case of Amazonis (region A) and Tharsis (region B) is shown in Figure 3.8. From the figure, it is clear that the Th mass fractions within Amazonis are meaningfully greater than those within Tharsis, as all the bar chart values exceed unity. For example, Th mass fractions within Amazonis are typically greater than those within Tharsis typically by 10 % or more, and may even be greater than the Tharsis counterparts by up to 38 %. Therefore, the mass fraction distributions are clearly different, with a typical enrichment of about 20 % relative to Tharsis (ratio of the medians). It is also important to note that the collective dynamic range within the two regions may be mostly due to numerical uncertainties alone, as the error bars span the entire bar chart. This provides a qualitative indication that any compositional heterogneity within either region may be insignificant relative to the precision of the data as discussed in greater detail in Section 3.4.3.

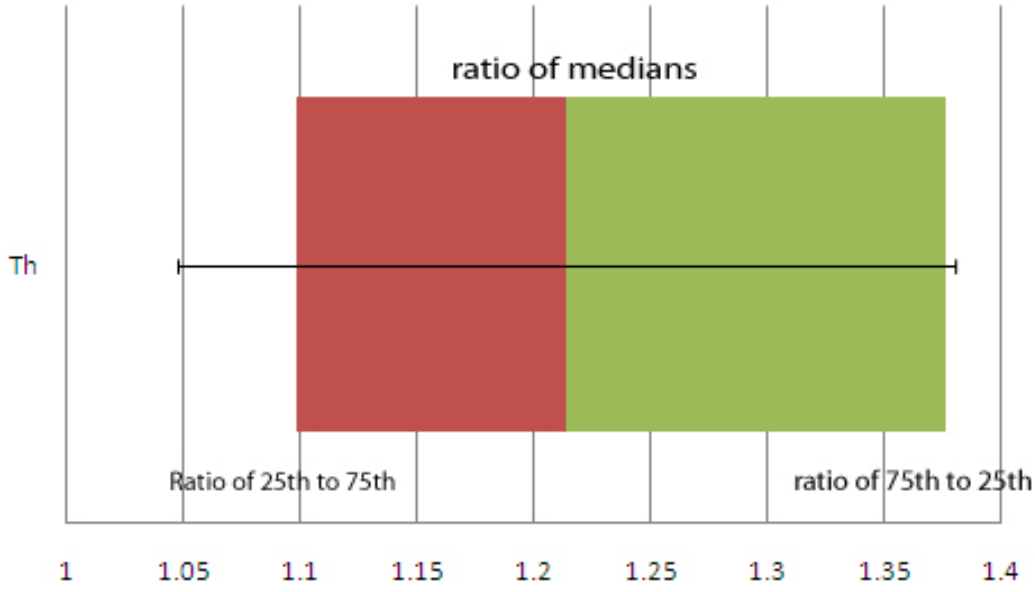

Figure 3.8: The distribution of the Th mass fraction within Amazonis compared graphically with that within Tharsis as discussed in Section 3.4.1. The 25th percentile within Amazonis is divided by the 75th within Tharsis to illustrate how low Amazonis values can get relative to those within Tharsis. The 75th percentile within Amazonis is divided by the 25th within Tharsis to show how high Amazonis values can get relative to those within Tharsis. The ratio of the medians represents the typical difference. The error bars indicate the numerical uncertainty, not the standard error of the median.

3.4.2 Query 3: Comparing Averages

In response to the third key query, one posed commonly in regional comparisons of Mars, it is possible to utilize a standard statistical test. As stated before, the null hypothesis is that the average value of the attribute in region A is identical to that in region B. The parameters used for this test are the mean (m) and standard error (s_m). In the absence of spatial autocorrelation in homoscedastic data, it is possible to compute both from bin data with Equations 3.1 and 3.8, respectively. When the data are heteroscedastic but spatial autocorrelation is

negligible, the proper equations are 3.2 and 3.9. Unfortunately, as discussed in Section 3.1, the GS-derived elemental mass fractions and other datasets that are subject to extensive spatial filtering are significantly affected by spatial autocorrelation. While techniques that account for the corresponding loss in the degrees of freedom exist, we feel that the most robust choice is to obtain the regional average and the standard error from direct instrumental observation over the entire region (Section 2.2).

Once the regional mean and corresponding standard error of an attribute have been estimated, it is possible to compute a test parameter, t, as follows:

$$t = \frac{m_A - m_B}{\sqrt{s_{mA}^2 + s_{mB}^2}} \tag{3.22}$$

where the prefixes A and B denote the two regions, and other symbols are as previously defined. t approximates a Student's-t distribution (e.g., *Helsel and Hirsch*, 2002; *Press et al.*, 2007, former p. 126; latter p. 728) as long as the standard errors are not extremely different. Thresholds for the significance of difference are available in literature (e.g., *Press et al.*, 2007, p. 730). The degrees of freedom (f) for the Student's-t distribution is given by

$$f = \frac{(s_{mA}^2 + s_{mB}^2)^2}{\frac{s_{mA}^4}{N_{mA}-1} + \frac{s_{mB}^4}{N_{mB}-1}} \tag{3.23}$$

where N is the number of data. Once t and f are known, we simply estimate the two-tailed Student's-t distribution probability (p) that the computed t could be at least as extreme as the observed due to chance alone. Should $p \leq (1 - \tau)$, where τ is the desired statistical confidence, we may conclude that the two regional means are distinct. For example, if $p = 5\%$, we may be confident that

the two regions have distinct average attribute values at 95 % confidence. The tail probabilities may be obtained from tabulations or from commercial software (e.g., Mathematica StudentTPValue function).

When the mean and standard error are estimated directly without using bin data, it is possible to use the number of observations, spectral integration time, or similar counting statistic in place of N. For our case study with the GS involving Amazonis and Tharsis, the integration times are sufficiently large that f is essentially infinite, causing t to approximate a standard normal distribution. Substituting reported values (e.g., *Newsom et al.*, 2007, Table 2) for the two regions in Equation 3.22, we obtain $t = 2.46$. The corresponding probability of t in a standard normal distribution is 1 %. Clearly, and as summarized by *Newsom et al.* (2007), Amazonis and Tharsis have distinct average Th mass fractions at 95 % confidence.

Alternative Tests

For situations where such rigor is unnecessary, two alternative tests can be used. One simply consists of rephrasing the result of Equation 3.22 in terms of the standard errors, i.e., the means are distinct to a confidence of ts_m (t-standard errors). For our case study, we may state that the mean Th mass fractions within Amazonis and Tharsis are distinct to 2.46-standard errors. By means of standard uncertainty propagation (e.g., *Bevington and Robinson*, 2003; *Young*, 1962, pp. 96–101), this may also be illustrated as in Figure 3.9, by using the denominator of Equation 3.22 as the length of an error bar, and the difference between the two mean values as the datum. The extent to which the difference exceeds zero relative to the length of an error bar signifies the confidence with which the two

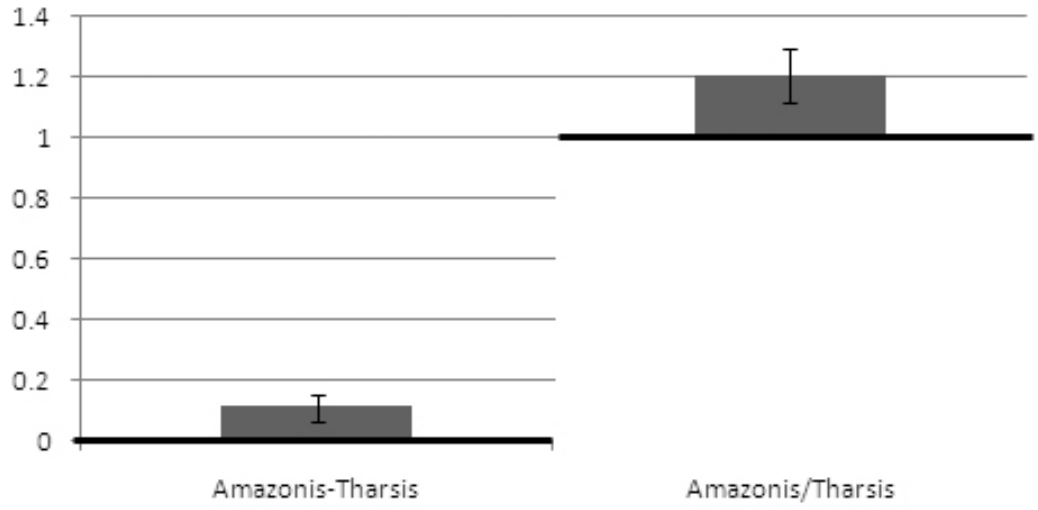

Figure 3.9: The directly estimated mean Th mass fraction within Amazonis compared to that within Tharsis. Graph on the left shows the difference between the two with the error bars as described in Section 3.4.2. The extent to which this value differs from zero reflects the significance. Graph on the right shows the ratio of the two values. The difference of the ratio from unity indicates the significance of the distinctness.

mean values may be considered distinct.

The second alternative test is to compute the ratio of the two mean values and to apply standard uncertainty propagation (e.g., *Bevington and Robinson*, 2003; *Young*, 1962, pp. 96–101) to the ratio using the two standard errors, analogous to Equation 3.21. Next, we compute a parameter t as the magnitude of the difference of the ratio from unity divided by the propagated numerical uncertainty. We may then state the two mean mass fractions to be distinct at a confidence of t-standard errors. For our case study with Amazonis and Tharsis the ratio of the mean mass fraction of Th within Amazonis to that within Tharsis is 1.21, and the propagated uncertainty is 0.09, yielding a 2.4-standard error

confidence in the distinctness of the means. The graphical counterpart consists of the ratio as the datum and the propagated uncertainty as the length of an error bar (Figure 3.9). In this case, the emphasis is on the extent to which the datum differs from unity relative to the length of an error bar. It is important to note that both alternative tests are subject to the caveats of the standard test, becoming less reliable when the standard errors of the attribute within the two regions are strikingly different.

3.4.3 Query 4: Heterogeneity of the Regional Distribution

Particularly in geochemical investigations, it can be important to know whether an attribute is distributed heterogeneously within a region of interest, or whether it is essentially homogeneous. As the fourth of our five key queries, it is especially relevant where the mean of an attribute within one region is compared with that in another as in response to our third query in Section 3.4.2. We may concoct three tests in response: comparison of simulated K-S distributions, fraction of distinct data pairs, and apparent dispersion versus numerical precision. The first reveals whether the numerical uncertainties are sufficiently large that they alone could cause the attribute distribution to vary. The second and third tests reveal whether the apparent variations in the attribute are meaningful in the context of numerical uncertainties.

Simulated K-S Distributions

We apply the K-S test (Section 3.4.1) to compare simulated distributions of the sample to the sample itself. Analogous to Section 3.4.1, we generate each simu-

lated distribution by randomly sampling each datum (c_i) from a gaussian distribution as given by Equation 3.3. If the probability (P) that the simulated distribution could be as different from the sample due to chance alone (Equation 3.18) is greater than the desired confidence level, we may be assured that the numerical uncertainties are unlikely to cause significant variations in the attribute within the region.

For greater confidence, we typically estimate P for 100 simulations to compute the average of P (Equation 3.1) and its standard deviation, s (Equation 3.10). The standard error of the average P may then be computed with Equation 3.8 where $N = 100$. As a conservative measure, we then require the average P to exceed the desired statistical confidence by at least the standard error of P. For example, if average $P = 99\%$, and the standard error is 2 %, we can be more than 95 % confident that the numerical uncertainties do not meaningfully affect the observed distribution.

For our case study with Amazonis and Tharsis, the effect of the numerical uncertainties on the distribution of Th may also be evaluated graphically using the same approach as in Section 3.4.1 and Figure 3.5. In theory the resulting Figure 3.10 is identical to Figure 3.5, while differences are due to the limited number of simulations. As evident in Figure 3.10, the distribution is not affected severely by the underlying numerical uncertainties. Nevertheless, the average P and corresponding standard error for Amazonis is $(48 \pm 3)\%$, which while large, does not quite pass the conservative threshold of 95 %. The same holds for Tharsis at $(17 \pm 1)\%$. Therefore, we conclude that the heteroscedasticity of Th within each region is significant at 95 % statistical confidence. The implication is that numerical uncertainties may contribute significantly to the

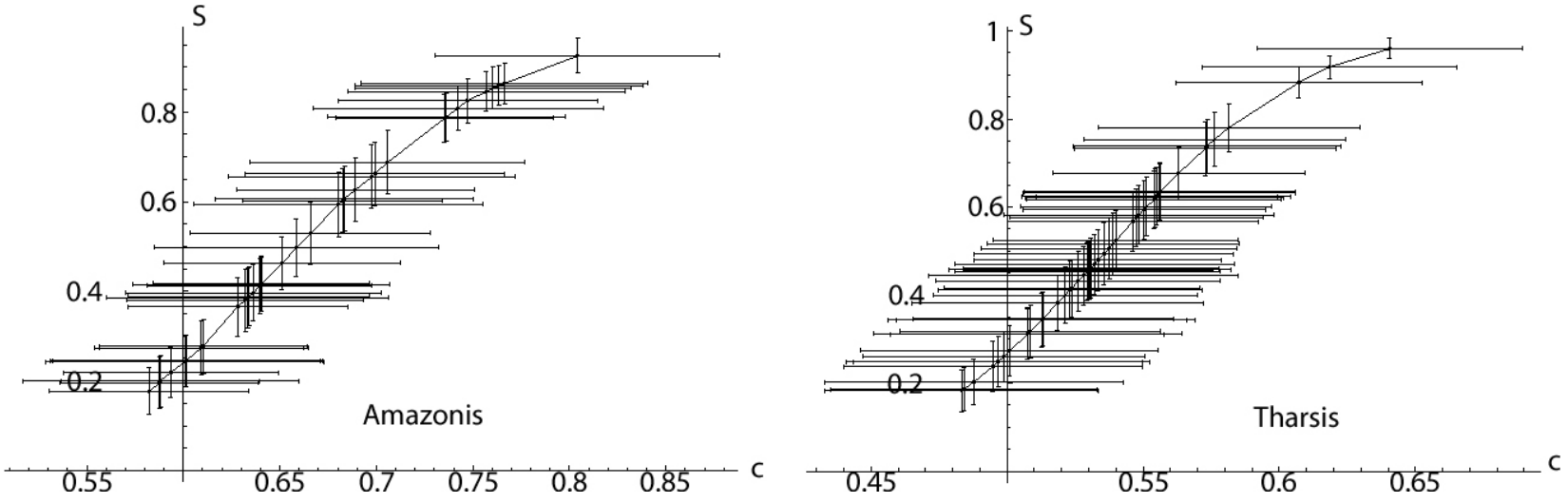

Figure 3.10: Plots of the cumulative probability function of the mass fraction of Th (S_N) for Amazonis and Tharsis regions revealing the effect of numerical uncertainties, s_i. The mass fraction in mg/kg is the abscissa, while the ordinate is S_N. Abscissa error bar is the standard error of the datum, s_i, while the ordinate error bar is the standard deviation of the S_N at each datum.

apparent variability (i.e., dispersion) of Th mass fraction within each region.

Fraction of Distinct Data Pairs

This test applies the comparison of the mean attribute values within two regions at the scale of individual bins (i.e., data). For a region of interest, we first partition the data into all possible pairs, $\left\{c_i, c_j\right\}$ where $i \neq j$. The comparison of the means test is then applied to each bin pair at the desired level of confidence, exactly as described in Section 3.4.2. The number of bin pairs that pass the test at the desired confidence is taken as a fraction of the total number of pairs, $\frac{N}{2}(N-1)$, where N is the number of data. This fraction is a rough indicator of the extent to which the apparent variability of the data within the region is statistically meaningful in the context of numerical uncertainties. For example, 3 % of the data pairs of Th mass fraction are distinct within Amazonis at 95 % confidence, and 1 % are distinct within Tharsis. Therefore, we may conclude that most of the data are indistinct from each other within both Amazonis and Tharsis at 95 % confidence. Stated differently, Amazonis and Tharsis are both homogeneous in their Th content at 95 % confidence in light of numerical uncertainties.

Apparent Dispersion Versus Numerical Precision

As discussed in Section 3.2.2, the standard deviation (s) is the key measure of dispersion (i.e., variability) of an attribute within a region of interest. A simple measure of the meaningfulness of the apparent dispersion would be to compute the ratio $d = s/s_{\text{rms}}$, where s is as given by Equation 3.10 and s_{rms} is as given by Equation 3.12. By analogy to the discussion of the global midlatitudi-

nal distributions in Section 3.2.3, we may consider a region to be meaningfully heterogeneous when the ratio exceeds a desired value. A conservative approach is to require the ratio to exceed $100 + \tau$, where τ is the desired statistical confidence (e.g., $\tau = 95\%$). For the distribution of Th within Amazonis, $d = 96\%$ and for that within Tharsis, $d = 67\%$. Since both are considerably less than 195, neither region shows unambigous evidence for compositional heterogeneity at 95 % confidence. In short, each appears to be homogeneous in Th within numerical uncertainties.

3.4.4 Query 5: A Matter of Ratios

The final query we seek to answer in this chapter is whether our responses to the preceding questions would be directly applicable when the ratio of two attributes is being characterized within a region of interest. An example application with the GS dataset is the ratio of K mass fraction to that of Th (*Taylor et al.*, 2006a). The primary issue with regard to attribute ratios occurs in the uncertainty propagation. When values at individual bins are derived from a multi-step process, such as the mass fractions of capture-derived elements with the GS (Section 2.3.4), the ratio will eliminate any multiplicative terms of the derivation. An example would be the CCF (Section 2.3.4) for the GS data that are applied identically to all capture-derived elemental mass fractions as a multiplicative term. While such terms will be eliminated implicitly in the ratio of capture-derived elements, unless the corresponding uncertainty term is removed from the standard errors, the computed standard errors of the ratios would be unnecessarily large. In the GS context this becomes a simple rule of thumb: Whenever the mass fractions of two capture-derived elements are ra-

tioed over the same bins or region, the error propagation (which would be analogous to Equation 3.21) must use standard errors that exclude the uncertainty due to the capture correction factors. In all other cases, it would be reasonable to use uncertainties that include those due to capture correction.

An additional issue arises when the "average ratio" of two attributes is sought, as it may be computed in two distinct ways. One is to compute the ratio at each bin ($c_{i1,i2}$) where 1 and 2 denote the two attributes, and to calculate the average of the ratios subsequently. The other is to compute the attribute averages first, then their ratio. These two are always different, and ideally only one should be used to avoid confusing the reader. Furthermore, one may be more appropriate than the other depending on the context. For example, when applying the alternative to the K-S test on the distinctness of distributions between two regions (Section 3.4.1), the average of the ratios needs to be used, not the ratio of the averages. In contrast, when evaluating whether the mean value of the ratio in one region is distinct from that in another, it is necessary to compute the ratio of the averages within each region. In particular, it is important to remember that directly estimated regional averages, i.e., those from cumulative spectra over a region of interest, can only yield ratios of the mean values.

3.5 Conclusions and Future Work

In this chapter, we described simple tests that respond to commonly asked questions in investigations with remotely-sensed planetary data sets, and applied those tests with the GS as a case study. These methods are also applicable for data sets that are more local in scope, but still involve distinct regions of interest

and a sufficient number of data. We considered two distinct groups in our work, those consisting of one datum for a region and those consisting of data binned on a uniform spatial grid. These provide distinct, but complementary perspectives on regions of interest. The former is essential to estimate rigorously the regional mean of an attribute and corresponding standard error. The latter is essential to estimate the standard deviation (i.e., dispersion) and the distribution of an attribute within a region. As such, it helps determine the degree to which a single parameter for a region, such as the regional average, actually represents the region as a whole. For example, the usefulness of the regional average becomes suspect for a region within which the attribute is significantly heterogeneous. Furthermore, while the bin data provide the most detailed insight into the spatial distribution of attributes, the nature of their derivation may preclude the computation of regional parameters from them, such as the standard error in the case of GS data.

As observed in our case study with the GS data, the tests for distinct distributions (Section 3.4.1) may sometimes converge with the tests for distinct means (Section 3.4.2). However, that is by no means necessary. When the two do diverge, additional insight may be gained, mostly due to the difference in the spatial impact of small-scale and large-scale geologic processes on the distribution of planetary attributes. In such situations, the qualitative evaluation of distributions as discussed in Section 3.4.1 can yield important insight.

As utilized and summarized by *Hahn et al.* (2007), *Keller et al.* (2006b), *Newsom et al.* (2007), and *Taylor et al.* (2006a) the techniques we describe can greatly enhance the robustness of geochemical investigations while simultaneously enhancing analytical clarity. In addition to their utility in ongoing work (Chap-

ter 6), we also anticipate their use in future missions of both global (such as the MESSENGER Gamma-Ray and Neutron spectrometers, GRNS, at Mercury) and local (such as the Mars Science Laboratory) scope. We also hope that this discussion and its companion work (Chapter 4) demonstrate both the importance and the ease of using well-established statistical techniques in geochemical analyses and the ways in which to apply them. As Mars and other planets are scrutinized with instruments of ever-increasing sophistication, such methods will enable us to make fundamental statistics the reality check that moderates our exuberance and creativity, not the "magic carpet" for flights of fancy. If so, we shall remain safe beyond the reach of "lies, damn lies, and statistics."

CHAPTER 4

SEEKING MULTIVARIATE CORRELATIONS WITHOUT IGNORING UNCERTAINTIES

4.1 Fundamentals, and Mars as Case Study

Mars is an excellent case study for the search of correlations among many variables, as planetary missions have observed an array of surficial variables at global scales. As mentioned in the preceding chapters, some examples include elemental mass fractions from the GRS instrument suite's GS (*Boynton et al.*, 2007), areal fractions of surface types from the MGS-TES (*Bandfield et al.*, 2000), and thermal inertia from the Viking IRTM (*Christensen and Malin*, 1988). Such data are typically assigned to spatial bins that define a latitude-longitude grid covering the planetary surface without overlap. Attribute values are usually associated with the spatial centroid of each bin. Bin sizes may be modified to obtain spatially corresponding bins across different datasets, which is essential to investigate the relationships among different attributes. Such "rebinning" into similar grids is often necessary in the search for attribute correlations that help constrain models of surface evolution.

we first introduce the basic mathematical concepts in the following subsections, then discuss the relevant equations for multivariate analyses in detail (Section 4.2). Sections 4.3 and 4.4 describe diagnostics of the fits and analyses. The last three sections consist of real-life applications of these methods with planetary data.

4.1.1 Linear Relationships

Several commonly used statistical terms need to be described in the context of this chapter before we explore attribute relationships. The strength and direction of interdependence (i.e., covariability) among attributes is known as *correlation*. When line or planar fits in two dimensions or multiple dimensions are in use, we identify them as *linear* fits, since they involve first-degree polynomials (e.g., $y = b_0 + b_1 x_1 + b_2 x_2$). Such fit procedures constitute *regression*, as one attribute is expressed as an optimized function of several others. The selection of one or more subsets of correlated attributes on the basis of relative statistical significance is designated as *hierarchical*. A fit in two dimensions also involves exactly two variables and is identified by the term *bivariate*, while a fit involving many attributes would be *multivariate*. Two terms that are conceptually distinct but often notationally similar are the *standard error* indicating the net (combined instrumental and statistical) numerical uncertainty of a value and *variance* indicating the variability of values about the mean. The latter is usually computed as the average of squared differences from the mean. *Cohen and Cohen* (1983, pp. 3–24) and *Stuart et al.* (1999, pp. 466–533) present a lucid discussion of these terms, concepts, and their origins.

Bivariate scatter plots and their linear bivariate (also known as sample-linear, product-moment, zero-order, and Pearson's) correlation coefficients are the simplest methods to identify first-order relationships among attributes (e.g., *Bevington and Robinson*, 2003, pp. 197–203). Unfortunately, such analysis yields an incomplete picture, since planetary subsurface properties are often dependent on simultaneous relationships among many attributes, which can lead to misleading apparent correlations when only two variables are considered at a

time (e.g., *Davis*, 1985; *Blalock*, 1964). Furthermore, as commonly evaluated, bivariate correlations fail to consider the effect of spatial autocorrelation: the mutual dependence of spatially proximate values (e.g., *Haining*, 2003, p. 74–88, 273–324). Lastly, such analyses are often reported without the diagnostics that test the effectiveness of results and appropriateness of the methods. These weaknesses can be overcome effectively with hierarchical linear multivariate correlation analyses and their detailed diagnostics.

Linear multivariate analyses offer the ability to identify relationships among attributes that are otherwise hidden in bivariate analyses while discarding apparent bivariate relationships that have originated solely due to covariability with a third variable. Meanwhile, the hierarchical approach selects subsets of attributes with the most significant correlations. With the increasing availability of global data for many planetary bodies, multivariate correlation methods can be "power tools" for the planetary scientist and exploit the synergy among different missions and datasets. We discuss the simplest and most intuitively accessible multivariate methods in an application-oriented manner, with references to literature for more advanced treatment.

It is possible to model only the spatial variability with multivariate correlations, that is, exploratory analysis (e.g., *Haining*, 2003, p. 181–270, 292–311, 325–349) as Gasnault et al. (2008, Quantitative Geochemical Mapping of Martian Provinces, in preparation) are applying for Mars. We do not discuss that approach, since our interest is in describing global variations in one attribute (e.g., mass fraction of K) in terms of others (e.g., mass fraction of Th and areal fractions of surface types with distinct infrared spectral features), that is, explanatory analysis (e.g., *Haining*, 2003, 312–324, 350–378). The attribute whose

variability is being modeled is termed the response (or dependent), variable, while the others are appropriately termed the predictor (independent, input, or regressor) variables.

4.1.2 The Power Tool Trio

Three distinct and complementary techniques are available to estimate correlations among variables. The simplest among them, Ordinary Linear Regression (OLR), evaluates the unique correlation of the response variable with each predictor variable. Spatially Weighted Linear Regression (SWLR) modifies OLR to account for spatial autocorrelation. The third and most numerically intensive method, Heteroscedastic Response Linear Regression (HRLR), accounts for the variation of uncertainties in the response variable from one datum to the next. We discuss the application of these methods in detail after a summary introduction.

The relationship between the response variable and each predictor variable can be estimated as an individual regression coefficient defining the functional dependence. The corresponding unique interdependence – that is, correlation – between the response-predictor pair as all other predictors are held constant is a partial correlation coefficient, r_i, of the response (e.g., *Cohen and Cohen*, 1983, p. 91–92, 102–103). Ordinary Linear Regression (OLR) directly evaluates these parameters. The consequent optimal correlation between the whole set of predictors and the response variable is given by the multiple correlation coefficient, R. Its square, R^2, known as the coefficient of determination, indicates the extent to which the variability of the response variable is associated with the entire set

of predictors. For example, $R^2 = 0.8$ would imply that 80 % of the response variance is attributable to the set of predictors as modeled by the regression (e.g., *Stuart et al.*, 1999, p. 523–533).

Global binned data used in correlation analyses are typically from orbiters, not flyby spacecraft, landers, or rovers. As a result, the spacecraft footprint may necessitate bins of coarse spatial scales. For example, the GS footprint, defined as the nadir-centered region within which ≈ 50 % of the signal originates has a 3.7° radius (corresponding to 220 km linear radius) (*Boynton et al.*, 2007, and Chapter 2). This footprint and spatial effects of data reduction (e.g., *Boynton et al.*, 2007) cause significant spatial autocorrelation at bin resolutions finer than $5^\circ \times 5^\circ$. The resulting mutual dependence of spatially proximate attribute values is evident even at $5^\circ \times 5^\circ$ bin scales, much of it contributed by the spacecraft footprint (e.g., *Boynton et al.*, 2004; *Boynton et al.*, 2007; *Evans et al.*, 2006; *Kim et al.*, 2006a) and the processing of mass fractions with a constant-arc radius mean filter as discussed elsewhere (e.g., *Boynton et al.*, 2007, and Chapter 2).

Unlike the GS, remote instruments with collimating devices, such as the MGS-TES and IRTM, typically have much smaller footprints enabling finer bin scales. For example, bin scales as fine as $1^\circ \times 1^\circ$ are available for MGS-TES derived areal fractions, IRTM-derived thermal inertia, and IRTM-derived rock areal fractions. Even though the global coverage is not as extensive, several other instruments are capable of mapping at spatial resolutions much finer by orders of magnitude, such as the Mars Odyssey Thermal Imaging System (THEMIS) at 100 m (*Christensen et al.*, 2003), the Mars Express Observatoire pour la Minéralogie, l'Eau, les Glaces, et l'Activité (OMEGA) at 5 km (*Bibring et al.*, 2005), and the Mars Reconnaissance Orbiter Compact Reconnaissance Imaging

Spectrometer (CRISM) at 200 m (*Pelkey et al.*, 2007).

In the context of multivariate correlation analyses, spatial autocorrelation presents two key effects: spatial clustering of attribute values and reduction in the degrees of freedom. The former may often be an intrinsic property of the planetary subsurface, and warrant the investigation of correlations within subregions or of correlation variations as continuous functions of location (e.g., *Gasnault et al.*, 2002, Section 3 and Figure 4). As *Haining* (2003, p. 312–316) and *Jones and Casetti* (1992) discuss, estimating the correlation as a function of location, also known as the "expansion method", sheds local insight on global relationships among attributes. Even though we do not discuss the expansion method since it would digress from our emphasis on global relationships, we present quantitative and visual tests for clustering effects.

Spatial autocorrelation reduces the degrees of freedom as a consequence of information redundancy. In practical terms, if the spatial dataset has N data, spatial autocorrelation would reduce the number of statistically independent data to $N' < N$. This biases correlation coefficients leading to type 1 errors as discussed by *Bivand* (1980) and *Haining* (2003, p. 273–274). Type 1 errors occur when the null hypothesis, the absence of correlation, is rejected even though the data are consistent with the null hypothesis at the desired level of confidence (e.g., *Easton and McColl*, 1997). As explained by *Easton and McColl* (1997) and *Helsel and Hirsch* (2002, p. 106–107) such errors are considered more serious than type 2 errors, where the null hypothesis is not rejected even though the data are inconsistent with it.

Analysts consequently strive to regulate for the presence of spatial autocorrelation using one of two distinct approaches: adjusting the correlation coeffi-

cients to account for spatial autocorrelation, or applying filters (i.e., prewhitening) to reduce spatial autocorrelation. Prewhitening can cause undesirable loss of information (*Clifford et al.*, 1989), so we utilize adjustments to the estimated correlations instead. This may be achieved either by estimating the true number of independent data, N' as discussed by *Clifford et al.* (1989), *Dutilleul et al.* (1993), and *Haining* (2003, p. 278–279), or by employing a spatial adjacency weights matrix (i.e., spatial proximity weights matrix), $\mathbf{W}$ (*Upton and Fingleton*, 1985, p. 176–186, 277–312). Since computation methods for the former can be controversial (e.g., *Dutilleul et al.*, 1993), we utilize the $\mathbf{W}$ matrix instead. Throughout the chapter, we refer to this as the Spatially Weighted Linear Regression (SWLR) method (Section 4.2.2).

The SWLR method does not account for variation in the standard error from one datum to the next. This variation is termed heteroscedasticity and affects instruments such as the GS and NS where variations in atmospheric thickness, composition, and duration of observation contribute to measurement uncertainties. Heteroscedasticity makes the erroneous rejection of the null hypothesis (i.e., type-1 errors) more likely (e.g., *Rawlings et al.*, 1998, p. 412–417, 507–508). Nevertheless, Ordinary Liner Regression (OLR) may be easily adjusted when only the response variable is heteroscedastic, which we describe in detail as the Heteroscedastic Response Linear Regression (HRLR) method (Section 4.2.1). However, the predictor variables can be heteroscedastic as well. Representing the net uncertainty (i.e., standard error estimate) of the i^{th} bin by $\hat{\sigma}_i$, a predictor variable by x, and the response variable by y, predictor heteroscedasticity has an insignificant effect on the reliability of OLR as long as the standard errors of each predictor variable $\left(\hat{\sigma}_{x,i}\right)$ are less than that of the response $\left(\hat{\sigma}_{y,i}\right)$ by much more than the regression coefficient, $\frac{\partial y}{\partial x}$. Analytically, we may express this as

$\hat{\sigma}_{x,i}\frac{\partial y}{\partial x} \ll \hat{\sigma}_{y,i}$ for all i (*Bevington and Robinson*, 2003, p. 102).

Unfortunately, the condition above is not realized for the datasets of some instruments, the GS being an example for which $\hat{\sigma}_{x,i} \approx \hat{\sigma}_{y,i}$. In such cases, additional insight into multivariate relationships can be gleaned by modifying OLR to account for heteroscedasticity in all variables (*Press et al.*, 2002, p. 666–670). We describe this as the Heteroscedastic Linear Regression (HLR) method. While offering additional insight, HLR is computationally intensive due to heavy reliance on simulations. In addition, confidence intervals from HLR are frequently unreliable due to the lack of analytically distributed uncertainties, reducing the usefulness of HLR as a distinct method of evaluating multivariate correlation coefficients. Therefore, we recommend HLR mostly as a supplementary diagnostic tool to evaluate results from Spatially Weighted Linear Regression (SWLR) and Heteroscedastic Response Linear Regression (HRLR).

we utilize additional diagnostic tools to evaluate both the effectiveness of the regression and violations of methodology assumptions. The former is expressed in terms of R^2, confidence intervals for regression coefficients, and probability estimates for correlation coefficients. The confidence intervals and probability estimates use Student's-t (for OLR and HRLR) and standard normal (for SWLR) distributions. While the Student's-t distribution is more rigorous as it avoids the use of standard deviation and average estimated from the sample, the difficulty of properly accounting for degrees of freedom makes the standard normal distribution preferable for SWLR.

For OLR and HRLR, it is possible to estimate both univariate and Bonferroni confidence intervals for the regression coefficients with Student's-t distributions. As discussed in the text accompanying Equation 4.20, the univariate

confidence intervals are determined separately for each coefficient. In contrast, the Bonferroni confidence intervals, which are discussed in the text attending Equation 4.25, reflect how effectively the entire model fits the data. We discuss only the univariate intervals for the SWLR method as given by Equation 4.21, since Bonferroni confidence intervals would be less reliable due to the difficulty of estimating the actual degrees of freedom, N'. Several additional diagnostics of the effectiveness of regression are available to evaluate the OLR and HRLR methods: R^2 adjusted for the degrees of freedom; expected R^2 if the response variable were uncorrelated with any of the predictors; and a one-tailed probability estimate for R^2 based on the Fisher-Snedecor distribution (F-distribution).

Our use of three different test parameters based on Student's-t (in Equations 4.20 and 4.25), Standard Normal (in Equation 4.21), and Fisher-Snedecor (in Equation 4.24) probability density functions (pdfs) enables the statistical confidence values and intervals to be determined in a manner most appropriate for the corresponding correlation and regression parameters. Since the probabilities and confidence intervals based on the three distributions are commonly available in software and a detailed discussion of integrating pdfs is beyond the scope of this work, we refer the reader to tables and software as appropriate.

Diagnostics to identify violations of methodology assumptions consist of visual and quantitative components. Visual diagnostics include: scatter plot of the residuals (i.e., difference between the modeled and observed response, the i^{th} of which is given by $\hat{e}_i$) versus modeled response ($\hat{y}_i$); global maps of $\hat{e}_i$; Durbin Watson test for the presence of serial correlations among residuals; Shapiro-Francia test to determine whether the residuals are random normal; and Moran's I_k test to reveal spatial autocorrelation and the possibility of hid-

den predictors. The latter three include quantitative results as well. The purpose and implementation of each test are discussed in succeeding sections.

4.2 Multivariate Methods

A key aim of all multivariate analysis methods is to determine the regression coefficient for each predictor. This also yields the partial correlation coefficient between the response and each predictor variable. Given our aim to describe the simplest possible techniques without sacrificing rigor, we do not discuss nonlinear multivariate regression. Nevertheless, linear regression methods can be generalized for the nonlinear regime (*Press et al.* (2002, p. 671–689), *Rawlings et al.* (1998, p. 235–268, 485–544), and *Upton and Fingleton* (1985, p. 312–329) provide detailed derivations). Three primary methods of linear correlation analysis are at our disposal: OLR, HRLR, and SWLR. As summarized in Section 4.1, each has its strengths and weaknesses. The OLR and HRLR methods are intuitively appealing, since they are conceptual extensions of line fits to bivariate scatter plots. Without supplemental information from the SWLR method however, both OLR and HRLR estimates for spatial data may be significantly in error.

A few concepts need to be summarized before we discuss the techniques (refer to *Upton and Fingleton* (1985, p. 264–312) and *Rawlings et al.* (1998) for details). Among them, the distinction between population and sample is key. In the current context, we may regard the population as the (unknown) complete range of values for each variable, while the sample is what we have observed subject to numerical and spatial uncertainties (e.g., *Haining*, 2003, p. 51–54). Pa-

rameters such as regression coefficients, determined from the sample are considered estimates, which are indicated by circumflexes. Another key concept is the symbolic form of the response and predictor variable relations involving regression coefficients, b_j. For each modeled (i.e., estimated) response value, $\hat{y}_i$, and each value of the j^{th} predictor variable, $X_{i,j}$, the symbolic relationship is $\hat{y}_i = b_0 + b_1 X_{i,1} + b_2 X_{i,2} + \cdots + b_j X_{i,j} + \cdots + b_{k-1} X_{i,k-1}$. The index, i, refers to the i^{th} spatial bin, so for N data (bins), i varies from 1 to N. $k - 1$ is the number of predictor variables in the model.

In essence, for $j > 0$, each regression coefficient, b_j, is a constant and $b_j = \frac{\partial y}{\partial X_j}$. In other words, the regression coefficient represents the change in y per unit change in X_j, when all other predictors are held constant. In three dimensions (i.e., two predictors) b_0 is the intersection of the model-fit plane with the y axis. For the multivariate case b_0 generalizes as the expected value of y when the predictor variables are all identically zero. Using matrix notation, which is simpler than algebraic notation, we may write the relationships discussed so far (with matrices indicated in boldface and transpose denoted by ′) as:

$$\mathbf{y} = \hat{\mathbf{y}} + \mathbf{e} = \mathbf{X}\mathbf{b} + \mathbf{e} \tag{4.1}$$

where $\mathbf{y}$ is an $N \times 1$ column matrix of all N sample data such that $\mathbf{y} = \begin{bmatrix} y_1 \\ y_2 \\ \vdots \\ y_i \\ \vdots \\ y_N \end{bmatrix}$

$\mathbf{X}$ is an $N \times k$ matrix containing the values of all the predictor variables at

each spatial bin, $\mathbf{X} = \begin{bmatrix} 1 & X_{1,1} & X_{1,2} & \cdots & X_{1,j} & \cdots & X_{1,k-1} \\ 1 & X_{2,1} & X_{2,2} & \cdots & X_{2,j} & \cdots & X_{2,k-1} \\ \vdots & \vdots & \vdots & & \vdots & & \vdots \\ 1 & X_{i,1} & X_{i,2} & \cdots & X_{i,j} & \cdots & X_{i,k-1} \\ \vdots & \vdots & \vdots & & \vdots & & \vdots \\ 1 & X_{N,1} & X_{N,2} & \cdots & X_{N,j} & \cdots & X_{N,k-1} \end{bmatrix}$

$\mathbf{b}$ is an $N \times 1$ column matrix of the k unknown regression coefficients, $\mathbf{b} = \begin{bmatrix} b_0 \\ b_1 \\ \vdots \\ b_i \\ \vdots \\ b_k \end{bmatrix}$

Lastly, $\mathbf{e}$ is an $N \times 1$ column matrix of N unknown statistical errors, $\mathbf{e} = \begin{bmatrix} e_1 \\ e_2 \\ \vdots \\ e_i \\ \vdots \\ e_N \end{bmatrix}$

Equation 4.1 is the basis of OLR and entails the unobserved regression coefficients $\mathbf{b}$ and errors $\mathbf{e}$. The former are key parameters of interest for a given model. There are two intuitive and established methods for seeking a solution. One, known as least squares, is to minimize the sum of squared residuals, $\Delta = \sum_{i=1}^{N} \hat{e}_i^2 = \hat{\mathbf{e}}'\hat{\mathbf{e}}$, where $\hat{\mathbf{e}} = \mathbf{y} - \hat{\mathbf{y}}$. Clearly, minimizing Δ maximizes the agreement between $\mathbf{y}$ and $\hat{\mathbf{y}}$ (*Stuart et al.* (1999, p. 97–98, 538–557) and *Upton*

and Fingleton (1985, p. 266–283) describe least squares in detail). The second method, known as maximum likelihood, is to consider the set of observed values, $\{y_i\}$, as the most likely response values and maximize an expression, L, that represents their joint probability density function. Given its direct association with the probabilistic context, we utilize the maximum likelihood method in our derivations.

Both least squares and maximum likelihood methods are known to yield the optimal regression and correlation results as long as criteria of the Gauss-Markov theorem are satisfied (e.g., *Rawlings et al.* (1998, p. 325–339), *Stuart et al.* (1999, p. 542–543), and *Upton and Fingleton* (1985, p. 266)). The primary criterion of the theorem is for $\{y_i\}$ to be mutually independent and subject to identical uncertainties (i.e., Independent and Identically Distributed: IID). This ensures that the residuals $\{e_i\}$ are mutually independent with each belonging to a random normal distribution with zero mean and variance (i.e., dispersion, the square of standard deviation) σ^2. In statistical notation, this criterion is often stated as the "variance-covariance" matrix of $\{e_i\}$ taking the form $\mathbf{V} = \sigma^2\mathbf{I}$, where $\mathbf{I}$ the identity matrix. Secondarily, $\left\{X_{i,j}\right\}$ are to be mutually independent exact measurements constituting the complete set of predictors. Once these conditions are satisfied, the estimators of the regression coefficients $\left(b_j\right)$, denoted as the set $\left\{\hat{b}_j\right\}$, become the most precise and unbiased (i.e., $\hat{\mathbf{b}} = \mathbf{b}$) estimates (i.e., Best Linear Unbiased Estimators: BLUE).

4.2.1 Ordinary and Heteroscedastic Response Linear Regression

As discussed above, the OLR method yields rigorous regression and correlation coefficients whenever the Gauss-Markov conditions are satisfied. Furthermore, the response variable is Independent and Identically Distributed (IID) in such cases. Consequently, the probability distribution for the unknown error at the i^{th} bin, e_i (Equation 4.1) is also standard normal. The probability density function, P, which is the likelihood of observing an error between e_i and $e_i + h\Big|_{h \overset{Lim}{\to} 0}$ is then given by $P(e_i) = \frac{1}{\sigma\sqrt{2\pi}} \exp\left(\frac{-e_i^2}{2\sigma^2}\right)$, where σ is the unknown standard deviation (i.e., square root of the variance) of $\{e_i\}$. Therefore, the joint probability density function becomes $L = \prod_{i=1}^{N} P(e_i) = \prod_{i=1}^{N} \frac{1}{\sigma\sqrt{2\pi}} \exp\left(\frac{-e_i^2}{2\sigma^2}\right)$. In vector notation:

$$L = \frac{1}{\sigma^N (2\pi)^{N/2}} \exp\left(\frac{-\mathbf{e}'\mathbf{e}}{2\sigma^2}\right) \tag{4.2}$$

L and its natural logarithm, $\ln(L)$, have coincident maxima. Substituting for $\mathbf{e}$ with $\mathbf{b}$, $\mathbf{X}$, and $\mathbf{y}$ using Equation 4.1, we obtain: $\mathbf{e}'\mathbf{e} = (\mathbf{y} - \mathbf{X}\mathbf{b})'(\mathbf{y} - \mathbf{X}\mathbf{b})$. We may consequently write:

$$\ln(L) = c - \frac{N}{2} \ln\left(\sigma^2\right) - \frac{1}{2\sigma^2} (\mathbf{y}'\mathbf{y} - 2\mathbf{b}'\mathbf{X}'\mathbf{y} + \mathbf{b}'\mathbf{X}'\mathbf{X}\mathbf{b}) \tag{4.3}$$

Treating $\left\{X_{\mathrm{i,j}}\right\}$ and $\{y_{\mathrm{i}}\}$ as observables and σ as a constant, we maximize L by estimating $\mathbf{b}$ for $\frac{\partial \ln(L)}{\partial \mathbf{b}} = -2\mathbf{X}'\mathbf{y} + 2\mathbf{X}'\mathbf{X}\mathbf{b} = 0$. Consequently, the OLR estimate of $\mathbf{b}$ is:

$$\hat{\mathbf{b}} = (\mathbf{X}'\mathbf{X})^{-1}\,\mathbf{X}'\mathbf{y} \tag{4.4}$$

Under Gauss-Markov conditions, the variance-covariance matrix of $\{b_j\}$ is determined as a $k \times k$ matrix $\mathbf{E} = \sigma^2\,(\mathbf{X}'\mathbf{X})^{-1}$. The unknown σ^2 is estimated with the sum of squared residuals and degrees of freedom as

$$\hat{\sigma}^2 = (\hat{\mathbf{e}}'\hat{\mathbf{e}})\,/(N-k) = \left\{(\mathbf{y}-\hat{\mathbf{y}})'\,(\mathbf{y}-\hat{\mathbf{y}})\right\}/(N-k) \tag{4.5}$$

Therefore, the estimated variance-covariance matrix of $\{b_j\}$ takes the form of:

$$\hat{\mathbf{E}} = \frac{1}{N-k}\left\{(\mathbf{y}-\hat{\mathbf{y}})'\,(\mathbf{y}-\hat{\mathbf{y}})\right\}(\mathbf{X}'\mathbf{X})^{-1} \tag{4.6}$$

Equations 4.4 and 4.6 lead us to ratios, $\{t_j\}$, of particular significance in both multivariate correlation coefficients and diagnostics:

$$t_j = \left(\hat{b}_j - 0\right)/\sqrt{\hat{E}_{j,j}} \tag{4.7}$$

where $\hat{E}_{j,j}$ from Equation 4.6 is the estimated variance of the regression coefficient $\hat{b}_j$ (*Rawlings et al.* (1998, p. 17, 121–123, 165–167), *Stuart et al.* (1999, p. 735–738), and *Upton and Fingleton* (1985, p. 270–272) provide detailed derivations). With $\{t_j\}$ determined, it is possible to estimate the multivariate correlation coefficients as:

$$r_j = \frac{t_j}{\sqrt{t_j^2 + N - k}} \tag{4.8}$$

where r_j denotes the partial correlation coefficient between the response variable and the j^{th} predictor variable (i.e., the unique correlation between the response and a given predictor) (e.g., *Cohen and Cohen*, 1983, p. 107, 483). It is also possible to determine the partial correlation coefficients without using $\{t_j\}$ (e.g., *Stuart et al.*, 1999, p. 510–523).

As discussed in Section 4.1, spatial datasets can deviate from Gauss-Markov conditions due to heteroscedasticity in the response variable. As long as that is the only deviation from Gauss-Markov conditions, a modification to the variance-covariance matrix of error as $\mathbf{V} = \sigma^2\mathbf{D}$ with $\mathbf{D}$, a diagonal matrix unequal to $\mathbf{I}$, enables transformation of variables to satisfy Equation 4.1 with $\{e_i\}$ remaining IID. This constitutes HRLR. The transformation gives greater significance to data with less uncertainty (containing more information) than to those with greater uncertainty (containing less information). When the net uncertainty of the response variable at each bin, $\hat{\sigma}_{y,i}$, is known explicitly (such as the data from MGS-TES, NS, GS, and IRTM instruments) it is possible to implement the transformation by defining the $\mathbf{D}$ matrix as $\hat{\mathbf{D}} = \begin{pmatrix} \hat{\sigma}^2_{y,1} & 0 & 0 & \dots & 0 & 0 & 0 \\ 0 & \hat{\sigma}^2_{y,2} & 0 & \dots & 0 & 0 & 0 \\ \vdots & \vdots & \vdots & & \vdots & \vdots & \vdots \\ 0 & 0 & \dots & \hat{\sigma}^2_{y,i} & \dots & 0 & 0 \\ \vdots & \vdots & \vdots & & \vdots & \vdots & \vdots \\ 0 & 0 & 0 & \dots & 0 & 0 & \hat{\sigma}^2_{y,N} \end{pmatrix}$. In order to retain the regression coefficients in terms of the original variables, Equation 4.4 is modified as (e.g., *Press* (1982, pp. 218–229) and *Rawlings et al.* (1998, pp. 414–417)):

$$\hat{\mathbf{b}} = \left(\mathbf{X}'\hat{\mathbf{D}}^{-1}\mathbf{X}\right)^{-1}\mathbf{X}'\hat{\mathbf{D}}^{-1}\mathbf{y} \tag{4.9}$$

The resulting estimate for σ is given by

$$\hat{\sigma}^2 = \left(\mathbf{y} - \mathbf{X}\hat{\mathbf{b}}\right)' \hat{\mathbf{D}}^{-1} \left(\mathbf{y} - \mathbf{X}\hat{\mathbf{b}}\right) \frac{1}{N-k} \tag{4.10}$$

The variance-covariance matrix for $\left\{b_j\right\}$ is estimated as $\hat{\mathbf{E}} = \sigma^2 \left(\mathbf{X}'\hat{\mathbf{D}}^{-1}\mathbf{X}\right)^{-1}$. Substituting the estimate for σ^2 we obtain:

$$\hat{\mathbf{E}} = \left(\mathbf{y} - \mathbf{X}\hat{\mathbf{b}}\right)' \hat{\mathbf{D}}^{-1} \left(\mathbf{y} - \mathbf{x}\hat{\mathbf{b}}\right) \frac{1}{N-k} \left(\mathbf{x}'\hat{\mathbf{D}}^{-1}\mathbf{x}\right)^{-1} \tag{4.11}$$

By substituting the values of $\left\{\hat{E}_{j,j}\right\}$ (Equation 4.11) and $\left\{\hat{b}_j\right\}$ (Equation 4.9) in Equation 4.7, the $\left\{t_j\right\}$ ratios are determined as before. Partial correlation coefficients then follow from Equation 4.8.

4.2.2 Spatially Weighted Linear Regression

In the presence of spatial autocorrelation, the error terms in Equation 4.1 cease to be mutually independent. Stated differently, errors corresponding to spatially proximate bins become mutually dependent relative to those that are distant. Given the benefits of satisfying Gauss-Markov conditions, we may express such errors in terms of their transformation into a mutually independent set by utilizing the **W** matrix. For this purpose, we assume that two other criteria are satisfied: homoscedasticity of the response variable (i.e., the net uncertainty is the same across all bins, as opposed to varying from one bin to the next as happens in heteroscedastic data) and exact-valued predictors. The transformation takes the form of $\mathbf{e} = \rho\mathbf{W}\mathbf{e} + \mathbf{u}$, with ρ an optimizing scalar. This allows $\{u_i\}$ to be from a standard normal distribution (i.e., zero mean and variance σ^2) with

$\mathbf{u} = (\mathbf{I} - \rho\mathbf{W})\,\mathbf{e}$. It is then possible to express the maximum likelihood function, L, by modifying Equation 4.2 as:

$$L = |\mathbf{A}| \frac{1}{\sigma^N (2\pi)^{N/2}} \exp\left\{\frac{-(\mathbf{Ae})'\,\mathbf{Ae}}{2\sigma^2}\right\} \tag{4.12}$$

where $\mathbf{A} = (\mathbf{I} - \rho\mathbf{W})$. Analogous to Equation 4.3, $\ln L$ can then be used to estimate both $\mathbf{b}$ and σ:

$$\hat{\mathbf{b}} = (\mathbf{X}'\mathbf{A}'\mathbf{AX})^{-1}\,\mathbf{X}'\mathbf{A}'\mathbf{Ay} \tag{4.13}$$

$$\hat{\sigma}^2 = \frac{(\mathbf{y}'\mathbf{A}'\mathbf{Ay}) - 2\hat{\mathbf{b}}'\mathbf{X}'\mathbf{A}'\mathbf{Ay} + \left(\hat{\mathbf{b}}'\mathbf{X}'\mathbf{A}'\mathbf{AX}\hat{\mathbf{b}}\right)}{N} \tag{4.14}$$

Once Equation 4.14 is evaluated, it is possible to determine $\hat{\mathbf{E}}$ analogous to Equations 4.6 and 4.11. Given the complexity introduced by the spatial weighting, the matrix cannot be simplified to the level of Equations 4.6 or 4.11 (e.g., *Upton and Fingleton*, 1985, p. 299):

$$\hat{\mathbf{E}} = \hat{\sigma}^{\mathbf{4}} \begin{pmatrix} N/2 & \hat{\sigma}^2 \mathrm{tr}\,(\mathbf{U}) & 0 \\ \hat{\sigma}^2 \mathrm{tr}\,(\mathbf{U}) & \hat{\sigma}^4\,\{\mathrm{tr}\,(\mathbf{U}'\mathbf{U}) - \kappa\} & 0 \\ 0 & 0 & \hat{\sigma}^2\mathbf{X}'\mathbf{A}'\mathbf{AX} \end{pmatrix} \tag{4.15}$$

where $\mathbf{U} = \mathbf{WA}^{-1}$, "tr" is the trace of a matrix, $\kappa = -\sum_{i=1}^{N} \nu_i^2 / (1 - \rho\nu_i)^2$, and ν_i is the i^{th} eigenvalue of the $\mathbf{W}$ matrix. The $\hat{E}_{j,j}$ values from Equation 4.15 may be substituted in Equation 4.7 to obtain the t_j parameters. Substitution of t_j values in Equation 4.8 yield the partial correlation coefficients $\left(r_j\right)$ as before.

ρ is implicit in Equations 4.13, 4.14, and 4.15. Maximum likelihood derivation enables this parameter to be estimated by minimizing a new scalar, $M(\rho) = \ln(\mathbf{y}'\mathbf{A}'\mathbf{P}\mathbf{A}\mathbf{y}) - \frac{2\ln|\mathbf{A}|}{N}$. Since local minima are generally not a concern in the minimization of M, one of many minimization algorithms may be used. We utilize an adaptation of the "Golden Section" minimization method (e.g., *Press et al.*, 2002, p. 397–402). First, we evaluate M for equispaced values of ρ. Based on our case studies, a spacing of $\rho_r \times 0.01$, where ρ_r is the dynamic range of ρ, appears to be sufficient. Second, M values are partitioned as triplets. Third, any triplet satisfying $M(\rho_1) \geq M(\rho_2) \leq M(\rho_3)$, where $\rho_1 < \rho_2 < \rho_3$ is selected. These three steps are repeated for the selected triplet at each iteration, with the spacing as $n \times \frac{\rho_r}{100}$ (where n is the iteration and ρ_r is the dynamic range of ρ) to prevent meaninglessly fine precision.

Multiple trials convinced me that four iterations are usually sufficient to identify the value of ρ that minimizes M. The minimization is also visualized with a graph of M versus ρ at each iteration. This estimation method for ρ requires the dynamic range of ρ to be known. Fortunately, as long as all the rows of $\mathbf{W}$ are normalized to unity, the dynamic range is constrained to $(-1, +1)$ (e.g., *Upton and Fingleton*, 1985, p. 282). *Upton and Fingleton* (1985, p. 281–297) and *Doreian* (1980) derive, in detail, the SWLR method and corresponding parameters.

Spatial weights matrix: W

The primary goal of $\mathbf{W}$ is to assign a weight to the spatial proximity between a bin of interest and any other bin. For N bins, this leads to an $N \times N$ matrix, with the i^{th} row containing weights for the spatial proximity of all other bins to the i^{th}

bin. While in theory all the weights could be non-zero, in practice only a limited number of bins would be mutually dependent. This is observed to be true in the GS context where typically less than 10 % of the bins are meaningfully dependent. When the grid data are at a resolution similar to or coarser than that of the instrument, such for the IRTM and MGS-TES, the fraction of dependent bins would be even less. We consider the region of meaningful spatial dependence to be the neighborhood (Equation 4.16 and related text) of the i^{th} bin and assume it to be independent of all bins that are beyond the neighborhood. The **W** matrix is consequently sparse, greatly easing the computational burden of a matrix that would otherwise contain as many as $\approx 7 \times 10^6$ elements.

Besides the row normalization of **W** and exclusion of each bin as its own neighbor (i.e., $W_{i,i} = 0$), there is much leeway in assigning values to its elements. In the binned planetary data context, it is meaningful to define functions of either angular or linear separation as the spatial weights, $W_{i,j}$. These can still take many different forms (refer to *Doreian* (1980), *Haining* (2003, p. 83–87), and *Upton and Fingleton* (1985, p. 176–185)). Nevertheless, when the planet is assumed to be a sphere, the angular and linear separations are directly proportional and may be determined with direction cosines. For example, when the spatial dependence is reasonably isotropic (i.e., independent of direction) a suitable function for the spatial weights for neighbors of the i^{th} bin is given by:

$$w(i, j) = \left(1 - \delta_{i,j}\right) \exp\left\{ s\left(\left(\mathbf{d_i} \cdot \mathbf{d_j}\right) - 1\right)\right\} \tag{4.16}$$

where $\delta_{i,j}$ is the Kronecker delta and j varies as the index of any bin in the neighborhood of bin i. $\mathbf{d_i}$ is the direction cosine vector of the centroid of bin i, while $\mathbf{d_j}$ is that of bin j. The scalar, s, varies the rate of decay of spatial proximity

weights with angular separation. We define the boundary (i.e., angular radius of a neighborhood) as the angular separation from the i_{th} bin, θ_{b}, beyond which spatial dependence is considered negligible. Consequently, $w(i, j) = 0$ for bins beyond the boundary of the neighborhood of i. While inessential, s may be chosen to minimize discontinuity across the boundary such that $w(i, j)\Big|_{\theta \overset{Lim}{\rightarrow} \theta_b} \approx 0$. For the calculation of $w(i, j)$, the latitude (φ_i) and longitude (λ_i) coordinates of the centroid of a bin i are converted to the corresponding cartesian direction cosine vector as $\mathbf{d_i} = \{\cos\varphi_\mathbf{i} \cos\lambda_\mathbf{i}, \cos\varphi_\mathbf{i} \sin\lambda_\mathbf{i}, \sin\varphi_\mathbf{i}\}'$ (e.g., *Arfken and Weber* (2005, p. 123–133) and *Bugayevskiy and Snyder* (1995)). The row-normalized form of $\mathbf{W}$ is computed as $W_{i,j} = \frac{w_{i,j}}{\sum_{j=1}^{N} w_{i,j}}$.

Proper determination of $\mathbf{W}$ also requires the boundary, θ_{b}, to be quantified for each bin. When the dominant cause of spatial autocorrelation is known, it is possible to model the boundary. In the GS data context, the dominant factors are the instrument footprint and the application of a mean filter of constant radius (Chapter 2), which introduce an isotropic and locationally invariant spatial autocorrelation. While the radius differs from one chemical element to the next, for the sake of simplicity without significant loss of accuracy, we define the boundary to be 10° (i.e., $\theta_{\text{b}} = 10°$) throughout the planet. Our choice is an intermediate value considering the 3.7° footprint radius and the radii of mean filters for the majority of elements: 15° for Si; 10° for Cl, Fe, and H; and 5° for K. Similar reasoning may be used to estimate θ_{b} for other instruments.

Where needed however, as long as the spatial autocorrelation is isotropic and locationally invariant, it is also possible to estimate the boundary by means of a global semi-variogram. The semi-variogram, as a plot of the similarity of values (ψ) versus angular separation (θ), effectively reveals the angular separa-

tion (i.e., θ_b) at which values of an attribute become mutually independent. The similarity function, ψ, which relies on the sum of squared differences between the values of bin pairs at a given separation, is formulated as:

$$\psi(\theta) = \frac{1}{2n(\theta)} \sum_{i=1}^{N} \sum_{j} \{c(i) - c(j)\}^2 \tag{4.17}$$

where j varies as the indices of bins that are at an angular separation θ from bin i, $n(\theta)$ is the number of bin pairs that are θ apart, c is the attribute value, and N is the total number of bins (e.g., *Haining*, 2003, pp. 74–79). θ_b may then be evaluated such that $\psi(\theta)\Big|_{\lim_{\theta \to \theta_b}} = C$, where C is a constant. While this method rigorously identifies the boundary, θ_b, it can be computationally costly, even for datasets with only thousands of bins unless θ is restricted to a reasonable range. Alternatives to ψ, which convey the same information, such as the autocovariance are equally costly. Furthermore, $\psi(\theta)$ has to be used with care as it could reflect spatial autocorrelation due to intrinsic properties of the regolith, in addition that from data reduction.

4.3 Hierarchical Modeling and Fit Diagnostics

Evaluating the degree to which the model, consisting of the predictor variables, can describe the global variations of the response variable is an essential step for hierarchical modeling. As discussed in Section 4.1, several diagnostic tools to evaluate the fit are common to OLR, HRLR, and SWLR: coefficient of determination (R^2), probability estimates for correlation coefficients, and confidence intervals for regression coefficients. The first two are also the key parameters in hierarchical modeling.

In the absence of collinearity, the direct linear dependence among two or more predictors, the coefficient of determination as well as the probability estimates for correlation coefficients can be very effective at identifying the most statistically significant predictors for the global variability of the response variable (e.g., *Rawlings et al.*, 1998, pp. 197–200). While unguided hierarchical modeling based solely on statistical parameters is possible (e.g., *Rawlings et al.*, 1998, pp. 208–231), in the planetary context investigators can typically use their knowledge of surface properties to guide the selection of predictor subsets.

In hierarchical modeling, subsets of predictors are selected iteratively from a given set (e.g., the set of all predictors). For the j^{th} candidate predictor we first evaluate the probability $\left(p_j\right)$ that a sample of N data from a parent population where the response is uncorrelated with the predictor could yield a partial correlation $\left(r_j\right)$ at least as extreme as the observed. Conceptually, this reveals the statistical significance of the unique correlation between the j^{th} predictor and the response variable. For example, $p_j = 0.05$ would mean that we have a 95 % statistical confidence in the observed partial correlation, r_j (Equation 4.8). In some cases, one or more predictors would fail to be significant at a commonly used level of confidence (e.g., 68 % or 95 %). However, for large N in the order of 10^3, it may be difficult to eliminate most predictors on the basis of the confidence threshold. Nevertheless, the p_j values may differ by several orders of magnitude from one predictor to the next. We exploit such differences and select predictors that have p_j values at least an order of magnitude or two smaller than the rest. In our case studies with GS and other remote data of Mars, this difference was typically two to three orders of magnitude.

we analyze the subset of predictors selected with p_j values to determine R^2

for the new model. Should it remain comparable with that of the parent set, we compute p_j values for the new model to select the next subset. The process is repeated until all predictors are equally significant within an order of magnitude, or R^2 decreases significantly for the new subset. It is possible to frame the optimal hierarchical subset selection in a quantitative context, by plotting the coefficient of determination against the reduction in predictor variables with each subset. If so done, one may choose a threshold value beyond which R^2 begins to decrease rapidly. However, in our case studies the optimal subset was usually apparent enough that a quantified approach was not worth the additional effort. In essence, our method of hierarchical modeling is a simplified adaptation of stepwise regression by backward elimination (e.g., *Rawlings et al.*, 1998, p. 213).

Given our focus on the correlations as opposed to the linear multivariate fit, we do not utilize the regression coefficients in further study. However, we review their univariate and Bonferroni confidence intervals as a supplementary method to eliminate predictor attributes for which the regression coefficients straddle zero even though the correlation coefficients satisfy the p_j threshold. Where possible, two additional fit diagnostics, the F-test for R^2 and expected R^2 $\left(R_0^2\right)$ for the sample when the response is uncorrelated with all predictors in the population, are reviewed to confirm the validity of the predictor model. As a conservative measure, we also report R^2 adjusted for the degrees of freedom $\left(R_{\text{df}}^2\right)$ where feasible.

4.3.1 Fit Diagnostics

we compute the coefficient of determination, R^2, simply as the square of the multiple correlation coefficient between the modeled ($\hat{y}$) and observed (y) response (*Upton and Fingleton*, 1985, pp. 271–272). Stated in this manner, the analytical expression takes the form:

$$R^2 = \frac{\left\{N \sum_{i=1}^{N} \hat{y}_i y_i - \sum_{i=1}^{N} \hat{y}_i \sum_{i=1}^{N} y_i\right\}^2}{\left\{N \sum_{i=1}^{N} \hat{y}_i{}^2 - \left(\sum_{i=1}^{N} \hat{y}_i\right)^2\right\}\left\{N \sum_{i=1}^{N} y_i^2 - \left(\sum_{i=1}^{N} y_i\right)^2\right\}} \tag{4.18}$$

(e.g., *Young*, 1962, p. 130). The definition of R makes it a nonnegative quantity, with the range $[0, 1]$. The conceptual use of R^2 as the fraction of the variability (i.e., variance) of the response contributed by the model is evident in an alternative expression (e.g., *Upton and Fingleton*, 1985, pp. 271–272) that yields the same value as the above:

$$R^2 = \frac{\sum_{i=1}^{N} (y_i - \bar{y})^2 - \hat{e}'\hat{e}}{\sum_{i=1}^{N} (y_i - \bar{y})^2} \tag{4.19}$$

where $\bar{y}$ is the arithmetic mean of $\{y_i\}$ and the remaining symbols are as defined in Section 4.2. In OLR (i.e., when spatial autocorrelation and heteroscedasticity are assumed absent), the coefficient of determination also equals the sum of partial correlation coefficients, $R^2 = \sum_{j=1}^{k-1} \left(r_j\right)^2$ (e.g., *Cohen and Cohen*, 1983, pp. 86–89).

The estimate of p_j, introduced earlier, utilizes the parameter t_j (Equation 4.7). In OLR and HRLR analyses, t_j follows a Student's-t distribution with $N - k$ degrees of freedom (e.g., *Cohen and Cohen*, 1983), while in SWLR a standard normal distribution may be used as a rough approximation (e.g., *Upton and Fingle-*

ton, 1985, pp. 298–300). When the confidence of both the sign (i.e., positive or negative) and magnitude of r_j is important, p_j is estimated as a one-tailed probability for t_j with either distribution. When only the magnitude of the partial correlation $\left(\left|r_j\right|\right)$ is of interest, p_j is computed as a two-tailed probability. These probabilities are readily available in lookup tables (e.g., *Mascagni et al.*, 2002) and software (Appendix B)

The univariate confidence interval for the j^{th} regression coefficient $\left(b_j\right)$ is estimated using the corresponding standard deviation, $\sqrt{\hat{E}_{\text{j,j}}}$, and an appropriate probability distribution. For both OLR and HRLR the confidence interval may then be stated using the Student's-t distribution as

$$\hat{b}_j \pm t_{(\alpha/2,N-k)} \sqrt{\hat{E}_{\text{j,j}}} \tag{4.20}$$

where $\alpha = 1-\tau$ with τ the desired statistical confidence (e.g., for 95 % confidence, $\tau = 0.95$ and $\alpha = .05$). $t_{(\alpha/2,N-k)}$ is the value of the Student's-t distribution variable with an upper tail probability of $\alpha/2$ for $N-k$ degrees of freedom (e.g., *Rawlings et al.*, 1998, pp. 135–139). The univariate confidence interval for SWLR with a Standard Normal distribution yields

$$\hat{b}_j \pm z_{(\alpha/2)} \sqrt{\hat{E}_{\text{j,j}}} \tag{4.21}$$

where $z_{(\alpha/2)}$ is the value of the Standard Normal variable with an upper tail probability of $\alpha/2$ (e.g., *Upton and Fingleton*, 1985, p. 298). $t_{(\alpha/2,N-k)}$ and $z_{(\alpha/2)}$ values are readily available in literature (e.g., *Mascagni et al.*, 2002) and from software (Appendix B).

OLR and HRLR fit diagnostics

Additional fit diagnostics are available for both OLR and HRLR analyses. As mentioned in Section 4.1 these are three-fold for the coefficient of determination: R^2 adjusted for the degrees of freedom $\left(R^2_{\text{df}}\right)$, expected R^2 if the response were uncorrelated with any of the predictors $\left(R^2_0\right)$, and the F-distribution one-tailed probability of R^2 (p_{R}). The first is expressed as (e.g., *Cohen and Cohen*, 1983):

$$R^2_{\text{df}} = 1 - (1 - R^2)\frac{N-1}{N-k} \tag{4.22}$$

As evident in the expression, R^2_{df} asymptotically approaches R^2 as $\frac{k}{N} \overset{\lim}{\rightarrow} 0$. Consequently, for a given number of predictors, R^2_{df} is significantly less than R^2 only for smaller N. In such cases, R^2_{df} is valuable not only as a better estimate of effectiveness of the model fit, but also as a measure of the usefulness of linear regression.

The second parameter, $\left(R^2_0\right)$, also helps to establish whether linear regression is meaningful for the given dataset and number of predictors. R^2_0 is expressed as (e.g., *Cohen and Cohen*, 1983):

$$R^2_0 = \frac{k-1}{N-1} \tag{4.23}$$

Therefore, even when the response is uncorrelated with the model in the population, the sample may yield a non-zero correlation. R^2_0 quantifies the expectation value of such an apparent correlation, which may be conceptualized as the mean of the coefficient of determination for all possible samples of a given size from the uncorrelated response-predictor population. That linear regression/correlation (be it bivariate or multivariate) would be meaningless in some

cases can be demonstrated by considering an extreme example of three data ($N = 3$) and one predictor ($k = 2$), which yields $R_0^2 = 0.5$. In other words, two uncorrelated variables are likely to indicate an apparent Pearson's correlation of $\sqrt{0.5} = 0.7$ if only three data are used for regression, no matter how precise the values may be! However, R_0^2 is not as informative for very large N since $R_0^2\Big|_{\frac{k}{N}\overset{\lim}{\to}0} = 0$.

The third goodness-of-fit parameter associated with R^2 is the measure of its probability (p_{R}) estimated in a manner analogous to p_j (Section 4.3.1). p_{R} is the probability that a sample of N data from a population where the response is uncorrelated with the set of predictors could yield a coefficient of determination at least as extreme in magnitude as the observed. Only the magnitude is of concern, since both R and R^2 are nonnegative as apparent in Section 4.3.1. The probability (p_{R}) is estimated with a variable, t_R, that follows the F-distribution:

$$t_R = \frac{R^2 (N - k)}{(1 - R^2)(k - 1)} \tag{4.24}$$

where the numerator has $N - k$ degrees of freedom and the denominator $k - 1$ degrees of freedom (refer to *Upton and Fingleton* (1985, pp. 271–272) and *Cohen and Cohen* (1983) for details). The probability, p_{R}, is evaluated as the one-tailed F-distribution probability for t_R. Software often contain functions to evaluate F-distribution probabilities (Appendix B), while lookup tables are also available (e.g., *Mascagni et al.*, 2002).

The final goodness-of-fit parameters relevant for OLR and HRLR are the Bonferroni confidence intervals (e.g., *Rawlings et al.*, 1998, pp. 137–143). These confidence intervals of the regression coefficients $\{b_j\}$ ensure that the statistical confidence of the overall fit is maintained at the desired τ value. As a result,

the dynamic range for each coefficient is usually larger than the corresponding univariate confidence interval. The smaller range of the univariate confidence intervals usually lead to less than τ confidence in the overall fit. The Bonferroni confidence interval for the j^{th} regression coefficient estimate $\left(\widehat{b_j}\right)$ is given by:

$$\widehat{b_j} \pm t_{(\alpha/2k,N-k)} \sqrt{\widehat{E_{j,j}}} \tag{4.25}$$

4.3.2 HLR as a Fit Diagnostic

Even though HLR is essentially a regression method, given inherent difficulties in establishing confidence intervals, we describe it primarily as a tool to determine whether regression results from other methods are significantly skewed due to heteroscedasticity (e.g., Section 4.1). It is important to reiterate that HLR is unnecessary whenever the uncertainties of the predictor values are much smaller than those of the response. We do not report HLR results in the case studies of Section 4.6 as several sample analyses did not indicate it to be particularly informative.

The underlying concept of HLR is to weight each value, of response and predictors, by its standard error, which ensures that values with proportionally higher uncertainties are given less significance than those with lower uncertainties. Besides the weighting, HLR follows the same principles as OLR by seeking to minimize the sum of squared differences between the observed and modeled response as denoted by the merit function χ^2 (e.g., *Press et al.*, 2002, p. 666):

$$\chi^2 = \sum_{i=1}^{N} \frac{\left\{ y_i - \left(b_0 + b_1 x_{i,1} + \ldots + b_j x_{i,j} + \ldots + b_{k-1} x_{i,k-1} \right) \right\}^2}{\widehat{\sigma}_{i,y}^2 + \widehat{\sigma}_{i,1}^2 + \ldots + \widehat{\sigma}_{i,j}^2 + \ldots + \widehat{\sigma}_{i,k-1}^2} \tag{4.26}$$

where $\widehat{\sigma}_{i,j}$ is the estimated standard error of the i^{th} datum for the j^{th} predictor, and remaining symbols are as defined previously. Since χ^2 cannot be minimized analytically, one of many well-established numerical minimization techniques such as Nelder – Mead, differential evolution, simulated annealing, random search etc., needs to be used. The algorithms and underlying reasoning of these methods are available in literature (e.g., *Press et al.*, 2002), and are also built into most mathematical software (Appendix B). A significant drawback to the HLR technique is that numerical minimization techniques can converge to local, instead of global, minima due to the effect of the $\{b_j\}$ initialization values. In order to avoid this possibility, the OLR estimates of the $\{b_j\}$ coefficients may be used as initialization values, at the expense of mutual independence from OLR nevertheless.

Since the numerical minimization of χ^2 does not yield analytical uncertainties for the standard errors of $\{b_j\}$ in the presence of heteroscedasticity, we use a Monte Carlo Bootstrap (MCB) simulation method to estimate the standard errors (e.g., *Press et al.*, 2002, pp. 691–693). The MCB method consists of sampling the response variable, each of the predictor variables, and the standard errors of each with replacement as discrete uniform distributions. For example, x_j, the j^{th} predictor, would be sampled by generating a list of random uniform integers from the interval $[1, N]$ which act as the $\{i\}$ indices of a simulated $\{x_{i,j}\}$ dataset. The values and standard errors of x_j which define each set of MCB simulated data for x_j are extracted with the $\{i\}$ indices, and the process repeated for the desired number of simulations, M (we typically use $M = 300$).

Each of the MCB simulated datasets – consisting of a response variable, predictor variables, and corresponding standard errors – is then used to generate a set of simulated regression coefficients, $\left\{b_j^*\right\}$, by minimizing the corresponding χ^2. The distribution of the M simulated $b_j - b_j^*$ values represent the uncertainty of the b_j coefficient, with the τ confidence interval for b_j estimated using the $\left(0.5 - \frac{\tau}{2}\right)^{\text{th}}$ quantile as the lower bound and $\left(0.5 + \frac{\tau}{2}\right)^{\text{th}}$ quantile as the upper bound. Joint confidence intervals may be obtained with scatter plots of the $b_j - b_j^*$ for two regression coefficients at a time. The confidence intervals may be compared with univariate OLR and SWLR confidence intervals for agreement, with greater M producing more rigorous results.

4.4 Analysis Diagnostics

While Section 4.3.1 discussed methods to evaluate the effectiveness of the model in describing the variability of the response variable, the current section focuses on identifying potential violations of assumptions inherent to the OLR and HRLR methods, with a qualitative diagnostic (bivariate plot of residuals versus response) for the SWLR method. As outlined in Section 4.1 there are two main components to these diagnostics: visual and quantitative. These often complement each other to give the analyst a comprehensive intuitive sense as to the validity of the analysis given the data at hand. On the other hand, using only one of the two may lead to premature rejection of the analysis. It is important to note that should significant violations of methodology assumptions be present, all regression and correlation parameters become suspect, even if model fit diagnostics suggest otherwise. We discuss visual and quantitative diagnostics below in terms of residuals versus response, map of residuals, Durbin-

Watson, Shapiro-Francia, and Moran's-I_k. Most of these tests make extensive use of residuals.

4.4.1 Residuals Versus Response

The most general visual diagnostic of methodology assumptions is the scatter plot of $\widehat{e_i}$ (Equation 4.1) versus $\widehat{y_i}$ (e.g., *Rawlings et al.*, 1998, pp. 342–350). When the data satisfy the analysis assumptions, $\widehat{e_i}$ varies randomly (about zero) with $\widehat{y_i}$. However, statistical effects of a finite N may cause the residuals to deviate slightly from a standard normal distribution (e.g., *Upton and Fingleton*, 1985, p. 340), which we account for by standardizing the residuals. Standardization uses the regular z-score conversion given by:

$$\widehat{e_i^*} = \frac{\widehat{e_i} - \overline{\widehat{e_i}}}{\widehat{\sigma_e}}$$

where $\overline{\widehat{e_i}} = \frac{\sum_{i=1}^{N} \widehat{e_i}}{N}$, and $\widehat{\sigma_e}$ is the standard deviation of the residuals. An example of a scatter plot with simulated data that satisfy methodology assumptions for OLR and HRLR (i.e., IID response and exact-valued mutually independent predictors) is shown in Figure 4.1. Figure 4.1 also illustrates a simulated case where assumptions are violated.

4.4.2 Map of Residuals

A global map of residuals is another essential visual diagnostic tool. Its key utility is to highlight the presence of spatial clustering effects in the data (e.g., *Haining*, 2003), which would encourage regression analysis within subregions

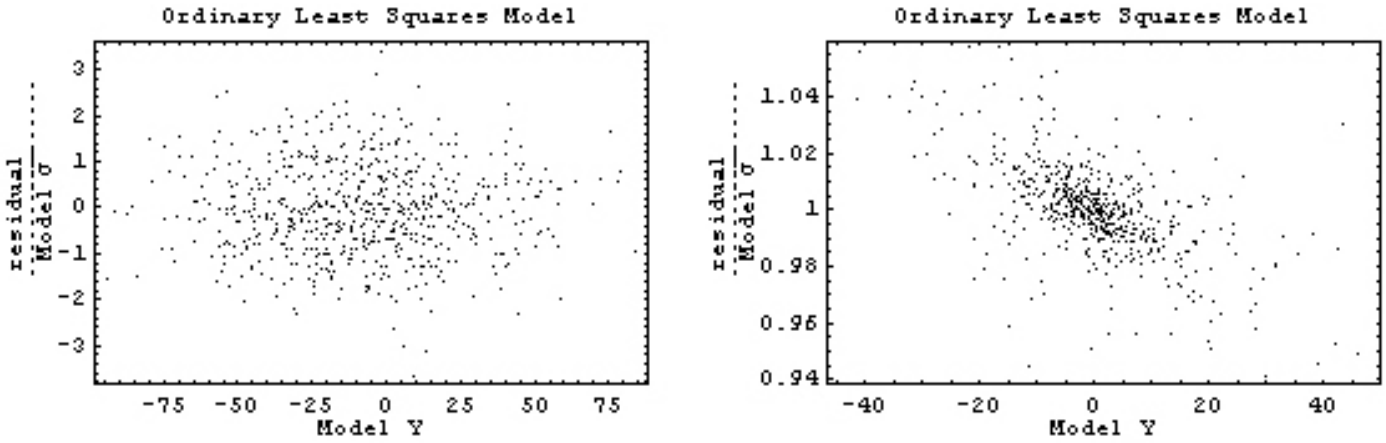

Figure 4.1: Scatter plot of standardized residuals $\left(\widehat{e_i^*}\right)$ versus modeled response $\left(\widehat{y_i}\right)$ simulated for the case of a three-predictor model and response satisfying Gauss-Markov conditions with N = 648 (left). Example where Gauss-Markov conditions are violated by spatial autocorrelation and measurement error in all variables is on the right. In both simulations, the response covaries with only two of the three predictors in the model.

for additional insight. Such evidence may also indicate that the set of predictors lacks one or more statistically significant variables (e.g., *Upton and Fingleton*, 1985, pp. 336–349). Usually, mapping the sign of the residuals would be sufficient, even though the relative variations may also be plotted to further discern patterns to the variability. Figure 4.2 contrasts global maps of both sign and relative variations of residuals for simulated data that satisfy analysis assumptions with those that violate the assumptions. The difference between the two can be muted in the presence of isotropic spatial autocorrelation, though it is usually quite apparent in the presence of clustering and/or anisotropic spatial autocorrelation.

4.4.3 Durbin-Watson

As the plot of each residual $\left(\widehat{e}_i\right)$ versus its immediate predecessor $\left(\widehat{e}_{i-1}\right)$, this test often reveals serial correlations among residuals. Most often, serial correlations result from time series effects in data that vary as a function of time (e.g., *Rawlings et al.*, 1998, pp. 354–355). However, other factors may also cause serial correlation in geospatial data. For example, the mean filter used to process the GS data can introduce a serial effect, due to the large overlap of consecutive filter windows. In the presence of serial correlation, the scatter plot would yield a clear positive slope. A simulated example of serial correlation is given in Figure 4.3 along with one where it is absent. While a minor correlation would not undermine linear regression results, a strong correlation would call for the underlying factor to be included in the model or to be mentioned as a caveat.

The quantitative component of the Durbin-Watson test uses a parameter, d,

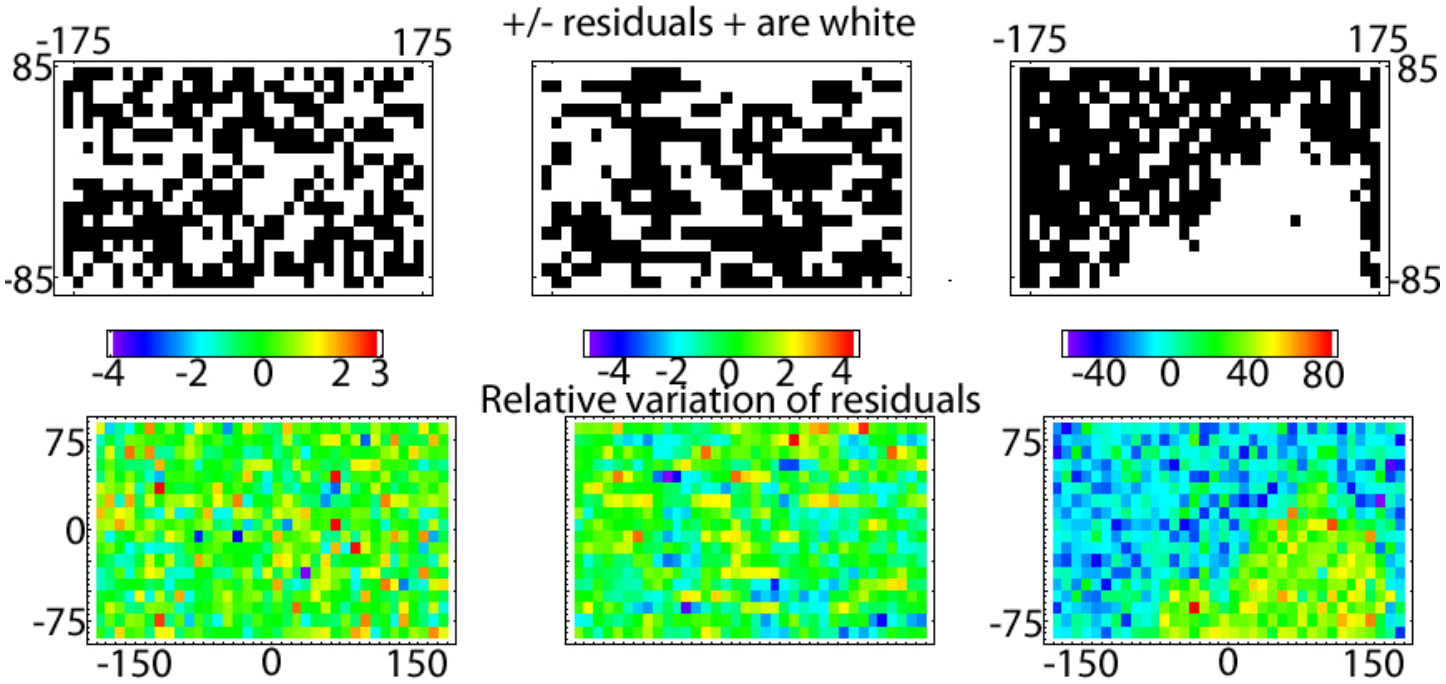

Figure 4.2: Global sketches of residuals for data that satisfy analysis assumptions (left), for heteroscedastic data with spatial autocorrelation (middle), and for data with strong spatial clustering in the response variable (right). Case of three predictors modeling the response variable, of which the predictor covaries with only two at $10^\circ \times 10^\circ$ bin resolution and $N = 648$. Sketches of residual sign are shown above, while (standardized) relative variations of residuals are shown below.

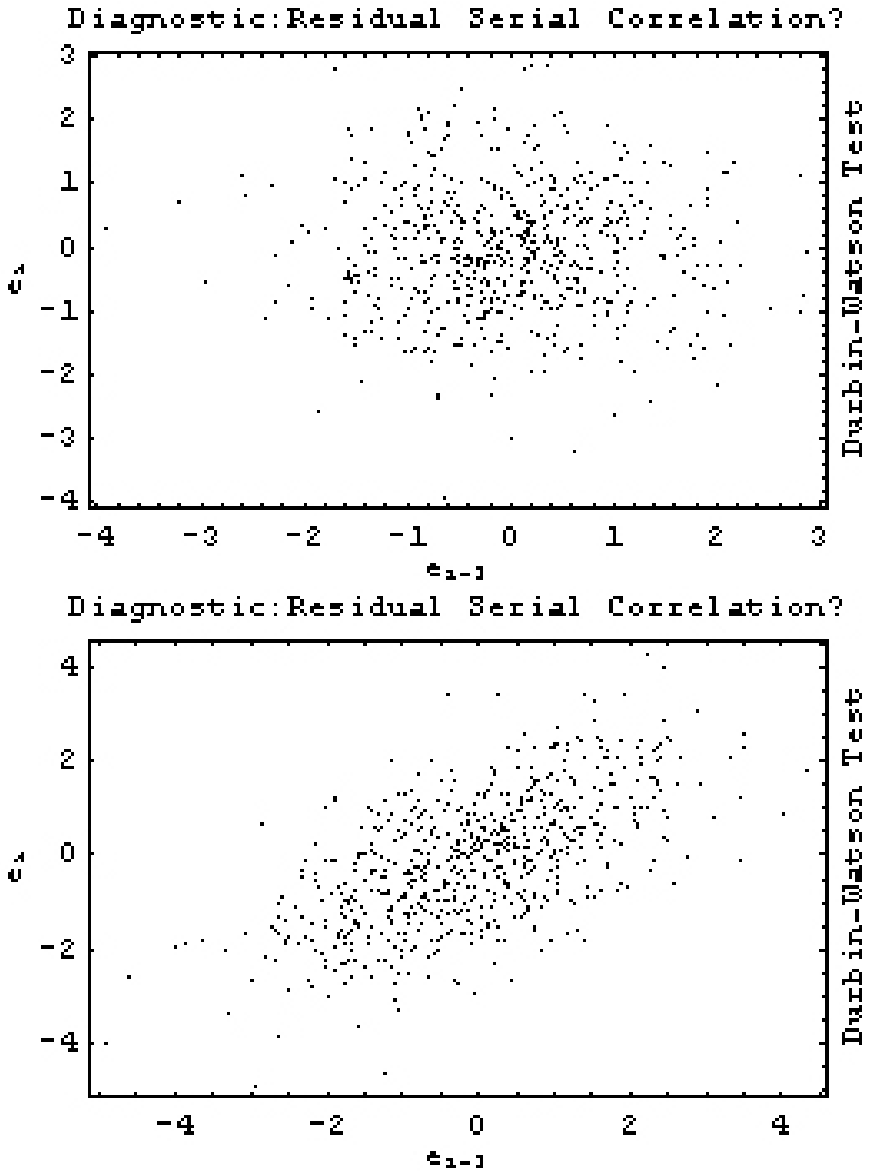

Figure 4.3: Scatter plot of $\left(\widehat{e}_i\right)$ versus $\left(\widehat{e}_{i-1}\right)$ for two predictors using simulated data with $N = 648$. The random variations in the absence of serial correlation is shown at the top, while the positive slope in the presence of serial correlation is shown at the bottom.

with a range $[0, 2]$ varying inversely with serial correlation among residuals (e.g., *Rawlings et al.*, 1998):

$$d = \frac{\sum_{i=2}^{N} \left(\widehat{e}_i - \widehat{e}_{i-1}\right)^2}{\sum_{i=1}^{N} \widehat{e}_i^2} \tag{4.27}$$

This parameter approximates twice the difference of the serial correlation of residuals from unity. As a result, the closer d is to 2, the less likely that the residuals are serially correlated. While d does not easily lend itself to a statement of statistical confidence, the fractional difference of d from 2 can be used as a proxy measure of confidence. Therefore, if $\frac{2-d}{2} \leq \alpha$, ($\alpha$ as defined in Section 4.3.1) we could state that serial correlation of residuals is not evident at roughly τ confidence. For example, if $d = 1.90$ the serial correlation of residuals is not evident at $\approx 95\,\%$ confidence (i.e., $\tau = 0.95$ and $\alpha = 0.05$).

4.4.4 Shapiro-Francia

The visual component of the Shapiro-Francia test consists of a scatter plot of sorted residuals versus sorted values of a standard normal variable, z. As discussed in Section 4.2, if the Gauss-Markov conditions are satisfied by the data, residuals would also belong to a standard normal distribution. In such cases, the scatter plot would yield a correlation that approximating unity at the desired statistical confidence. Finite sample sizes would cause deviations from a perfect correlation, making the plots uninformative for datasets with small N. For larger datasets, major deviations from a correlation of unity would indicate that the residuals are non-normal (i.e., not IID). Such deviations constitute serious violations of analysis assumptions leading to biased confidence intervals and

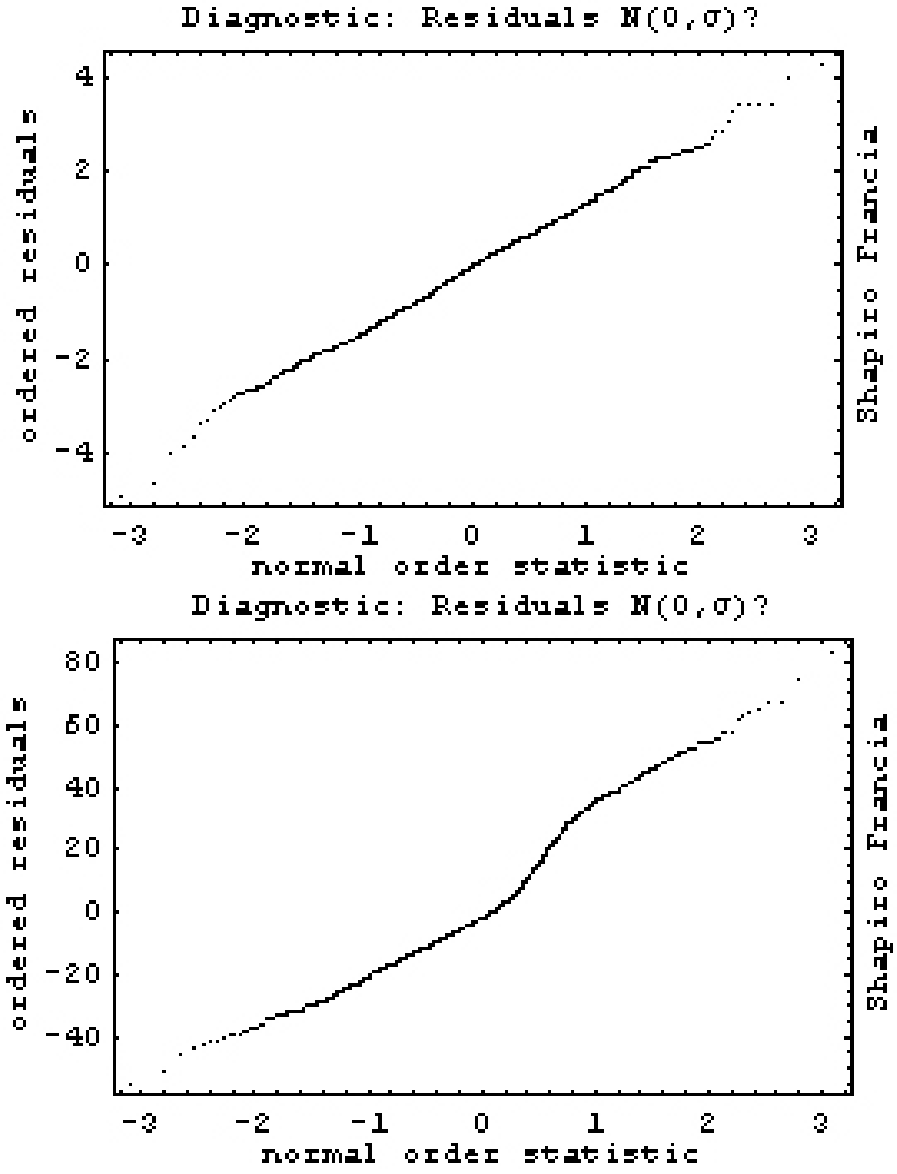

Figure 4.4: Scatter plot of sorted residuals $\left(\widehat{e_i}\right)$ (for two predictors using simulated data with $N = 648$) versus normal order statistics $\left(\widehat{z_i}\right)$. IID residuals are shown at the top, while non-normal residuals are shown at the bottom.

probabilities for regression/correlation parameters (e.g., *Rawlings et al.*, 1998). Examples of scatter plots for both normal and non-normal simulated residuals are given in Figure 4.4. *Rawlings et al.* (1998, pp. 356–359), for example, discuss such plots in detail, including inferences from the manner of deviation from

normality.

The sorted values of z are termed normal order statistics, while the sorted residuals are termed sample order statistics. Since N residuals are being evaluated, the sample size of the $\{z_i\}$ would also be N. There are two ways to generate the set, $\{z_i\}$. One is to utilize a pseudorandom algorithm (e.g., *Press et al.*, 2002) or software to generate M samples of size N of a standard normal variable (Appendix B). Once sorted, the mean of values with the same index across all sets, $\frac{\sum_{l=1}^{M} z_{i,l}}{M}$, generates the i^{th} normal order statistic. The second method to generate normal order statistics uses the inverse cumulative distribution function (CDF) for a standard normal distribution, which is available in most mathematical software (Appendix B). For samples with $N \geq 5$, such software can generate the normal order statistics as $z_i = \phi^{-1}(p_i)$ where ϕ^{-1} is the inverse CDF, and $p_i = \frac{i-3/8}{N+1/4}$ (e.g., *Rawlings et al.*, 1998). Note that i is the index of sorted residuals, varying as ordinals 1 to N.

The Shapiro-Francia test proper, the quantitative test for normality of residuals, is presented in detail by *Upton and Fingleton* (1985, pp. 332–336). The test utilizes a variable, H, derived from the Pearson's correlation coefficient between the sample order and standard normal statistics, r_{N}. We compute r_{N} with a simplified formula for Pearson's correlation, $r_{\text{N}} = \frac{\sum_{i=1}^{N} z_i \widehat{e_i}}{\sqrt{\sum_{i=1}^{N} z_i^2 \sum_{i=1}^{N} \widehat{e_i}^2}}$ where z_i is as defined earlier. H is estimated as $\widehat{H} = \frac{(1-r_{\text{N}}^2)^{\eta}-1}{\eta}$, where $\eta = -0.048\,16 + 0.019\,72S - 0.011\,91S^3$ and $S = \ln N - 5$. The variable H follows a normal distribution with expectation $\overline{H} = -\exp\left(1.693 + 0.1442S - 0.018\,49S^2 + 0.031\,07S^3 + 0.005\,572S^4\right)$ and variance $\sigma_{\text{H}}^2 = \exp\left(-0.5107 - 0.1160S - 0.006\,702S^2 + 0.054\,47S^3 + 0.008\,740S^4\right)$. With these two values, we may estimate the probability that a sample of size N from a population where $r_{\text{N}} = 1$ could yield an H at least as extreme as the

observed. The probability, p_{H}, is evaluated as the two-tailed probability for the standard normal variable $z = \frac{\widehat{H}-\overline{H}}{\sigma_{\mathrm{H}}}$. If $p_{\mathrm{H}} \geq \tau$, the residuals are IID at τ confidence. The data would then satisfy Gauss-Markov conditions at τ confidence as well.

4.4.5 Moran's I_k

The Moran's I_k coefficient is one of the most suited parameters to determine the presence of spatial autocorrelation (e.g., *Upton and Fingleton*, 1985, p. 336). For a given set of residuals, the coefficient is computed as:

$$I_k = \frac{\widehat{\mathbf{e}'\mathbf{W}\mathbf{e}}}{\widehat{\mathbf{e}'\mathbf{W}\mathbf{e}}} \tag{4.28}$$

where all the symbols are as defined in preceding sections. The visual diagnostic compares the I_k for the given set of residuals with I_k coefficients from sets of simulated IID residuals. Each set of simulated IID residuals are computed by first generating N simulated values, z_i, from a standard normal distribution (refer to *Press et al.* (2002) for an algorithm and Appendix B for software commands). These yield simulated residuals, $\widehat{e_i}$, by means of $\widehat{\mathbf{e}} = \mathbf{M}\mathbf{z}$, where $\mathbf{M} = \mathbf{I} - \mathbf{X}(\mathbf{X}'\mathbf{X})^{-1}\mathbf{X}'$. The simulated residuals are transformed to zero mean values with $\widehat{e_i} - \widehat{\overline{e}}$ where $\widehat{\overline{e}} = \frac{\sum_{i=1}^{N}\widehat{e_i}}{N}$. The transformed residuals are substituted in Equation 4.28 to compute an I_k. The distribution of I_k for random samples from a population that satisfies analysis assumptions may be approximated with $\approx$ 1000 simulated I_k values. A plot of these versus an unranked index illustrates the ideal distribution of I_k values, and plotting the sample I_k in the same figure visualizes whether it is typical or atypical of expected values

(Figure 4.5). If the sample I_k is atypical, strong spatial autocorrelation in the data may be suspected. Alternatively, analogous visual comparisons may be made by plotting the sample I_k on a histogram of the simulated I_k values.

The comparison may also be quantified by estimating the probability, p_{I}, that a random sample from a parent population without spatial autocorrelation could yield an I_k at least as extreme as the observed. If $p_{\mathrm{I}} \geq \tau$, we may consider the data to be consistent with the absence of spatial autocorrelation at τ confidence. p_{I} may be approximated as the proportion of simulated I_k values that are at least as extreme as the observed. More detailed discussion and derivation of the Moran's-I_k is provided by *Upton and Fingleton* (1985, pp. 336–340).

4.5 Guide to Implementation

Given the variety of symbols and terminology that has been introduced in the preceding sections, we first present them in summary form with appropriate references to the text in Appendix A. Some commercially available function modules are noted in Appendix B.

In spite of the focus of our work on multivariate correlations, it is reasonable to ask what, if any, of the techniques discussed in the previous sections are applicable in the bivariate case. Even though bivariate analyses have significant shortcomings when a multivariate dataset is available, it is clearly the only viable approach when only two attributes are known. Furthermore, since the geochemical community frequently uses bivariate scatter plots, they are useful for comparisons with literature. Indeed, the techniques we have discussed so far are applicable without modification in the bivariate case with the sole, and

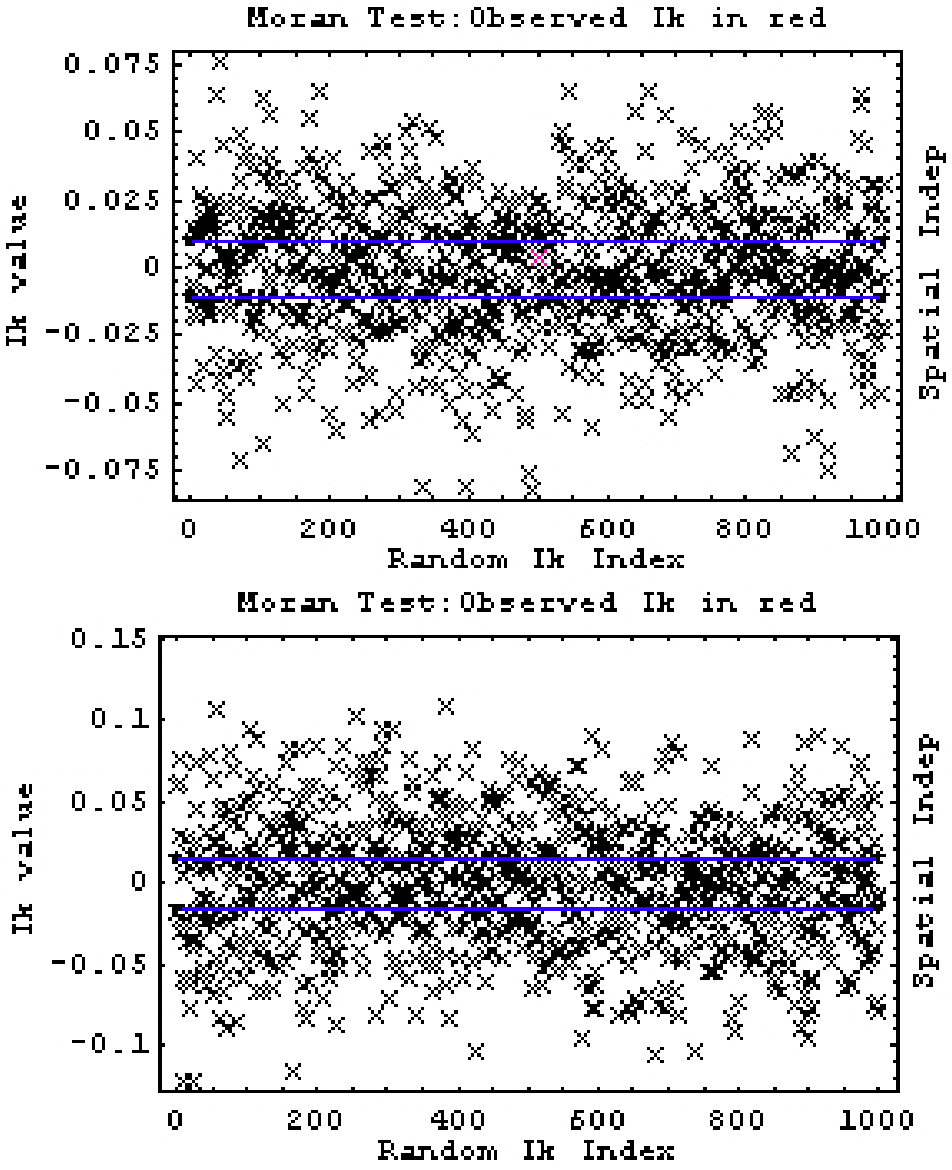

Figure 4.5: Distribution of I_k coefficients corresponding to simulated IID data as a plot of I_k versus an unranked index with the 95 % confidence interval in blue. In the top figure, the I_k in red represents one from a simulated IID dataset. I_k for the simulated spatially autocorrelated dataset is beyond the bounds of the IID I_k values as evident by its absence in the bottom graph.

obvious, exception of hierarchical modeling.

A researcher attempting to elucidate the unique correlations of one variable with each of a set of others can obviously select just one of OLR, HRLR, and SWLR methods. Nevertheless, these methods are also complementary, as the strength of each lies in how it accounts for a particular aspect of the instrumentation and data reduction. A reasonable approach to using the available methods is to first utilize OLR, its fit diagnostics, and its method diagnostics, as it is by far the simplest even though it assumes the data to be IID. The sets of predictors required for this step can consist of all available predictors, those that are striking in bivariate scatter plots, or those that are anticipated to be relevant geochemically. Clearly, all the data sets need to consist of spatially corresponding points.

The primary diagnostic of the meaningfulness of apparent correlations - be they from bivariate or multivariate analyses - is the fit diagnostic, R_0^2. A sufficiently small value of R_0^2 would confirm that there are enough data (i.e., N is sufficiently large) to evaluate multivariate correlations. As a conservative measure, any apparent correlation may be considered insignificant if R_0^2 exceeds 0.10. While an arbitrary constraint, the particular threshold reduces the likelihood that the apparent variance contribution of any selected model, R_{df}^2, would exceed 10 % should the response and predictors be uncorrelated in the population. Generally speaking, this would help researchers to avoid reporting correlations in support of geochemical interpretations unless the correlations are actually meaningful. Even if the analysis meets the threshold condition, it must additionally satisfy $p_R \leq \alpha$, which would indicate whether the overall model is statistically significant at the desired τ confidence.lness of apparent correla-

tions - be they from bivariate or multivariate analyses - is the fit diagnostic, R_0^2. A sufficiently small value of R_0^2 would confirm that there are enough data (i.e., N is sufficiently large) to evaluate multivariate correlations. As a conservative measure, any apparent correlation may be considered insignificant if R_0^2 exceeds 0.10. While an arbitrary constraint, the particular threshold reduces the likelihood that the apparent variance contribution of any selected model, R_{df}^2, would exceed 10 % should the response and predictors be uncorrelated in the population. Generally speaking, this would help researchers to avoid reporting correlations in support of geochemical interpretations unless the correlations are actually meaningful. Even if the analysis meets the threshold condition, it must additionally satisfy $p_R \leq \alpha$, which would indicate whether the overall model is statistically significant at the desired τ confidence.

Once the statistical usefulness of apparent correlations is established in the OLR context, further analyses with HRLR and SWLR are also more likely to yield meaningful results. On the other hand, if OLR shows the model and data to be unsuitable for correlation analyses, the researcher may simply avoid the effort of HRLR analyses, SWLR analyses, and hierarchical modeling.

Even when the response appears to correlate meaningfully with the overall model, additional analysis diagnostics are required to determine the appropriateness of OLR. Among them, the visual diagnostics of residuals versus response (discussion: Section 4.4.1; example: Section 4.6.1) and map of residuals (discussion: Section 4.4.2; example: Section 4.6.1) provide the qualitative context in which to understand the quantitative evaluations from the Shapiro-Francia (introduction: Section 4.4.4) and Durbin-Watson (introduction: Section 4.4.3) tests. Collectively, these tests identify the caveats that must be mentioned in a

rigorous discussion of multivariate or bivariate correlations using OLR.

Once OLR analysis is verified to be sufficiently robust for the data at hand, the resulting partial correlations may be used in interpretations subject to detailed fit diagnostics. The key fit diagnostic for the j^{th} correlation coefficient (r_j) is p_j. For OLR and HRLR in particular, this is complemented by the univariate confidence intervals, Bonferroni confidence intervals, and HLR-based confidence intervals for the regression coefficient, b_j. These fit diagnostics in general, and the p_j values in particular, drive the hierarchical modeling with OLR, HRLR, and SWLR as discussed in Section 4.3.

The nature of the dataset can be used to further constrain the relevance of HRLR and SWLR analyses. Though unlikely for planetary data, if the response variable is known to be homoscedastic, HRLR would clearly be unnecessary. In contrast, SWLR would almost invariably be necessary for correlation analyses with mapped data from remote sensing instruments such as the MErcury Surface, Space ENvironment, GEochemistry, and Ranging (MESSENGER) mission's Gamma Ray and Neutron Spectrometer, Mercury Laser Altimeter, and X-Ray Spectrometer (e.g., *McNutt et al.*, 2006).

However, when the data are from locations spatially separated by much more than the resolution limit of the corresponding instrument, SWLR would be unnecessary. For example, SWLR would not shed much insight into correlations involving elemental mass fractions derived from the Alpha Particle X-ray Spectrometer (APXS) of the Mars Exploration Rovers (MER), since any two samples are usually separated by more than the diameter of the APXS turret. In contrast, correlation analyses involving thermally-derived variables estimated from (locally) remote-sensing instruments such as the MER Miniature Thermal

Emission Spectrometer are likely to benefit from SWLR. Even when the instrumental spatial resolution relative to the spatial separation of data is unknown, the Moran's-I_k diagnostic will usually reveal the need for SWLR.

The implementation of HRLR and SWLR, should they appear necessary on the basis of the previous considerations, is essentially a repeat of the OLR steps above with appropriate modifications as outlined in Sections 4.2.1 and 4.2.2, respectively. A suitable W matrix is needed for the SWLR method, where estimating the scale of spatial autocorrelation would be the greatest challenge. While a modeled value would be reasonable when it is known relatively well as for the GS and Neutron Spectrometers of Mars Odyssey, a semi-variogram may be needed in most other cases.

It is important to note that OLR, HRLR, and SWLR correlation results and the consequent relative statistical significance of predictors will typically diverge depending on how heteroscedasticity and spatial autocorrelation cause the data to deviate from IID assumptions. While such disparities would not make the data unsuitable for correlation analyses, it is essential to account for them during hierarchical modeling.

Occasionally, all three techniques will identify the same key predictors, facilitating the modeling process. When the three methods do not offer any key predictor in common, it is possible to select predictors that are not rejected by any as candidate subsets. Should that also be impractical, several models may need to be considered at each hierarchical step and the final subset chosen on the basis of variance contribution (i.e., the highest value of R^2). The correlation coefficients and other parameters of the final hierarchical model can be summarized as the average of their values derived from OLR, HRLR, and SWLR,

emphasizing the complementary nature of the analyses.

However, should it appear that the three techniques lead to distinct final models, it would be best to present the models separately instead of attempting to force a convergence. In our experience with the GS and TES datasets, such scenarios appeared more likely whenever the response had a low R^2 irrespective of the model or analysis method. All these consideration are an added processing burden. Nevertheless, our methodology reflects a more nuanced approach to correlation analysis that accounts for the effects of spatial autocorrelation and heteroscedasticity and provides a much more robust understanding of variable correlations than afforded by bivariate regression and scatter plots in general, and those without statistical confidence estimation in particular.

4.6 Application: Case Study with K

We now apply the methods developed so far, with a set of Martian geospatial data as an example and Section 4.5 as a general guide. The data are: (1) mass fraction of Cl (2) mass fraction of Fe (3) mass fraction of H as represented by the stoichiometrically computed mass fraction of H_2O (4) mass fraction of K (5) mass fraction of Si (6) mass fraction of Th (7) areal fraction of surface type 1 (ST1) (8) areal fraction of surface type 2 (ST2) (9) thermal inertia (TI) (10) albedo (alb) (11) rock areal fraction (roc). We conduct the analyses in a Mathematica© version 5.2, Windows XP Professional©, 2.8 GHz processor, and 1 GB random access memory software/hardware environment.

The first six attributes were determined with the GS as reported and illustrated by *Boynton et al.* (2007). The next two are based on the derived data from

the MGS-TES instrument (e.g., *Bandfield et al.*, 2000), subject to a 10° constant arc-radius median filter to reduce noise as described and illustrated in Chapter 5. The last three attributes are from the Viking IRTM as reported by *Christensen and Malin* (1988), *Christensen* (1988), and *Christensen* (1986), respectively. For the case study, we consider the spatial variability of the concentration of K in terms of the remaining ten variables. The challenge at hand is to select the optimal set of predictors for the response variable, K, in a multivariate space of eleven dimensions.

As outlined in Section 4.5, the case study follows the steps described in Sections 4.2 through 4.4, and we include specific section and equation references as needed. The first, and essential, step is to bin the values of each attribute into spatially corresponding grids. In this process, the attributes determined with the coarsest spatial resolution dictate the bin size. Since the GS has the coarsest spatial resolution, we use $5^\circ \times 5^\circ$ bins for all datasets. This step precludes additional insight from the recent high resolution mapping of albedo (*Christensen et al.*, 2001), rock areal fraction (*Nowicki and Christensen*, 2007), and thermal inertia (*Christensen et al.*, 2001; *Putzig et al.*, 2005).

The second step is to constrain the spatial extent of all datasets to that with the most limited spatial extent. The two datasets with the most limited spatial extent are the GS elemental data (variables 1–6) and the rock areal fraction data (variable 11). The former do not include the extreme latitudes for non-radioactive (e.g., Cl, Fe, H, and Si) elements primarily due to the difficulty of accounting for the effect of neutron moderation, by elevated H content, on the derived compositions. While K and Th data are available at the extreme latitudes, their concentrations are diluted by the high H concentrations in the polar

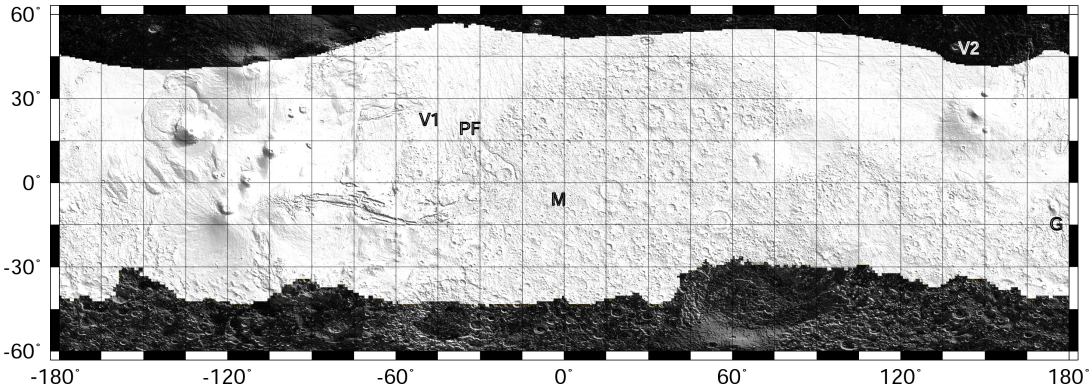

Figure 4.6: Map of the "regression mask" that constrains the spatial extent of all geospatial variables in this case study.

regions as well. Therefore, as *Boynton et al.* (2007) describe, the midlatitudinal region within which all elemental abundances could be accurately determined with the GS is defined by an "H-mask". Meanwhile, reported rock areal fraction data also exclude the extreme latitudes, but more so in the southern hemisphere relative to the GS. Therefore, for this study we delineate the excluded regions by combining the spatial constraints of the two, termed the "regression mask" as illustrated in Figure 4.6.

The next step of multivariate regression is to determine the nature and extent of spatial autocorrelation as discussed in Section 4.2.2. As with the regression mask, the GS data, which have the most severe spatial autocorrelation at the chosen $5^\circ \times 5^\circ$ bin resolution, dictate the model that we use. As discussed in Section 4.2.2, it is possible to rigorously quantify the extent of spatial autocorrelation with the semi-variogram. However, since the primary source of spatial autocorrelation for the GS data is known, we instead assign $\theta_b = 10^\circ$ as described in Section 4.2.2. In order to facilitate computational work, we also use $s = 10^4$ in the spatial weights function (Equation 4.16).

With the datasets assigned to spatially corresponding bins, the spatial extent

constrained, and the spatial autocorrelation quantitatively expressed, it is possible to apply the multivariate correlation analyses methods proper. In order to develop a sense of the basic correlation structure present among our datasets, we begin by visualizing pairwise correlations in the form of a correlation matrix (Figure 4.7) and computing the corresponding Pearson's correlation coefficients. It is immediately apparent that most elements do not demonstrate compelling correlations even in bivariate space, with the exception of K and Th. With the aid of this figure and the differences among data sources we can consider two broad categories of predictors for the mass fraction of each element: (1) mass fractions of the other elements and (2) thermally-derived attributes. We apply OLR, HRLR, and SWLR to these two subsets and the complete set of predictor-response combinations, with our desired statistical confidence as $\tau = 0.95$.

we discuss the case study of K, which shows one of the strongest global-scale correlations with any another attribute, as a detailed example. Multivariate correlations results for Cl are presented summarily by *Keller et al.* (2006b), while those for all the elements are summarized in Chapter 5.

4.6.1 All Predictors Model for K: Results and Fit Diagnostics

As evident from Pearson's correlation coefficients and the bivariate correlation matrix (Figure 4.7), Th mass fraction and rock areal fraction are the two variables with which the K mass fraction shows the greatest magnitude bivariate correlations.

The results of OLR are shown in Figures 4.8 and 4.9. Partial correlations with Cl and H fail the 95 % confidence threshold (Figure 4.8) while the regres-

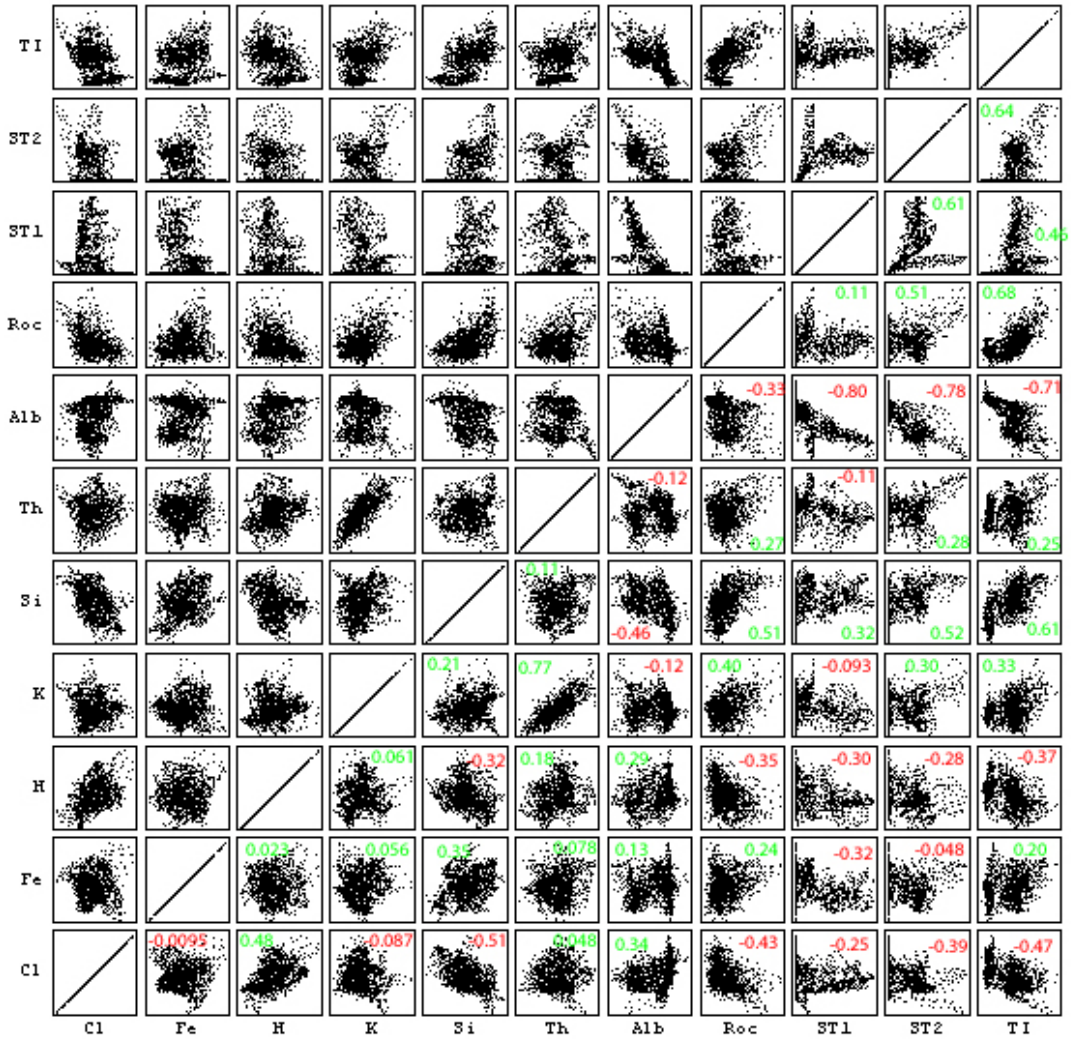

Figure 4.7: Scatter plot matrix of all data as constrained by the regression mask. Elemental mass fractions notated as Cl, Fe, H (represented by stoichiometrically equivalent H_2O), K, Si, and Th. Thermally-derived attributes are albedo (Alb), rock areal fraction (Roc), median-filtered surface type 1 areal fraction (ST1), median-filtered surface type 2 areal faction (ST2), and thermal inertia (TI). Axes units suppressed for qualitative emphasis. The Pearson's correlation coefficient is noted in each graph, with anti-correlations indicated in red.

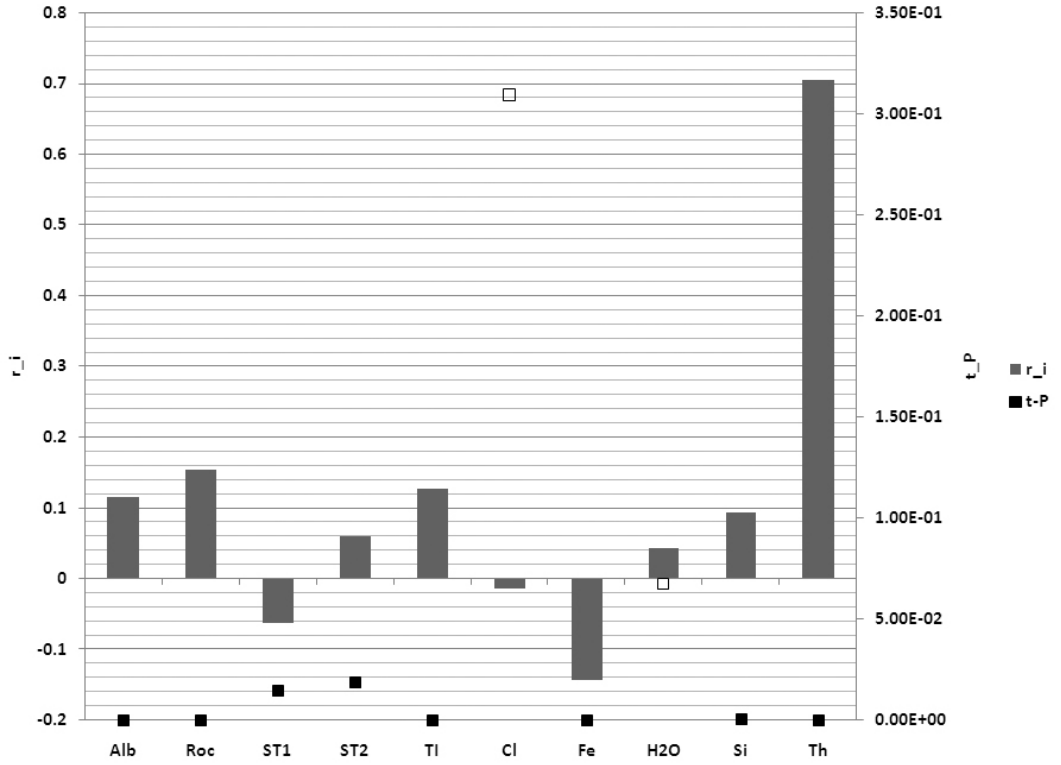

Figure 4.8: OLR correlation results with K as the response and the remaining 10 attributes as predictors. Regression results are shown in Figure 4.9. Predictor variable name abbreviations are as in Section 4.6. r_i is the value of partial correlation shown as a solid column, denoting the unique correlation between the predictor and the response. $t - P$ is the probability that the unique correlation could be as extreme as the observed when sampled from an uncorrelated population. $t - P$ values failing to meet the 95 % confidence level are outlined squares, while the rest are solid squares. The results are interpreted in Section 4.6.1.

sion coefficients of ST1 and ST2 fail the Bonferroni confidence interval (Figure 4.9). There are a few attributes with unusually high statistical confidence (corresponding to the smallest "t-P" values) in Figure 4.8. While Th is by far the most significant among them, rock areal fraction, Fe, and thermal inertia also appear viable as members of the next predictor subset.

The variance contribution of the model as given by R^2, is 66 % under OLR

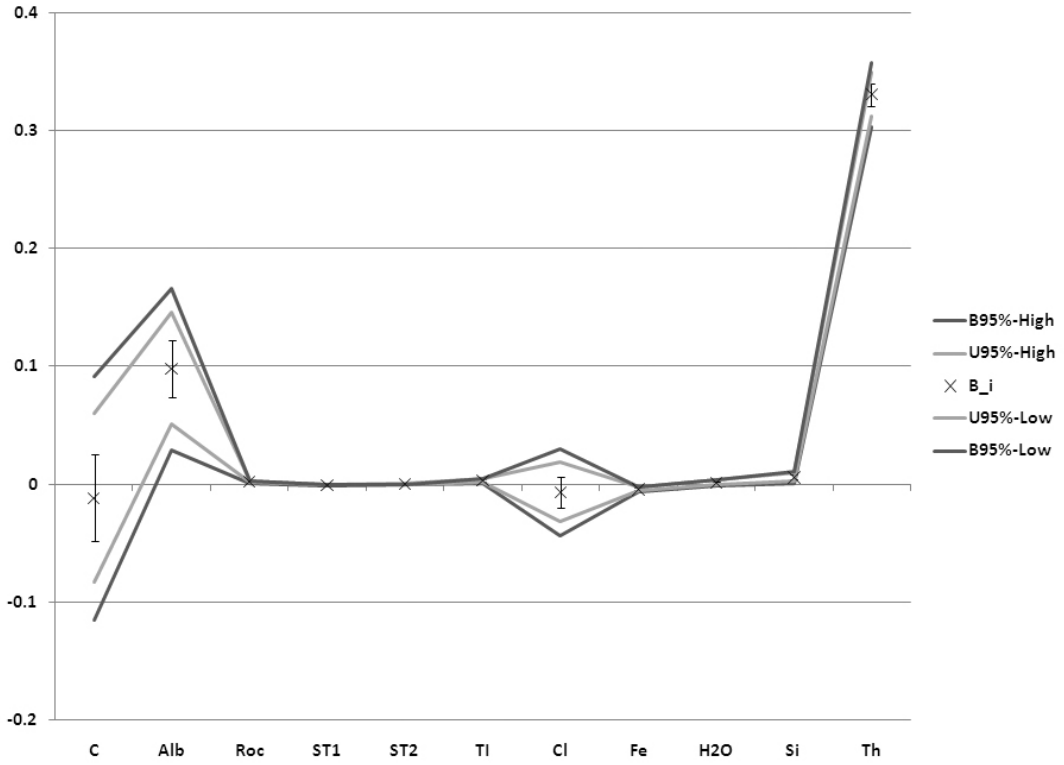

Figure 4.9: OLR regression results with K as the response and the remaining 10 attributes as predictors. Correlations results are shown in Figure 4.8. B_i denotes the regression coefficients with error bars at one standard error ($1s_m$). The constant of regression is identified as "C". 95 % univariate (U95%) and bonferroni (B95%) confidence intervals are shown as bounding lines. The results are interpreted in Section 4.6.1. Regression coefficients are dimensionless except that of thermal inertia in units of $\mathrm{cal}^{-1}\mathrm{cm}^2\mathrm{Ks}^{0.5}$, which we denote as $2.39 \times 10^{-5}\,\mathrm{tiu}^{-1}$ following the notation of *Putzig and Mellon* (e.g., 2007, Eq 4).

analysis. As anticipated, it is statistically significant in excess of 95 % confidence since the F-distribution probability of the R^2 test parameter, with a value of 1×10^{-11}, is essentially zero. We have verified that the size of our datasets with $N = 1237$ is sufficiently large and every predictor model sufficiently effective to yield a statistical significance of essentially 100 % for R^2. Furthermore, the expected R^2 for a population where none of the predictors correlate with

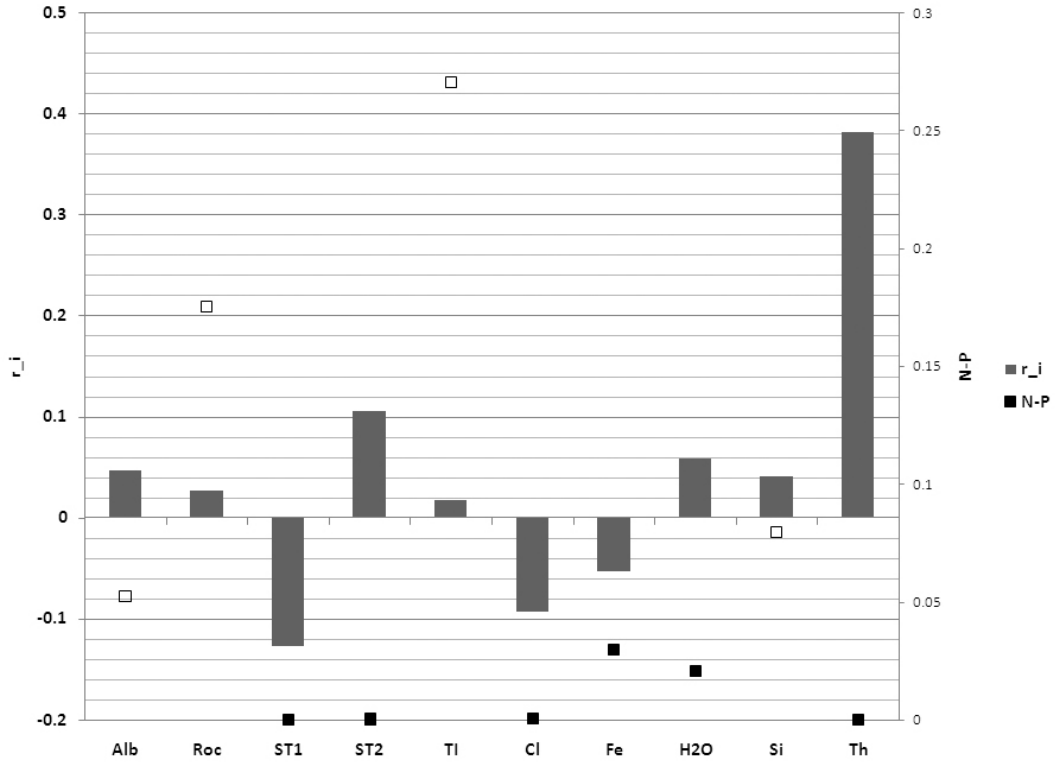

Figure 4.10: SWLR correlation results with K as the response and the remaining 10 attributes as predictors. Regression results are shown in Figure 4.11. Predictor variable name abbreviations are as in Section 4.6. Most symbols are analogous to those of Figure 4.8, with $N - P$ the Gaussian analog to $t - P$. The results are interpreted in Section 4.6.1.

the response, with a value of 0.01, is insignificant relative to the observed for our predictor models. Therefore, we omit the diagnostics of R^2 in the remaining discussion.

SWLR analysis paints a slightly different picture than OLR as shown in Figures 4.10 and 4.11. On the basis of both the statistical confidence of partial correlation coefficients and the univariate confidence intervals of the regression coefficients, the attributes Fe, Si, albedo, rock areal fraction, and thermal inertia may be rejected. However, as before, Th remains strikingly significant. Among

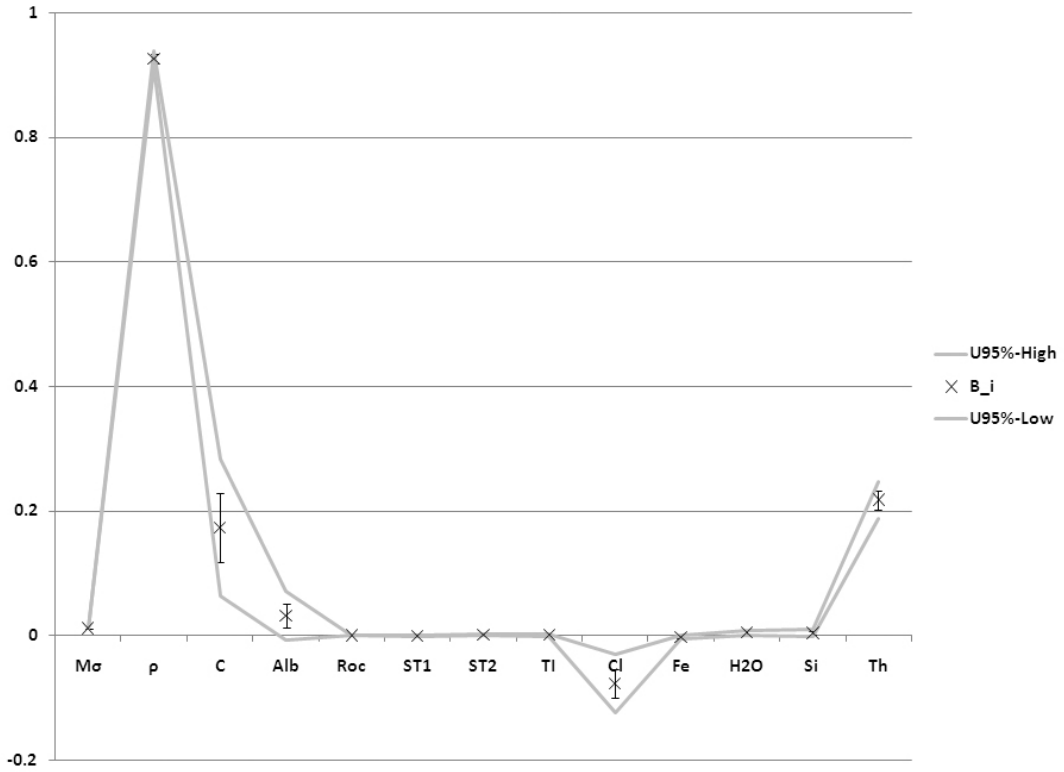

Figure 4.11: SWLR regression results with K as the response and the remaining 10 attributes as predictors. Correlation results are shown in Figure 4.10. Predictor variable name abbreviations are as in Section 4.6. Most symbols are analogous to those of Figure 4.9. "Model σ" is the uncertainty of the overall spatial autocorrelation fit, and ρ is the scalar of the spatial weights matrix (Section 4.2.2). The results are interpreted in Section 4.6.1.

the rest, ST1, ST2, and Cl are tentatively more significant. R^2 indicates a variation contribution of 60 %.

HRLR reveals (Figures 4.12 and 4.13) Th to be the most significant predictor with rock areal fraction, albedo, and ST2 as the other key variables. Cl, Fe, H, and ST1 fail to meet the statistical confidence criteria. The variance contribution is 66 %.

The exclusion of some predictors in favor of others has to reflect the out-

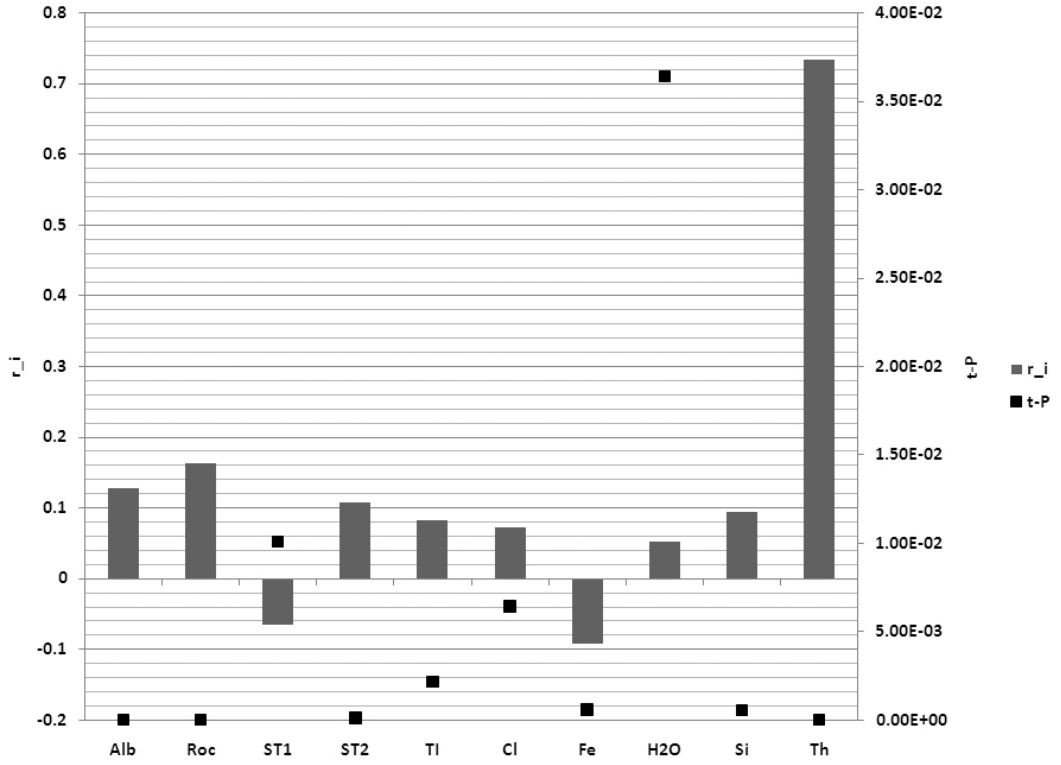

Figure 4.12: HRLR correlation results with K as the response and the remaining 10 attributes as predictors. Regression results are shown in Figure 4.13. Predictor variable name abbreviations are as in Section 4.6. Symbols are the same as in Figure 4.8. The results are interpreted in Section 4.6.1.

comes of all three methods. As expected, the results of the three methods show significant disparities (Section 4.5), and we select attributes for the next hierarchical model after first tabulating the results in Table 4.1. As noted before, the key goal is to reduce the number of predictors without severely degrading the model's variance contribution. Clearly, Th must be retained as a predictor. The results in Table 4.1 also allow limiting the variables to those that are evaluated as key predictors by any one method and rejected by none, yielding Th and ST2 as the predictors for the hierarchical model.

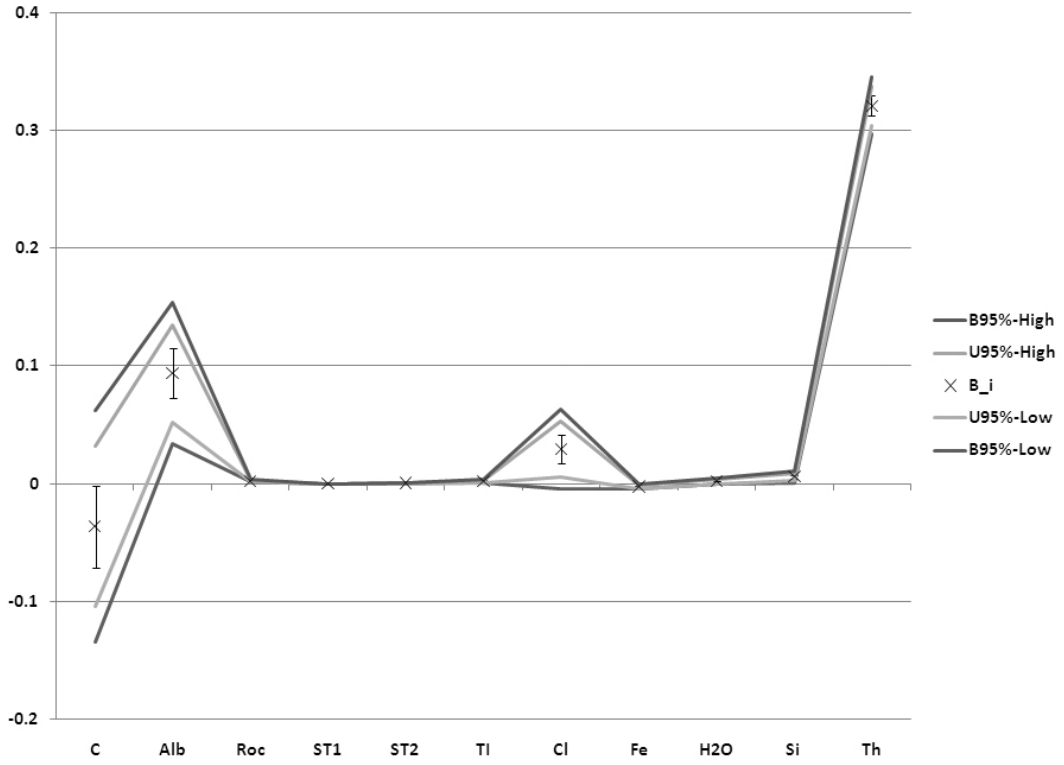

Figure 4.13: HRLR regression results with K as the response and the remaining 10 attributes as predictors. Regression results are shown in Figure 4.12. Predictor variable name abbreviations are as in Section 4.6. Symbols are the same as in Figure 4.9. The results are interpreted in Section 4.6.1.

Method diagnostics

Three primary qualitative diagnostics of OLR, normalized residuals versus $\hat{y}$, i^{th} residual versus $i-1^{\text{th}}$ residual, and ordered residuals versus normal order statistics are shown in Figure 4.14. If OLR method assumptions (Section 4.2.1) were completely satisfied, as outlined in Section 4.4.1 the top graph would show the residuals to vary randomly with $\hat{y}$. While this is not realized, neither are obvious trends evident. However, the middle graph indicates a visually strong serial correlation of residuals. As described in Section 4.4.3, while such co-dependence is usually a sign of time series effects, we attribute it to spatial autocorrelation

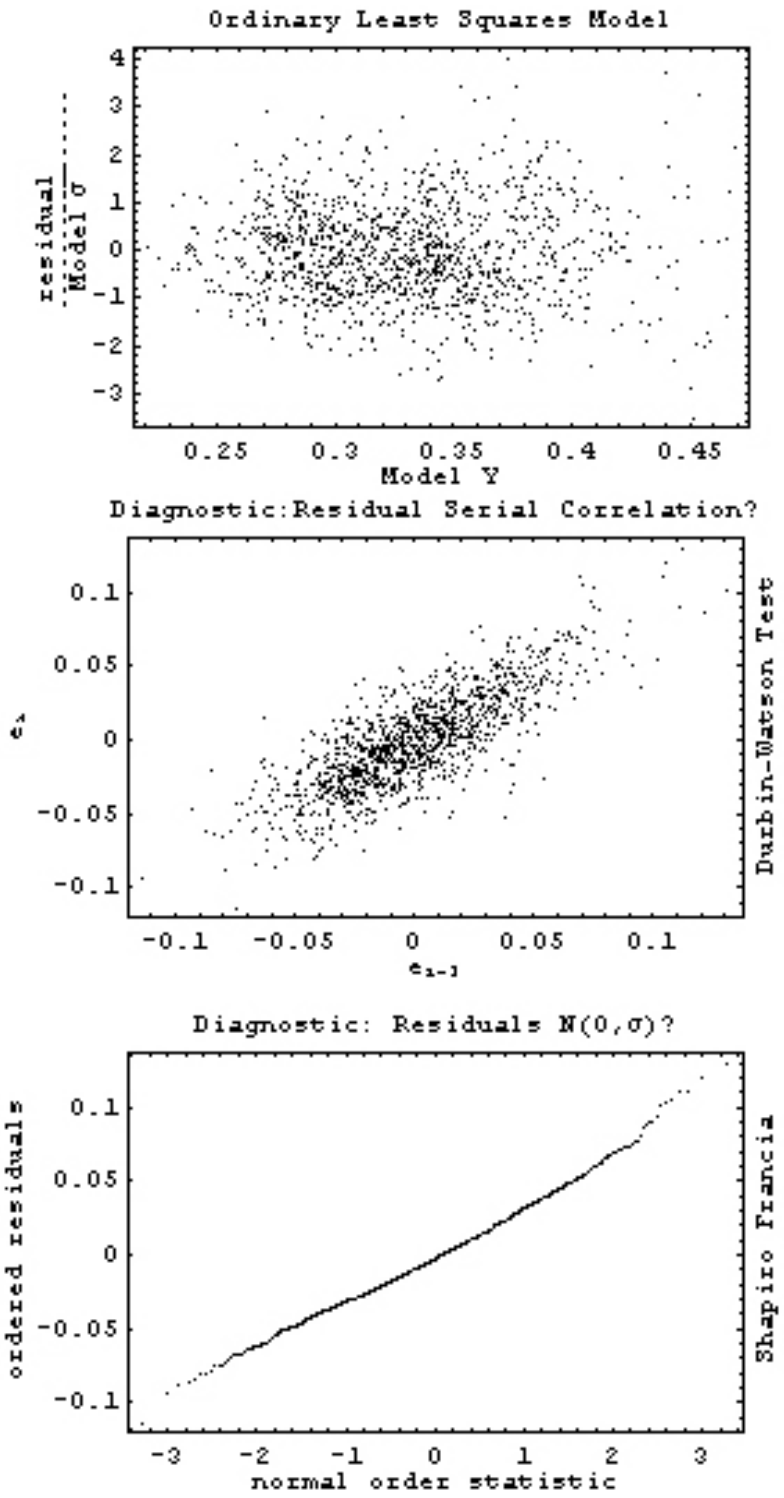

Figure 4.14: Qualitative diagnostics of the OLR analysis with K as the response and the remaining 10 attributes as predictors. Top: Normalized residuals versus $\hat{y}$; Middle: i^{th} residual versus $i-1^{\text{th}}$ residual; Bottom: ordered residuals versus normal order statistics.

Table 4.1: Key predictors, rejected predictors, and variance contribution (as %) in the modeling of the K mass fraction with all other attributes. Predictors are rejected if the partial correlation coefficient, univariate interval of the regression coefficient, or Bonferroni interval of the regression coefficient fails at 95 % confidence. Those listed as key predictors are significant in excess of 99 % confidence and listed in the order of relative significance. The selection of key predictors relies on relative differences of statistical significance among the different predictors. Rock areal fraction is denoted by roc, thermal inertia by TI, and albedo by alb.

Method	Key predictors	Rejected predictors	Variance contribution
OLR	Th, roc, Fe, TI	H, Cl	66
SWLR	Th, ST1, ST2, Cl	Fe, Si, alb, roc, TI	60
HRLR	Th, roc, alb, ST2	Cl, Fe, H, ST1	66

from the mean filter application for the GS data (e.g., Section 2.3.2). As seen in the bottom graph, ordered residuals correlate strongly with normal order statistics, indicating that the residuals mostly belong to a random normal distribution (Section 4.4.4). Therefore, the overall qualitative diagnostics suggest that OLR method assumptions are satisfied approximately, though not perfectly.

The quantitative counterpart of the residual serial correlation plot of Figure 4.14, the Durbin-Watson parameter, is 0.4. Based on the rule-of-thumb threshold we established in Section 4.4.3, the OLR method fails the Durbin-Watson test at our desired 95 % confidence level. This quantitative confirmation of residual serial correlation reinforces the qualitative observation (Figure 4.14), while its probable origin from spatial autocorrelation necessitates the comparison of OLR results with SWLR results at all steps of hierarchical modelling.

The quantitative counterpart of the bottom graph of Figure 4.14 is the

Shapiro-Francia test of normality (Section 4.4.4). Even though the corresponding correlation coefficient of 0.997 is essentially unity, the test is very conservative for large N and the residuals fail to demonstrate normality at 95 % confidence (i.e., the two-tailed probability for $\hat{H}$ to be as extreme as the observed is only $2. \times 10^{-4}$). Nevertheless, on the basis of the value of r_N and the qualitative evaluation, we may consider the residuals to be approximately random normal with OLR yielding meaningful correlation coefficients. The net evaluation from qualitative and quantitative diagnostics of the OLR method is that SWLR results are essential, even though OLR yields fairly reliable results.

The effect of spatial autocorrelation is illustrated and the possible presence of unknown variables revealed by the global maps of residuals in Figure 4.15. These maps reveal distinct regional clusters of positive and negative residuals. While the relative variations in the residual values are somewhat less strongly clustered, they reinforce the general pattern observed in the sign. Qualitatively, this hints of regional variations to the global scale correlations while indicating the presence of spatial autocorrelation and the possibility of unknown predictors. Additional verification of spatial autocorrelation is provided by the position of the observed $I_k = 0.79$ relative to simulated I_k values that are free of spatial autocorrelation (Section 4.4.5). As evident in Figure 4.16, the observed I_k does not even plot within the dynamic range of the simulated I_ks. This observation is reinforced by the comparison of observed I_k with the 95 % confidence interval $-8.4 \times 10^{-3} - -5.2 \times 10^{-3}$ in the absence of spatial autocorrelation, indicating that spatial autcorrelation, if present at the 10° arc-radius spatial scale, cannot be ignored.

HRLR method diagnostics yield conclusions consistent with those of OLR:

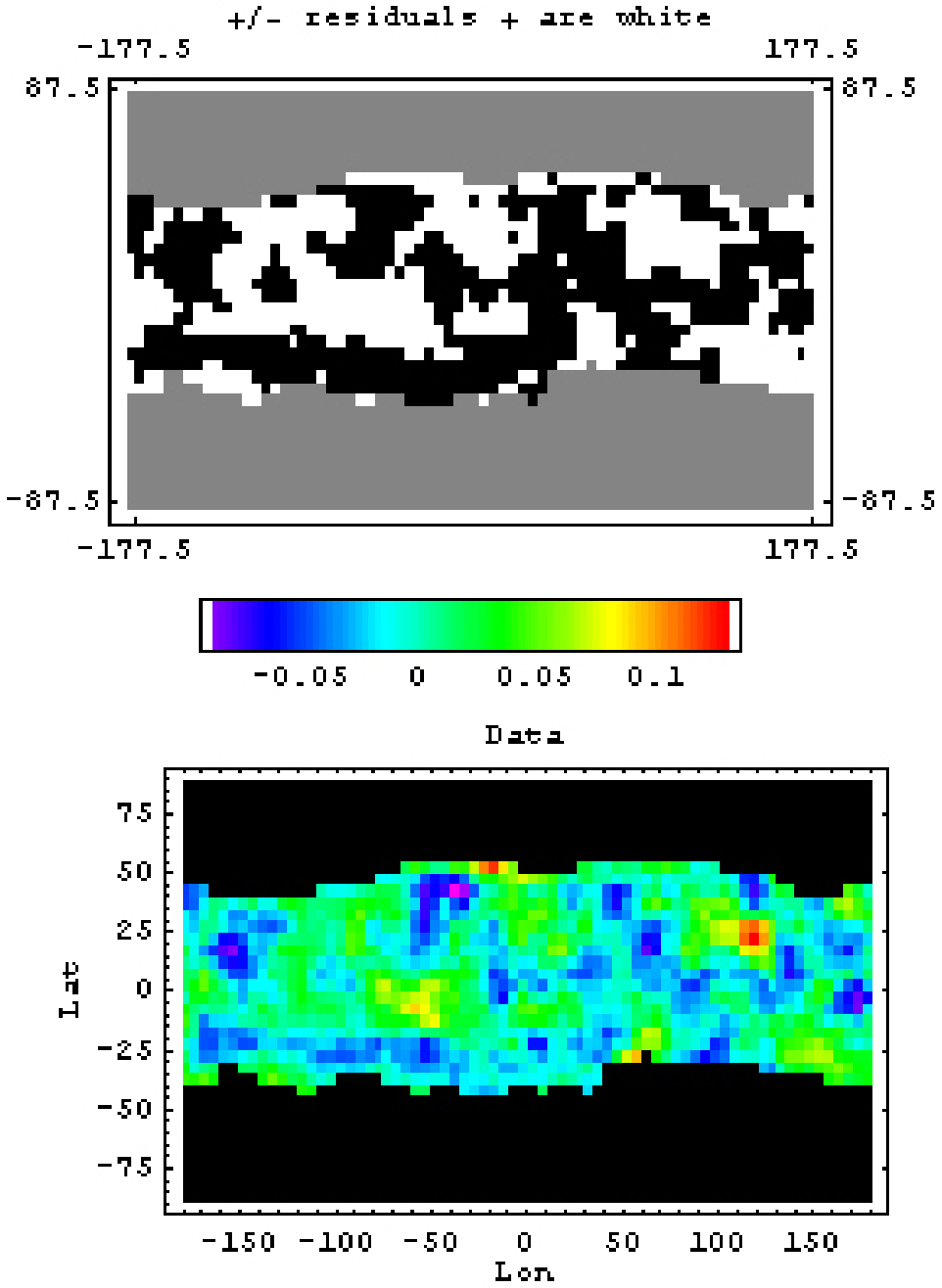

Figure 4.15: Global maps of residuals from OLR analysis with K as the response and the remaining 10 attributes as predictors. Top: Spatial distribution of the sign of residuals. Bottom: Spatial distribution of the residual values.

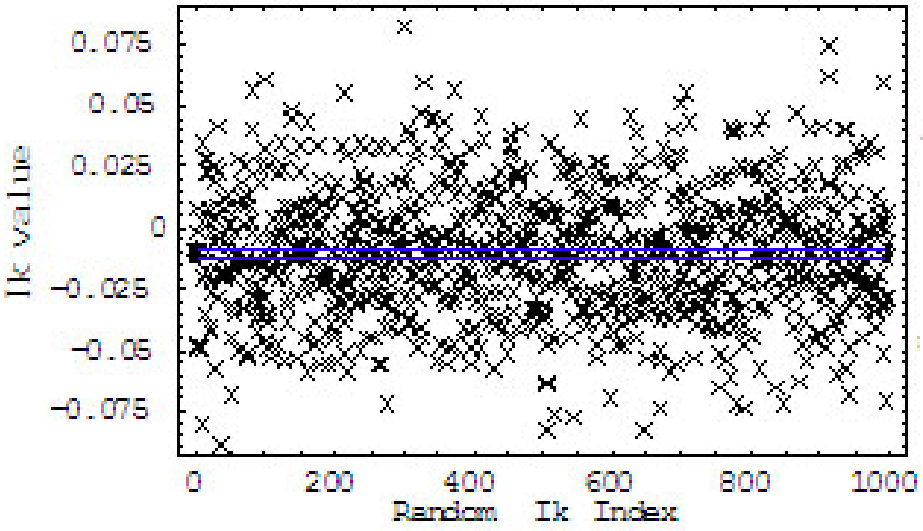

Figure 4.16: Visual application of Moran's I_k test to evaluate the presence or absence of spatial autocorrelation for the case of K as the response and the remaining 10 attributes as predictors. Boundary between blue lines indicate the 95 % confidence interval.

The method is fairly robust even though spatial autocorrelation effects are too severe to be ignored. For example, the HRLR counterpart of Figure 4.14 is Figure 4.17, which indicates that the residuals are nearly random normal in spite of the significant serial correlation due to spatial smoothing. This is reinforced by the quantitative Moran's I_k test (observed $I_k = 0.80$ with the 95 % confidence interval $-9.8 \times 10^{-3} - -6.4 \times 10^{-3}$), Durbin-Watson test (0.4), and Shapiro-Francia test ($r_N = 0.994$ in spite of failing to be significant at 95 % confidence). Lastly, the plot of normalized residuals versus $\hat{y}$ for the SWLR method - the need for which is reinforced by the OLR and HRLR diagnostics - indicates nearly random residuals as seen in Figure 4.18. Note however, that the dynamic range of residuals is significantly more pronounced than for either OLR (Figure 4.14) or HRLR (Figure 4.17). The increased dynamic range may reflect issues with our estimate of the nature and severity of spatial autocorrelation in the datasets.

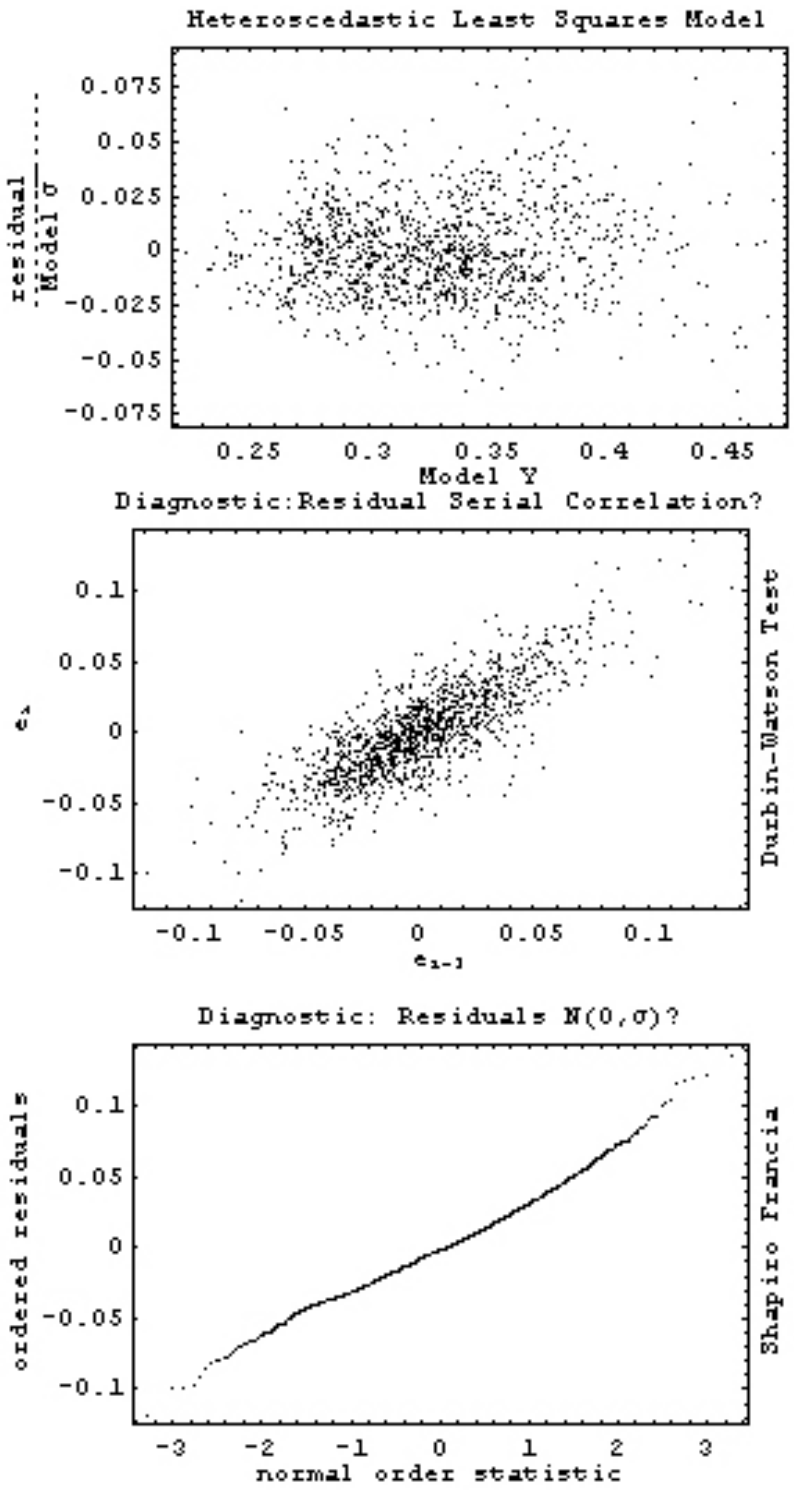

Figure 4.17: Qualitative diagnostics of the HRLR analysis with K as the response and the remaining 10 attributes as predictors. Top: Normalized residuals versus $\hat{y}$; Middle: i^{th} residual versus $i - 1^{\text{th}}$ residual; Bottom: ordered residuals versus normal order statistics.

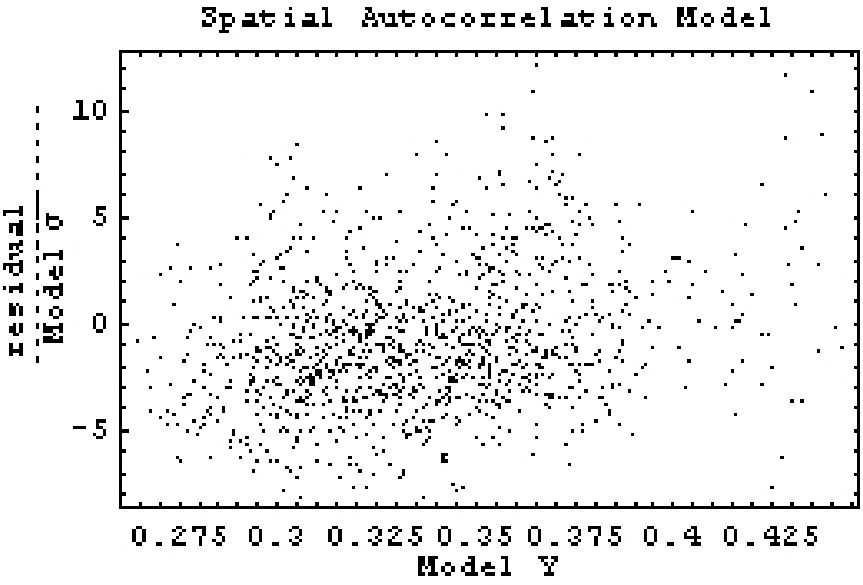

Figure 4.18: Qualitative diagnostics of the SWLR analysis with K as the response and the remaining 10 attributes as predictors. Normalized residuals versus $\hat{y}$.

4.6.2 Thermally-Derived Predictors Model for K: Results and Fit Diagnostics

The results of OLR are shown in Figures 4.19 and 4.20. Albedo fails the univariate 95 % confidence interval for regression (Figure 4.20). ST1 and ST2 are the attributes with highest statistical confidence corresponding to the smallest "t-P" values in Figure 4.19, even though thermal inertia is also highly significant. The variance contribution of the model is 27 % under OLR analysis. This low value is nevertheless statistically significant as discussed in Section 4.6.1.

SWLR analysis yields slightly different significant attributes as shown in Figures 4.21 and 4.22. On the basis of both the statistical confidence of partial correlation coefficients and the univariate confidence intervals of the regression coefficients, the attributes albedo, rock areal fraction, and thermal inertia may

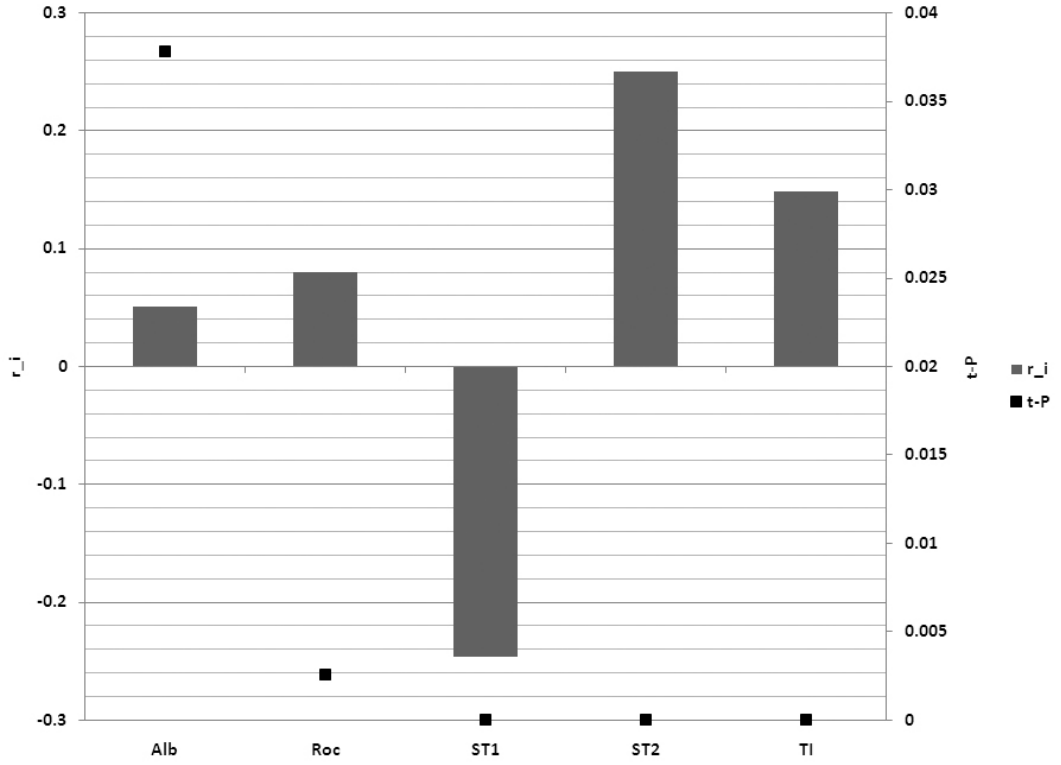

Figure 4.19: OLR correlation results with K as the response and the 5 thermally-derived attributes as predictors. Regression results are shown in Figure 4.20. Predictor variable name abbreviations are as in Section 4.6. Symbols are the same as in Figure 4.8. The results are interpreted in Section 4.6.2.

be rejected. However, as before, ST1 and ST2 are the most statistically significant attributes. R^2 indicates a variation contribution of 15 %.

HRLR reveals (Figures 4.23 and 4.24) ST2, ST1, thermal inertia, and albedo to be the most significant attributes in the order of decreasing significance. Rock areal fraction fails to meet the statistical confidence criteria. The variance contribution is 26 %.

As before, the selection of predictors has to incorporate the results from all three methods. Since the three methods show significant disparities, we select

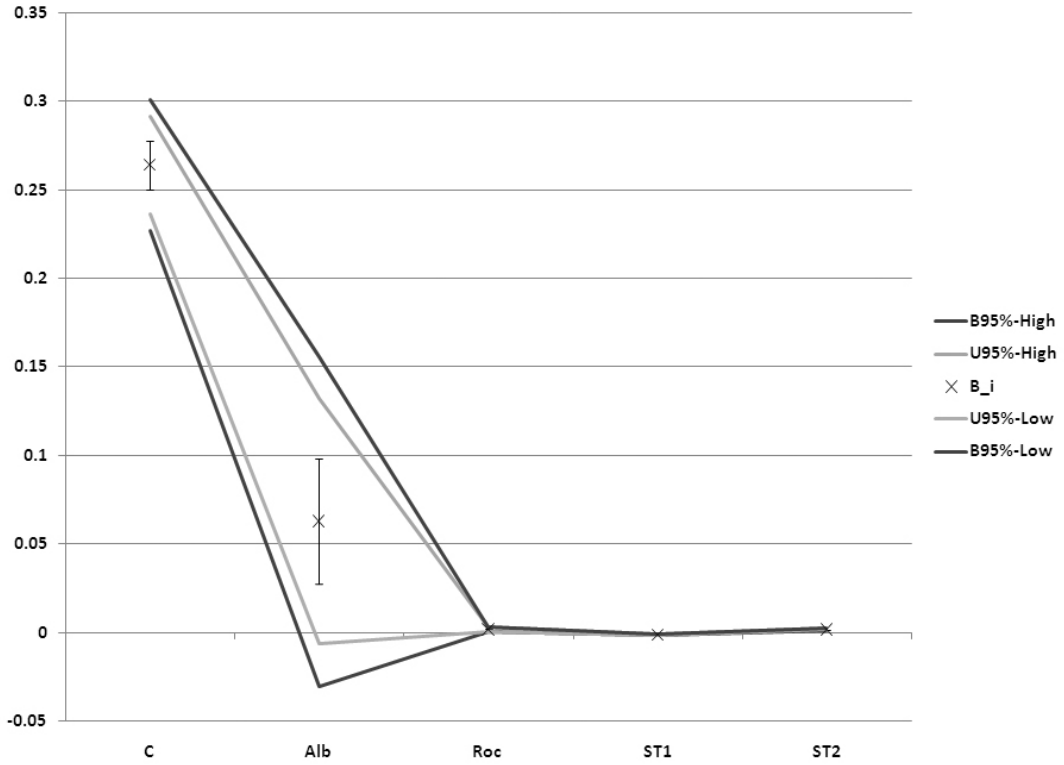

Figure 4.20: OLR regression results with K as the response and the 5 thermally-derived attributes as predictors. Correlation results are shown in Figure 4.19. Predictor variable name abbreviations are as in Section 4.6. Symbols are the same as in Figure 4.9. The results are interpreted in Section 4.6.2.

attributes for the next hierarchical model after first tabulating the results in Table 4.2. As noted before, the key goal is to reduce the number of predictors without severely degrading the model's variance contribution. We restrict the model to variables that are evaluated as key predictors by any one method and rejected by none: ST1 and ST2. However, since the thermally-derived predictors consistently contribute less than 27 % of the variance of K unlike the elemental predictors which contribute more than 50 %, it is clear that the elemental predictors must take precedence over thermally-derived predictors during hierarchical modeling.

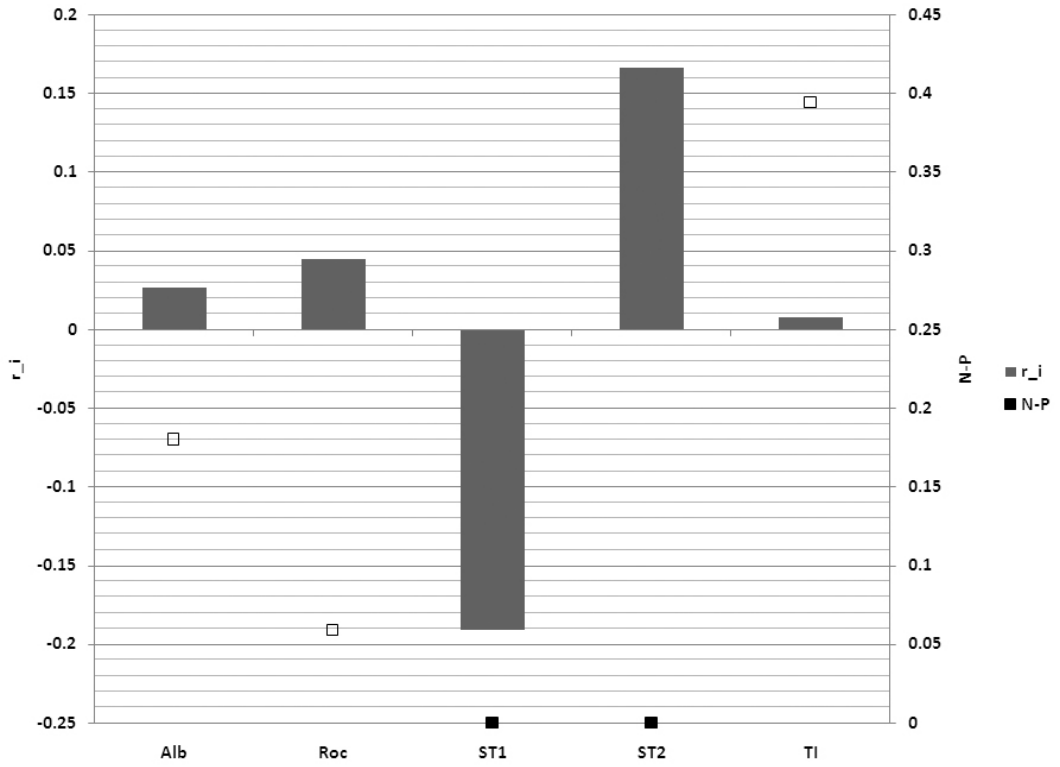

Figure 4.21: SWLR correlation results with K as the response and the 5 thermally-derived attributes as predictors. Regression results are shown in Figure 4.22. Predictor variable name abbreviations are as in Section 4.6. Symbols are identical to those of Figure 4.10. The results are interpreted in Section 4.6.2.

Table 4.2: The key predictors, rejected predictors, and the variance contribution (as %) in the modeling of the K mass fraction with thermally-derived attributes, selected and listed as outlined in Table 4.1.

Method	Key predictors	Rejected predictors	Variance contribution
OLR	ST2, ST1, TI		27
SWLR	ST1, ST2	Alb, Roc, TI	15
HRLR	ST2, ST1, TI, Alb	Roc	26

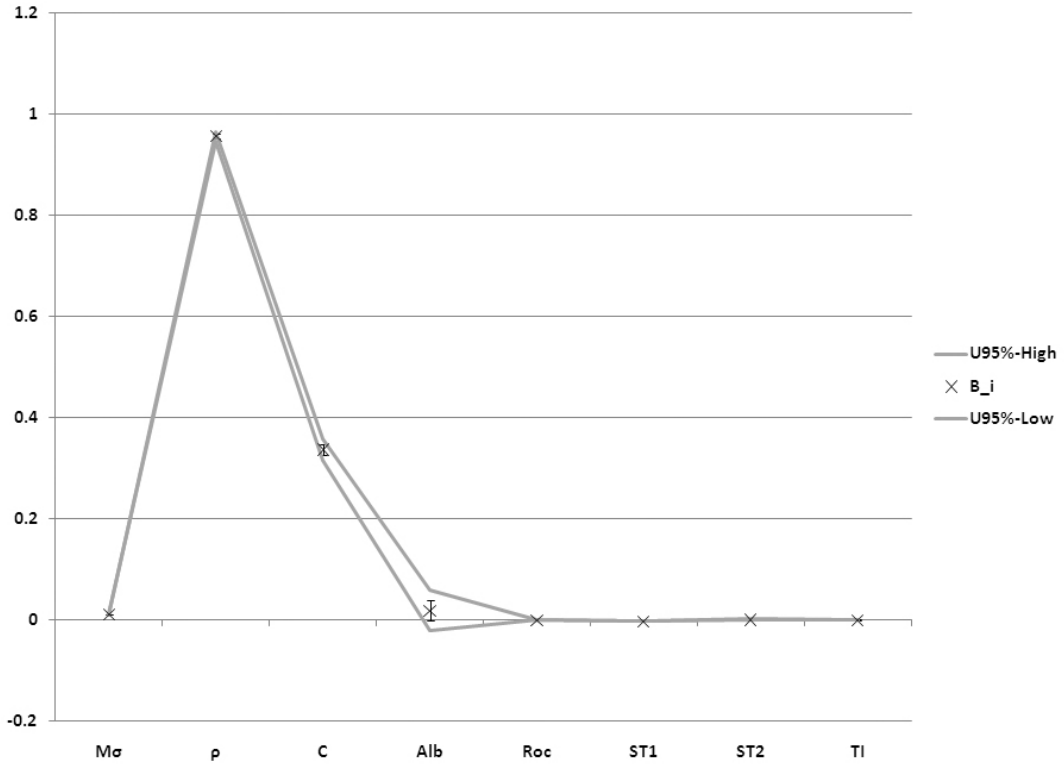

Figure 4.22: SWLR regression results with K as the response and the 5 thermally-derived attributes as predictors. Correlation results are shown in Figure 4.21. Predictor variable name abbreviations are as in Section 4.6. Symbols are identical to those of Figure 4.11. The results are interpreted in Section 4.6.2.

Method diagnostics

The diagnostics are generally consistent with those of OLR in Section 4.6.1. For example, while the residuals do not vary randomly with $\hat{y}$, neither are obvious trends evident (Figure 4.25). Furthermore, the middle graph of Figure 4.25 indicates a visually strong serial correlation of residuals, again consistent with the discussion in Section 4.6.1. As before, we attribute it to spatial autocorrelation from the mean filter application on the GRS data (Section 2.3.2) and conclude that the residuals are mostly random normal on the basis of the bottom graph

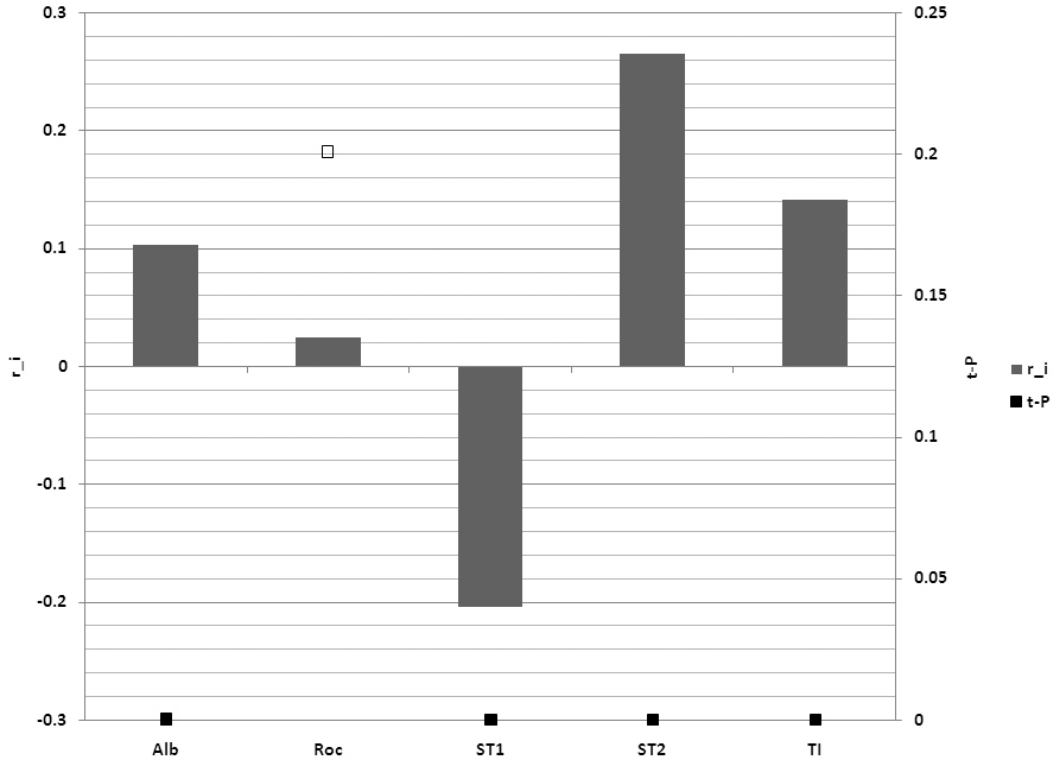

Figure 4.23: HRLR correlation results with K as the response and the 5 thermally-derived attributes as predictors. Regression results are shown in Figure 4.24. Predictor variable name abbreviations are as given at the start of Section 4.6. Symbols are the same as in Figure 4.12. The results are interpreted in Section 4.6.2.

(Figure 4.25). Therefore, the overall qualitative diagnostics suggest that OLR method assumptions are satisfied approximately, though not exactly.

The effect of spatial autocorrelation is illustrated and the possible presence of unknown variables revealed by the global maps of residuals in Figure 4.26. These maps, as well as the Moran's I_k comparison where the observed is beyond the dynamic range of the simulated (Figure 4.27) are consistent with the observations involving all variables in Section 4.6.1 indicating that spatial autocorrelation at 10° arc-radius spatial scales cannot be ignored.

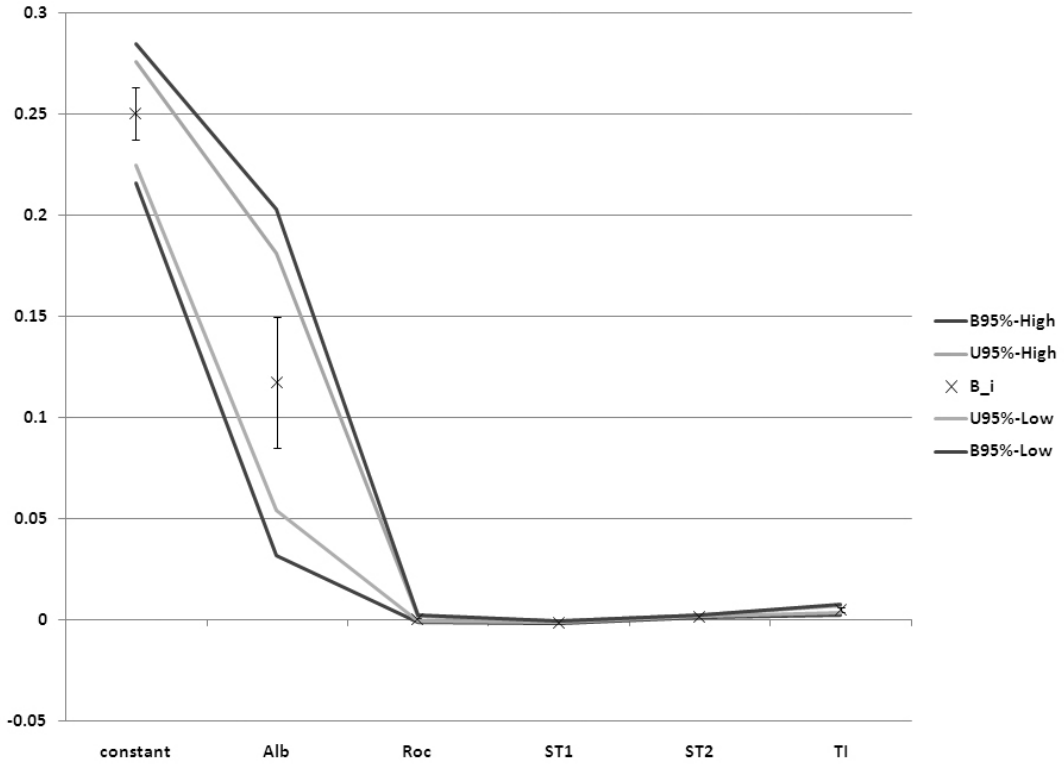

Figure 4.24: HRLR regression results with K as the response and the 5 thermally-derived attributes as predictors. Correlation results are shown in Figure 4.23. Predictor variable name abbreviations are as given at the start of Section 4.6. Symbols are the same as in Figure 4.13. The results are interpreted in Section 4.6.2.

The quantitative tests consisting of the Durbin-Watson parameter (0.2) and Shapiro-Francia test of normality (r_N = 0.999) reveal the residuals to be approximately random normal with OLR yielding meaningful correlation coefficients. As observed in Section 4.6.1, the net assessment from qualitative and quantitative diagnostics of the OLR method is that SWLR results are essential, even though OLR yields fairly reliable results. As before, HRLR method diagnostics yield conclusions similar to those of OLR: The method is fairly robust even though spatial autocorrelation is too severe to be ignored (e.g., Figure 4.28).

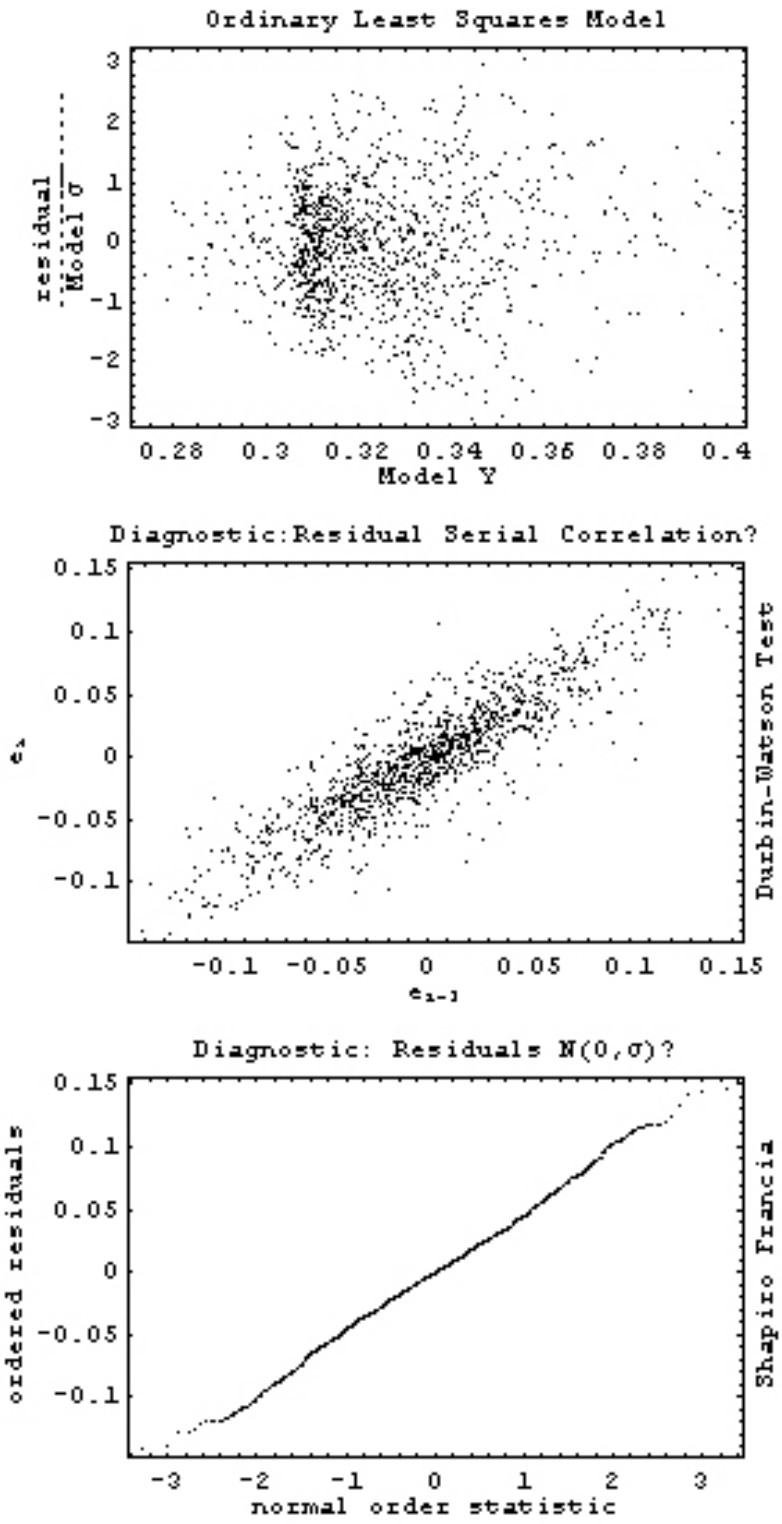

Figure 4.25: Qualitative diagnostics of the OLR analysis with K as the response and the 5 thermally-derived attributes as predictors. Top to bottom: Normalized residuals versus $\hat{y}$; i^{th} residual versus $i-1^{\text{th}}$ residual; ordered residuals versus normal order statistics.

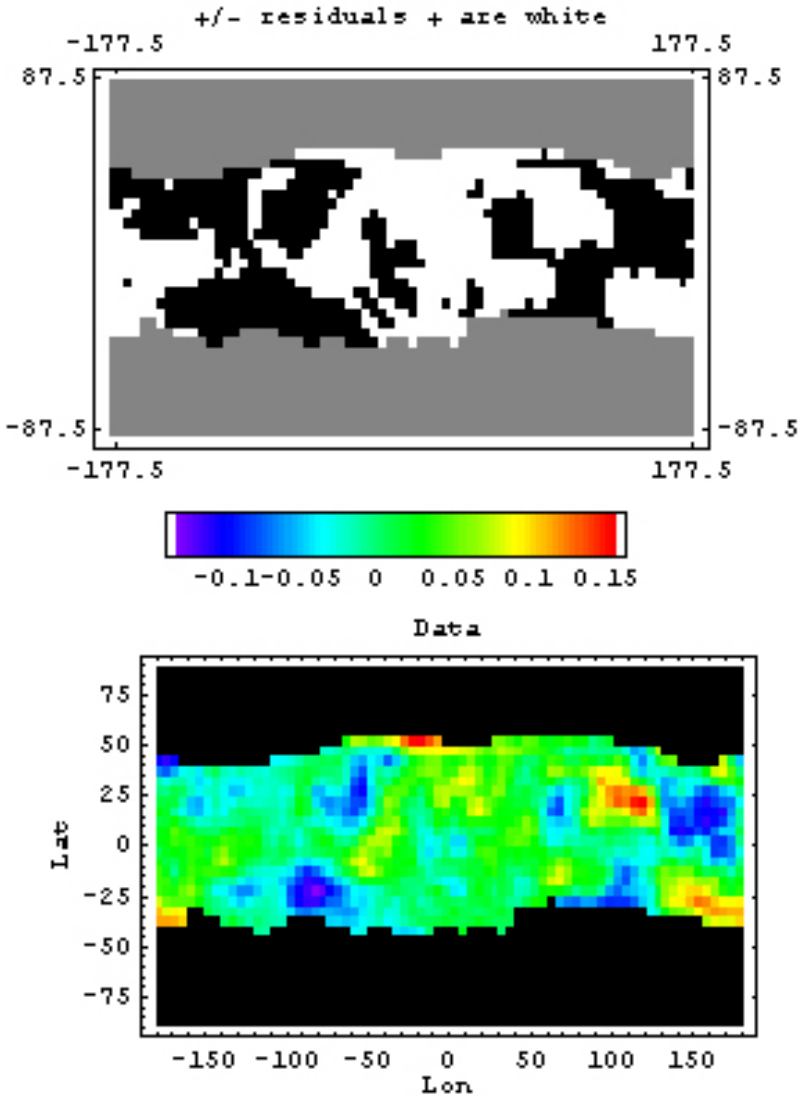

Figure 4.26: Global maps of residuals from HRLR analysis with K as the response and the 5 thermally-derived attributes as predictors. Top: Spatial distribution of the sign of residuals. Bottom: Spatial distribution of the residual values.

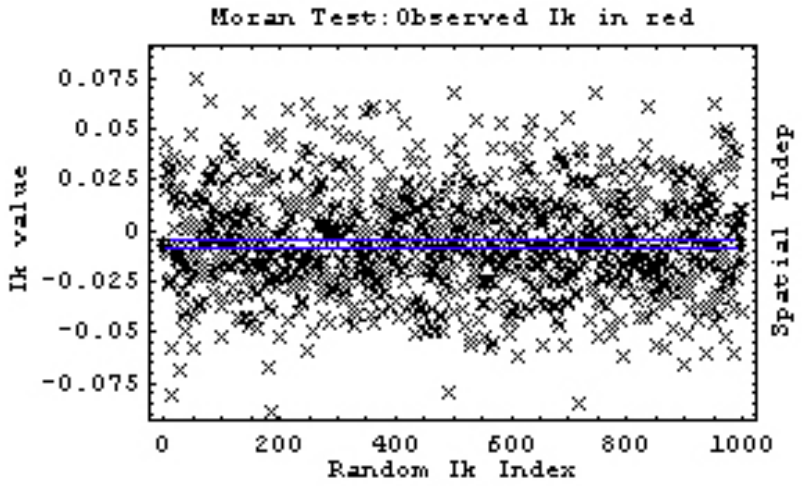

Figure 4.27: Visual application of Moran's I_k test to evaluate the presence or absence of spatial autocorrelation for the case of K as the response and the 5 thermally-derived attributes as predictors. Boundary between blue lines indicate the 95 % confidence interval. Note that the observed I_k is beyond the simulated dynamic range.

4.6.3 Elemental Predictors Model for K: Results and Fit Diagnostics

The results of OLR are shown in Figures 4.29 and 4.30. Fe and H fail at 95 % confidence levels (Figure 4.29, "t-P" outlined squares; Figure 4.30, univariate and Bonferroni 95 % confidence intervals). Th has the highest statistical significance (corresponding to the smallest "t-P" value) in Figure 4.29, even though Cl and Si are also highly significant. The variance contribution of the model is 62 % under OLR analysis. This high value is also statistically significant as discussed in Section 4.6.1, and significantly exceeds the relatively low contribution from the model of all thermally derived variables (Section 4.6.2).

SWLR analysis yields slightly different attributes as shown in Figures 4.31 and 4.32. On the basis of both the statistical confidence of partial correlation

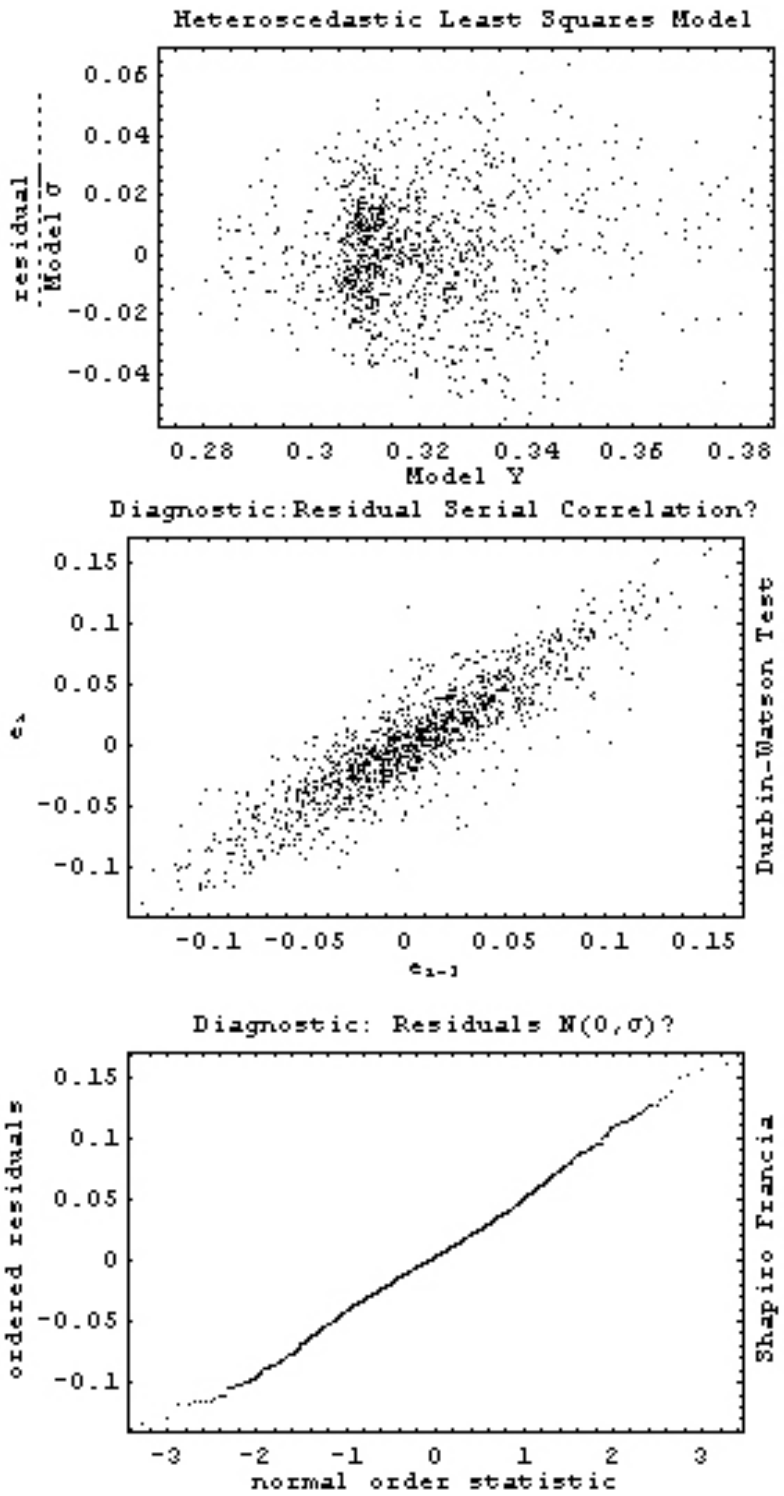

Figure 4.28: Qualitative diagnostics of the HRLR analysis with K as the response and the 5 thermally-derived attributes as predictors. Top: Normalized residuals versus $\hat{y}$; Middle: i^{th} residual versus $i - 1^{\text{th}}$ residual; Bottom: ordered residuals versus normal order statistics.

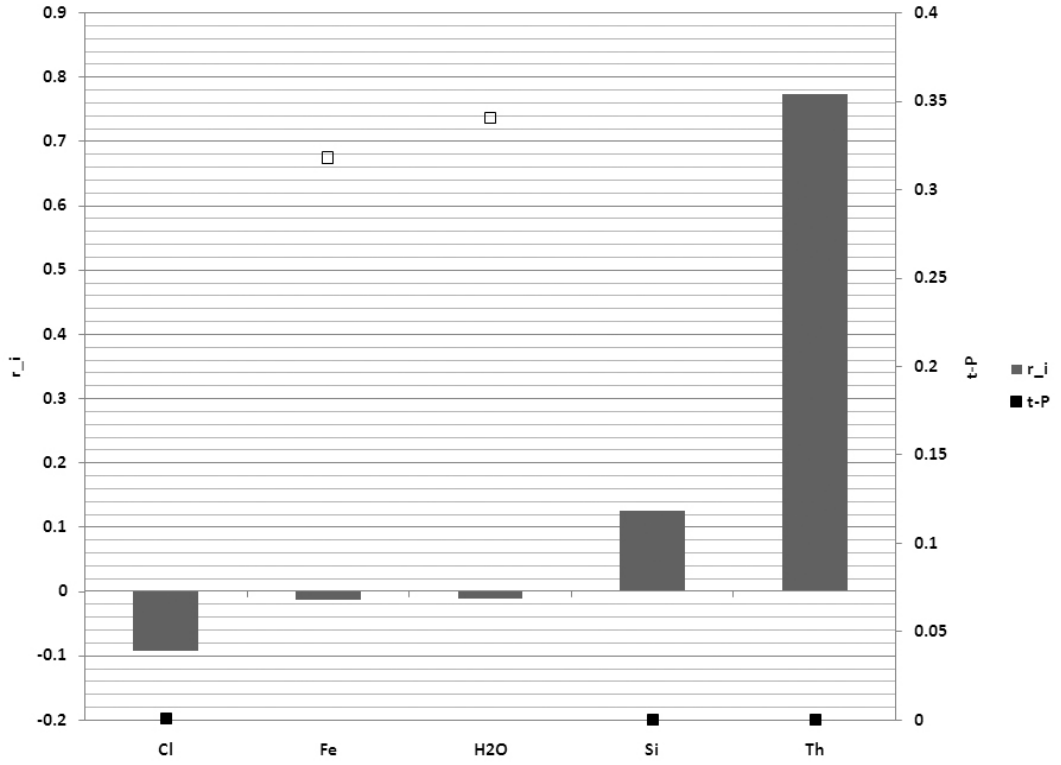

Figure 4.29: OLR correlation results with K as the response and the 5 elemental attributes as predictors. Regression results are shown in Figure 4.30. Predictor variable name abbreviations are as in Section 4.6. Symbols are the same as in Figure 4.8. The results are interpreted in Section 4.6.3.

coefficients and the univariate confidence intervals of the regression coefficients, Fe and Si may be rejected. Th is the most significant attribute, while Cl and H are also highly significant. R^2 indicates a variation contribution of 59 %. HRLR reveals (Figures 4.33 and 4.34) Th and Si to be the most significant variables, while all others fail the statistical confidence criteria. The variance contribution as determined by HRLR is 61 %.

As noted in the preceding sections, a subset of predictors has to be selected by incorporating the outcomes of all three methods. With the results of the three methods showing significant disparities as before, we select attributes for

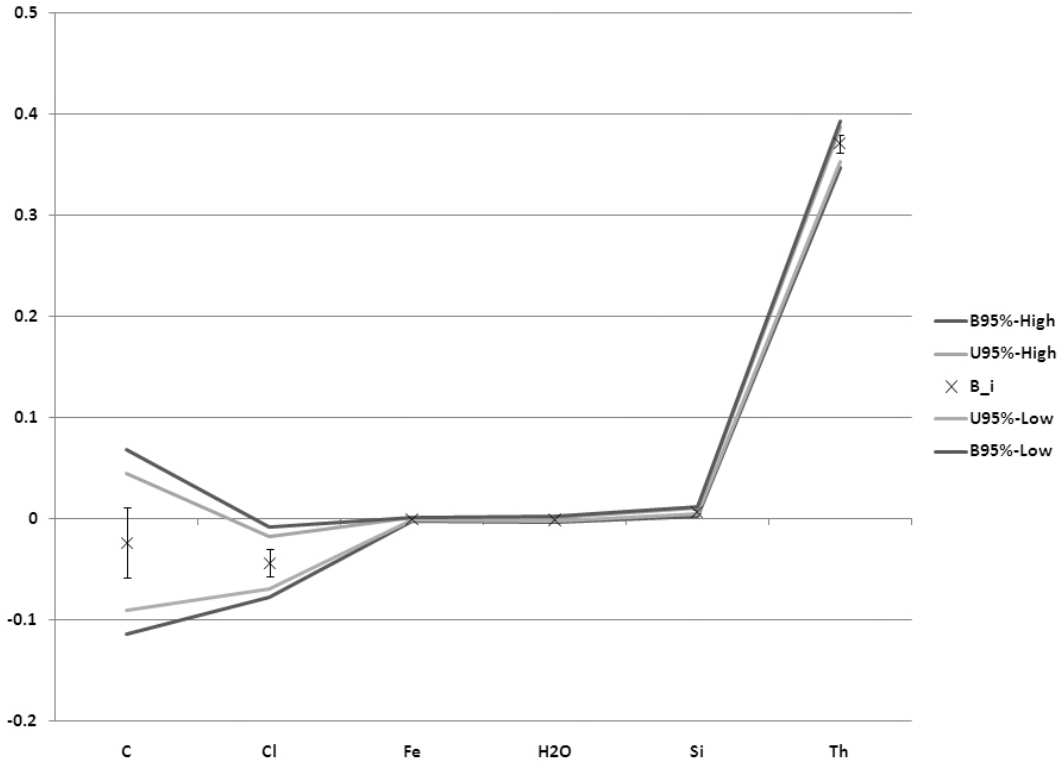

Figure 4.30: OLR regression results with K as the response and the 5 elemental attributes as predictors. Correlation results are shown in Figure 4.29. Predictor variable name abbreviations are as in Section 4.6. Symbols are the same as in Figure 4.9. The results are interpreted in Section 4.6.3.

the next hierarchical model after tabulating the results (Table 4.3). The key goal remains to reduce the number of predictors without severely degrading the model's variance contribution. Th is consistently identified as the key variable, while the significance of the remaining elements differs somewhat from one method to the next. Nevertheless, as evident by $R^2 \geq 0.59$, the elemental attributes clearly contribute much more to the variance of K than the thermally-derived variables.

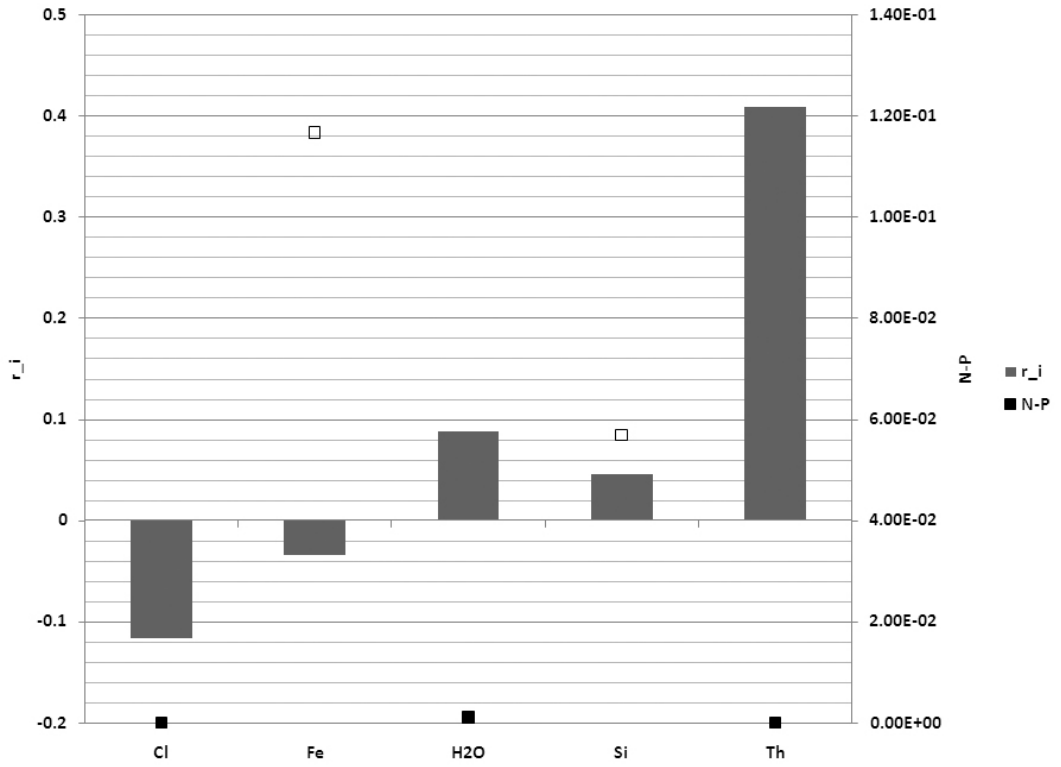

Figure 4.31: SWLR correlation results with K as the response and the 5 elemental attributes as predictors. Regression results are shown in Figure 4.32. Predictor variable name abbreviations are as in Section 4.6. Symbols are identical to those in Figure 4.10. The results are interpreted in Section 4.6.3.

Table 4.3: The key predictors, rejected predictors, and the variance contribution (as %) in the modeling of the K mass fraction with the mass fractions of other elements, selected and listed as outlined in Table 4.1.

Method	Key predictors	Rejected predictors	Variance contribution
OLR	Th, Si, Cl	H, Fe	62
SWLR	Th, Cl, H	Fe, Si	59
HRLR	Th, Si	Cl, Fe, H	61

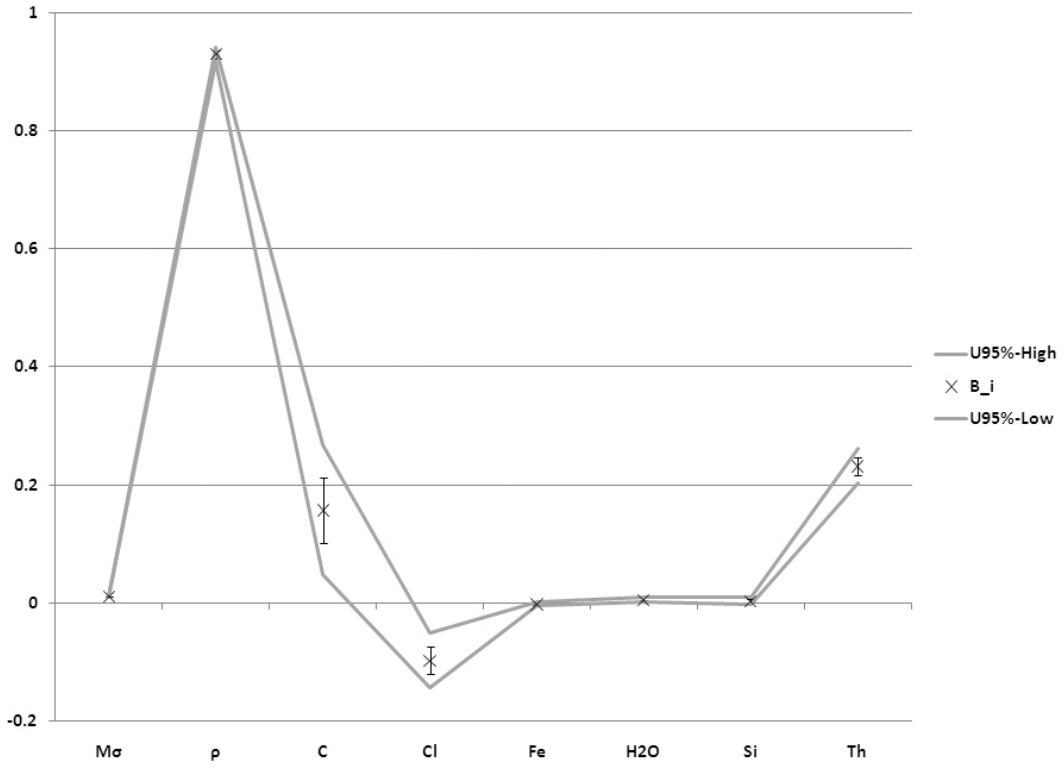

Figure 4.32: SWLR regression results with K as the response and the 5 elemental attributes as predictors. Correlation results are shown in Figure 4.31. Predictor variable name abbreviations are as in Section 4.6. Symbols are identical to those in Figure 4.11. The results are interpreted in Section 4.6.3.

Method diagnostics

The method diagnostics for the elemental attributes are consistent with those determined earlier for all variable and thermally-derived variable models. In summary, the qualitative and quantitative diagnostics suggest that OLR method assumptions are satisfied approximately, though not exactly. However, spatial autocorrelation cannot be ignored and insight from SWLR is essential. Since the method diagnostics remain consistent as hierarchical modeling is applied using the results from Sections 4.6.1, 4.6.2, and 4.6.3, we do not discuss method

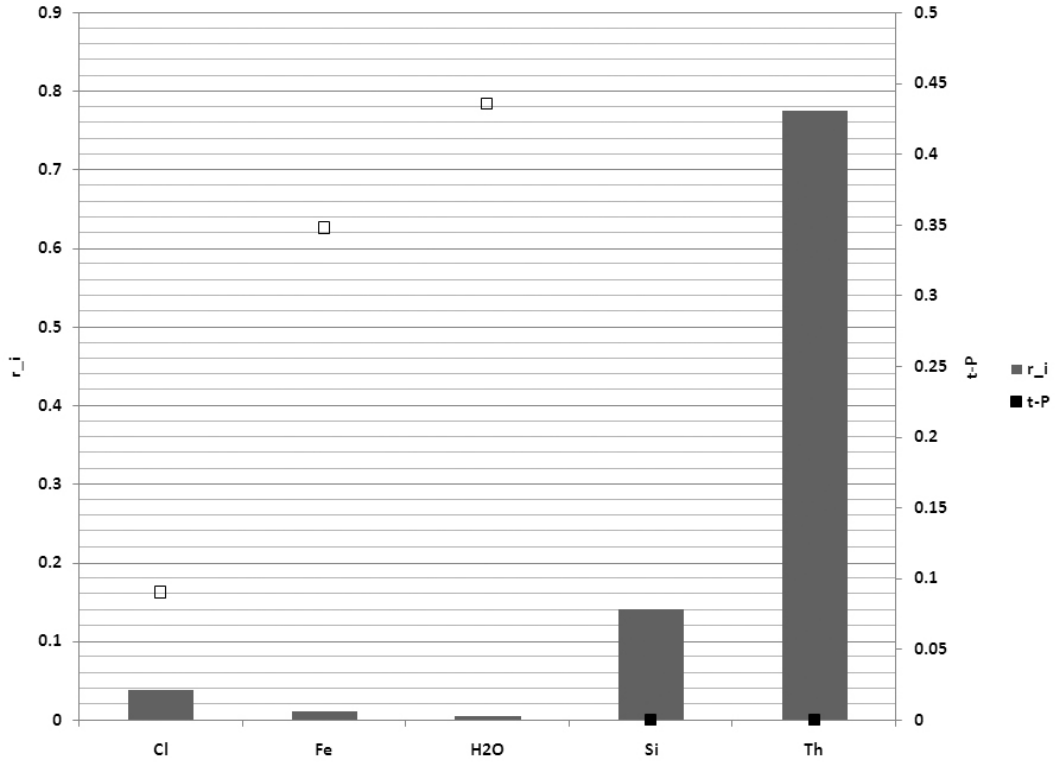

Figure 4.33: HRLR correlation results with K as the response and the 5 elemental attributes as predictors. Regression results are shown in Figure 4.34. Predictor variable name abbreviations are as in Section 4.6. Symbols are the same as in Figure 4.12. The results are interpreted in Section 4.6.3.

diagnostics in the succeeding sections.

4.6.4 Modeling K Hierarchically

As discussed in Section 4.6.1 the optimal subset of variables for the hierarchical model from the all-attribute initial model would be Th and ST2 (Table 4.1). This is reinforced by the consistent evaluation of Th as the key predictor in the model of all elements (Section 4.6.3). However, given the highly restrictive nature of such a model, the determination that Fe is key predictor in OLR analysis of

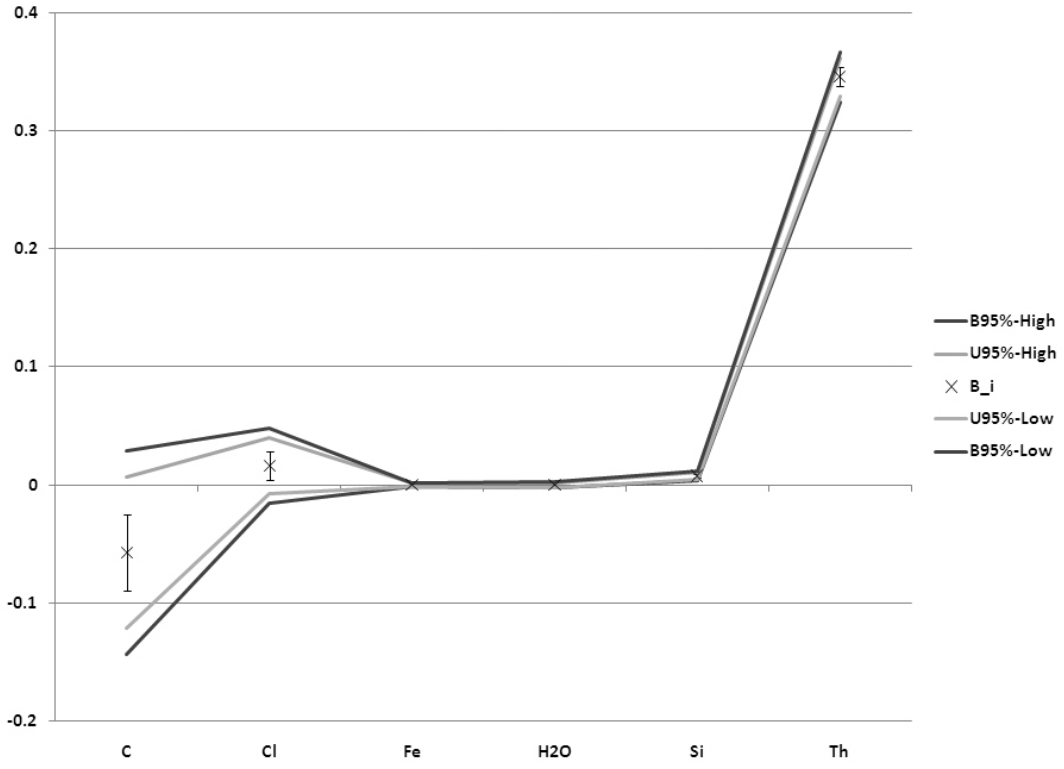

Figure 4.34: HRLR regression results with K as the response and the 5 elemental attributes as predictors. Correlation results are shown in Figure 4.33. Predictor variable name abbreviations are as in Section 4.6. Symbols are the same as in Figure 4.13. The results are interpreted in Section 4.6.3.

the all-variable model (Table 4.1), and the high variance contribution of the all-elements model (Section 4.6.3), we also include Fe. Furthermore, both ST1 and ST2 are consistently selected as key variables of the thermally-derived variable models (Section 4.6.2 and Table 4.2). Therefore, our hierarchical Model 1 consists of Th, Fe, ST1, and ST2.

On the other hand, if we were to rely solely on the largest-magnitude bivariate correlations as revealed qualitatively by the bivariate correlations matrix and quantitatively by the Pearson's correlation coefficients (Figure 4.7), a hierarchical Model 2 would consist of Th and rock areal fraction. As in the preceding

Table 4.4: Key predictors, rejected predictors, and variance contribution (as %) in Model 1 for the K mass fraction consisting of Th, Fe, ST1, and ST2. Selection process is as outlined in Table 4.1.

Method	Key predictors	Rejected predictors	Variance contribution
OLR	Th, ST2, ST1	Fe	62
SWLR	Th, ST1, ST2	Fe	56
HRLR	Th, ST2, ST1	Fe	62

Table 4.5: Key predictors, rejected predictors, and variance contribution (as %) in Model 2 for the K mass fraction consisting of Th and rock areal fraction (roc). Selection process is as outlined in Table 4.1.

Method	Key predictors	Rejected predictors	Variance contribution
OLR	Th, roc		65
SWLR	Th	roc	61
HRLR	Th, roc		65

sections, we analyze each model with OLR, HRLR, and SWLR, the results of which are summarized in Tables 4.4 and 4.5 for Models 1 and 2, respectively. In the progression of hierarchical modeling that follows, we keep in mind the initial observation that the model of all thermally-derived attributes (Section 4.6.2) contributes much less to the variance of K than the model of all elements (Section 4.6.3). Therefore, we retain at least one element in each hierarchical model.

Results from Model 1 (Table 4.4) yield the hierarchical Model 3 consisting of Th, ST1, and ST2. Results from Model 2 (Table 4.5) are more ambiguous, with SWLR indicating that Th should be the only key variable. However, Model 2 contributes slightly more to the variance of K than Model 1. Therefore, we construct hierarchical Model 4 with Th, rock areal fraction, ST1, and ST2. The

Table 4.6: Key predictors, rejected predictors, and variance contribution (as %) in Model 3 for the K mass fraction consisting of Th, ST1, and ST2. Selection process is as outlined in Table 4.1.

Method	Key predictors	Rejected predictors	Variance contribution
OLR	Th, ST2, ST1		62
SWLR	Th, ST1, ST2		52
HRLR	Th, ST2, ST1		62

Table 4.7: Key predictors, rejected predictors, and variance contribution (as %) in Model 4 for the K mass fraction consisting of Th, rock areal fraction (roc), ST1, and ST2. Selection process is as outlined in Table 4.1.

Method	Key predictors	Rejected predictors	Variance contribution
OLR	Th, roc	ST2	65
SWLR	Th, ST1, ST2	roc	56
HRLR	Th, roc, ST1	ST2	65

results of Model 3 are summarized in Table 4.6, and consistently indicate that Th, ST2, and ST1 – in that order – are the key predictors for the variability of K across the Martian surface.

However, inconsistencies among the results of Model 4 (Table 4.7) suggest several additional predictor models that should be considered before we may conclude that Model 3 is the optimal hierarchical choice for K. We compose Th and ST1 as Model 5 by selecting the variables that do not evaluate false in Table 4.7. Combining the summary results in Table 4.7 with the consistent message from the elemental (Section 4.6.3) and thermally-derived (Section 4.6.2) models, we select Th and ST2 as Model 6. Model 7 consists of Th, ST1, and rock areal fraction to reflect the OLR and HRLR results for Model 4 in Table 4.7, while

Model 8 consists of Th, ST2, and rock areal fraction as a possible alternative. Finally, Model 9 is Th alone given that it is consistently assessed as a key variable in all models that include it.

We evaluate the additional candidate models as before. Model 5 results are inconclusive, but consistently highlight Th as the key predictor with a maximum model variance contribution of 60 %. Model 6 is similar with variance contribution at 61 %, and also reveals Th to be the key predictor. Model 7, with a maximum variance contribution of 65 %, consistently identifies Th and ST1 to be key predictors, but places the significance of the rock areal fraction in doubt. Model 8 suggests a maximum variance contribution of 65 % and identifies Th as the key predictor, but places the significance of both ST2 and rock areal fractions in doubt. Lastly, Th is consistently significant in Model 9, with a variance contribution of 60 %. Therefore, the overall conclusion we may reach from these alternative models is that Th has to be present in the final hierarchical model. The variance contribution of Models 7 and 8 containing rock areal fraction is marginally (≈ 7 %) greater than than that of the Th-ST1-ST2 Model 3. However, the model predictors do not consistently evaluate true for either case, significantly undermining the increased variance contribution due to the rock areal fraction.

4.7 Discussion of K and Beyond

Given the outcome of alternatives to Model 3 above, we conclude that Model 3 – consisting of Th, ST1, and ST2 – is indeed the optimal set of predictors that relate to the variability of K on the surface of Mars. To account for the variability of

Table 4.8: Candidate predictors, statistically most significant predictors, partial correlation coefficients (r), and total variance contribution (R^2) in the optimal hierarchical model (Section 4.6.4 and Table 4.6) for K. Note that the sum of the squares of the partial correlation coefficients does not equal R^2 due to the modeling of heteroscedasticity and spatial autocorrelation.

Candidates	Key predictors	r	R^2
			0.6
Cl mass fraction			
Fe mass fraction			
H mass fraction			
Si mass fraction			
Th mass fraction	Th	0.5	
Albedo			
Rock areal fraction			
ST1 areal fraction	ST1	−0.2	
ST2 areal fraction	ST2	0.2	
Thermal inertia			

estimated partial correlations, we report the average of OLR, HRLR, and SWLR output as our K hierarchical modeling results in Table 4.8. These results validate the correlation of K with Th and ST2 as anticipated intuitively from the global maps (e.g., *Boynton et al.*, 2007). They also reveal how some apparent bivariate correlations, such as that between K and rock areal fraction, may be misleading. Therefore, multivariate correlation analyses are not only effective at untangling the numerous potential relationships among globally observed attributes, but are also essential in avoiding misconceptions that arise from qualitative visual observations and bivariate analysis. However, as with any form of correlation

analysis, it is important to remember that correlation does not indicate causation and to assiduously avoid inferring causation on the basis of correlation.

As exemplified by the work of *Keller et al.* (2006b) and Chapter 5, even though correlation does not imply causation, multivariate correlation analyses are indispensable to constrain geochemical models for the evolution of the Martian surface. But is it worth the effort evident in the preceding modeling steps for K? we feel that the answer is a resounding "yes."

Why so? In the case of K for example, the final hierarchical model discussed here (Table 4.8) enables us to conclusively state that K and Th have not fractionated from each other at global spatial scales in Chapter 5. It implies either that geologically recent geochemical process on the Martian surface have subdued earlier fractionation, or that the dominant processes have not fractionated the two elements in the first place. Sustained aqueous alteration at neutral to high pH, for example, is effectively excluded. While additional subtleties arise under low pH conditions (e.g., *Taylor et al.*, 2006a), the strong correlation between K and Th will need to be addressed in any future work that proposes extensive and temporally sustained aqueous alteration of the Martian surface. Moreover, multivariate correlation analyses identify K, Th, ST1, and ST2 as a strikingly correlated group of variables, consequently constraining geochemical processes that would yield an ST2-type mineralogy to those that also cause the simultaneous enrichment of K and Th (e.g., *Wyatt*, 2007; *Rogers et al.*, 2007b). As such, multivariate correlation analyses have provided key insight into the origin of ST2.

Subsequent to the *Karunatillake et al.* (2006, and Chapter 5) tabulation of key predictors using the methodology highlighted in the preceding sections, two

additional elements have been mapped by the GRS at comparable spatial resolution. Preliminary multivariate analyses do not indicate that the two, Al and Ca, are key predictors for the remaining elements. Furthermore, detailed multivariate analyses described in the preceding sections with Al and Ca each as the response variable only indicate weak correlations with the six elemental (Cl, Fe, H, K, Si, and Th mass fractions) and four thermally-derived (albedo, rock areal fraction, ST1 areal fraction, ST2 areal fraction, and thermal inertia) attributes. Therefore, we leave the multivariate hierarchical modeling of Al and Ca correlations for future work until the data sets are refined further.

4.7.1 Future Applications

Further insight into surficial processes of Mars may be gleaned by including additional continuous-valued and globally mapped attributes, such as elevation, in multivariate correlation analyses. Regional insight may also be obtained by limiting the analyzed areas to those for which infrared spectral indices are available. Spectral indices of Fe^{3+}, nanophase ferric oxide, pyroxene (e.g., *Poulet et al.*, 2007), and olivine (e.g., *McSween et al.*, 2006) may be used in such investigations. Such data and future orbiter missions with both finer spatial resolution and global coverage will further refine the multivariate correlations that we have presented in this and previous work.

The methods that we have described and applied with MGS-TES, Viking IRTM, and Mars Odyssey GS data as a case study with Mars are directly applicable to other planetary datasets as well. Mercury would be an excellent candidate once the MESSENGER mission enters the science orbit in 2011, particularly

since data from some of its instruments, such as the Gamma Ray and Neutron Spectrometer (GRNS) (e.g., *Solomon et al.*, 2007), will share many of the properties of the GS data. The multivariate methodology can also be applied with data from the SELenological and Engineering Explorer (SELENE) "Kaguya" Lunar mission, given its extensive instrumentation including the Lunar Magnetometer, Laser Altimeter, X-Ray Spectrometer, Gamma Ray Spectrometer, and Spectral Profiler (*Kato et al.*, 2007). We foresee an increasingly important role for multivariate correlation analyses as robust techniques providing insight into the relationships among an ever-increasing number of surficial attributes that are being mapped from orbit and measured in situ for the planetary bodies of our solar system.

CHAPTER 5

RIDDLE OF THE NORTHERN LOWLANDS*

5.1 Nature of the Riddle

Mid-infrared spectra from the Mars Global Surveyor Thermal Emission Spectrometer (TES) instrument indicated two distinct mineralogical units concentrated respectively in northern and southern low albedo regions of Mars, in addition to a pervasive surface fine component (dust) (*Bandfield et al.*, 2000). Material comprising "surface type 1" (ST1) is found primarily in low albedo regions in the southern hemisphere. TES spectra of this material, referred to as "Syrtis type" spectra (*Ruff*, 2003; *Wyatt and McSween*, 2002), have been compared to the spectra of terrestrial volcanic rocks, leading to the interpretation that ST1 is dominated by minimally weathered basalt, although recent investigations suggest some heterogeneity (*Rogers*, 2005; *Rogers et al.*, 2007a; *Rogers and Christensen*, 2007).

However, spectral comparisons with terrestrial mineral mixtures have not yielded a unique composition for the material concentrated within northern low albedo regions, collectively named "surface type 2" (ST2). Several candidate mineral mixtures give equivalently good fits to portions of these "Acidalia type" spectra not obscured by atmospheric absorptions. In principle, some mineral mixtures might be distinguished from one another by examining variability in the $5\,00 - 800\,\mathrm{cm}^{-1}$ region, but a strong atmospheric CO_2 absorption band obscures this part of the spectrum.

*Originally published by Karunatillake, S., et al. (2006), Composition of northern low albedo regions of Mars: Insights from the Mars Odyssey Gamma Ray Spectrometer, *J. Geophys. Res. Planets*, 111(E3), E03S05, doi:10.1029/2006JE002675.

Models for the mineralogy of ST2 that appear consistent with TES data include oxidized Shergotty–Nakhla–Chassigny (SNC) type basalts, silica-coated basalts, igneous processes related to basaltic andesite, aqueous weathering processes of basalts, and palagonitized basalt (e.g., *Ruff*, 2003; *Ruff and Christensen*, 2007). Among these candidates, the basaltic andesite model has received the most attention, in large part because of data from Mars Pathfinder. Pathfinder Alpha Proton X-Ray Spectrometer (APXS) data yielded a SiO_2 mass fraction, $w(SiO_2)$, of 0.57 with a net uncertainty, (s_m), of 0.06 (i.e., $w(SiO_2) = (57 \pm 6)\%$ at 68 % confidence; refer to *Mills et al.* (1993); *Göbel et al.* (2006) for conventions on uncertainty, units, and symbols used throughout this chapter) for several boulders at the site (*Wänke et al.*, 2001), consistent with an andesitic composition. Recent analyses of Mars Odyssey Thermal Emission Imaging System (THEMIS) and MGS-TES spectra also suggest that evolved high silica lava could be an important component of ST2 materials (*Christensen et al.*, 2005). A large expanse of basaltic andesite on Mars would have interesting geophysical implications, since it might imply that some form of crustal recycling process has been at work. The weathered basalt model is subject to some constraints as well, since Ca montmorillonite, Na montmorillonite, and Fe smectite appear to be excluded as potential weathering products on the basis of TES data (*Ruff*, 2003; *Ruff and Christensen*, 2007). Ongoing analyses of OMEGA data may alter some of these constraints, as apparent in the tentative identification of nontronite that was not evident in TES spectra (*Bibring et al.*, 2005).

In addition, ST2 terrain may have significant contributions from the ancient crust and younger volcanic provinces. Such mixing may be due in part to late-stage, Tharsis (and to a lesser extent, Elysium (*Tanaka et al.*, 2003))-related flood inundations (*Baker et al.*, 1991; *Dohm et al.*, 2001a,b), which *Fairén et al.* (2003) hy-

pothesized to be transient, be laden with sediments, and postdate a more extensive Noachian-era ocean. The post-Noachian inundations may have involved aqueous environments significantly different from the later–stage inundations (e.g., difference in acidity (*Fairén and Dohm*, 2004; *Fairén et al.*, 2004)). Evaporites may have formed in such environments from flood and spring-fed brines (from leached highland crustal materials) and potentially contribute to the observed GS signature.

5.2 Data Processing

In this chapter, we attempt to establish additional constraints on candidate models for ST2 using data from the GS subject to the details of operation and data processing that were discussed in Chapter 2. *Boynton et al.* (2007); *Boynton et al.* (1992); *Evans et al.* (2006) describe the processing steps applied to GS data in detail.

As in Chapter 2, "rocks" refer to material ≥ 0.1 m in size (e.g., loose blocks and exposed outcrops) that have high thermal inertia, have abundances consistent with the Viking Infrared Thermal Mapper (IRTM) data (e.g., *Christensen*, 1986; *Golombek et al.*, 2005), and are immobile under current eolian conditions. "Nonrocks" refer to fine materials that are mobilized by wind, and encompass a variety of regolith components identified at the five landing sites. Typical examples are: bedform armor, clasts, concretions, drift, dust, rocky fragments, sand, and soil (e.g., *Golombek et al.*, 2005; *Sullivan et al.*, 2005; *Yen et al.*, 2005). While our classification of the regolith into rocks and nonrocks is very broad, it suits the GS data context, given the hundreds-of-kilometer scale instrument footprint

and upper few tens of centimeter sampling depth (e.g., *Boynton et al.*, 2007, and Chapter 2).

We processed GS data in two distinct ways to perform our study. First, we determined the mean element concentrations in regions dominated by ST1 and ST2, enabling a direct compositional comparison between the two units. We selected ST1 and ST2 regions for our summations by first applying a circular median filter to TES-derived maps of ST1 and ST2 abundances (reported as areal fractions) shown in Figure 5.1 (Christensen, 2003, personal communication). The primary aim of the filter was to smooth and clearly delineate the boundaries of the two surfaces; a median filter was chosen for its strength at removing impulse noise while preserving edges (*Pitas*, 2000). Circular filter windows of 10° arc-radii were applied simultaneously over the entire planet, replacing the value of the pixel at the center of each window with the median of the values within the window (Figure 5.2). Smoothing was applied at 0.5°×0.5° grid resolution. The 10° arc-radius was chosen to reflect the effective GS spatial resolution after smoothing as summarized in Section 2.3.2.

Next, we selected threshold values to delineate ST1 and ST2 regions on the smoothed maps. These values were chosen with the competing goals of maximizing the areal extent of each region and minimizing areal overlap between the two regions. The threshold selection algorithm optimized a function of areal overlap between, and areal extent of, the regions. The function also applied a numerical factor to represent the importance given to minimizing overlap over maximizing spatial extent. We first verified that resulting mean element abundances were consistent for several numerical factors. Since we desired to identify the elemental differences between the two surface types without ambiguity,

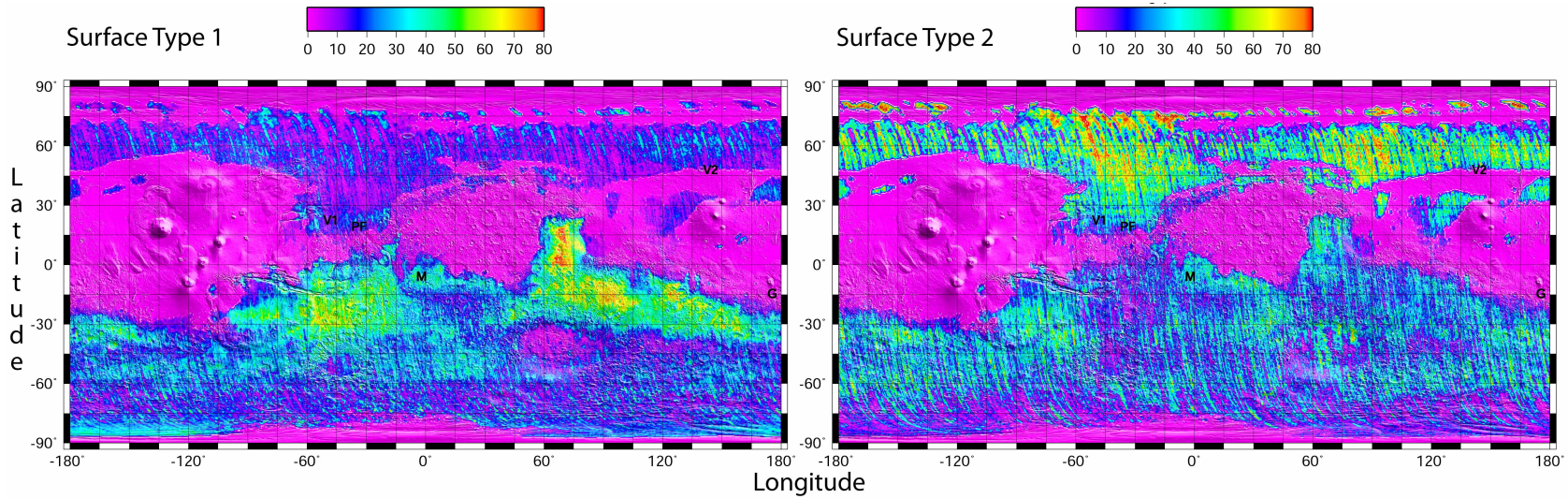

Figure 5.1: Global TES-derived Surface Type 1 (ST1) and Surface Type 2 (ST2) areal fractions (as %) before median filter application. These and all subsequent maps use Plate-Carrée (Geographic) projection and East Longitude convention, rendered at 0.5°×0.5°. Landing coordinates of surface instruments denoted by G (Gusev: Spirit Rover), M (Meridiani: Opportunity Rover), PF (Pathfinder), V1 (Viking 1), and V2 (Viking 2).

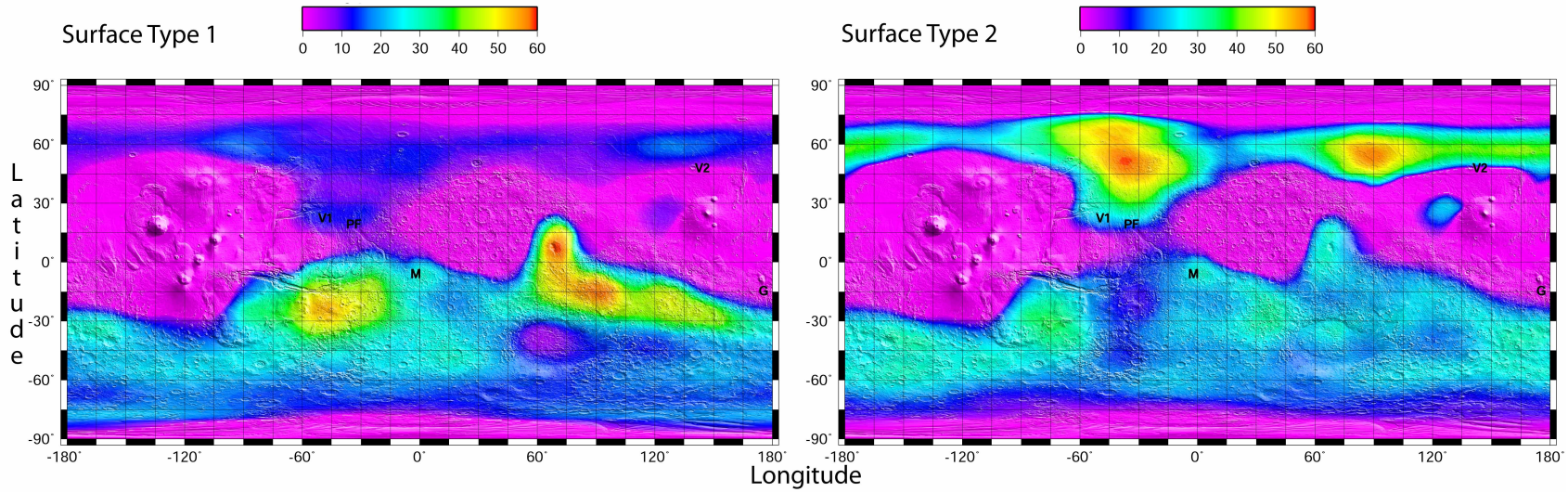

Figure 5.2: Global ST1 and ST2 areal fractions (as %) after smoothing with a 10° arc-radius median filter.

we chose a factor that eliminated overlap. The resulting thresholds were ST1 areal fractions exceeding 17 %, and ST2 areal fractions exceeding 36 %. The relative change in areal extent due to the filter and thresholds was a 70 % loss for ST2 and a 17 % gain for ST1. As evident by comparing Figure 5.2 with 5.3, this difference is mostly due to the narrower threshold range for ST2 (36 – 100 %) relative to ST1 (17 – 100 %).

We computed mean element concentrations over threshold regions after applying the Hmask to remove any effects of polar ice. These Hmasked regions for ST1 and ST2 are "region type 1" (RT1) and "region type 2" (RT2), respectively (Figure 5.3). We verified that areal sampling issues from the resulting 94 % relative loss in areal extent of ST2 were less grave than data accuracy issues of retaining the higher latitudes (*Boynton et al.*, 2007). We computed mean mass fractions and instrumental uncertainties of the mean mass fractions (s_m) for Cl, Fe, H_2O (computed stoichiometrically from H), K, Si, and Th in the two regions using cumulative γ spectra that originated from within region boundaries (Table 5.1). As described in Section 3.4.2, we also computed the ratios of mean element concentrations, $\frac{m_{RT2}}{m_{RT1}}$, and propagated corresponding s_m to estimate the net uncertainty of each ratio (Figure 5.4).

In the second form of data processing, we created global maps of element concentrations, spatially binned at a latitude-longitude resolution of 5°×5°, with the same processing and spatial constraints as discussed, for the case of K, in Section 4.6. With the consequent global maps (Figures 5.5– 5.7), we rigorously determined correlations among various element concentrations, abundances of ST1 and ST2, and other variables of interest.

As described in Chapter 4 our correlation coefficient algorithm was based on

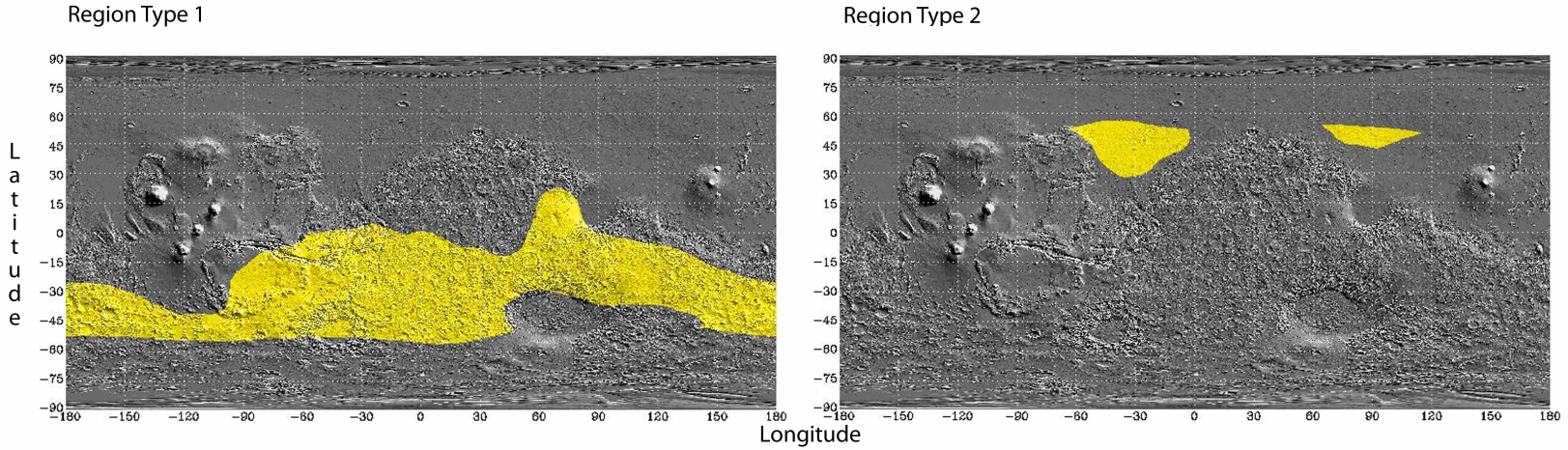

Figure 5.3: Region type 1 (RT1) as defined by the 17 % areal fraction threshold and region type 2 (RT2) by the 36 % threshold. Threshold regions are defined with the median filtered maps in Figure 5.2, constrained by the Hmask, and highlighted in yellow.

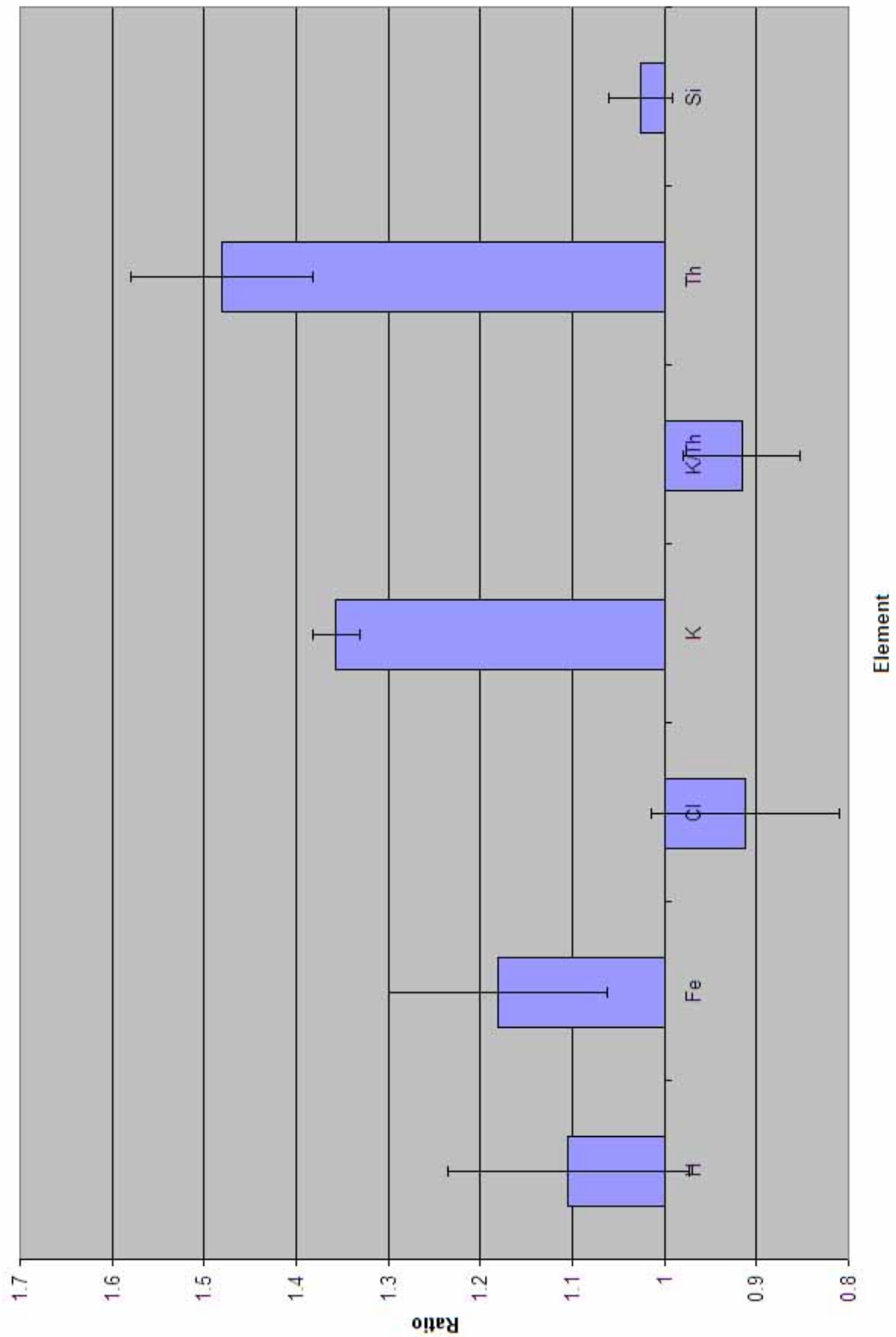

Figure 5.4: Ratios of mean element concentrations in RT2 to those in RT1.

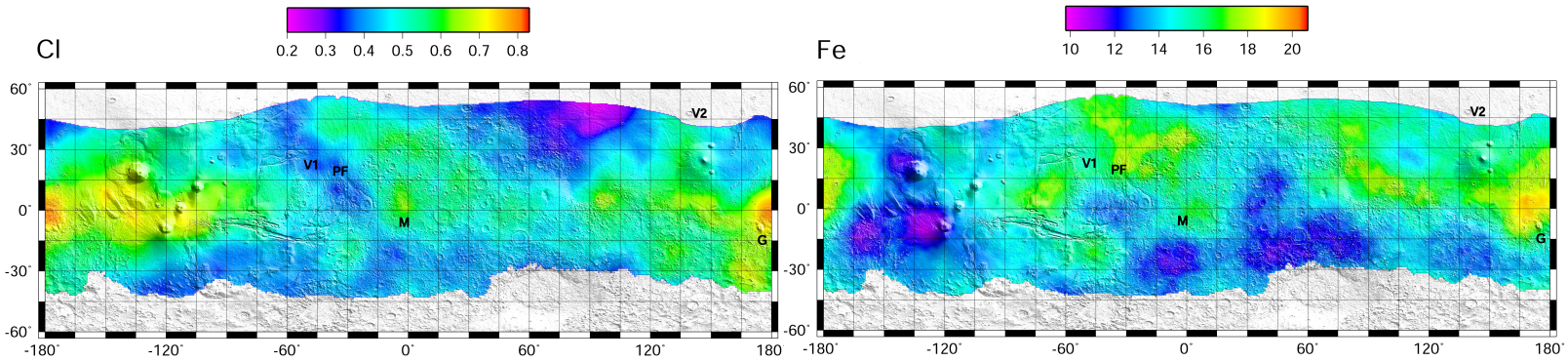

Figure 5.5: Global element mass fractions (as %) subject to the regression mask. Underlying spatial correlations are quantified in Table 5.2. Continued in Figure 5.6.

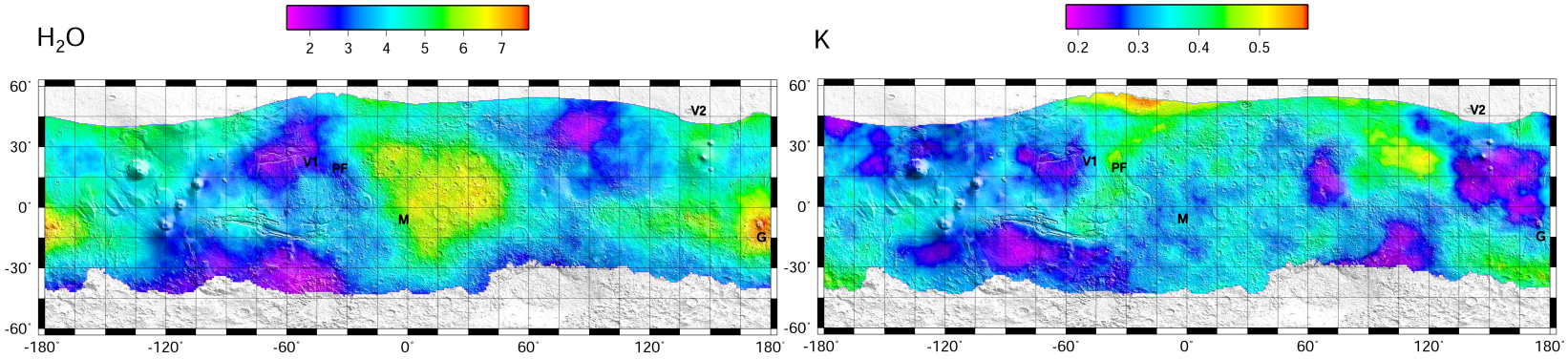

Figure 5.6: Global element mass fractions (as %) subject to the regression mask continued from Figure 5.5. Continued in Figure 5.7.

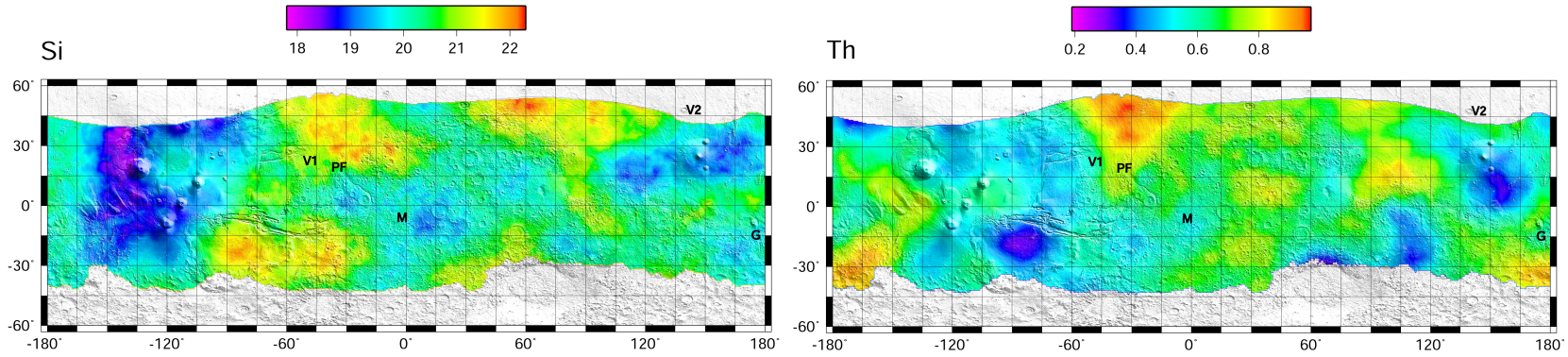

Figure 5.7: Global element mass fractions (as % for Si and mg/kg for Th) subject to the regression mask continued from Figure 5.6.

Table 5.1: GS derived mean mass fractions for Cl, Fe, H_2O–equivalent H, K, Si, and Th (as % with the exception of Th) in region type 1 (RT1) and region type 2 (RT2). Ratio of the mean K (m_K) to Th (m_{Th}) in each region is also given. s_m is the net uncertainty of each value.

	Element mass fractions and K/Th ratio to $1s_m$	
	RT1	RT2
Cl	0.46 ± 0.03	0.42 ± 0.04
Fe	13.5 ± 0.8	16.0 ± 1.3
H_2O	3.39 ± 0.20	3.7 ± 0.4
K	0.3195 ± 0.0014	0.433 ± 0.008
Si	20.9 ± 0.3	21.4 ± 0.7
Th	(0.633 ± 0.023)mg/kg	(0.94 ± 0.05)mg/kg
$\frac{m_K}{m_{Th}}$	$(5.05 \pm 0.18) \times 10^3$	$(4.6 \pm 0.3) \times 10^3$

three distinct methods of linear multivariate regression analysis: ordinary linear regression (OLR), heteroscedastic response linear regression (HRLR) (*Cohen and Cohen*, 1983; *Press*, 1982; *Rawlings et al.*, 1998) and spatially weighted linear regression (SWLR) (*Haining*, 2003; *Upton and Fingleton*, 1985). We also implemented hierarchical modeling to eliminate redundant predictor variables and generate a limited set that would correlate significantly with the response variable at confidence levels > 95 % as discussed in Section 4.6 for the case of K.

As in Section 4.6, the variables of our regression analyses were mean-filtered global element concentrations (Figures 5.5– 5.7); median-filtered ST1 and ST2 abundances (Figure 5.2); albedo (*Christensen*, 1988); thermal inertia (*Christensen and Malin*, 1988); and rock areal fraction (*Christensen*, 1986). All variable values were binned at 5°×55° and subject to the regression mask (Figure 4.6 in Sec-

tion 4.6) to establish spatially corresponding points across the datasets.

For each element, we used its global concentration data (Figures 5.5– 5.7) as response variable values. In each case, the concentrations of the remaining elements, thermal inertia, rock abundance, albedo, ST1 abundance, and ST2 abundance formed one initial set of predictor variables. The thermophysical variables alone (thermal inertia, rock abundance, and albedo) constituted another set, while the elements alone formed the third. These three initial models were necessary as the variance contributions from thermophysical variables and elements were frequently lopsided as evident in our case study with K (Section 4.6).

We employed the same approach as in Section 4.6 to identify an optimal subset of predictors for each element. Consequently, each element generally required six to seven steps including comparisons (primarily of the variance contribution, i.e., the coefficient of determination, R^2) of different predictor variable subsets to establish a final subset of predictor variables. We used this select set as predictor variables for a final regression analysis to yield "final" correlation coefficients (Table 5.2). The unique spatial correlation coefficients (r) and coefficients of determination (R^2) in Table 5.2 are averages of results from OLR, HRLR, and SWLR analyses and includes the results presented earlier for K in Table 4.8. The "Key" column lists the final subset of predictor variables for each element.

Many factors can reduce the usefulness of multivariate regression. Our primary concerns were collinearity, strong spatial autocorrelation, missing predictor variables, and serial correlation of residuals (e.g., *Rawlings et al.*, 1998; *Upton and Fingleton*, 1985). While methodology diagnostics described in de-

Table 5.2: Unique spatial correlation (r), of each element with each member of the set of most significant predictor variables ("Key") from all potential predictors ("Entire"). r is statistically significant in excess of 95 % confidence. R^2 is the coefficient of determination. Both r and R^2 are averages of OLR, HRLR, and SWLR analyses. See text for analysis methods, selection of predictor variables, and significance of unique correlations. Continued in Table 5.3.

Element	Entire	Key	r	R^2
Cl				0.4
	H	H	0.2	
	Fe			
	K			
	Si	Si	−0.2	
	Th			
	Albedo			
	Rock abundance			
	ST1 abundance			
	ST2 abundance			
	Thermal inertia			

tail in Sections 4.6 and 4.7 indicated the presence of issues at 95 % confidence levels, none were sufficiently severe to compromise regression results. Furthermore, collinearity, which would have necessitated exploration of the correlational structure with principal component analysis and Gabriel's biplots, was not evident in our data.

Even though RT1 and RT2 appear mineralogically distinct, in the context of eolian and other processes that modify the surface of Mars, they each contain mixtures of rock and nonrock regolith. Therefore, as a supplement to our re-

Table 5.3: Unique spatial correlation (r), of each element with each member of the set of most significant predictor variables ("Key") from all potential predictors ("Entire") continued from Table 5.2. Continued in Table 5.4.

Element	Entire	Key	r	R^2
Fe				0.3
	Cl			
	H			
	K			
	Si	Si	0.3	
	Th			
	Albedo			
	Rock abundance			
	ST1 abundance	ST1 abundance	−0.3	
	ST2 abundance			
	Thermal inertia			
H				0.2
	Cl	Cl	0.3	
	Fe			
	K			
	Si			
	Th			
	Albedo			
	Rock abundance			
	ST1 abundance			
	ST2 abundance			
	Thermal inertia			

Table 5.4: Unique spatial correlation (r), of each element with each member of the set of most significant predictor variables ("Key") from all potential predictors ("Entire") continued from Table 5.3. Continued in Table 5.5.

Element	Entire	Key	r	R^2
K				0.6
	Cl			
	Fe			
	H			
	Si			
	Th	Th	0.5	
	Albedo			
	Rock abundance			
	ST1 abundance	ST1 abundance	−0.2	
	ST2 abundance	ST2 abundance	0.2	
	Thermal inertia			
Si				0.5
	Cl	Cl	−0.3	
	Fe	Fe	0.3	
	H			
	K			
	Th			
	Albedo			
	Rock abundance			
	ST1 abundance			
	ST2 abundance	ST2 abundance	0.2	
	Thermal inertia	Thermal inertia	0.2	

Table 5.5: Unique spatial correlation (r), of each element with each member of the set of most significant predictor variables ("Key") from all potential predictors ("Entire") continued from Table 5.4.

Element	Entire	Key	r	R^2
Th				0.6
	Cl			
	Fe			
	H			
	K	K	0.5	
	Si			
	Albedo			
	Rock abundance			
	ST1 abundance	ST1 abundance	−0.1	
	ST2 abundance	ST2 abundance	0.2	
	Thermal inertia			

gion analysis, we also analyzed element concentrations within areas of lower nonrock areal fractions and those of higher nonrock areal fractions in non-polar regions of Mars as identified by the Hmask. These region categories were qualitatively defined by collectively considering rock (*Christensen*, 1986), ST1, and ST2 (Figure 5.2) abundances. The resulting mean element concentrations are listed in Table 5.6.

Table 5.6: Mean elemental mass fractions (as %, with the exception of Th) in lower nonrock abundance (R) and higher nonrock abundance (NR) regions in the mid-latitudes. Uncertainty is given to $1s_m$, the net uncertainty of the mean.

	Combined NR	Combined R
Cl	0.58 ± 0.04	0.45 ± 0.03
Fe	14.2 ± 0.8	14.1 ± 0.8
H_2O	4.5 ± 0.3	3.22 ± 0.2
K	0.3146 ± 0.0021	0.3319 ± 0.0022
Si	19.9 ± 0.3	21.2 ± 0.3
Th	(0.64 ± 0.03)mg/kg	(0.67 ± 0.03)mg/kg

5.3 Results

An important result of our analysis is that RT2 is enriched in K and Th by more than 30 % relative to RT1 (Figure 5.4). Interestingly, the mean K to mean Th ratios, $\frac{m_K}{m_{Th}}$, for RT2 and RT1 overlap within propagated uncertainties of the mean values. We may complement this direct compositional comparison with results from our multivariate regression analyses (Table 5.2). As we initially discussed in Section 4.7, the correlation of the spatial distribution of K at the highest statistical significance levels with only Th concentration (unique correlation, $r = 0.5$), ST2 abundance ($r = 0.2$), and ST1 abundance ($r = -0.2$) is among the most striking. Similarly, the statistically most significant variables for the spatial distribution of Th are K ($r = 0.5$), ST2 ($r = 0.2$), and ST1 ($r = -0.1$). Furthermore, the fractional variance of Th and K accounted for by each "statistically best" set of predictor variables is nearly 60 %. This is significantly higher than the $20 - 50$ % range for other elements, and suggestive of a more limited set of dominant geo-

chemical processes leading to the current spatial distribution of K and Th. Figures 5.2 and 5.5– 5.7 visually reinforce these results.

As we discussed in Chapter 2, comparison of GS data with landing site compositions is subject to severe spatial resolution concerns. However, as considered in Section 2.7.4, relative to other landing sites the Pathfinder site is subject to such issues the least. Therefore, we compared the mean composition of RT2 with that of the Pathfinder landing site computed in Section 2 and presented in Tables 2.2 and 2.4. The results are discussed in Section 5.4.3.

5.4 Interpretation

Important instrumental limitations must be kept in mind in reaching conclusions with our results. In particular, we did not investigate kilometer depth scale processes on Mars since GS data are limited to upper few tens of centimeter depths (*Boynton et al.*, 2007). Many Martian geomorphic features originate from much deeper processes, including the Vastitas Borealis formation (*Greeley and Guest*, 1987; *Scott and Tanaka*, 1986; *Tanaka et al.*, 1992, 2003, 2005) that shows significant spatial overlap with RT2. This formation could potentially consist of a low percentage of extremely ancient crustal rocks mixed with dominant basaltic material from relatively younger volcanic provinces, which include Tharsis (*Scott and Tanaka*, 1986) and Elysium (*Greeley and Guest*, 1987; *Tanaka et al.*, 1992).

One factor that must be considered when interpreting any observed spatial variability in element concentrations on Mars is that the Martian surface is a mix of rock and nonrock of differing compositions (e.g., *Yen et al.*, 2005). These

differences are evident in our analysis involving the mid–latitudes of Mars classified into regions as R (lower areal fraction of nonrock) and NR (higher areal fraction of nonrock) (Table 5.6). Physical processes like impact gardening and wind transport that vary the nonrock/rock ratio could account for variations in bulk elemental composition. Our regression analyses test this idea by the use of albedo, thermal inertia, and rock abundance as predictor variables. All of these physical variables might reasonably be expected to vary with the nonrock/rock abundance ratio over the depth range relevant to the GS.

However, as revealed in Table 5.2 these are not key predictor variables for most of the elements, including K and Th, indicating that variations in composition are not strongly coupled with variations in the nonrock/rock ratio. Nonrocks are areally dominant on Mars, as evident in the IRTM 5°×5° dataset's mean global nonrock/rock ratio of $\approx$ 10 and in case studies by *Newsom et al.* (2007). Should nonrocks be globally homogeneous, dilution effects could then mask the compositional variability due to rocks. This is unlikely, since, as evident in both our multivariate correlation analyses and ST1 and ST2 abundance variability, regolith elemental and mineralogical compositions both vary meaningfully across the planet.

Furthermore, significant compositional variability is evident even among regions potentially dominated by nonrocks (e.g., *Newsom et al.*, 2007) while in situ observations suggest that nonrocks may be compositionally much less variable than rocks (e.g., *Yen et al.*, 2005). This reinforces the possibility that while physical processes may vary the relative areal fractions of rocks and nonrocks, geochemical processes determine compositional variability, such as the strong covariance among K, Th, ST1, and ST2. Therefore, we conclude that a suitable

model for ST2 must explain K and Th enrichment relative to the basalts of ST1 on the basis of rock composition rather than variations in nonrock/rock ratio. Due to the significant mixing depths by eolian, impact gardening, and other physical processes in the Martian surface over geologic time scales, the relative difference between GS and TES sampling depths should not affect our inferences.

Among the models for ST2 mentioned in Section 5.1, the leading candidates are basalts altered by aqueous processes (*Wyatt and McSween*, 2002) and unaltered basaltic andesite (*Bandfield et al.*, 2000). We discuss each possibility below. We do not include Cl and H in our interpretation, since the latter is affected by the presence of subsurface ice and an unknown amount of bound water, while the former may be influenced by the mobile component of the regolith (*Keller et al.*, 2006b).

5.4.1 Alteration by Water

Fresh basaltic lavas may be altered by subaerial weathering and by subaqueous water-rock reactions. A subaqueous weathered basalt model for ST2 (*Wyatt and McSween*, 2002) may be consistent with K enrichment if the water chemistry were similar to terrestrial ocean water. The elemental concentration changes that occur during submarine basalt weathering on Earth are driven by the elemental composition of seafloor basalt, chemical composition and pH of water, temperature, and water/rock volume ratio. Ocean water is rich in K $\approx 400\,\mathrm{mg/kg}$ (*Drever*, 1997)) and severely depleted in Th $< 0.5\,\mathrm{ng/kg}$, leading to very high K/Th in ocean water $> 8 \times 10^8$ compared to K/Th in the continental

crust (2600; *Taylor and McLennan* (1985)).

The large increase in K/Th in ocean water is not caused simply by dissolution of high-K continental rocks because continental rocks are also enriched in Th. Instead, it is due to the higher solubility of K compared to Th in approximately neutral water. Dissolution of typical Martian crust would still lead to high K/Th in Martian surface water. If the water/rock ratio were high, the ambient temperature were low $< 150\,^{\circ}C$, and the subaqueous environment were chemically similar to terrestrial oceans (high K/Th), alteration in the northern plains may resemble that in terrestrial seafloors. Such alteration would enrich the rocks in K (e.g., *Honnorez*, 1981), while the Th content would remain unaffected, as shown by studies of altered Mid-Ocean Ridge Basalt (MORB) (*Jochum and Verma*, 1996; *Staudigel et al.*, 1996). For example, *Staudigel et al.* (1996) show that K/Th in altered basalt is 3 to 90 times greater than in typical unaltered MORB. Therefore, the concentration of K, decoupling of K and Th distributions, and the K/Th ratio are good markers for submarine alteration.

Our data indicate a 30 % higher mass fraction of K in RT2 compared to RT1, but the K/Th ratio is indistinguishable in the two regions (Table 5.1, Figure 5.4). The clear coupling of K and Th distributions with each other and ST2, as evident in our regression analyses (Table 5.2), reinforces these results. In contrast, if chemical conditions in a Martian sea were comparable to those in terrestrial oceans, we would have expected a decoupling of K and Th distributions along with a strong enhancement in the K/Th ratio. The absence of either scenario suggests that submarine aqueous alteration of basalt, at least under terrestrial submarine chemical and thermal analogs, is unlikely to explain the difference between ST1 and ST2.

On the other hand, subaerial aqueous alteration under approximately neutral conditions (pH of 5-8, normal for terrestrial weathering) would lead to different compositional expectations. Studies of terrestrial weathering profiles show that K is mobile while Th, because of the low solubility of Th complexes, is relatively immobile, although it can be carried away as colloids (e.g., *Daux et al.*, 1994; *Nesbitt and Markovics*, 1997; *Nesbitt and Wilson*, 1992; *Patino et al.*, 2003). For example, *Nesbitt and Wilson* (1992) show that K/Th varies from about 2300 in the least weathered basaltic rock to less than 100 in the most weathered. If ST2 were a result of normal weathering, one would expect that K would be preferentially removed and that K/Th would be lower than elsewhere on Mars. This is not observed, although it is possible that K redistribution was local on a scale much smaller than the GS spatial resolution, and consequently undetectable.

Furthermore, common Earth analogs may not provide the best guide to alteration processes on Mars. Analyses of MER data and corresponding laboratory simulations suggest that the outcrops in at least 2×10^5 km^2 (*Christensen and Ruff*, 2004) of Meridiani, and rocks within the ≈ 150 km diameter Gusev Crater may have formed under acidic geochemical conditions rare on earth (e.g., *Clark et al.*, 2005; *Hurowitz et al.*, 2006; *McLennan et al.*, 2005; *Tosca et al.*, 2005). The fluid that evaporated to produce the Meridiani outcrops was likely dominated by aqueous Fe^{2+}, Mg^{2+}, SiO_2, SO_4^{2-}, and Ca^{2+} at low pH (*Tosca et al.*, 2005). This fluid chemistry, a result of basaltic mineral dissolution in H_2SO_4 and HCl acid-rich waters (e.g., *Rieder et al.*, 2004), contrasts with typical terrestrial weathering regimes at pH of 5–8. As a consequence, unlike in terrestrial evaporite formation, Na and K ions may not play a dominant role in Martian evaporite formation.

Under acidic conditions, as described by *Taylor et al.* (2006a), both Th solubility and the dissolution rate of phosphate minerals, a major host for Th, increase, fractionating K from Th. Unpublished experiments by G. Dreibus show that at pH of 3 to 4 solutions in contact with crushed samples of the Zagami shergottite have K/Th of 181 (versus 3160 in fresh Zagami) after 14 hours of reaction time. The altered Zagami residue had K/Th of 10^4. This leaching of Th was probably caused by a combination of rapid dissolution of merrillite, the main carrier of Th in Zagami, and enhanced solubility of Th at low pH. In contrast, K is concentrated partly in residual Si-rich glass and in plagioclase, both of which dissolve slower than does merrillite (see summary by *Taylor et al.* (2006a)). Therefore, if most rocks on Mars have similar host minerals for K and Th as found in SNC meteorites, K/Th might increase by subaerial weathering at low pH more effectively than it would decrease by weathering under neutral conditions. We do not know if the K and Th carriers in the Martian crust are like those in SNC meteorites. However, Mars appears to be enriched in moderately volatile elements (*Dreibus et al.*, 1996), elevating the modal abundances of phosphate minerals by a few percent and increasing the likelihood for the bulk of the Th to reside in phosphate minerals. The high K/Th ratio on Mars compared to Earth (*Taylor et al.*, 2006b) demonstrates the enrichment of moderately volatile elements. The slight enrichment of Fe in RT2 (Figure 5.4), though essentially inconclusive within $1s_m$ (propagated net uncertainty of the mean value ratio) error bars, is consistent with low pH evaporitic processes at Meridiani. Nevertheless, terrestrial submarine, neutral-pH subaerial, low-pH subaerial, and low-pH SNC alteration analogs all suggest that aqueous alteration under a range of physical conditions and durations is likely to fractionate K from Th, which we do not observe.

Alternatively, the weathering profile may have been homogenized by impact gardening (*Hartmann et al.*, 2001). Nevertheless, as seen in Figure 5.4, the similarity of K/Th in RT2 to the value in RT1 (and to the average crustal value (*Taylor et al.*, 2006b)) as well as their striking spatial correlation (Table 5.2) suggests that weathering under conditions that lead to the fractionation of K from Th did not cause the apparent difference between the two surface types. Other weathering models such as silica-coated basalt and oxidized basalt (*McLennan*, 2003; *Minitti et al.*, 2002) do not account in any simple way for the enrichment of K in RT2.

5.4.2 Igneous Processes

Remaining models for ST2 composition, such as basaltic andesite, also suffer from disparities between the expected and observed behavior of elements. Terrestrial basaltic andesites and basalts are distinguished primarily on the basis of Si concentration. The concentration of K can be higher for some basaltic andesites than basalts, but these two rock types generally overlap in K concentration. However, the statistically significant K enrichment we observe does not immediately exclude a basaltic model for ST2.

One igneous mechanism that could enrich K and Th in ST2 is fractional crystallization of basaltic magma (*Minitti and Rutherford*, 2000). However, our absolute Si measurements are tied to Pathfinder measurements (*Boynton et al.*, 2007, and Chapter 2), so we cannot meaningfully determine whether ST2 is andesitic on the basis of GS-derived Si concentration. This is reinforced by the disparity between TES-derived SiO_2 mass fractions for ST1 and ST2 of $\approx 53\,\%$ and

$\approx$ 57 % (*McSween et al.*, 2003), respectively, and GS-derived mean Si content (Table 5.1, Figure 5.8) corresponding to SiO_2 mass fractions of (44.7 ± 0.6)% for RT1 and (45.8 ± 1.4)% (uncertainty quoted as standard error of the mean, $1s_m$) for RT2. While these absolute value differences may in part be a consequence of the dramatic sampling depth difference between the TES and GS, evidence for Si enrichment in RT2 is inconclusive within $1s_m$ error bars (Figure 5.4). In light of these issues, in spite of the similarity of K and Th content in RT1 to the global average (*Taylor et al.*, 2006b), we cannot utilize an RT1 composition as proxy to the parent magma of ST2. Without a presumed source composition, it is unfeasible to test the possibility of fractional crystallization with our data.

Citing geological and geophysical evidence, several authors have suggested that plate tectonics (*Connerney et al.*, 1999; *Nimmo and Stevenson*, 2000; *Sleep*, 1994) may have occurred during an extremely ancient phase of the evolution of Mars (*Baker et al.*, 2002; *Fairén et al.*, 2004, 2002). Could ST2 be a calc-alkaline magma formed by subduction? Our data seem inconsistent with plate tectonics involving subducting slabs rich in fluids and hydrously altered basaltic rocks as they are on Earth. First and foremost, as discussed above, we do not see strong evidence for Si enrichment in ST2 (Figure 5.4). Since the Pathfinder normalization is a constant factor across the global Si dataset, GS estimates of relative variation (e.g., enrichment) in Si content are rigorous, while estimates of absolute Si content are not. As a result, we cannot meaningfully evaluate processes that require accurate knowledge of absolute Si content.

The chief characteristic of subduction zone magmatism on Earth is the formation of calc-alkaline magmas by hydrous partial melting of the mantle wedge above the wet subducting oceanic slab. Initial melts tend to be basaltic,

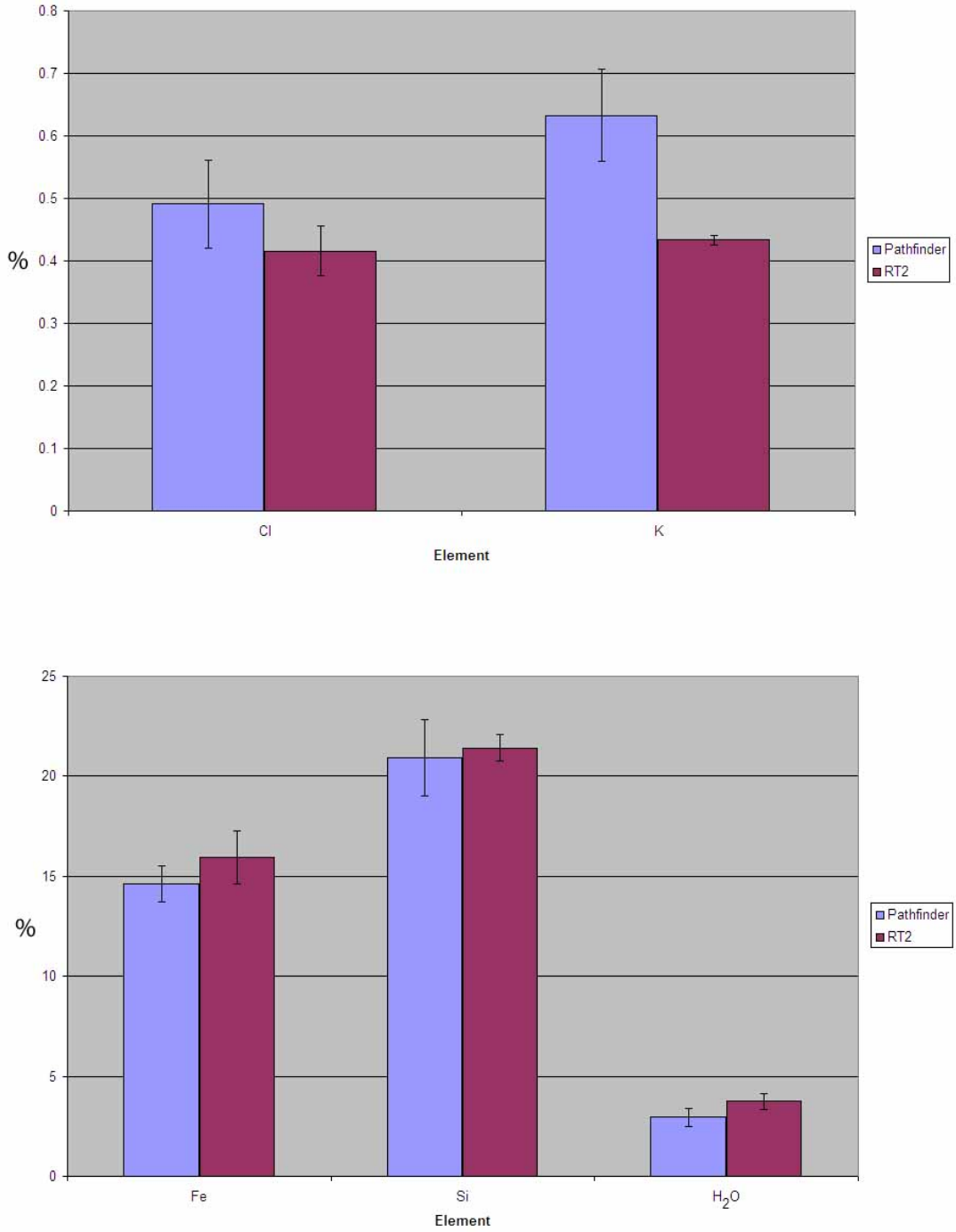

Figure 5.8: Comparison of Pathfinder and region type 2 (RT2) mean compositions. H_2O mass fractions are GS estimates. Fe, Cl, and K mass fractions are the only values for which Pathfinder and GS estimations are mutually independent. Error bars are shown to $1s_m$.

with basaltic andesite and andesite forming by fractional crystallization of the basaltic magma, accompanied by assimilation of the overlying silicic continental crust (*Grove et al.*, 2003, 2002; *Hawkesworth et al.*, 1997; *Rudnick*, 1995; *Stolper and Newman*, 1994). *McSween et al.* (2003) also provide a concise summary of the compositions and origin of calc-alkaline magmas. Major elements seem to be contributed by hydrous partial melting of the mantle wedge, whereas trace elements appear to come dominantly from the slab (e.g., *Grove et al.*, 2002).

Most important, the fluid fractionates the trace elements. K is distinctly enriched in the fluid from the water-rich oceanic slab. Many arc magmas are consequently enriched in K. Th appears less soluble in the fluid phase, so K/Th would be high (*Hawkesworth et al.*, 1997). In spite of some evidence for the mobility of Th and its accumulation in the fluid phase (*Brenan et al.*, 1995), *Hawkesworth et al.* (1997) convincingly argue that the way Th forms complexes in aqueous solutions prevents it from concentrating in the fluids rising from the slab. Thus, if a similar process operated on Mars, we might be able to detect it by anomalously high K content and high K/Th. On Earth, in spite of some variability, many arc magmas have K/Th ranging from two to five times the bulk silicate Earth value of 2900 (*Taylor and McLennan*, 1985). RT2 is enriched in K (Figure 5.4), but its K/Th ratio (Table 5.1) is typical for the Martian surface *Taylor et al.* (2006a,b). Therefore, decisive evidence for areally (not necessarily volumetrically) widespread formation of calc-alkaline andesite is lacking within ST2. Should ST2 material contain calc-alkaline andesites, it would probably be at spatial scales less than the GS's 440 km diameter footprint (Section 2.3.1).

An alternative to both localized fractional crystallization and plate subduction mechanisms is initial bulk differentiation processes on Mars producing

compositionally distinct magma source regions in the mantle. If that were true, and present crustal dichotomy generally follows the source regions, northern and southern basaltic provinces of distinct trace element compositions, including K and Th, could be produced. Differences in isotopic and trace element abundances, as well as oxygen fugacities in SNC meteorites are consistent with distinct source magmas (e.g., *Borg and Draper*, 2003; *Borg et al.*, 2003; *Herd*, 2003). The wide range in ϵ_{Nd} suggests that these sources remained separate at least until the magmatic production of SNC material (e.g., *Brandon et al.*, 2000; *Borg et al.*, 2003).

In addition, simulations of whole-mantle magma oceans, i.e., those in excess of 1500 km depths, on early Mars predict differentiation of the mantle into lateral components with distinct compositions. In these magma oceans, the cumulate vertical density profiles invariably become non-monotonic, leading to compositional differences. Such density profiles precipitate mantle overturn to yield the laterally heterogeneous compositions (e.g., *Elkins-Tanton et al.*, 2005b). Furthermore, among many simulations involving magma oceans with varying depth on early Mars, only those with whole mantle magma oceans yield crustal composition predictions consistent with surface and orbital data (*Elkins-Tanton et al.*, 2005a). Even though current simulations also predict differences in Si content (*Elkins-Tanton et al.*, 2005a), which we do not observe, the difference in K and Th content between RT2 and RT1 is generally consistent with whole mantle magma ocean models. Magma ocean crystallization and overturn would not significantly fractionate K from Th because both elements are incompatible (*Borg and Draper*, 2003), consistent with the uniformity in K/Th between ST1 and ST2. The extent of enrichment in Si (if any), K, and Th depends on a complex interplay of the bulk composition of each mantle source that gave rise to

ST1 and ST2, its mineralogy, and amount of partial melting. In general, magma ocean modeling is consistent with the idea that ST1 and ST2 are derived from compositionally distinct mantle sources.

5.4.3 Pathfinder Comparison

The Mars Pathfinder rocks have compositions consistent with basaltic andesite (e.g., *Wänke et al.*, 2001). With TES-derived ST1 and ST2 areal fractions of 13 % and 21 %, respectively, the Mars Pathfinder landing site is only a few degrees southwest of our RT2 boundary. Given the spatial proximity, it may be useful to compare the GS-derived composition of RT2 with APXS-derived Pathfinder landing site composition as ground truth. Any comparison must keep in mind that the spatial resolution of the GS is ≈ 440 km (*Boynton et al.*, 2007, and Chapter 2) while the Pathfinder APXS examined "dusty" surfaces only a few cm in diameter within a $\approx 100\,\mathrm{m}^2$ region (*Golombek et al.*, 1997).

Given the enormous difference in effective spatial resolution, GS-derived element concentrations for RT2 should correspond to some weighted average of the compositions of Pathfinder rock, Pathfinder nonrock, and probably other materials as well. Such a composition was estimated as described in Section 2.7.4 and summarized in Section 5.3. Furthermore, since the GS-derived Si concentration was normalized to a Pathfinder mean value (*Boynton et al.*, 2007, and Chapter 2) at the lander coordinates, comparisons are robust only for Cl, Fe, and K. As evident in Figure 5.8, the mean concentration of K at the Pathfinder landing site exceeds the GS-derived K concentration for RT2. This may indicate that rock surface compositions at the Pathfinder landing site are not representa-

tive of the bulk of ST2.

5.5 Conclusions and Future Work

Our investigation relied on elemental concentrations derived from Mars Odyssey GS data along with synergistic use of information from a variety of instruments such as MER, Pathfinder Sojourner APXS, MGS-TES, Viking Landers, and Viking IRTM, to evaluate geologic models for the origin of ST2. A key result is that K, Th, ST1, and ST2 are the most spatially correlated variables among these datasets. Consistent with this observation is the significant enrichment of K and Th in ST2, along with a K/Th ratio that is similar to the bulk planet. These observations collectively suggest that ST2 materials may be characterized by geochemical processes that enrich both K and Th, but not by those that fractionate K from Th. Both TES mineral library fits and Pathfinder APXS estimation of Si content suggest that ST2 is Si-enriched. However, GS data do not reveal a meaningful enrichment of Si in ST2 relative to ST1, and suggest that ST1 and ST2 may instead be distinct on the basis of K and Th content.

Silica coated basalt and oxidized basalt models do not explain the enrichment of K and Th in ST2, and the former is inconsistent with the similarity in Si content between ST1 and ST2. In addition, the behaviors of K and Th do not suggest typical terrestrial subaerial aqueous alteration. Given the similarity of K and Th spatial distributions, a Martian analog of terrestrial submarine aqueous alteration or alteration by low-pH fluids enriched with basaltic minerals is also unlikely as the dominant process that produced ST2. Instead, igneous environments, such as compositionally distinct magma sources, may have produced

the differences between ST1 and ST2. However, we do not observe compelling evidence for analogs of terrestrial plate tectonics.

Relative weakness of γ spectral intensities at spatial resolutions finer than 5°×5° and the ≈ 440 km diameter GS footprint (*Boynton et al.*, 2007) preclude mean element concentration calculations for ST1 and ST2 on a bin-by-bin basis. This necessitated the 17 % and 36 % thresholds that we employ. Since threshold regions exclude nearly 70 % of the original ST2 areal extent, they may conceal some compositional features of ST1 and ST2. However, by exclusively employing regions free of overlap between ST1 and ST2, we have ensured that the elemental distributions we observe enable unambiguous comparisons between the two surface types. Furthermore, our methods provide consistent results for different thresholds, minimize statistical error that would have otherwise prevented meaningful comparisons, and are consistent with multivariate regression analyses in the absence of thresholds. As such, we are confident that our conclusions reflect the best available data from the Mars Odyssey GS instrumentation.

At present, we are compelled to restrict our analyses to the mid-latitudes primarily due to the difficulty of accurately modeling heterogeneities in the distribution of hydrogen with depth. Modeling γ spectra to account for the physical mixing scale of different materials (*Squyres and Evans*, 1992), as well as employing layered-regolith models of differing compositions may complement our current approach to elemental concentration calculations. That may in turn allow us to make a more exhaustive comparison between ST1 and ST2 by including higher latitudes where ST2 dominates (Compare Figure 5.2 with 5.3). Even though recently mapped Ca (Chapter 6) within RT2 is similar to average Mars,

future improvements to elemental mass fraction estimation methods may provide additional insight from significant elements such as S and U at 5°×5° grid resolution. In addition, current ambiguities in Si and differences between ST1 and ST2 in Fe content may be reduced or eliminated, enabling better determination of compatible igneous models. Chemically striking regions on the surface discussed in Chapter 6 hint that the geochemistry of ST1 and ST2 may be characterized further by analyzing the extensive area of overlap between ST1 and ST2 as well. Occurring primarily in the 23° to −45° latitudes with moderate-to-low areal fraction (< 36 %) of ST2 and moderate-to-high areal fraction (> 25 %) of ST1, this area has the added benefit of freedom from the polar H_2O ice regimes.

CHAPTER 6

CHEMICALLY STRIKING REGIONS AND STEALTH REVISITED

6.1 Goals

The primary goal of our work is two-fold: to identify regions on Mars that are chemically striking and to describe one of them as a case study motivating future analysis of the remaining regions. We define a chemically striking region (CSR) as one where the mass fractions of two or more elements are significantly different from their midlatitudinal averages. We delineate these regions with the global midlatitudinal maps of elemental mass fractions generated by the Mars Odyssey team. Our case study also relies on several other missions - the MER, MGS-TES, and MRO High Resolution Imaging Science Experiment (HiRISE) key among them.

The primary instrumentation and data generation by the Mars Odyssey GRS is summarized in Chapter 2 and described in detail by *Boynton et al.* (2007); *Evans et al.* (2006); *Boynton et al.* (2004). We described the key statistical techniques to analyze remote sensing data on a global scale in Chapters 3 and 4. As mentioned before, the three instruments of the GRS, particularly the NS and GS, are complementary in their determination of H, with different sensitivities to mass fraction variabilities as well as different sampling depths (*Boynton et al.*, 2004). While the NS is capable of indirectly estimating the mass fractions of elements that affect the neutron energy spectrum, only the GS provides direct estimates for multiple elements by means of characteristic energies of γ photons emitted during nuclear de-excitations. For this reason and the focus of this work on defining CSRs, we rely solely on elemental mass fraction maps generated with

the GS data.

6.2 Delineating Chemically Striking Regions

We delineate chemically striking regions using the mass fractions of the seven elements for which uncertainties are reasonably small. These are Ca, Cl, Fe, H_2O (as the stoichiometric equivalent of the GS's H estimates), K, Si, and Th. While the uncertainties in the values and methodology of Al mass fraction estimates are being refined, we present regions that include Al for future study. The CSRs are delineated in two steps, beginning with the definition of *significant deviations* from bulk Mars for a single element - a gaussian tail cluster (GTC).

6.2.1 GS Mapping Summary

As we discussed in Chapter 2, the GS bin data subjected to temporal cumulation, multiple processing steps, and a mean filter to maximize signal-to-noise ratios, yield global maps of elemental mass fractions. We utilize the most extensive cumulation period currently available consisting of epochs 1 and 2 corresponding to the combined primary and extended mapping periods from 08 Jun 2002 (00:00:00) UTC to 02 Apr 2005 (20:20:00) UTC, and 30 Apr 2005 (00:00:00) UTC to 22 Mar 2006 (07:54:00) UTC, respectively. We choose a bin size of $5^\circ \times 5^\circ$ for the mass fraction maps to partially address spatial uncertainty in the form of spatial autocorrelation (Section 4.2.2) introduced primarily by the mean filter, the arc radius of which varies as discussed in Section 2.3.2.

6.2.2 Step 1: Delineating Gaussian Tail Clusters (GTCs)

An unfortunate consequence of the nearly gaussian distribution of the elemental mass fractions (Section 3.3) is that robust outliers do not exist in the distributions. However, spatially extensive regional variations in GS-chemical maps make a strong case for treating them as such, the lack of outliers notwithstanding. Therefore, we utilize an improvised test parameter, t, as a measure of deviation from the bulk of Mars for each element. For any given element, the test parameter evaluated at the i^{th} bin is:

$$t_i = \frac{c_i - m}{\sqrt{s_{\text{m},i}^2 + s^2}} \tag{6.1}$$

where c_i is the mass fraction of the element at the i^{th} bin, m is the global arithmetic mean mass fraction, $s_{\text{m},i}$ is the numerical uncertainty of c_i, and s is the standard deviation of the mass fractions. The key difference between t_i and the commonly used Student's-t parameter (e.g., *Helsel and Hirsch*, 2002; *Press et al.*, 2007, former p. 126; latter p. 728) is the inclusion of $s_{\text{m},i}$ in the denominator. This term ensures that the significance of deviations from the global mean is evaluated in the context of numerical uncertainties. Since the GS data follow gaussian distributions to first order (Section 3.3), our parameter is effective at identifying data in the distributional tails, i.e., the gaussian tail clusters (GTCs) of an element. In addition, the standard deviation (s) exceeds the root-mean-square uncertainty (s_{rms}) by more than 20 % for the elements (Section 3.2.3 and Figure 3.1), confirming that numerically meaningful deviations from the mean exist.

Due to the lack of outliers in the data and the use of $s_{\text{m},i}$ to enhance rigor, the

Table 6.1: The statistical significance of a given deviation from the mean computed as the cumulative tail probability of a Student's-t distribution. The significance of the magnitude of deviation (P_{mag}) is usually less than that of the directional deviation (P), as the former is bidirectional. s denotes the standard deviation and t is the test parameter in Equation 6.1.

t	Deviation exceeds	P_{mag}	P
1	$1s$	68 %	84 %
1.5	$1.5s$	87 %	94 %
2	$2s$	95 %	98 %
2.5	$2.5s$	99 %	99 %

magnitude of t_i does not exceed 3 in any of the elemental mass fraction maps. Therefore, the thresholds we utilize to identify GTCs are t_i no less than 1, 1.5, 2, and 2.5 which correspond to better than $1s$, $1.5s$, $2s$, and $2.5s$ confidence, respectively. Corresponding statistical confidence based on a Student's-t distribution is listed in Table 6.1.

The GTCs that result from two of the t thresholds are illustrated in Figures 6.1– 6.8. The preservation of GTC interiors at $t \geq 1$ (e.g., Figure 6.1, left) when the threshold is increased to 2 (e.g., Figure 6.1, right) is evidence that the GTCs are spatially meaningful. Those of Cl have been analyzed by *Keller et al.* (2006b), with particular emphasis on the Cl-enriched regions that extend west from the Tharsis area and overlap considerably with the Medusae Fossae Formation (MFF). As evident in the discussion in Chapter 5, GTCs that mark the enrichment of K and Th overlap strikingly with higher areal fractions of surface type 2 material (*Rogers et al.*, 2007a; *Rogers and Christensen*, 2007). Spatial coincidences of GTCs with secular units have been discussed by *Hahn et al.* (2007) and with Northern lowlands by Dohm et al. (2008, GRS Evidence and the Possibility

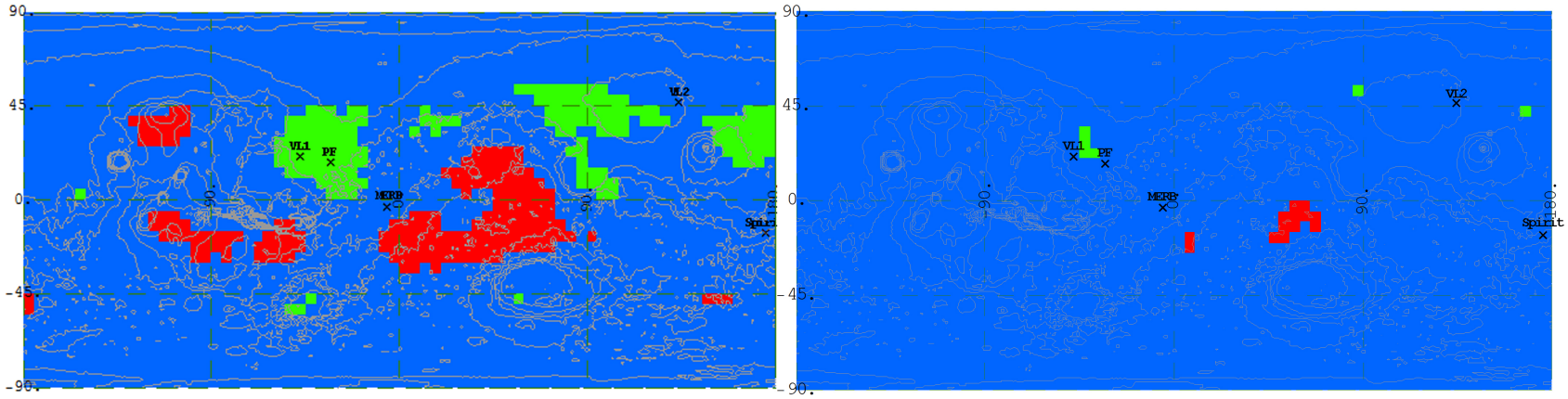

Figure 6.1: Gaussian Tail Clusters (GTCs) for two of the confidence thresholds used in this work for Al, illustrated solely to motivate future investigations as the Al maps are being refined. Other elements are shown in Figures 6.2- 6.8. A confidence of $t \geq 1$ (Table 6.1) is on the left, and $t \geq 2$ is on the right. Green indicates depletion and red indicates enrichment. Data are restricted to the midlatitudes (Section 6.2.1). As shown in Figure 6.10, overlap among GTCs of multiple elements yields the CSRs.

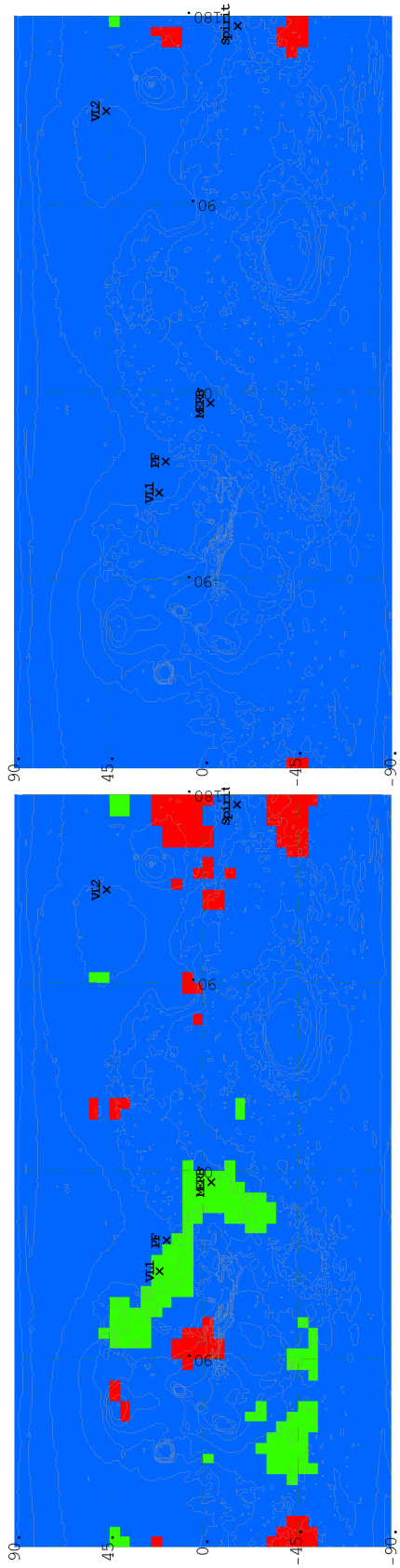

Figure 6.2: GTCs for Ca as described in Figure 6.1.

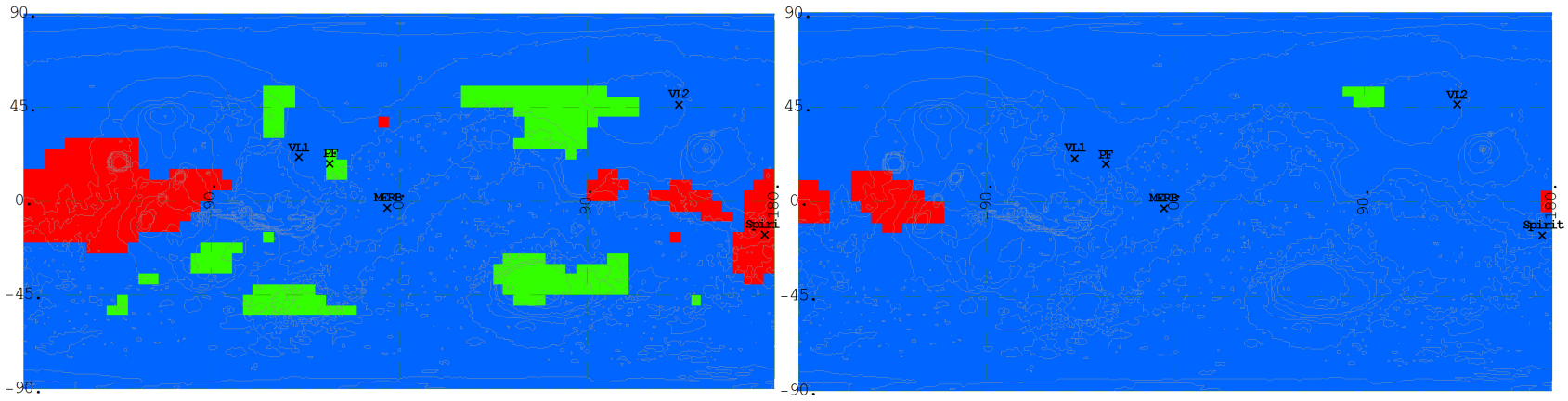

Figure 6.3: GTCs for Cl as described in Figure 6.1.

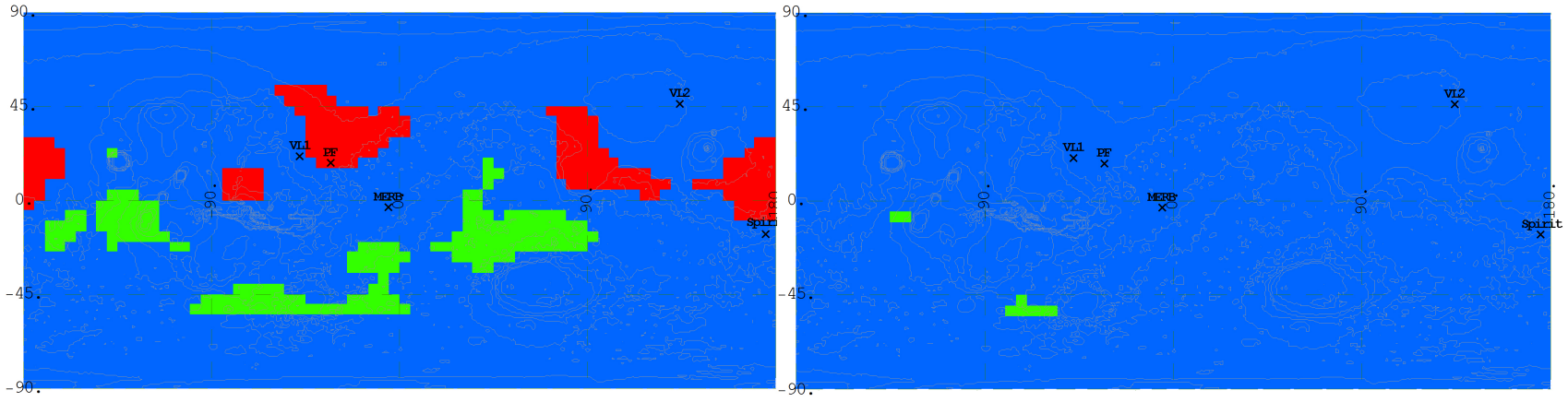

Figure 6.4: GTCs for Fe as described in Figure 6.1.

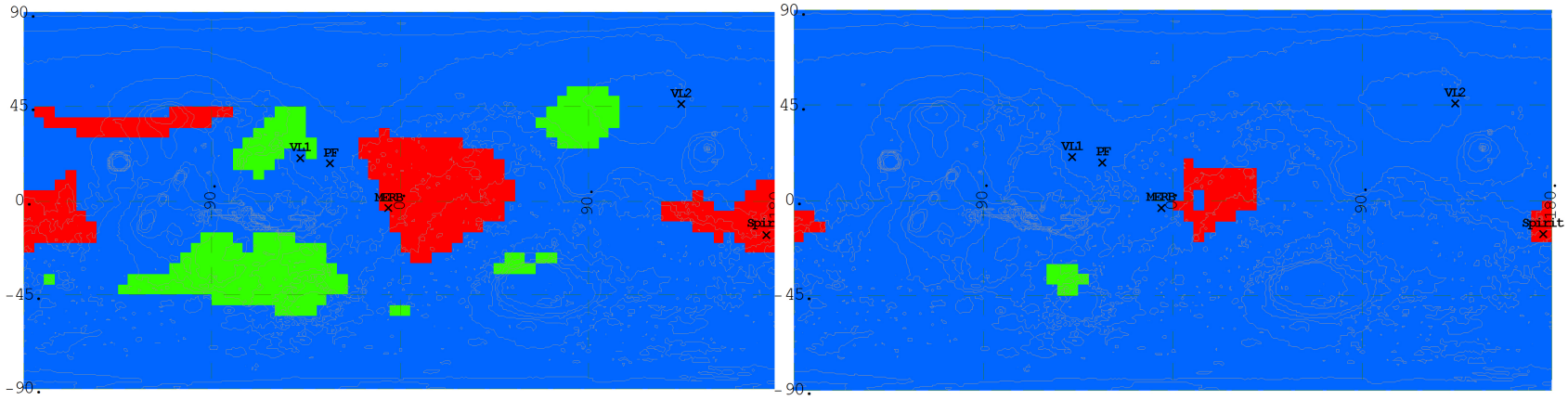

Figure 6.5: GTCs for H_2O as described in Figure 6.1.

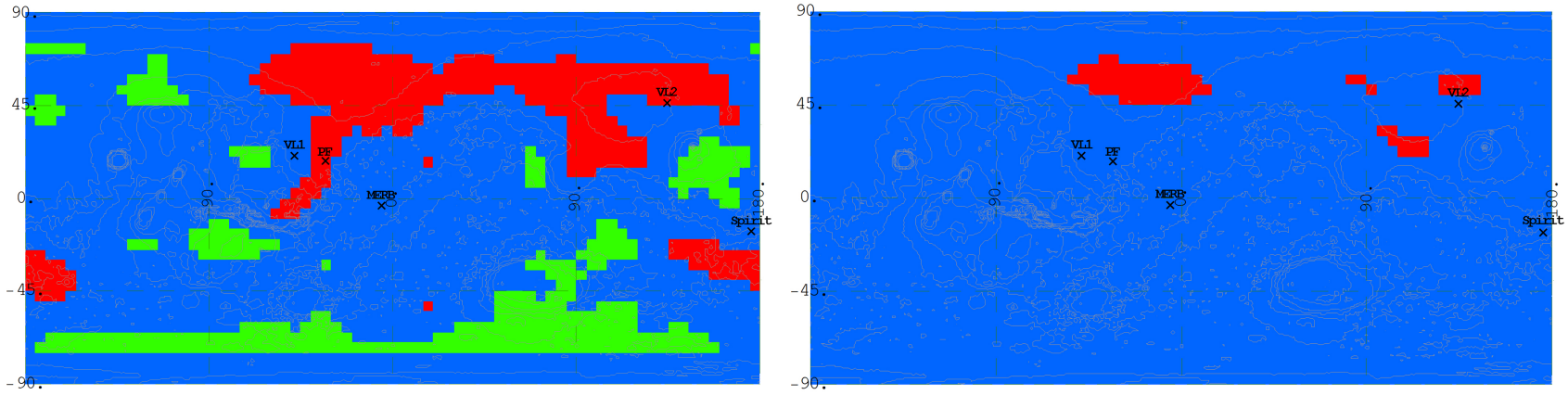

Figure 6.6: GTCs for K as described in Figure 6.1. Unlike the mid-latitudinal extent for the other elements, K and Th extend to ±75° (Section 6.2.1).

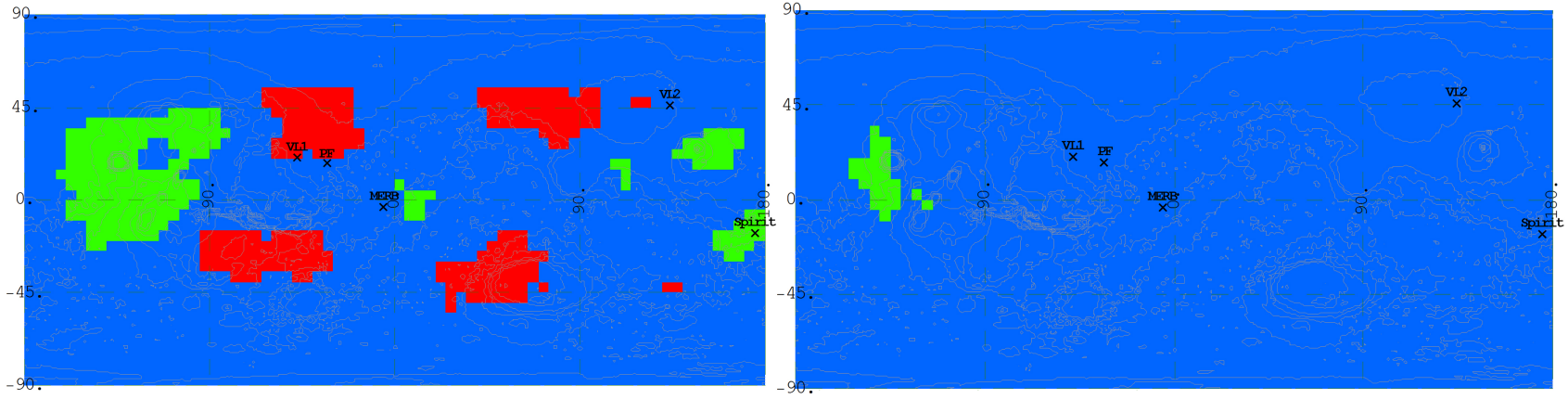

Figure 6.7: GTCs for Si as described in Figure 6.1.

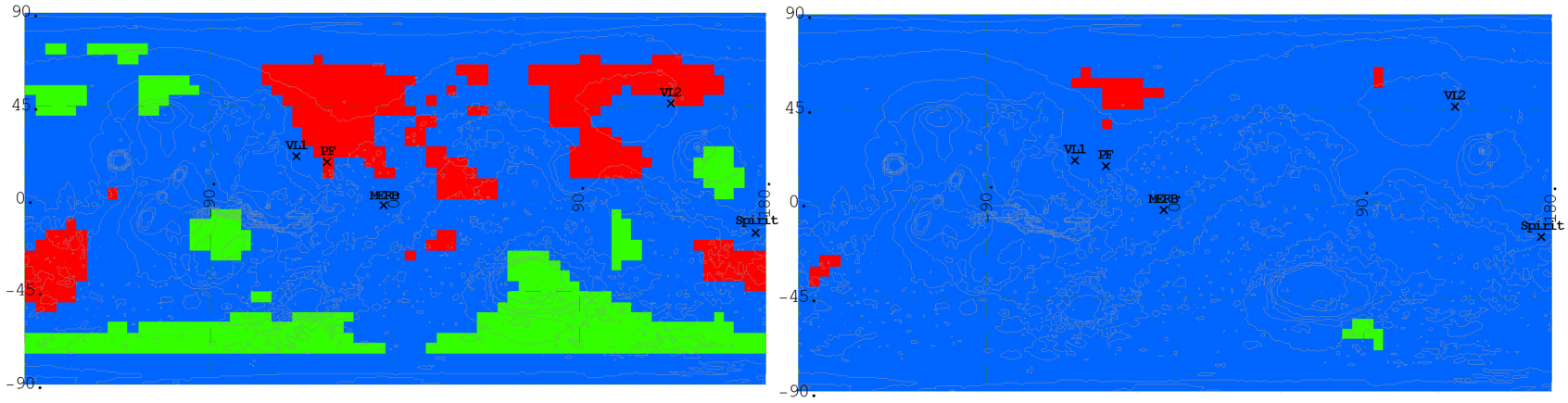

Figure 6.8: GTCs for Th as described in Figure 6.1. Unlike the mid-latitudinal extent for the other elements, K and Th extend to ±75° (Section 6.2.1).

Table 6.2: Arc-radius, linear radius, and approximate surface area of the mean filter used to generate the global map of each element/oxide. The linear radius and surface area assume Mars to be an exact sphere and utilize the MGS95J model 3.396×10^3 km planetary radius (*Konopliv et al.*, 2006).

Element/Oxide	Arc-radius	Linear radius km	Surface area km^2
Al, Ca, Si	15	8.9×10^2	2.5×10^6
Cl, Fe, H_2O, Th	10	5.9×10^2	1.1×10^6
K	5	3.0×10^2	2.8×10^5

of Ancient Oceans on Mars, submitted to Plant. Space Sci.). Given our emphasis on the spatial overlap of GTCs to define CSRs, we do not discuss GTCs of individual elements further in this work.

6.2.3 Step 2: Spatial Overlap of GTCs and Area Threshold

As described in the introduction, the chemically striking regions are defined to be those of overlap among the GTCs of multiple elements. Even when underlying GTCs are spatially expansive, uncertainties in the form of spatial autocorrelation (Chapter 4) may place their physical significance in doubt. As an analogy, any region that is smaller than the areal extent of the $\approx 7.4^\circ$ GS footprint may be considered as tenuous as a feature smaller than the ≈ 1.5 pixel point spread function (PSF) of an image generated by the HiRISE (e.g., *McEwen et al.*, 2007, Para. 18 and Fig. 9). For any given set of elements, we reduce the impact of this concern conservatively by identifying the CSRs that equal or exceed the area of the largest mean filter (Table 6.2). The area calculation is approximate, not exact, since it does not account for topography and assumes Mars to be a sphere.

Furthermore, as Gasnault et al. (2008, Quantitative Geochemical Mapping of Martian Provinces, in preparation) discuss, even our conservative constraints may not completely localize the proper area for study. Nevertheless, even a small CSR contained within those that show consistent chemical trends and satisfy area thresholds may prove insightful, as we will demonstrate below with our case study.

For the sake of consistency and simplicity, we delineate CSRs for each of the 247 possible sets of elements taken two or more at a time, including Al, using GTCs defined with the same statistical threshold, such as $t = 1$. Only seven sets, all two elements each, survive the thresholds as given in Table 6.3. We do not impose additional constraints - such as eliminating sets of elements that are unknown to show chemical covariability on Earth - in order to identify CSRs free of terrestrial bias.

The CSRs subsequent to area threshold application are illustrated in Figure 6.9. Comparisons with Figures 6.1– 6.8 reveals that while GTCs overlap spatially across most statistical confidence thresholds for sets of two elements, few actually exceed the area of the largest corresponding mean filter (Table 6.2). As a case in point, Figure 6.10 illustrates the region delineation steps for Cl and Si at $t \geq 1.5$. We also make a minor refinement to the area threshold method by discarding any bins with fewer than three edge or corner sharing neighbors. This effectively eliminates any narrow regions that are only a bin across with consequently higher spatial uncertainties. The delineation of GTCs, delineation of overlap, elimination of narrow regions, and the application of area thresholds for the 247 sets of elements were all implemented algorithmically without manual intervention. While many CSRs overlap with each other as evident in

Table 6.3: Key to the numerical code of Chemically Striking Regions (CSRs) in Figure 6.9. Each CSR is denoted by the corresponding set of elements in curly braces, confidence (Table 6.1) as an approximation to a multiple of the standard deviation (s), enrichment (E) and/or depletion (D) in element order, and arc radius of the area threshold (Table 6.2). For example, $\{Cl, Si\}\,1.5sED15^\circ$ would denote a bin belonging to a single CSR marked by the enrichment of Cl and depletion of Si at better than $1.5s$ confidence and exceeding a 15° radius area. On the other hand, $\{Cl, H\}\,1sEE15^\circ\,\{Cl, Si\}\,1sED15^\circ$ identifies a bin of overlap between two CSRs: One $\{Cl, H\}\,1sEE15^\circ$ and the other $\{Cl, Si\}\,1sED15^\circ$. Note that such bins generally do not delineate a sufficiently large contiguous area to be classified as a CSR in its own right. CSRs of Si and Th overlap completely with the CSRs of K and Th albeit at different statistical confidence levels. The one region on the basis of Al is solely to motivate future investigations as the Al map is being refined. Higher numerical uncertainties and weak correlation with other elements caused the absence of Ca-based CSRs. Continued in Table 6.4.

Key	Value
Unclassified	0
$\{Al, Fe\}\,1sED15^\circ$	5
$\{Cl, H\}\,1sEE15^\circ$	10
$\{Cl, H\}\,1sEE15^\circ\,\{Cl, Si\}\,1sED15^\circ$	15
$\{Cl, Si\}\,1.5sED15^\circ$	20
$\{Cl, Si\}\,1sDE15^\circ$	25
$\{Cl, Si\}\,1sDE15^\circ\,\{K, Th\}\,1sEE15^\circ$	30
$\{Cl, Si\}\,1sED15^\circ$	35
$\{Fe, Th\}\,1sEE15^\circ$	40

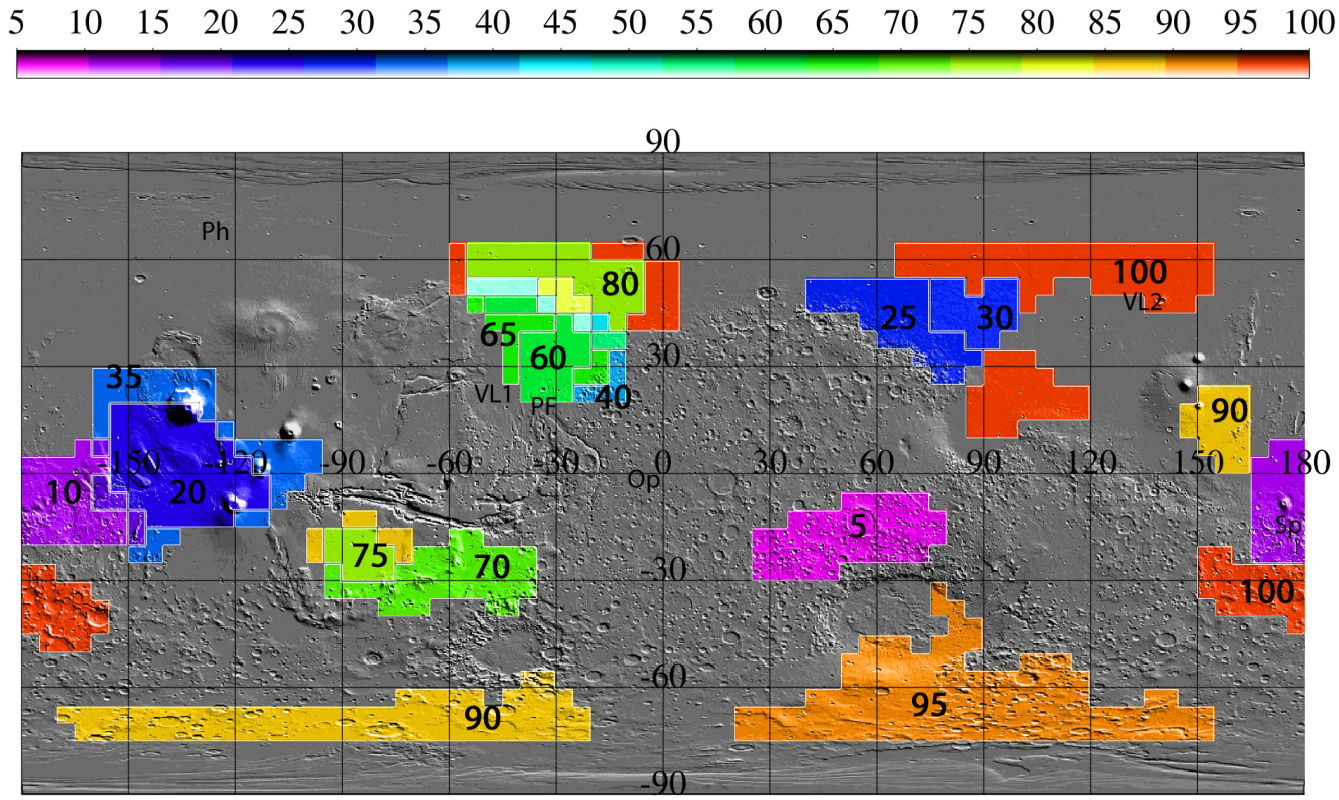

Figure 6.9: CSRs overlain on MOLA topographic map and cases of overlap among them numbered as given in Table 6.3. Landing sites marked as: Op (Opportunity), PF (Pathfinder), Ph (Phoenix), Sp (Spirit), VL1 (Viking Lander 1), and VL2 (Viking Lander 2).

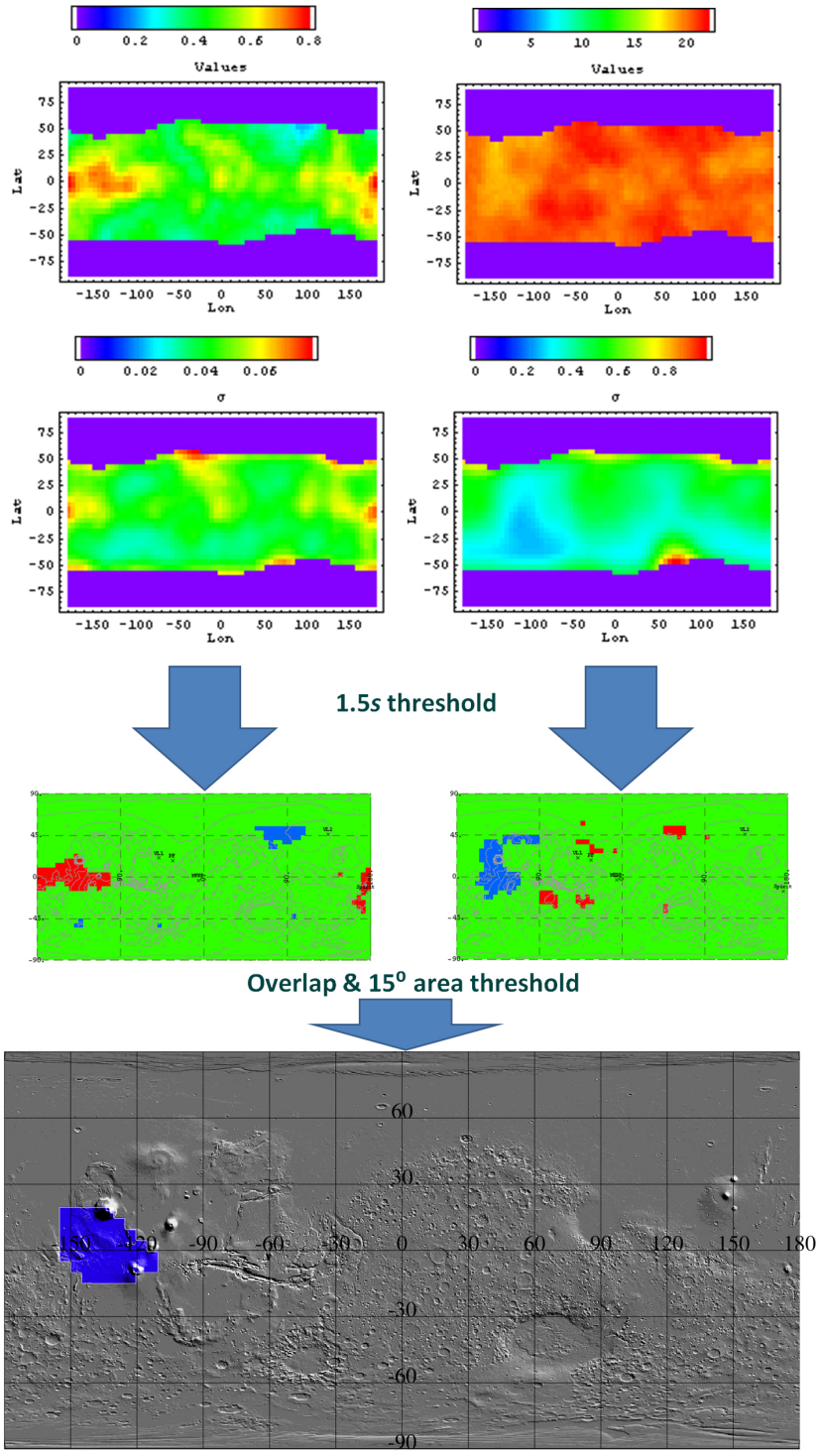

Figure 6.10: Illustration of the CSR delineation steps using Cl (left), Si (right), and $t \geq 1.5$ as an example. Note how the element with the smaller GTCs constrains the areal extent of the resulting CSRs.

Table 6.4: Key to the numerical code of Chemically Striking Regions (CSRs) in Figure 6.9 continued from Table 6.3.

Key	Value
$\{Fe, Th\}\ 1sEE15^\circ\ \{K, Th\}\ 1.5sEE10^\circ$	45
$\{Fe, Th\}\ 1sEE15^\circ\ \{K, Th\}\ 1.5sEE10^\circ\ \{Si, Th\}\ 1sEE15^\circ$	50
$\{Fe, Th\}\ 1sEE15^\circ\ \{K, Th\}\ 1sEE15^\circ$	55
$\{Fe, Th\}\ 1sEE15^\circ\ \{K, Th\}\ 1sEE15^\circ\ \{Si, Th\}\ 1sEE15^\circ$	60
$\{Fe, Th\}\ 1sEE15^\circ\ \{Si, Th\}\ 1sEE15^\circ$	65
$\{H, Si\}\ 1sDE15^\circ$	70
$\{H, Si\}\ 1sDE15^\circ\ \{K, Th\}\ 1sDD10^\circ$	75
$\{K, Th\}\ 1.5sEE10^\circ$	80
$\{K, Th\}\ 1.5sEE10^\circ\ \{Si, Th\}\ 1sEE15^\circ$	85
$\{K, Th\}\ 1sDD10^\circ$	90
$\{K, Th\}\ 1sDD15^\circ$	95
$\{K, Th\}\ 1sEE15^\circ$	100

Figure 6.9 and Table 6.3, we are unable to classify the resulting sub-regions as CSRs since they fail to satisfy the area thresholds.

6.3 Overview of the Chemically Striking Regions

To first order, two other independent methods of defining regions on the basis of elemental mass fractions - one a combination of principal component analysis, cluster analysis, hierarchical modeling, and a field-of-view filter (Gasnault et al., 2008, in preparation) and the other a combination of principal component analysis and cluster analysis implemented in ENVI (Taylor et al., 2008, JEFF,

WHAT IS THE TITLE?, in preparation) - also highlight the same broad regions of the planet as our approach. As discussed in the two companion papers, this reinforces the geochemical significance of CSRs in spite of spatial uncertainties.

As evident in Figure 6.9, several CSRs marked by enrichments involving Fe, K, Si, and Th occupy Chryse Planitia northward to Acidalia. Several other CSRs, involving the enrichments of K, Si, and Th, and depletion of Cl, exist in the regions NE of both Isidis and Arabia and the western perimeter of Utopia into Vastitas Borealis. Collectively, these regions are suggestive of strong chemical variations marking the lowlands proximate to the lowlands margin. Accordingly, they may help to constrain models that relate lowland geochemistry dominantly to aqueous alteration (e.g., Dohm et al., 2008, submitted) or dominantly to igneous processes (e.g., Chapter 5).

Several regions of high southern latitudes, mostly beyond the midlatitudinal constraint of the other elements (Section 6.2.1), are marked by the mutual depletion of K and Th which may be influenced in part by mass dilution effects of H enrichment closer to the polar regions. Two areas of the midlatitudinal southern highlands are also highlighted by the CSRs. One lies immediately south of Valles Marineris overlapping with Syria, Solis, and Thaumasia plateaus corresponding to CSRs delineated by the enrichment of Si and depletion of H, K, and Th. The second, marked by the mutual enrichment of K and Th, occupies the vicinity of Sirenum Terra and Terra Cimmeria. Tentatively, a third area delineated by the depletion of Fe and enrichment of Al on the NW perimeter of Hellas may provide useful insight once the Al map is refined further.

SE Elysium lava flows constitute nearly 70 % of the underlying surface in one of smallest CSRs, delineated by the simultaneous depletion of K and Th, as

mentioned later in Section 6.3.2. Abutting this region is the last broad area on Mars that is identified by the CSRs. It extends westward from the Tharsis bulge, through the MFF, and into Elysium Planitia. As mentioned in Section 6.2.2, the key underlying GTCs for this broad expanse are those of Cl enrichment. The individual CSRs essentially identify chemical heterogeneities within it. Those of Si depletion are limited to the Tharsis construct, while the western section is marked by H enrichment.

In our case study we focus on the chemical signatures evident in the eastern portion of the broad region, where the most expansive CSR consists of $\{ClSi1sED15^{\circ}\}$ (Table 6.3 and Figure 6.9) denoting (E)nrichment of Cl and (D)epletion of Si at $1s$ confidence exceeding the area of a 15° radius cap (Table 6.2). Abundances of these elements differ from global averages by over $1.5s$ throughout most of its SW portion. In turn, within the SW portion of the $\{ClSi1.5sED15^{\circ}\}$ CSR lies a region also depleted in Fe at better than $1s$ confidence. In spite of being smaller than the area threshold (Table 6.2) by $\approx 20\,\%$, we choose this smaller region for our case study due to two key reasons: (1) Consistent chemical trends in a spatially nested pattern that highlight the region; and (2) The marked depletion of both major elements detected by the GS, Fe and Si, making the region particularly unusual. This region, along with the larger CSRs that contain it, is illustrated in Figure 6.11.

Do the CSRs conform with the global correlations that we identified in multivariate space (Chapter 5)? To first order, they do. For example, the presence of CSRs delineated by the enrichment of both K and Th and the absence of those marked by the enrichment of one and depletion of the other is consistent with the strong positive correlation that exists globally between them as discussed

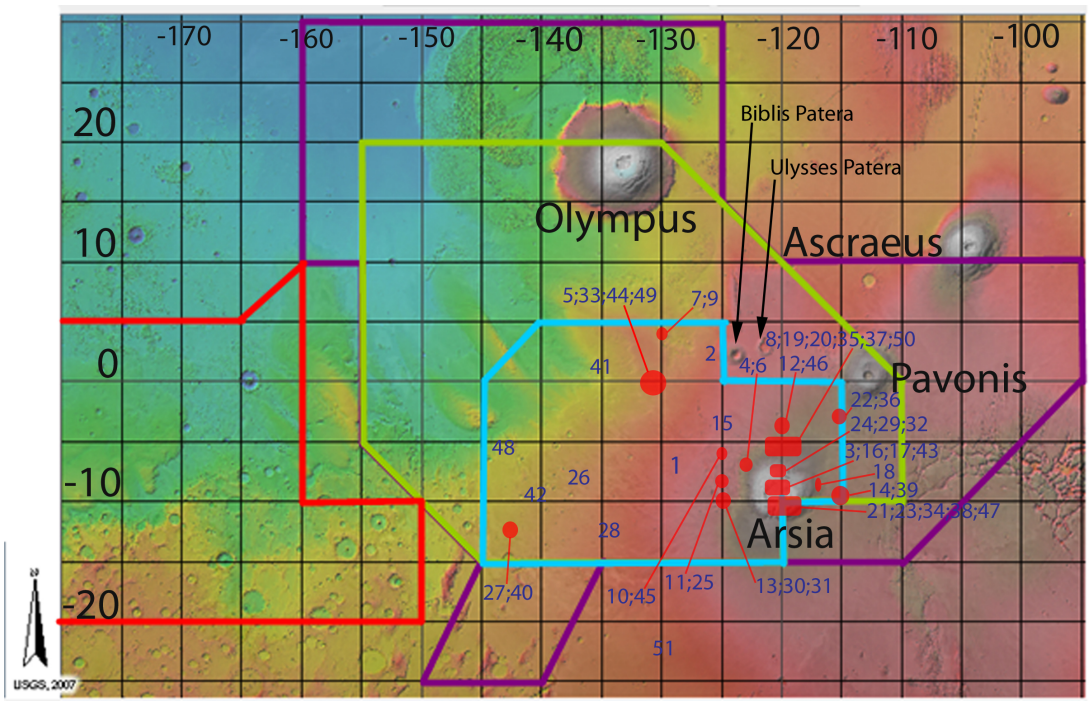

Figure 6.11: Sketch of our case study region (sky blue outline) that is marked by Cl enrichment and Fe, Si depletion along with the CSRs that surround it: $\{ClSiED1.5s15°\}$ in lime and $\{ClSiED1s15°\}$ in purple. Consistent chemical trends of Cl enrichment and Si depletion highlight our region. CSR to the west outlined in red is $\{ClHEE1s15°\}$. Overlain on the MOLA elevation map from PIGWAD at 1: 2.8×10^7 lateral scale. Reddish hues indicate higher elevation while bluish hues indicate lower elevation in the MOLA map. HiRISE images that are used to characterize the surface in Section 6.4.3 are also indicated by numerical tags corresponding to Table 6.5. The possibility of HiRISE sampling bias is noted in Section 6.4.3.

in Chapters 5 and 4. Global correlations and the CSRs are similarly consistent even for elements that are not as strongly correlated, such as Cl and Si. As was anticipated by the anticorrelation between Cl and Si (*Keller et al.*, 2006b, and Chapter 5), all of the CSRs delineated with Cl and Si show enrichment of one and depletion of the other. The CSRs delineated by Cl and H, such as those in the western MFF area, are consistent with their positive correlation (*Keller et al.*, 2006b, and Chapter 5) in multivariate space as well. Lastly, Ca, which

shows only weak multivariate correlations with others in preliminary analyses (Section 4.7), does not yield any CSRs that satisfy our area thresholds.

Summary comparisons with the global distributions of surface type 2, mapped geologic units, thermal inertia, albedo, and rock areal fractions in the following sections complete our overview of the CSRs.

6.3.1 Surface Type 2 Reconsidered

On the basis of a strong positive correlation among K mass fractions, Th mass fractions, and surface type 2 areal fractions, in Chapter 5 we favored igneous processes over aqueous alteration for the origin of surface type 2. Do the northern CSRs encourage our overall interpretation to be revisited? We consider this possibility using the same smoothed rebinned surface type 1 and 2 areal fraction datasets that were used in Chapter 5. In general, the CSRs are consistent with the global-scale positive correlation of K and Th mass fractions with surface type 2 areal fractions. Specifically, northern Chryse-Acidalia and Utopia-Vastitas Borealis CSRs of K and Th enrichment (Figure 6.9) are also those with the highest average areal fractions of surface type 2 (Figure 6.12) and lowest average areal fractions of surface type 1 (Figure 6.13).

Furthermore, Si enrichment does not distinguish surface type 2 from 1, as regions with a high areal fraction of each type overlap with high-Si CSRs. For example, the Syria-Solis-Thaumasia CSR of Si enrichment (Figure 6.9) has a particularly high average areal fraction of surface type 1 (Figure 6.13), while the Si-enriched Utopia-Vastitas Borealis CSR (Figure 6.9) has an unusually high areal fraction of surface type 2 (Figure 6.12). Nevertheless, the CSRs do indicate het-

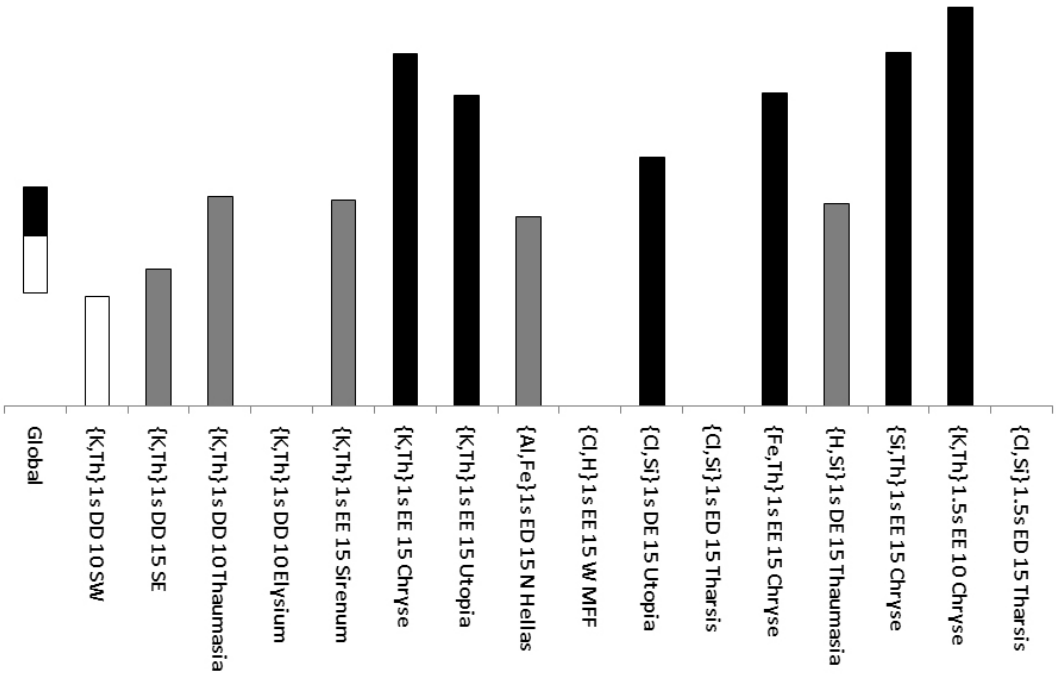

Figure 6.12: Qualitative comparison of the average surface type 2 areal fraction within each CSR with the global distribution. Data sources are identified in Sections 6.3.1 and 6.3.3. The "Global" box-plot marks the 25th percentile, median, and 75th percentile of the global distribution. Regional averages at or above the 75th percentile are identified by black columns, intermediate by light-gray, and at or below the 25th percentile by solid outlines. Each CSR is also tagged with the name of a nearby geographic feature to facilitate identification in Figure 6.9. Column charts are omitted for CSRs that lie mostly beyond the areal bounds of corresponding datasets. Figures 6.13– 6.18 similarly illustrate surface type 1 areal fraction, albedo, thermal inertia, and rock areal fraction, respectively.

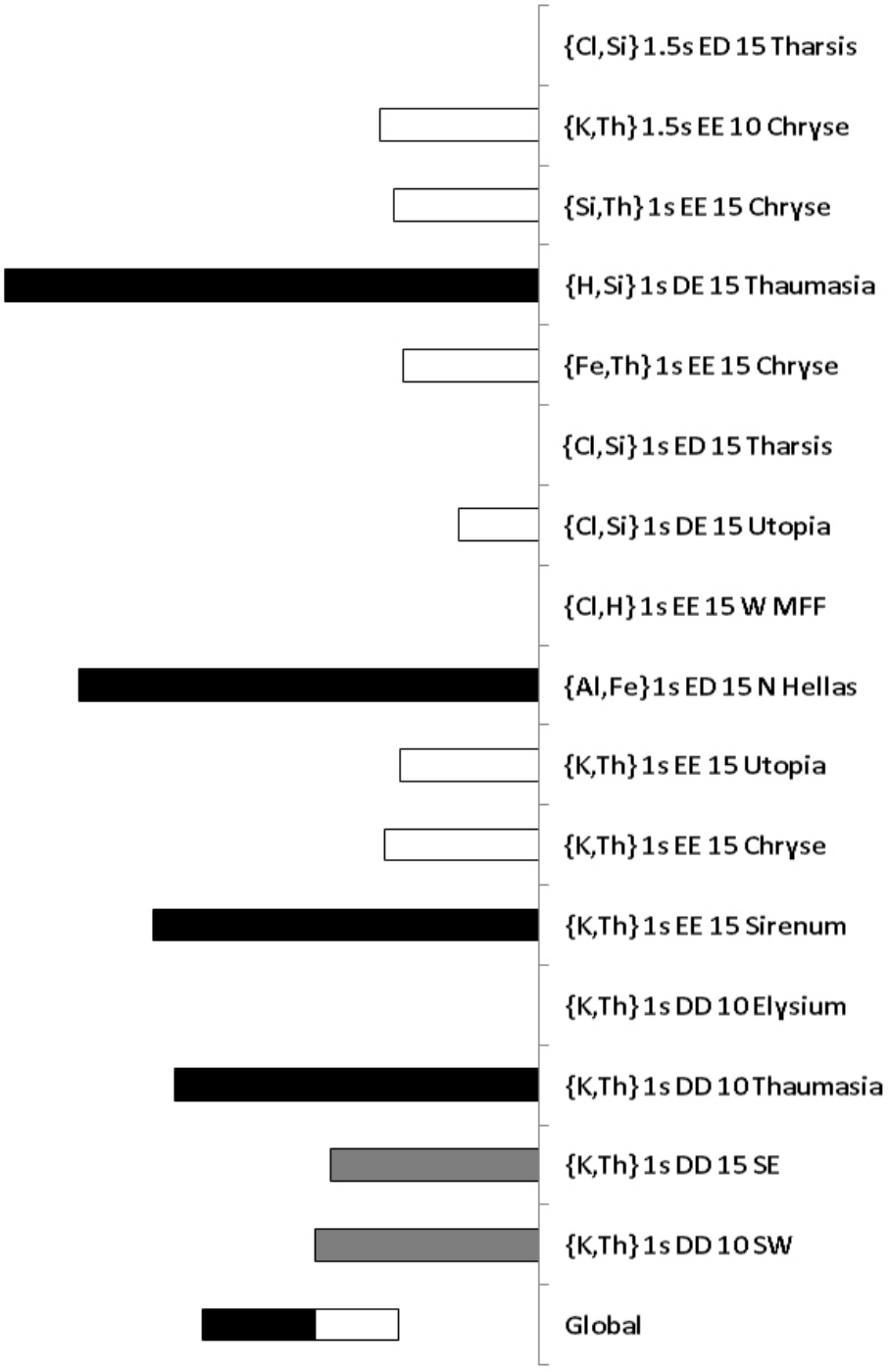

Figure 6.13: Qualitative comparison of the average surface type 1 areal fraction within each CSR with the global distribution as described in Figure 6.12.

erogeneities at smaller spatial scales such as the enrichment of Fe, K, Si, and Th in Chryse-Acidalia areas with high surface type 2 areal fractions (Figure 6.12), and the enrichment of K and Th in Sirenum-Terra Cimmeria areas with a high surface type 1 areal fraction and moderate-to-high surface type 2 (Figures 6.13 and 6.12).

In summary, the CSRs that we have delineated do not contradict what makes areas with surface type 2 distinct from their surface type 1 counterparts: a remarkable enrichment of K and Th, but not of Si (Chapter 5). Nevertheless, as anticipated in Chapter 5, they reveal regional exceptions to these general trends, particularly in equatorial regions where the areal fractions of surface types 1 and 2 are both high relative to their global distributions. A detailed investigation comparing and contrasting the eleven potential (*Rogers et al.*, 2007a) mineralogy type distributions (e.g., *Rogers and Christensen*, 2007) with these and other CSRs may yield a better understanding of surficial processes and their variation at depth. Taylor et al. (2008, in preparation) provide an overview of such comparisons in the context of vastly different sampling depths of the underlying instruments - the GRS at tens of centimeters, and the TES from 50 μm (*Christensen et al.*, 2004, Section 3.1.4 Para. 2) to probably no more than the Visible Near Infrared (VNIR) limit of 100 μm (*Poulet et al.*, 2007, Para. 21).

6.3.2 Geologic Overview

It is intriguing that the CSRs do not qualitatively appear to follow the spatial patterns of mapped geologic units (e.g., *Skinner Jr. et al.*, 2006), perhaps with the tentative exception of the planetary dichotomy (e.g., Dohm et al., 2008, in

preparation) as discussed earlier. Since the GS is only sensitive to compositions at tens of centimeter depths, this may indicate that the surficial processes and compositions reflected in the GS data are not closely linked to the underlying geology.

Given the GS's inherently coarse resolution (Section 6.2.1), we compile the areal fractions of mapped geologic units at $0.5^\circ \times 0.5^\circ$ spatial resolution within each CSR to evaluate the extent of direct spatial overlap between CSRs and particular geologic units. Since the CSRs are binned at $5^\circ \times 5^\circ$, we minimize the loss of geologic information by simply re-binning them at $0.5^\circ \times 0.5^\circ$. We use a sinusoidal equal area projected digital atlas of geologic units with a maximum resolution of $0.0625^\circ \times 0.0625^\circ$ at the equator (Ed Guinness, 2003, personal communication) linearly interpolated by row to a $0.5^\circ \times 0.5^\circ$ equi-rectangular grid (e.g., *Snyder*, 1987, p. 248) at zero interpolation order.

Our geologic atlas is based on the Viking legacy I-1802 series (available online `http://webgis.wr.usgs.gov/pigwad/down/mars\_geology.htm\#Mars\%20Global`) and lacks recent updates/revisions with MOLA and other datasets (e.g., *Skinner Jr. et al.*, 2006). However, preliminary comparisons indicate that at the coarse spatial resolution of the GS, area calculations with the updated maps would converge with the old. Therefore, we present our results based on the I-1802 series in Figures 6.14– 6.15, both for relative age and mapped geologic units.

As evident in Figure 6.14, one age unit typically dominates areally over others within most CSRs. However, we do not observe a consistent association of particular sets of elements or of particular CSRs with specific age units. Given the contiguous spatial extent of each age unit, this suggests that the apparent

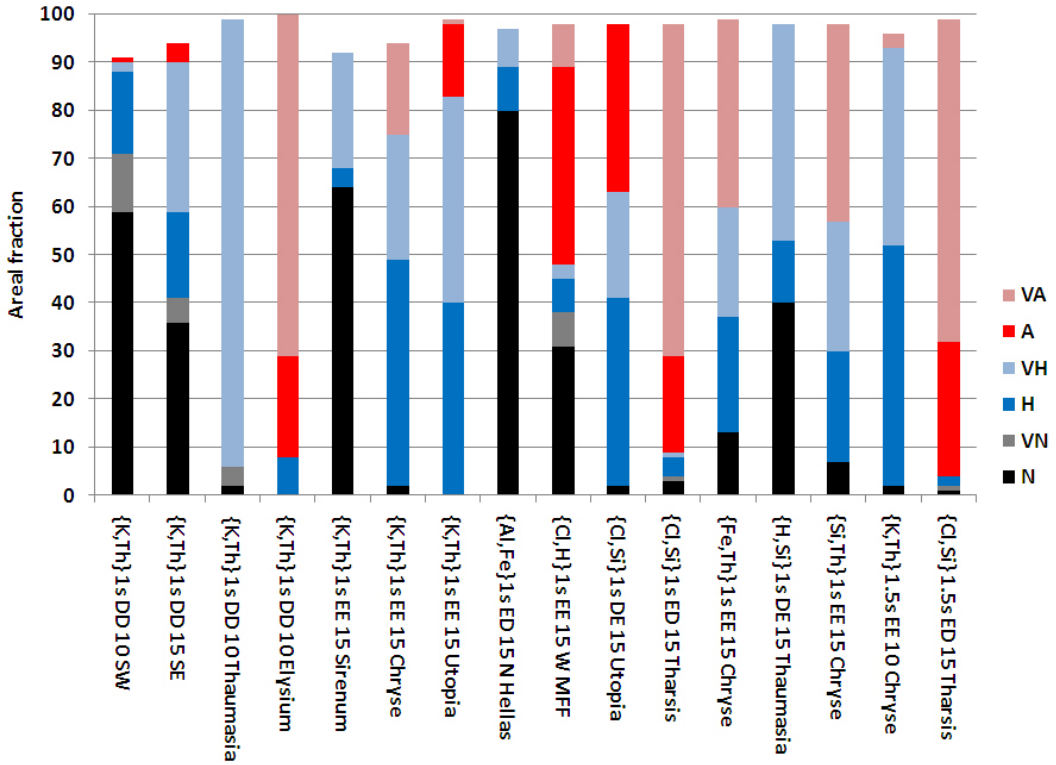

Figure 6.14: The areal fractions of relative geologic age and volcanic units of the I-1802 series within each CSR. Data source and processing are described in Section 6.3.2. The relative areal fractions of temporal and volcanic units within each CSR are shown in the top figure. "N" indicates Noachian, "H" Hesperian, and "A" Amazonian. The prefix "V" indicates the corresponding volcanic units. The area of the volcanic units corresponding to each temporal unit is shown in a lighter fill color. The total area often does not sum to 100 % since some units are uncategorized.

areal dominance of one within a particular CSR may just be coincidental instead of reflecting chemical processes representative of a particular era. Nevertheless, the dominant geologic age group may provide general constraints on surficial processes in detailed investigations, such as the area we selected for our case study (Figure 6.11).

As shown in Figure 6.14 the areal fractions of geologic units and secularly

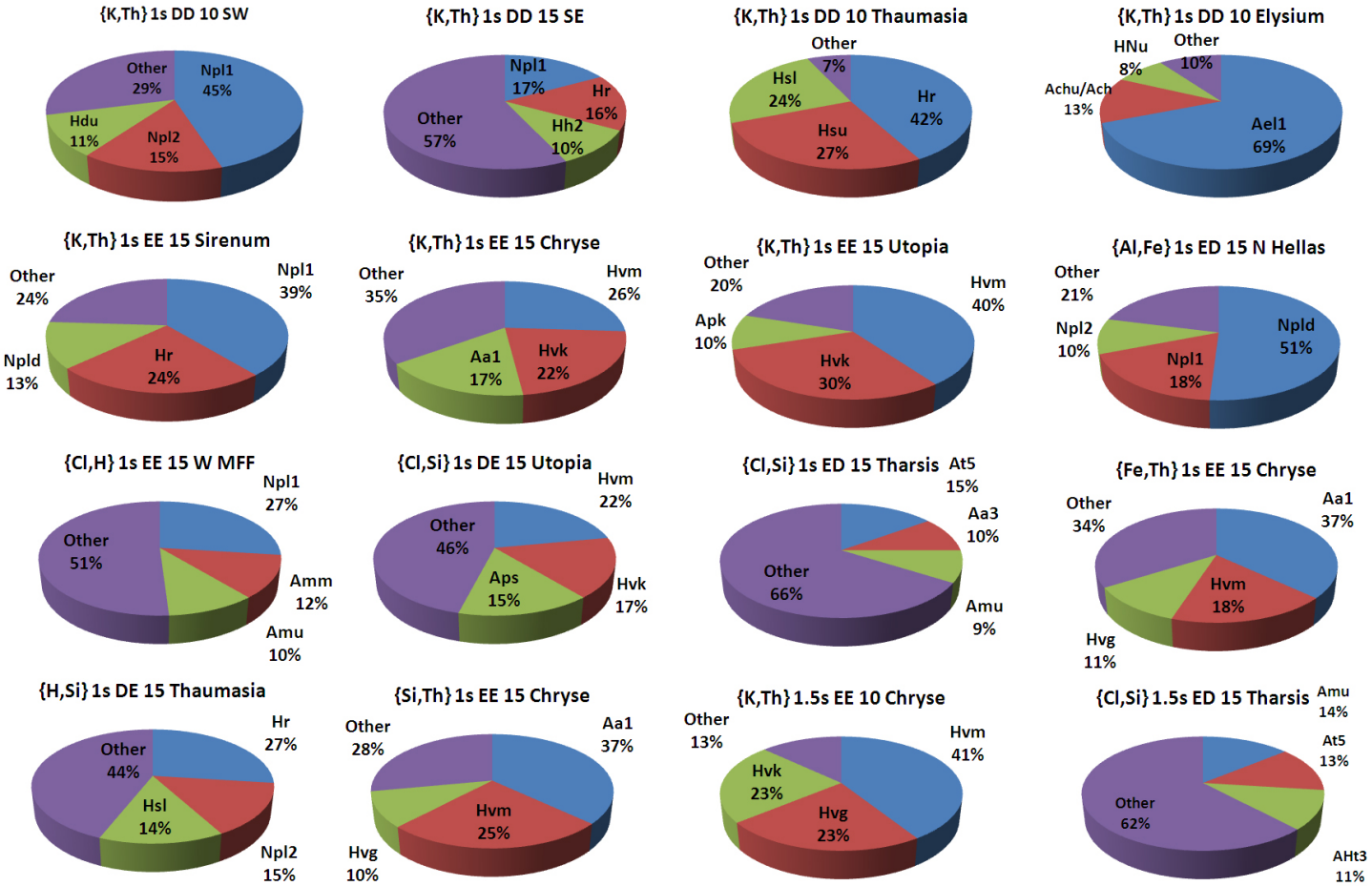

Figure 6.15: The three mapped geologic units with the highest areal fractions are shown for each CSR, with the total areal fraction of remaining units indicated in purple. Geologic units as defined in the I-1802 series (Figure 6.14).

categorized volcanic units are even less insightful than the relative ages since the areal dominance of a single unit within a CSR is quite rare. In fact, most CSRs contain similar areal fractions of many different units. The $\{K, ThDD1s10°\}$ CSR in the vicinity of Elysium (Figure 6.9) is a possible exception where nearly 90 % of the surface is underlain by Amazonian units of which $\approx$ 80 % consists of Elysium lava flows (Figures 6.14 and 6.15). Similarly, nearly 90 % of the $\{K, ThDD1s10°\}$ CSR in the vicinity of Syria-Solis-Thaumasia plateaus is underlain by Hesperian volcanic units. These are also the only CSRs in which the three geologic units with the greatest areal fractions constitute nearly 90 % of the total area (Figure 6.15). It is possible that detailed analyses of such CSRs would provide insight into igneous processes. The CSR in the vicinity of Thaumasia may be particularly insightful, as relatively low albedo (Figure 6.16) along with high thermal inertia (Figure 6.17) and rock areal fractions (Figure 6.18) suggest that the underlying bedrock may contribute meaningfully to the GS signal. In addition, detailed studies of geomorphology analogous to the work by *Dohm et al.* (2008) may reveal trends that are not apparent in our overview.

6.3.3 Overview of Thermally Derived Attributes

Remote sensing observations at Thermal InfraRed (TIR) wavelengths by the Viking missions first enabled detailed characterization of key surficial properties of the Martian surface, including albedo and thermal inertia. The latter was used in conjunction with radar reflectivity variations to estimate the areal fraction of fragments no smaller than 0.1 m, termed "rocks" (*Christensen*, 1986). While the spatial resolution and estimation methods have been refined with more recent instruments such as the Mars Global Surveyor Thermal Emission

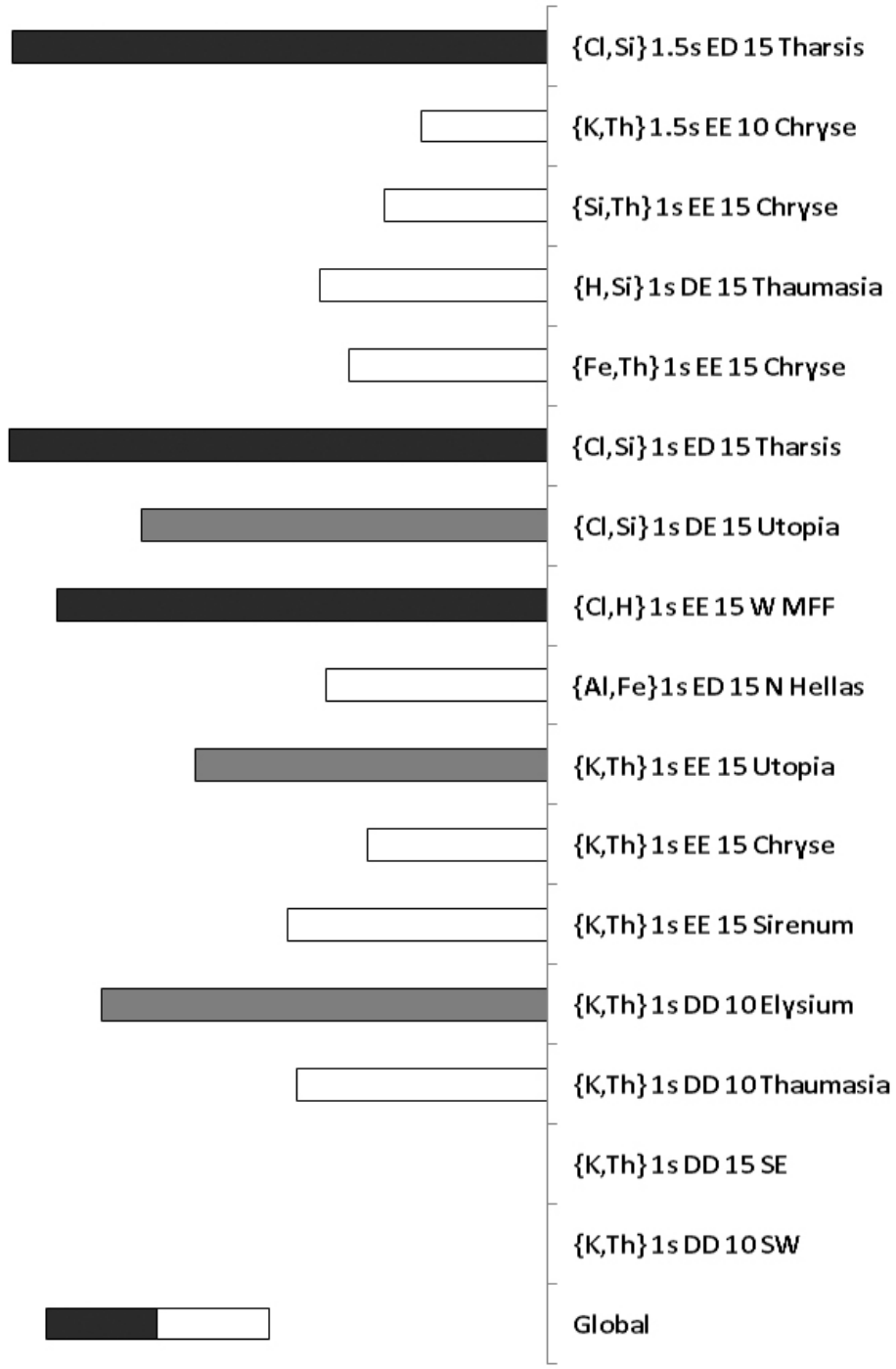

Figure 6.16: Qualitative comparison of the average albedo of each CSR with the global albedo distribution, as described in Figure 6.12

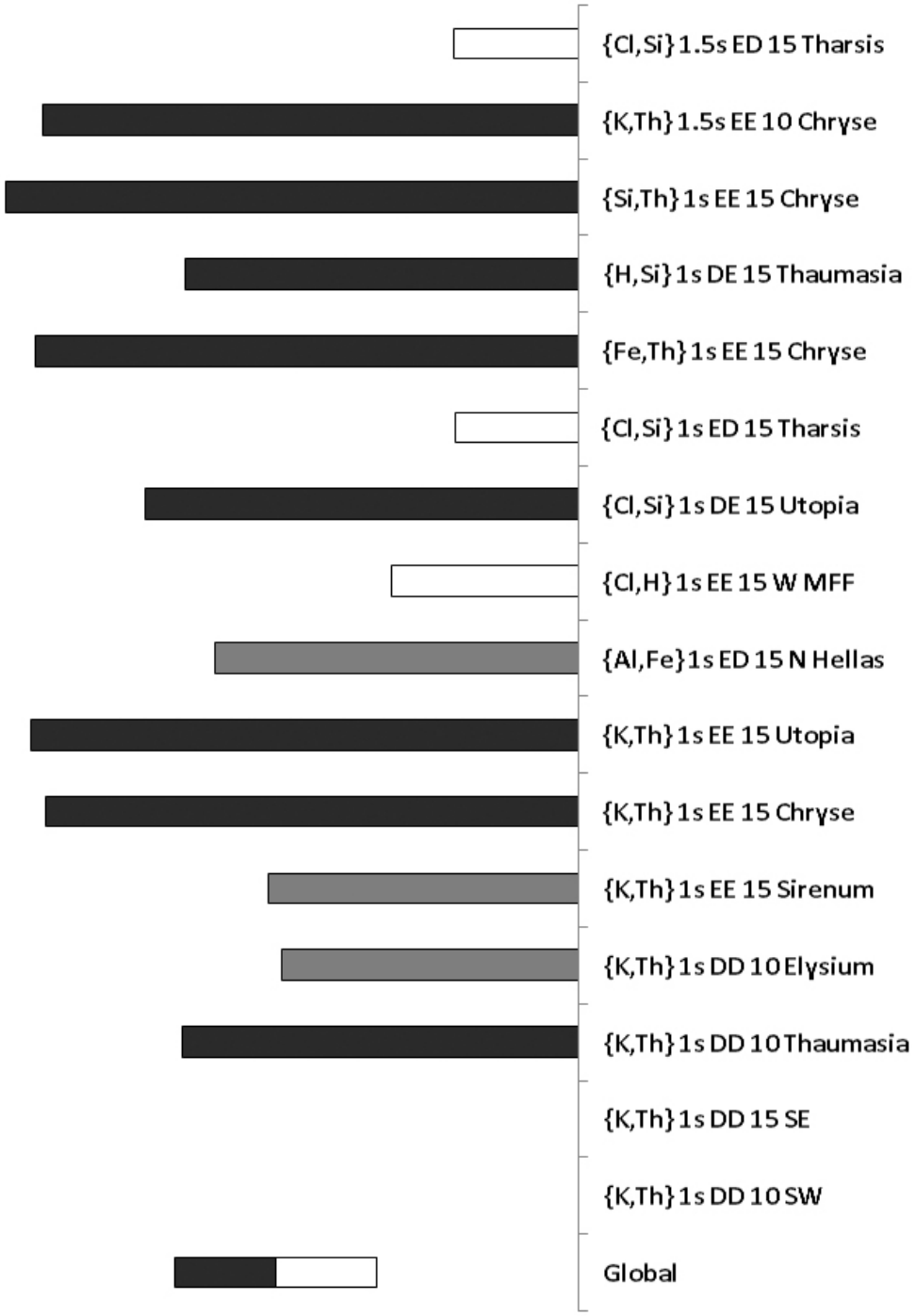

Figure 6.17: Qualitative comparison of the average thermal inertia within each CSR with the global distribution as described in Figure 6.12.

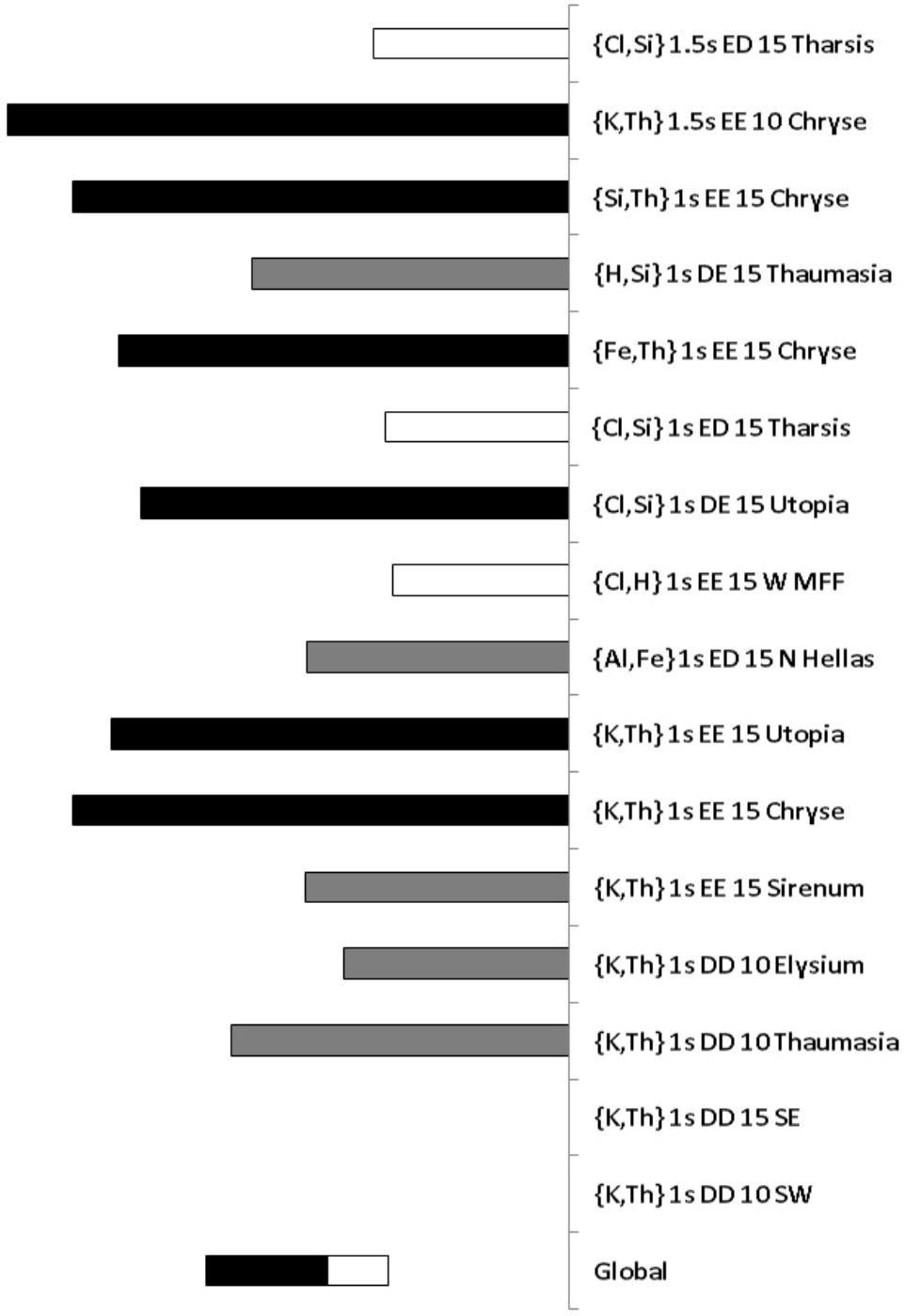

Figure 6.18: Qualitative comparison of the average rock areal fraction within each CSR with the global distribution as described in Figure 6.12.

Spectrometer (TES) (e.g., *Putzig et al.*, 2005; *Christensen et al.*, 2001), the resulting maps are generally consistent with their predecessors. In light of this and the context of our general discussion at the coarse spatial resolution of the GS, we use thermal inertia, albedo, and rock areal fractions derived with the Viking InfraRed Thermal Mapper (IRTM) (*Christensen*, 1986) as described in Chapter 5. The average value of each - computed as the arithmetic mean - relative to the corresponding global distribution is qualitatively illustrated in Figures 6.16–6.17.

In general, apparent rock areal fraction, thermal inertia and albedo values within CSRs are consistent with the observations in multivariate space (e.g., *Keller et al.*, 2006b, and Chapters 4, 5). For example, the northern CSRs with K and Th enrichment also feature higher rock areal fraction and thermal inertia values, along with low albedo values (Figures 6.16, 6.18, and 6.17). On the other hand, the CSRs in SW Tharsis with Cl enrichment and Si depletion have high albedo, low thermal inertia, and low rock abundance. It is also intriguing, and perhaps indicative of primary mineralogic effects, that the majority of the CSRs are relatively high thermal inertia and low albedo regions (Figures 6.16 and 6.17). Our subsequent case study involving the region of Cl enrichment and Fe, Si depletion (Figure 6.11) demonstrates how these attributes - specifically thermal inertia - can act as important constraints for candidate surficial processes. Nevertheless, it is important to recall that even the areas with the highest rock abundances are dominated by fine material, and as such, the chemistry may be more indicative of variations in the fine component than of underlying bedrock (*Newsom et al.*, 2007).

6.4 Region Among Volcanic Edifices (RAVE): A Case Study

In Section 6.3, we presented the key chemical reasons for selecting the only region on Mars with a remarkable enrichment of Cl and depletion of Fe and Si (Figure 6.11) for our case study. As one that does not quite satisfy our conservative area thresholds (Table 6.2), the insight we glean from this region further reinforces the utility and significance of the (larger) CSRs in general. For conciseness, we refer to it as RAVE (Region Among Volcanic Edifices) throughout the rest of this work.

6.4.1 Radar Stealth and Bulk Density

Even though we selected RAVE (Figure 6.11) solely due to spatially convergent chemical signatures across several CSRs (Section 6.3), it overlaps notably with a region highlighted by two independent datasets: radar reflectance observations from Earth at 1.35 cm (*Ivanov et al.*, 1998) and 3.5 cm (*Edgett et al.*, 1997) wavelengths. At both wavelengths, much of this region is an efficient absorber producing the classic signature of Stealth. The visually impressive nature of this overlap illustrated in Figure 6.19 is particularly relevant as the free-space vertical resolution at 1.35 cm and 3.5 cm wavelengths is comparable to the GS sampling depths. In fact, the bulk of the Stealth region at 3.5 cm overlaps much more compellingly with RAVE than it does with the easternmost MFF (Figure 6.19). In contrast, the Stealth features apparent across the broad MFF at much longer wavelengths of 13 cm (*Harmon et al.*, 1999), 15 m (*Carter et al.*, 2008), and $\approx$ 150 m (*Picardi et al.*, 2005) do not overlap with RAVE.

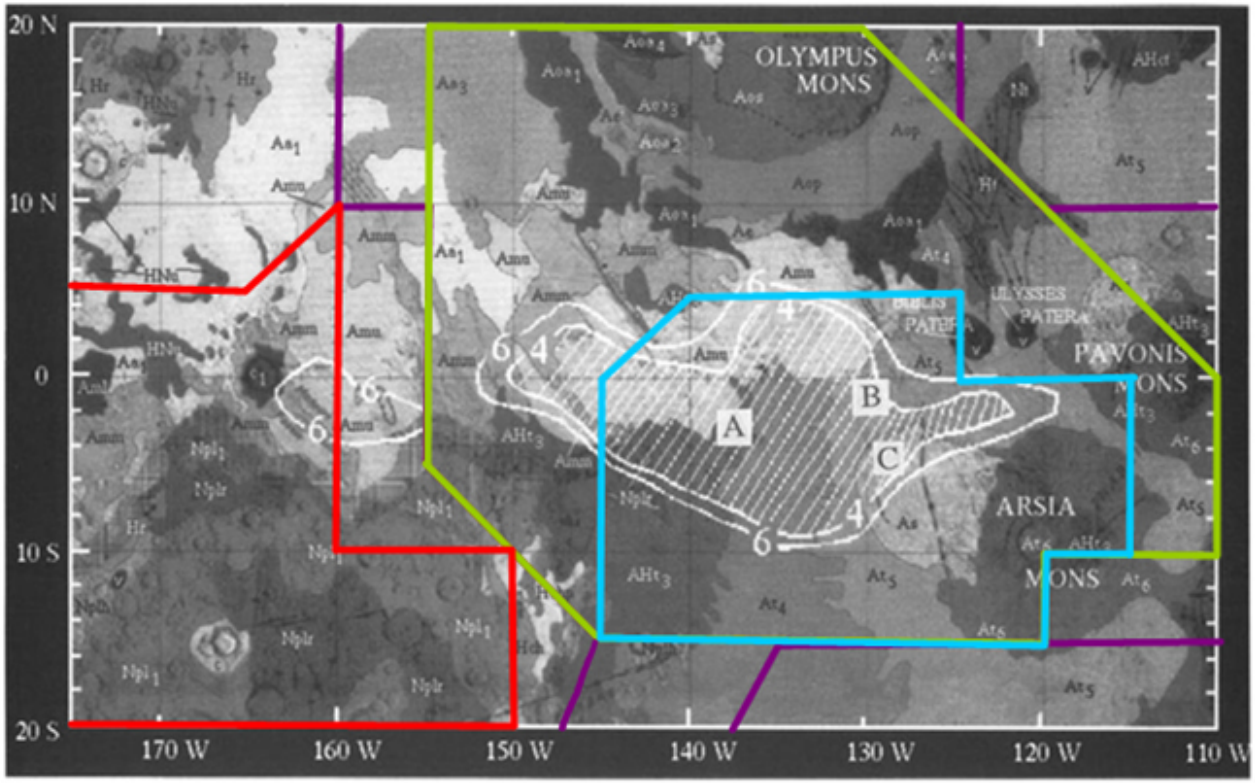

Figure 6.19: Sketch of RAVE (sky blue) overlaid on Stealth region at 3.5 cm and mapped geologic units (*Edgett et al.*, 1997, adapted from Figure 4). RAVE and Stealth of greatest confidence (hatched) overlap notably. Surrounding CSRs include $\{ClSiED1.5s15°\}$ in lime and $\{ClSiED1s15°\}$ in purple. Surficial chemical differences between western and eastern MFF are revealed by $\{ClHEE1s15°\}$ CSR (red) and $\{ClSiED1s15°\}$.

The spatial overlap between RAVE and 3.5 cm Stealth (*Edgett et al.*, 1997) has significant implications for the physical properties of the bulk material. Specifically, bulk density constrained by the real component of the dielectric constant is 0.4×10^3 kg m^{-3} (*Ivanov et al.*, 1998). This is consistent with the 1.9×10^3 kg m^{-3} upper bound for bulk density in the MFF (*Watters et al.*, 2007; *Keszthelyi and Jaeger*, 2008). Such low bulk densities are indicative of either high porosity or a matrix of $H_2O_{(s)}$ and fine material (*Watters et al.*, 2007; *Keszthelyi and Jaeger*, 2008).

Compaction modeling with potential terrestrial analogs, such as reticulite, indicates that high porosities may be sustained to kilometer depths (*Keszthelyi and Jaeger*, 2008). Similar stealth properties have been observed of the much smaller scale Mauna Kea scoriaceous deposits with 23 cm synthetic aperture radar (*Gaddis et al.*, 1989) on Earth, and of Montes Jura fine ejecta deposits at 3.8 cm, 70 cm, and 7.5 m wavelengths on the Moon (*Thompson et al.*, 2006). Nevertheless, the radar loss tangent (*Watters et al.*, 2007; *Carter et al.*, 2008) has been used in conjunction with pedestal craters at the MFF perimeter and morphologic similarities with polar layered deposits to favor a km scale deep $H_2O_{(s)}$ - fine material matrix model (e.g., *Schultz*, 2007).

6.4.2 Thermal Observations

The bulk physical properties inferred for RAVE with radar reflectivity may be characterized more descriptively with observations at Thermal Infrared (TIR) and VNIR wavelengths. As expected, the TIR rock areal fraction, albedo, and thermal inertia maps, which we discussed in Section 6.3.3, highlight RAVE and the surrounding CSRs as those dominated by fine material. That is, the general

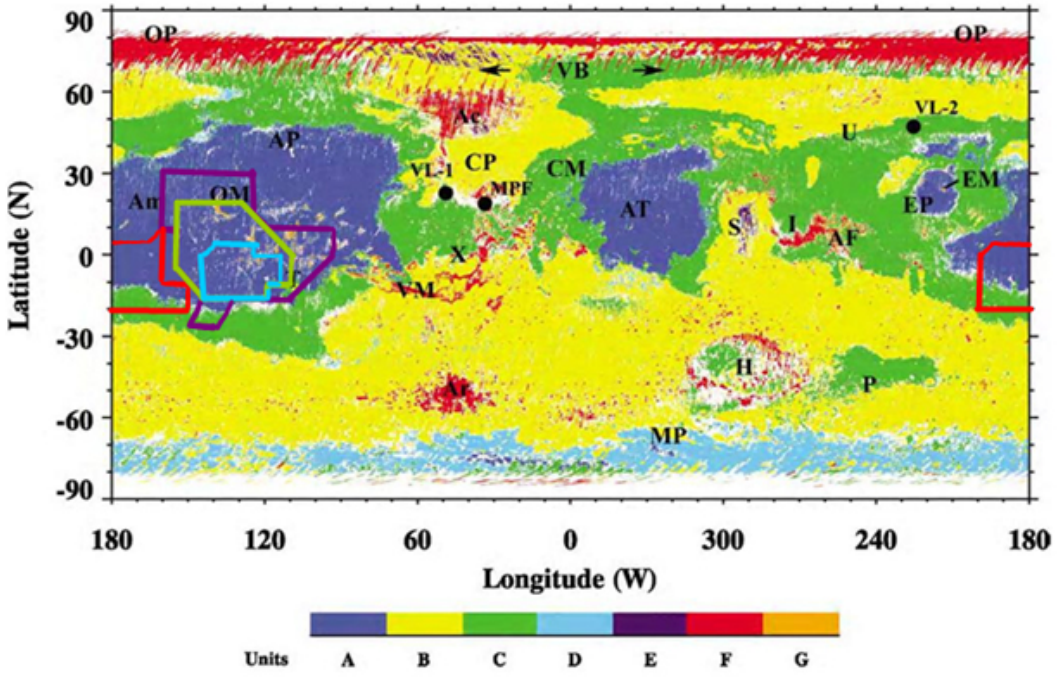

Figure 6.20: Sketch of RAVE (sky blue line) overlaid on the thermal inertia - albedo unit map (*Putzig et al.*, 2005, adapted from Figure 5). RAVE is contained entirely within the low thermal inertia - high albedo unit (blue) as is the bulk of the two surrounding CSRs. These are $\{ClSiED1.5s15°\}$ outlined in lime and $\{ClSiED1s15°\}$ outlined purple. The $\{ClHEE1s15°\}$ to the west is outlined red. The nearby high thermal inertia and medium albedo unit is colored green.

area is marked by very low rock abundance, thermal inertia, and very high albedo. In particular, RAVE is entirely contained within one of the low thermal inertia - high albedo units as delineated with the TES (Figure 6.20) (*Putzig et al.*, 2005). On the basis of apparent thermal inertia, *Putzig et al.* (2005, Sec. 3.2.1 and Fig 5 unit A) infer the fine material on the RAVE surface to be particles no greater than 40 μm across. We loosely call this coarse-to-medium silt on the Wentworth scale (`http://search.eb.com/eb/art-61244`) "dust".

Diurnal and seasonal variations in apparent thermal inertia have indicated

that hardpan, and perhaps even duricrust, is ubiquitous on the planet at ≈ 3 km spatial resolution occur

6.4.3 Surficial Morphology

We utilize HiRISE images to further characterize the radar and thermal implications that bulk RAVE has a low density (Section 6.4.1) with indurated material shallowly buried beneath dust (Section 6.4.2). The spatial distribution of the 50 HiRISE images that we viewed within RAVE is shown in Figure 6.11 along with identifiers in Table 6.5. Even though HiRISE images are available over most GS bins within RAVE, the sampling frequency is non-random (Figure 6.11) as the targeting was guided not by our work, but by research interests of the HiRISE team. Targeted imaging at additional locations within RAVE in the future should reveal whether there has been a resulting sampling bias. Nevertheless, the morphology of the broader region (Figure 6.11) has already been discussed by others, including *Bridges et al.* (2007); *Bridges et al.* (2008); *Keszthelyi et al.* (2008). In general, the tens-to-hundreds of meter scale topography of the broader area is obscured by a mantle of material of particles too fine to be resolved by HiRISE (*Bridges et al.*, 2007; *Keszthelyi et al.*, 2008) and its predecessor, the Mars Orbiter Camera (MOC) (e.g., *Bradley et al.*, 2002).

A bedform that is ubiquitous in the broader area resembles a fishing net draped over the surface (Figures 6.21 and 6.22), and is consequently coined a "reticulate bedform" (*Bridges et al.*, 2008) and (Bridges, Nathaniel T. et al., 2008b, "Dust Aggregate Bedforms and "Duststone" in Low Pressure, Low Gravity Environments: Evidence From High Resolution Imaging of Mars", submitted to

Table 6.5: HiRISE image identifiers, approximate coordinates (East longitude), image tags used in all figures and tables of this work, and map projected scale (resolution). North is up in all HiRISE figures. Continued in Table 6.6.

HiRISE identifier	Latitude	East longitude	Image tag	Resolution (cm/pixel)
PSP_001511_1730	−7°	−129.6°	1	25
PSP_001656_1835	3.3°	−126.3°	2	25
PSP_002157_1715	−8.4°	−119.9°	3	50
PSP_002289_1725	−7.3°	−123.8°	4	25
PSP_002764_1800	0°	−133.1°	5	25
PSP_002922_1725	−7.3°	−123.8°	6	25
PSP_003410_1840	3.8°	−129.9°	7	50
PSP_003647_1745	−5.5°	−118.6°	8	25
PSP_003832_1840	3.8°	−129.9°	9	50
PSP_004056_1735	−6.4°	−125.4°	10	25
PSP_004201_1735	−6.6°	−123.9°	11	25
PSP_004346_1755	−4.3°	−121.8°	12	25
PSP_004412_1715	−8.6°	−123.6°	13	25
PSP_004570_1705	−9.6°	−116.9°	14	50
PSP_004689_1765	−3.6°	−125.8°	15	25
PSP_004702_1705	−9.4°	−120.6°	16	25
PSP_004768_1705	−9.4°	−121°	17	25
PSP_004781_1710	−9°	−117.5°	18	50

Table 6.6: HiRISE image identifiers, approximate coordinates, image tags in our work, and map projected scale (resolution) continued from Table 6.5. Continued in Table 6.7.

HiRISE identifier	Latitude	East longitude	Image tag	Resolution (cm/pixel)
PSP_004847_1745	−5.5°	−118.6°	19	25
PSP_004913_1735	−6.3°	−121°	20	25
PSP_005058_1720	−7.8°	−119.7°	21	25
PSP_005071_1775	−2.7°	−115°	22	25
PSP_005124_1705	−9.2°	−120.3°	23	25
PSP_005203_1730	−6.7°	−119.5°	24	25
PSP_005256_1735	−6.6°	−123.9°	25	25
PSP_005296_1705	−9.3°	−137.8°	26	25
PSP_005349_1665	−13.4°	−143.9°	27	50
PSP_005375_1675	−12.5°	−134.8°	28	25
PSP_005414_1735	−6.5°	−120°	29	25
PSP_005467_1700	−9.8°	−125.7°	30	50
PSP_005612_1700	−9.9°	−125.5°	31	50
PSP_005625_1730	−6.7°	−119.5°	32	25
PSP_005665_1800	0°	−133.1°	33	25
PSP_005691_1685	−11.3°	−121.1°	34	25
PSP_005770_1745	−5.5°	−118.6°	35	25
PSP_005783_1775	−2.7°	−115°	36	25

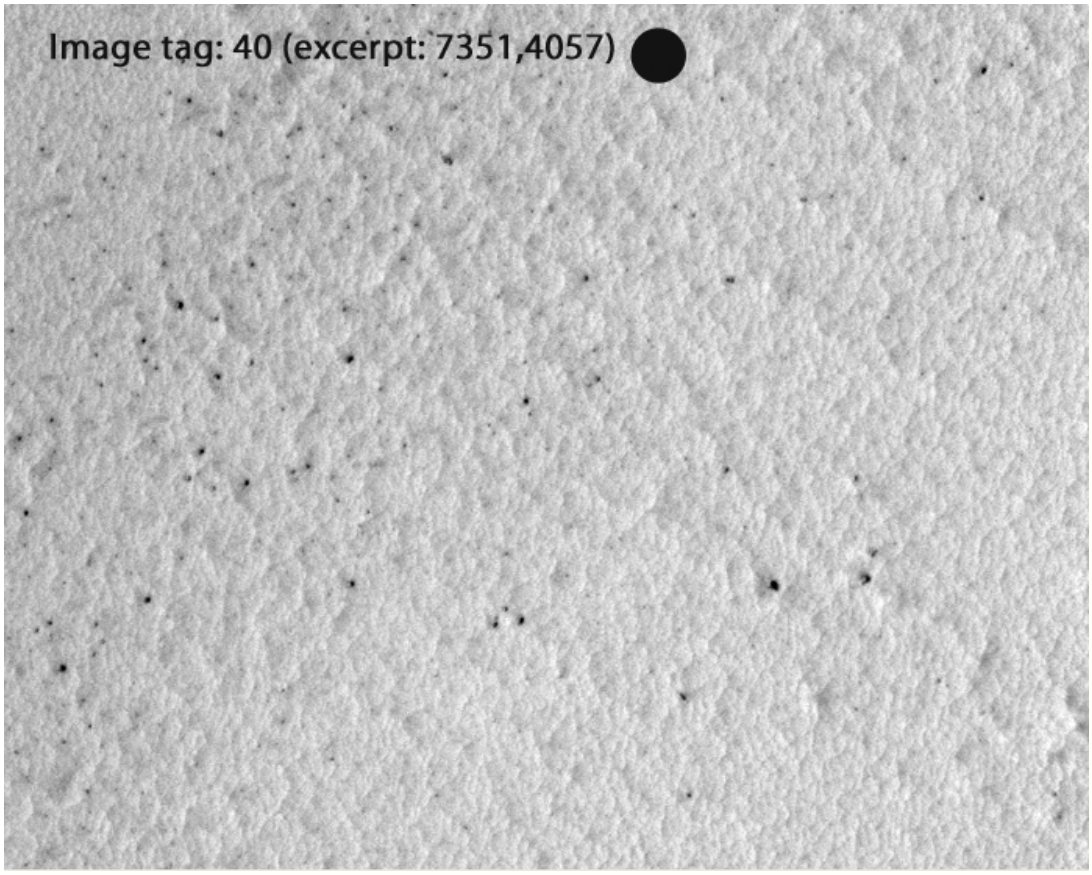

Figure 6.21: Examples of reticulate bedforms within RAVE in grayscale, continued in Figure 6.22. Image tags identify the approximate locations in RAVE as shown in Figure 6.11, with corresponding HiRISE image details in Table 6.5. Coordinates of each excerpt indicate its approximate location within the larger HiRISE image. Solid black circles are 10 m across while the glassy circles are 20 m across. Excerpt tagged 40 shows the generally subdued nature of reticulate bedforms away from Arsia, unlike surfaces on the flanks and caldera shown in the excerpts tagged 3, 8, and 16. Excerpt 3 is also a good example of prominent "honey-comb" shaped reticulate bedforms, while 8 shows the "accordion" distortion. The close spatial association of potential star dunes and reticulate bedforms on a crater (560 m across) floor just south of RAVE is apparent in the excerpt tagged 51.

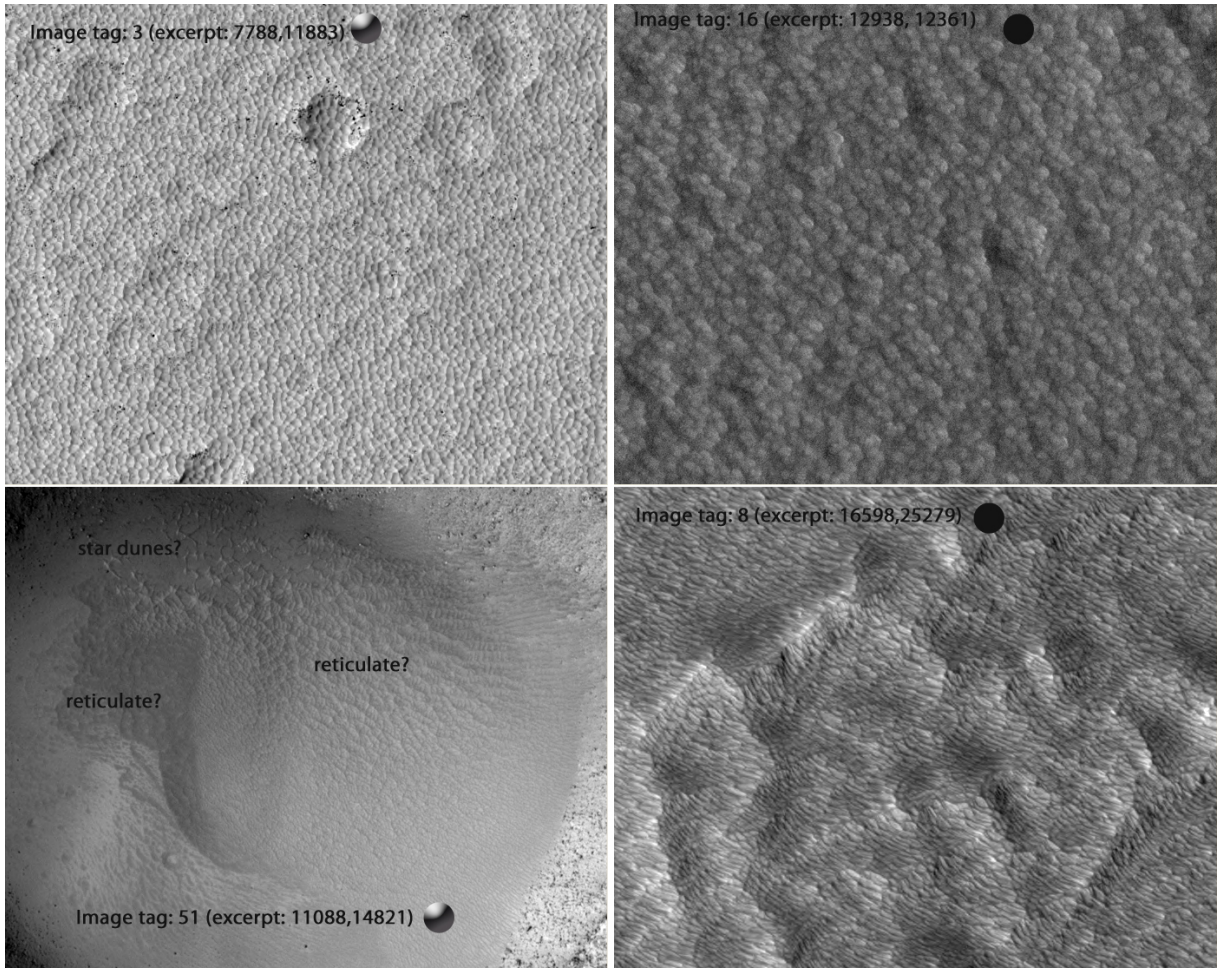

Figure 6.22: Examples of reticulate bedforms within RAVE in grayscale continued from and as described in Figure 6.21.

Table 6.7: HiRISE image identifiers, approximate coordinates, image tags in our work, and map projected scale (resolution) continued from Table 6.6.

HiRISE identifier	Latitude	East longitude	Image tag	Resolution (cm/pixel)
PSP_005836_1735	−6.3°	−121°	37	25
PSP_005902_1700	−10°	−122°	38	50
PSP_005915_1720	−7.8°	−117°	39	25
PSP_005916_1665	−13.3°	−143.7°	40	25
PSP_005942_1825	2.5°	−135.9°	41	25
PSP_005995_1700	−9.7°	−141.8°	42	25
PSP_006192_1700	−9.8°	−120.4°	43	25
PSP_006601_1825	2.4°	−129.3°	44	25
PSP_006680_1740	−6.2°	−125°	45	25
PSP_006693_1755	−4.3°	−120.8°	46	25
PSP_006759_1700	−9.9°	−121.1°	47	25
PSP_006773_1735	−6.4°	−144.2°	48	25
PSP_006878_1805	0.3°	−132.1°	49	25
PSP_006904_1755	−4.3°	−120.8°	50	25
PSP_003331_1580	−21.6°	−130°	51	50

the Geological Society of America Joint Session - Developments in Aeolian Research: Bridging the Interface between Soil, Sediment, and Atmosphere). The ridges delineate nested patterns, leading to reticulation at meter, tens of meter, and hundreds of meter size scales as described by *Bridges et al.* (2008). This bedform type is present almost exclusively within low thermal inertia regions that include RAVE, and resembles the surficial morphology of some yardangs such

Table 6.8: Long and short axis lengths of lenticular bedforms estimated using the samples shown in Figure 6.23. The image tag identifies detailed information of each HiRISE image in Table 6.5 and the location in Figure 6.11.

Lenticular type	Image tag	Long axis (m)	Short axis (m)
Smallest	7	8–9	3–4
Small	7	10–13	7–8
Typical	7	29–39	12–13
Largest	26	134–199	44–60

as those in Valles Marineris and White Rock within Pollack Crater (*Bridges et al.*, 2008; *Keszthelyi et al.*, 2008). The association with low thermal inertia surfaces and yardangs has been interpreted to indicate an eolian origin to reticulate bedforms (*Bridges et al.*, 2008). The similarity with yardangs and some light-toned bedrock (Bridges, 2008b, submitted) may indicate that reticulate bedforms are indurated, perhaps to the point of being duricrust (e.g., *Pain et al.*, 2007). While present throughout RAVE, we find this bedform to be pervasive and more easily discernable primarily on the flanks and caldera of Arsia Mons. Farther out, it becomes more subdued by a veneer of fine material as shown in Figure 6.21.

A second type of bedform, more common within RAVE than reticulate bedforms, consists of en echelon (with parallel long axes) teardrop to lens shaped hollows, such as the examples in Figure 6.23. We term these "lenticular bedforms." Nested lenticular bedforms are present in some localities, while others contain degraded ones. We use the samples in Figure 6.23 to estimate the long and short axes lengths of these bedforms as listed in Table 6.8. If eolian in origin, these bedforms could be deflation hollows. At 1:8 and coarser scale, surfaces dominated by lenticular bedforms bear a braided appearance, remarkably

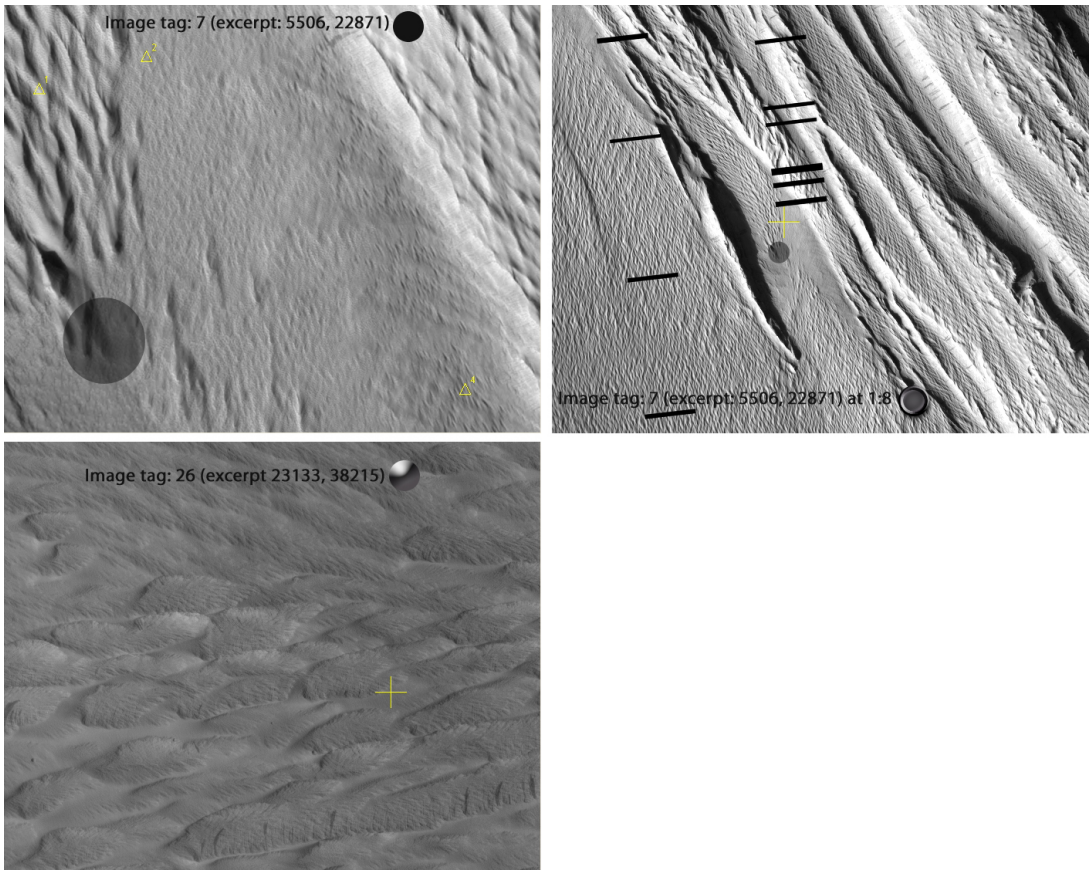

Figure 6.23: Examples of lenticular bedforms that occur at varying size scales within RAVE. Solid black circle is 20 m across, the glassy circle 40 m across, and the dimpled solid circle 160 m across. Excerpt tagged 7 illustrates the transitions among typical (marker 1), small (marker 2), and smallest (marker 4) lenticular bedforms. The surface texture of the same excerpt at coarse scale on the right is comparable to the bidirectional yardangs in the MFF as viewed by the MOC (*Bradley et al.*, 2002, Fig 10), and indicates that the long axes are oriented parallel to the fossae. For correspondence, dark ovals identify the same location in the fine (left) and coarse (right) scale excerpts. Excerpt tagged 26 contains some of the largest lenticular bedforms in RAVE.

similar to those in the MFF that *Bradley et al.* (2002, Section 5 Para. 22, 26 Fig 10) analyzed as bidirectional yardangs (Figure 6.23). They inferred that should the MFF be primarily composed of scoriaceous deposits, the bidirectional yardangs reflect cooling joints controlling eolian erosion in places.

In addition to the reticulate and lenticular bedforms, we are able to identify three other types of surface morphologies within RAVE. All three bear a strong similarity to terrestrial eolian formations - linear, barchanoid/transverse ridges, and ripples - as illustrated in Figure 6.24. The ripples are particularly difficult to discern due to their small size (ripple wavelengths average 1.7 m) except where illuminated obliquely. Could all five types be primarily eolian in origin? The last three appear clearly eolian due to their strong similarity to terrestrial dune formations, with the barchanoid/transverse ridges in particular comprising the largest equatorial dune field on the planet (*Edgett*, 1997, Fig 1 Item B). These three are sometimes interspersed with the two dominant bedforms - lenticular and reticulate as in Figure 6.25. Such a nearly seamless transition from barchanoid, to ripples, to reticulate bedforms that we observe reinforces the possibility that reticulate bedforms are eolian in origin, which is likewise supported by a transition between linear and reticulate bedforms (Figure 6.25). Lastly, the transition between lenticular and reticulate bedforms across a narrow gap connecting two pits shown in Figure 6.25 is consistent with an eolian origin to the lenticular bedforms. Such gaps are particularly likely to exert local topographic control on eolian turbulence.

The distribution and variations of lenticular bedforms lend additional support to an eolian origin. Where present among fossae, their long axes are generally oriented parallel to topographic ridges (Figure 6.23), consistent with the

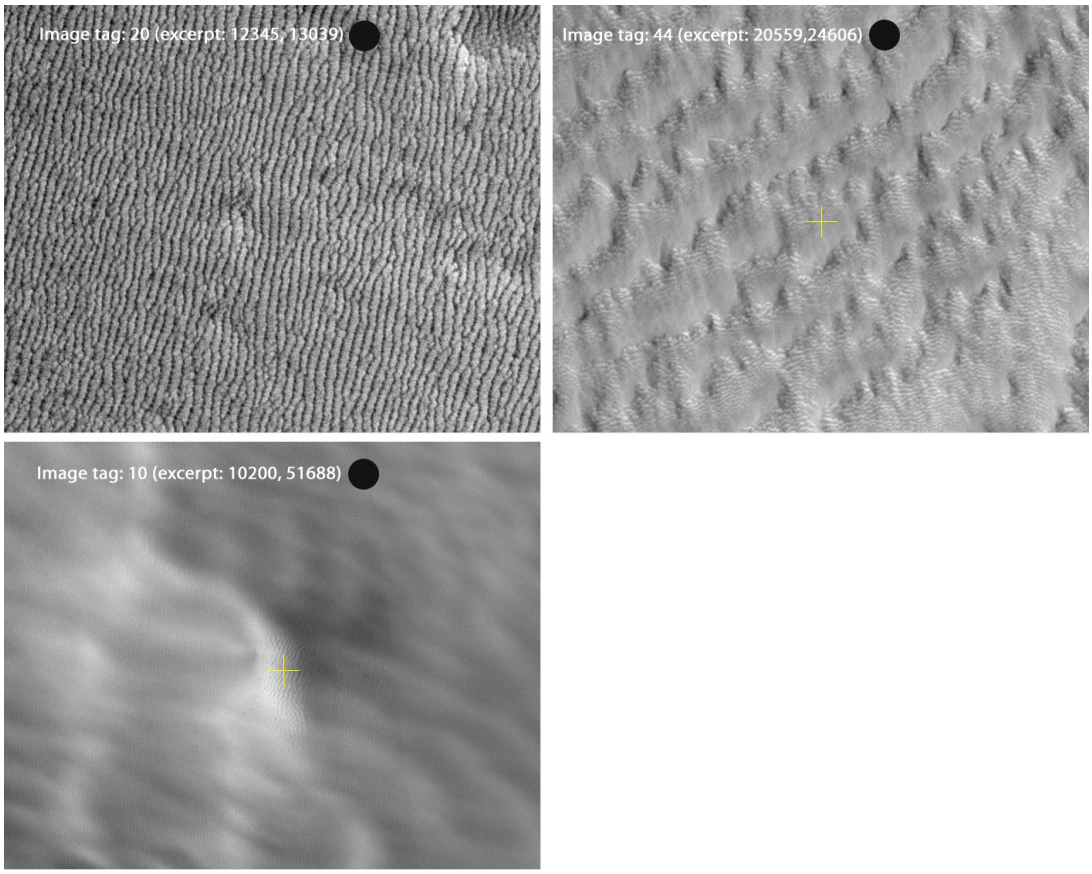

Figure 6.24: Examples of additional surface morphologies within RAVE. Solid black circles are 10 m across. Excerpt tagged 20 shows tentatively linear bedforms, 44 shows barchanoid ridges, and 10 shows ripples. The distinction between 20 and 10 is subtle, suggesting that what we consider to be linear bedforms may in fact be large scale indurated ripples instead of true linear dunes.

dominant wind direction. Their seamless transition from typical sizes (Table 6.8) to smaller sizes, separated by degraded ones of the former (Figure 6.23) may also reflect eolian modification at several different spatial scales. Variations of reticulate bedforms, typically between symmetric "honeycomb" and distorted "accordion" shapes (Figure 6.21) (*Bridges et al.*, 2008) as well as potential similarities with star dunes further reinforce an eolian origin. In fact, a crater floor about 7° south of the RAVE perimeter shows tentative evidence of a transition

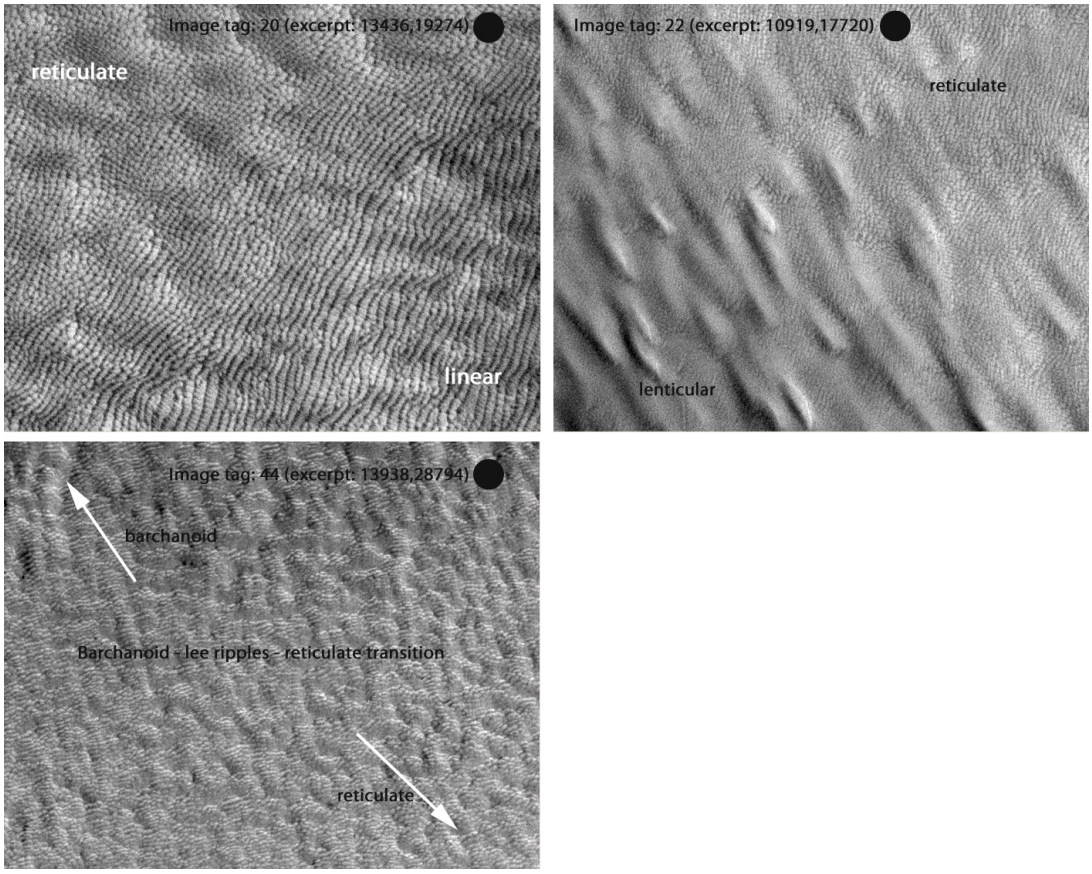

Figure 6.25: Potential transitions among bedforms. Solid black circles are 10 m across. Excerpt tagged 20 indicates a potential transition between reticulate and linear bedforms, and 22 between lenticular and reticulate bedforms across a topographic gap (imperceptible at fine resolution). Excerpt tagged 44 is a potential transition area among barchanoid ridges with ripples on their lee sides, and reticulate bedforms, with the barchanoid type dominating toward the NW beyond the excerpt border, while reticulate dominates to the SE.

between star dunes and reticulate bedforms (Figure 6.21).

Even though all five bedform types would be consistent with eolian origins, whether the requisite eolian conditions have existed at these high elevations (mostly > 2.5 km) is less clear. If the bedforms were to consist entirely of (unconsolidated) dust, current models of wind speed versus grain size to initiate saltation (e.g., *Almeida et al.*, 2008; *Merrison et al.*, 2007) pose a significant hurdle to forming any bedforms. Even electrostatic aggregation may be insufficient, as such aggregates tend to disaggregate upon entrainment (e.g., *Sullivan et al.*, 2008) leading to suspension. A reasonable possibility is that dust grains cemented into aggregates, e.g., by salts, saltated to generate the bedforms. Higher wind speeds needed in the rare atmosphere of RAVE to initiate saltation (*Greeley et al.*, 1976) may be achieved by a combination of turbulence due to local topography, katabatic winds from nearby volcanoes (e.g., Bridges, 2008b, submitted), and equatorial east-to-west winds (e.g., *Benson et al.*, 2006, Section 3.2) that are independent of obliquity (e.g., *Keller et al.*, 2006b, para 45). Nevertheless, recent models indicate that once initiated, saltation of sand-sized particles/aggregates may be sustained at speeds as low as $1\ \mathrm{ms}^{-1}$ (*Almeida et al.*, 2008; *Merrison et al.*, 2007).

Presuming an eolian origin to all five bedforms in RAVE, are they currently active or inactive? *Edgett* (1997) inferred that the barchanoid/transverse dune field within RAVE is inactive due to burial by dust. Alternatively, armoring or exhaustion of particles suitably sized for saltation (e.g., *Sullivan et al.*, 2008) may have inactivated these bedforms. Another possibility is that the dune analogs are not measurably active over the lifetime of Martian missions, since the time scales for dune migration on Mars may be longer by a factor of 10^4 than their ter-

restrial counterparts (*Claudin and Andreotti*, 2006, Section 4). While poorly constrained, this translates to migration times as long as tens (*Claudin and Andreotti*, 2006, Section 4) to several thousand (*Almeida et al.*, 2008, p. 6225) years per meter. It may also explain why only a few active dunes have been observed on Mars in recorded history in spite of their ubiquity (*Bourke et al.*, 2008). Obviously, a spatially varying combination of indurated bedforms, inactivated dunes, and active dunes is also possible.

However, we find a different scenario to be more likely within RAVE at least for the first four bedform types (reticulate, lenticular, barchanoid, and linear): induration of earlier bedforms at the level of hardpan to duricrust as opposed to just inactivation. One indication of this possibility is the similarity of reticulate bedforms to those found on the surfaces of probable duricrust such as White Rock (*Ruff et al.*, 2001) that we mentioned before. More compelling is the resistance of the bedforms to disruption by meter scale craters that postdate them (Figure 6.26). Where bedforms are disrupted by fresh impact craters, arcuate overhanging ridges are generated at least on occasion (Figure 6.26), suggesting induration to meter scale depths. These potentially indurated bedforms are unlikely to be thicker than 2 m, as *Fergason et al.* (2006b, Section 5.1) infer given the visibility of underlying decameter scale degraded impact craters. This is consistent with the protrusion of meter scale blocks in places, particularly where the bedforms appear to postdate block slides as shown in Figure 6.27.

Induration would certainly not be unusual, since duricrust in excess of many meters (*Pain et al.*, 2007) to in situ hardpan only centimeters thick (e.g., *Schatz et al.*, 2006, Para. 9) have been observed across a variety of Martian locations. Local relief related to duricrust has been identified at places as disparate as the

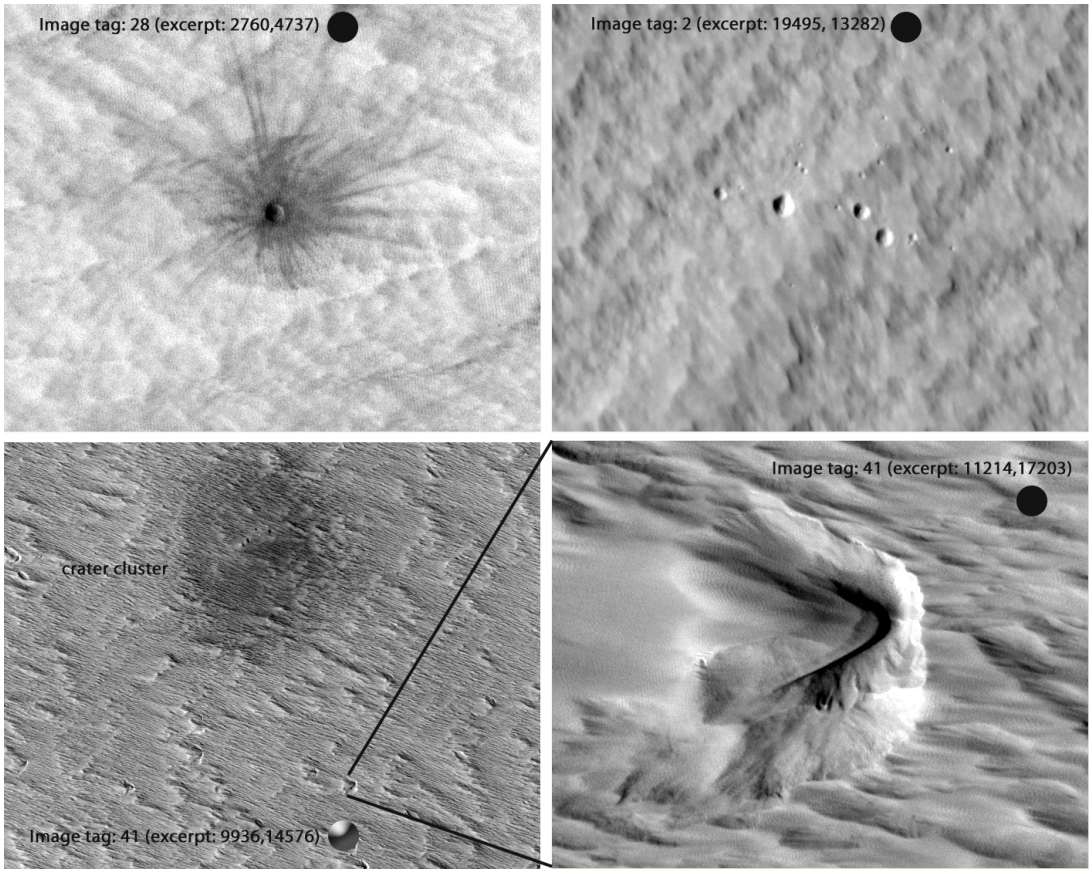

Figure 6.26: Examples that illustrate the strength of hardpan/duricrust within RAVE. Solid black circles are 10 m across, and the glassy circle is 160 m across. Excerpts tagged 2 and 28 show bedforms remaining intact subsequent to the formation of fresh impact craters (crater cluster in 2; crater ≈ 5 m across in 28). Even when bedforms were disrupted by meter scale crater forming impacts (bottom left tagged 41 at coarse scale), overhanging arcuate ridges had formed (bottom right at fine scale), indicating significant induration at meter scale depths.

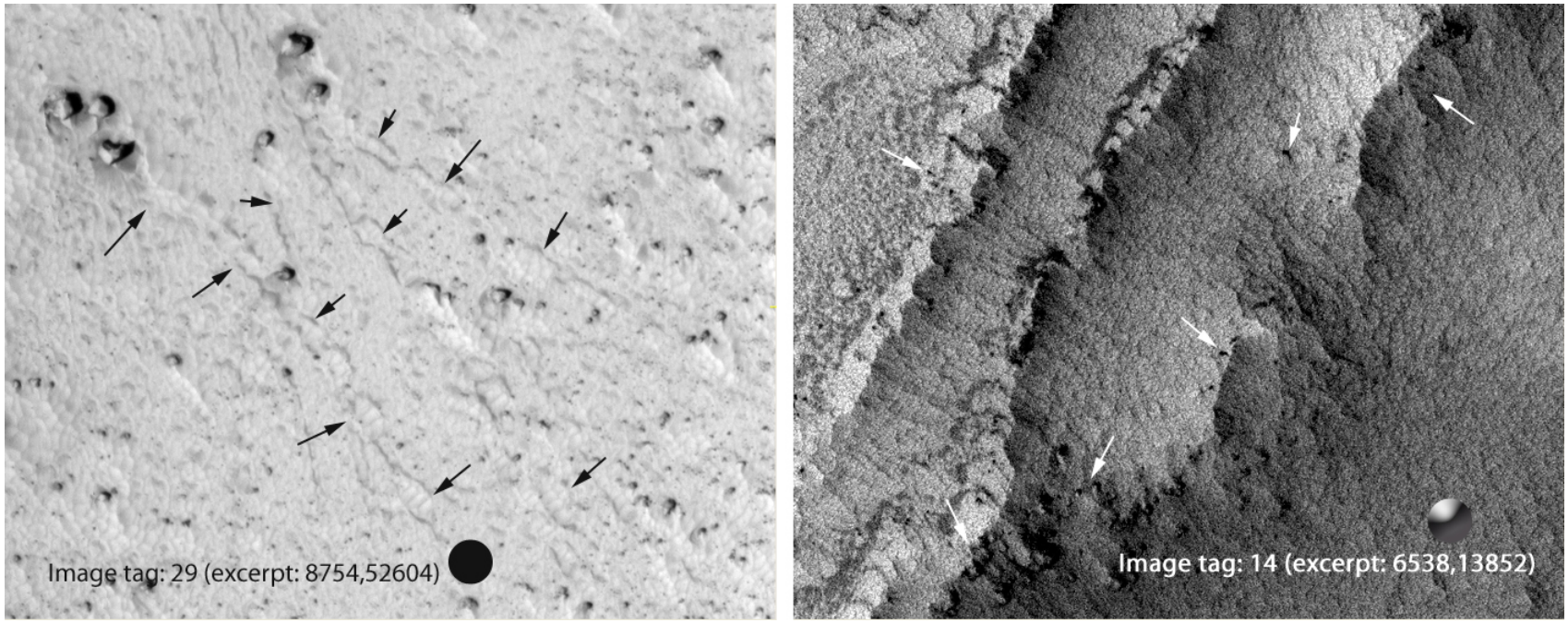

Figure 6.27: Example of block slides that predate bedform formation (left) and of blocks that protrude from the bedforms (right). Solid black circle is 10 m across and the glassy solid circle is 20 m across. The typical size of blocks constrains the thickness of the bedforms to meter scale.

flanks of Olympus Mons, Valles Marineris, and Arabia (*Pain et al.*, 2007, Fig 3). Such observations are bolstered by TIR observations as well, as we discussed in Section 6.4.2.

We posit further that what we infer to be hardpan/duricrust bedforms are likely buried beneath a veneer of dust, as evident in the low apparent thermal inertia of the RAVE surface (Section 6.4.2). The presence of km scale albedo banding, kilometers long potential dust devil tracks (active dust devils have been imaged in the general area as described by *Cantor et al.* (2006) and *Cantor* (2007) even though most dust devils occur within the $45 - -75$ N/S latitude bands (*Whelley and Greeley*, 2008)), and slope streaks of varying length scales that do not disrupt the bedforms make a strong case for such a veneer. As evident in Figure 6.28, these features generally fail to show discernable topographic effects in HiRISE images despite some exceptions (Figure 6.28, top left), suggesting that the dust veneer is unlikely to be thicker than some fraction of the 37.5 cm – −75 cm HiRISE PSF (Section 6.2.3).

The surficial morphology that we have discussed so far with HiRISE images appears to converge with inferences made with radar reflectivity (Section 6.4.1) and TIR observations (Section 6.4.2) that RAVE may consist mostly of one to two meter thick hardpan/duricrust - possibly with sulfate salts as cementation agents (consider *Pain et al.*, 2007, p. 486) - bedforms that are buried by dust shallower than the tens of centimeter sampling depth of the GS. In subsequent sections, we seek to constrain induration processes and the origin of the overall subsurface within RAVE by considering potential roles of volcanism, glaciation, and climate in the context of GS-derived chemistry.

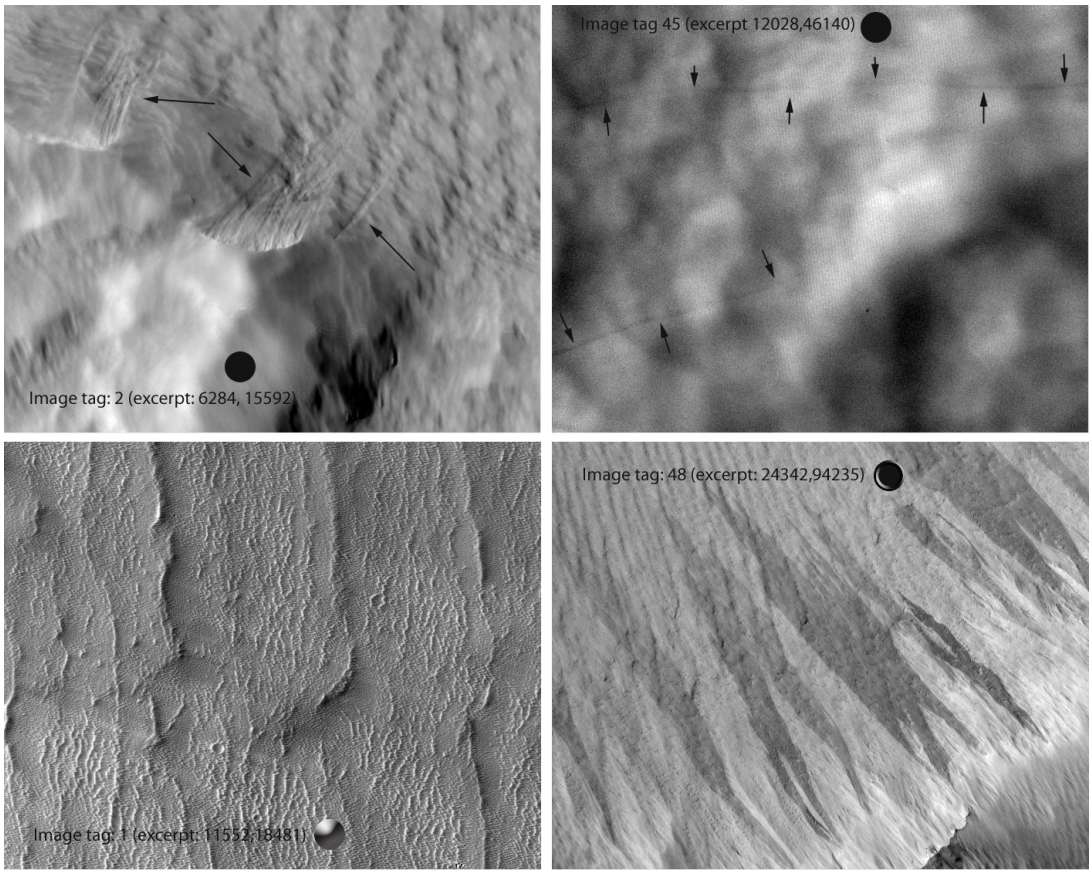

Figure 6.28: Examples of surficial features distinguishable only by albedo with little if any distinctive textures in HiRISE images within RAVE: Albedo banding oriented W-NW and E-SE visible in excerpt tagged 1, dust devil tracks in 45, and slope streaks in 48. However, potential avalanche scars that are distinct in topography but not albedo are also present as identified in excerpt tagged 2. Solid black circles are 10 m across, the dimpled solid circle is 40 m across, and the glassy solid circle is 160 m across.

6.4.4 Age of Volcanism

As shown in Figure 6.11, the closest volcanoes to RAVE are Arsia Mons, Biblis Patera, Pavonis Mons, Ulysses Patera, Olympus Mons, and Ascraeus Mons, in the order of increasing distance. With the exception of Biblis Patera and Ulysses Patera, which are inferred to be no younger than Hesperian in age (older than

≈ 1.9 Ga) (*Plescia*, 1994), volcanism in the remaining edifices may be as recent as late Amazonian (e.g., *Neukum et al.*, 2004). However, late-stage volcanism was probably not as extensive or voluminous as it was in Late Hesperian/Early Amazonian (*Dohm et al.*, 2002; *Scott and Dohm*, 1997). RAVE is essentially surrounded by the largest cluster of the highest volcanoes on the planet. Given the low areal density of impact craters (e.g., *Edgett*, 1997, p. 108) within RAVE, the younger Amazonian volcanic events may be more relevant to the evolution of its surface.

In fact, most of the underlying mapped geologic units of RAVE are Amazonian in age and volcanic in origin (Figures 6.14 and 6.19) with the possible exception of slide deposits on the W flanks interpreted by some to be of an Amazonian glacial origin (Section 6.4.5) suggesting that the surficial bedforms overlying them are even more recent. Specifically, sections of the Olympus Mons and Ascraeus caldera floor complexes may be as young as 100 Ma, and that of Arsia ≈ 130 Ma (*Neukum et al.*, 2004). While significant uncertainties exist (e.g., *McEwen et al.*, 2005), some of the lava flows on the Olympus Mons scarp have been estimated to be as recent at 2.5 Ma (*Neukum et al.*, 2004). The large-scale shape of most of these volcanic edifices and lava flow morphologies suggest that they are shield volcanoes with low-viscosity lava flows akin to the Hawaiian type (e.g., *Dohm et al.*, 2008, Section 2.3).

However, a host of features including putative cinder cones at the Pavonis Mons summit (*Mouginis-Mark*, 2002, Para. 3) and southern flank (*Keszthelyi et al.*, 2008, para 30-31 and Fig 6(c)), pit craters at elevations 5 km – 7 km below caldera rims (*Mouginis-Mark*, 2002, Table 1) (Figure 6.29), and edifice morphometry along with theoretical implications of magmatic gas expansion in a

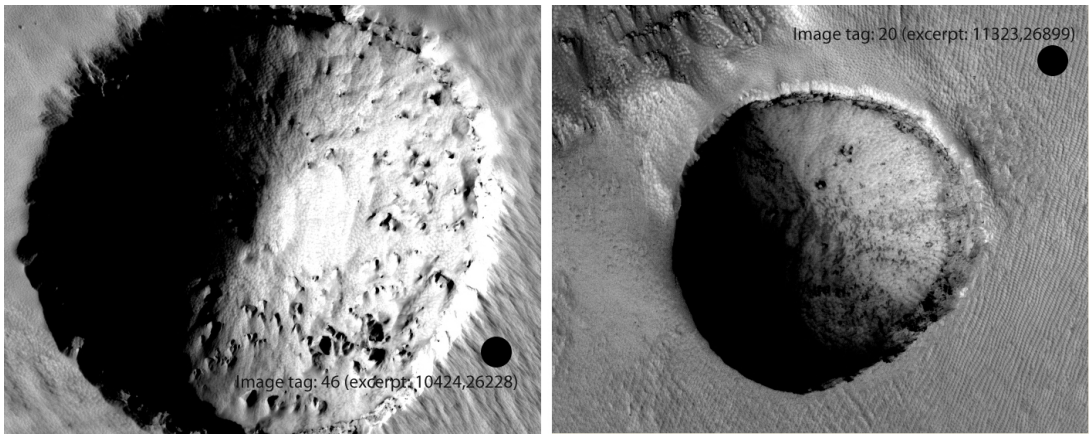

Figure 6.29: Examples of pit craters within RAVE, about 314 m across tagged 46 and ≈ 200 m across tagged 20. Solid black circles are 20 m across.

low-density atmosphere suggest that the Tharsis/Olympus volcanoes may be composite volcanoes (synopsis by *Hiesinger et al.*, 2007). In addition, deposits within the MFF, Candor chasm, Ophir chasm, and Arabia Terra have been interpreted to be constructs of Tharsis basaltic plinian eruptions occurring as recently as the late Amazonian (*Hynek et al.*, 2003). Olympus Mons eruptions may have also transitioned from less viscous, stable, and long-lived tube-forming systems to more viscous, episodic, and less stable channel-forming systems in the late Amazonian (*Bleacher et al.*, 2007). A higher abundance of channels relative to tubes is often characteristic of pyroclastic eruptions entailing greater volatile content (*Bleacher et al.*, 2007, Para. 30). Consistent with such inferences, lenticular bedforms in RAVE may reflect physical strength variations due to cooling joints in tephra (Section 6.4.3).

If explosive basaltic volcanism is a main contributor to the surficial material within RAVE, theoretical clast sizes upon eruption would be tens of μm to a few mm, while accretion (along with significant hydration) may lead to sizes between 0.1 and 1 mm upon deposition with less welding than on Earth (*Wil-*

son and Head, 2007, Section 5, 7). The scoriaceous tephra/ash would grade to more sorted finer and thinner deposits with distance from the vent or eruptive column with dispersal varying from 20 km (for mm clasts) to $> \times 10^4$ km (for clasts $< 50\,\mu$m) (*Wilson and Head*, 2007, Section 6, 7). Even though source vents have not been identified, *Hynek et al.* (2003) infer the layers to get thinner with distance from Tharsis. Another possible source of surficial material could be similar fragments produced through the massive flank failure processes which are interpreted to have occurred to Olympus Mons flanks producing its aureole deposits (*Morgan and McGovern*, 2005; *McGovern et al.*, 2004; *Tanaka*, 1985). Such massive movements would produce tremendous amount of material of the spatial extent discussed earlier, which could then be transported aerially to our region of interest.

Even if only some of the preceding interpretations were correct, significant pyroclastic deposits such as scoria and basaltic ash may have been present surficially, reworked chemically (particularly given significant hydration of lapilli) and mechanically into fine material, and distributed regionally from the flanks of the volcanoes into our region. Such regional dispersal would also be consistent with the current GCM simulations (Section 6.4.6). While such surficial volcanic contributions may be possible, it is important to remember that the volcanic units underlying RAVE (Figure 6.19) are probably too deeply buried to generate a signature in the γ or TIR spectra (Sections 6.4.2 and 6.4.3). Nevertheless, chemical composition of the overlying deposits may be influenced by these units (cf. *Newsom et al.*, 2007).

6.4.5 Glaciation

Akin to volcanic units in RAVE, any glacial $H_2O_{(s)}$ units are likely buried too deep to be evident as a strong enrichment in the GS stoichiometric H_2O map. In fact, RAVE is not particularly remarkable in H_2O (Figure 6.9) as we discuss later in Section 6.5 and only a tenuous spatial link exists between putative relict glaciers and interpolation of NS-based H maps (*Elphic et al.*, 2005, Fig 1). Nevertheless, any relict glaciers that are present nearby may have indirect chemical and physical effects though perhaps not as pronounced as inferred on the basis of long-wavelength radar reflectivity at km depth scales for the MFF (Section 6.4.1).

Relict glaciers have been hypothesized to exist primarily NW of each of the volcanoes, consistent with precipitation under higher obliquity (e.g., *Forget et al.*, 2006, Fig 1) and with compelling morphologic similarities to Antarctic piedmont glaciers (e.g., *Shean et al.*, 2007; *Russell and Head*, 2007, p. 327). The largest among them, extending 350 km (e.g., *Head et al.*, 2005, p. 348 bottom) along the NW flank of Arsia, lies in the SW portion of RAVE and may have formed as recently as 65 Ma ago (*Shean et al.*, 2007). The corresponding surface area and volume are estimated to be 166×10^3 km^2 and 3×10^5 km^3, respectively (*Shean et al.*, 2007, Para. 16).

As discussed in Section 6.4.1, incidental evidence for much larger ice-rich deposits encompassing the MFF include pedestal craters, radar loss tangent values, and layered terrain - all of which show more than a passing similarity to their counterparts in the polar layered terrain (e.g., *Schultz*, 2007). RAVE does contain pedestal craters at the periphery, examples of which are shown in Figure 6.30. *Kadish et al.* (2008) have argued that pedestal craters form only on

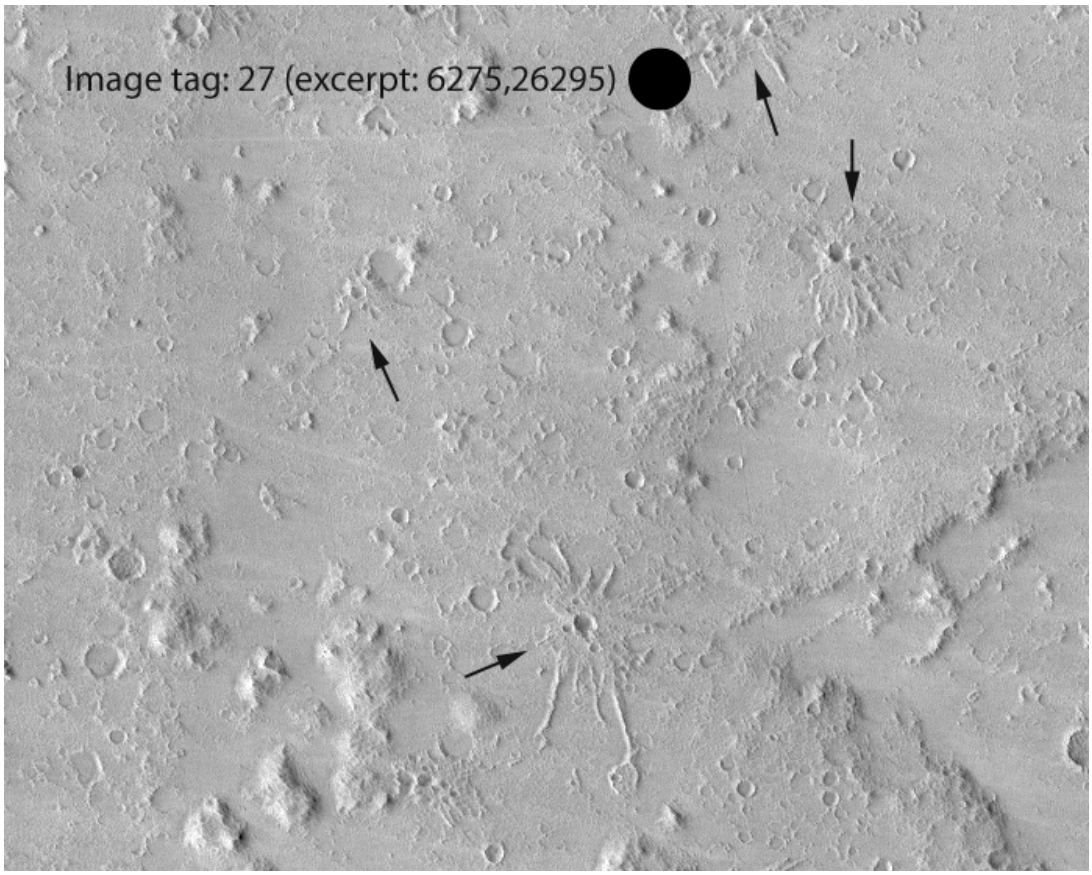

Figure 6.30: Example of pedestal craters at the southwestern periphery of RAVE may imply the presence of ground ice (*Kadish et al.*, 2008). Solid black circle is 80 m across.

volatile-rich substrates, on the basis of morphologic evidence and their occurrence only at high latitudes, except for the examples in RAVE and in the adjacent MFF.

Large scale flow features associated with the largest graben in RAVE have been interpreted by *Shean et al.* (2007, Fig 4) to indicate underlying relict piedmont glaciers. They also estimated that a meters-thick debris cover could have prevented significant sublimation of an underlying ice matrix as thick as 300 m over the last 50 Ma (*Shean et al.*, 2007, Para. 65). Features on the flank of Olympus Mons have also been interpreted as evidence of hydrothermal activity in

the presence of $H_2O_{(s)}$ (*Neukum et al.*, 2004, p. 977). Such hydrothermal activity could have generated a regional supply of sulfates and other salts, perhaps analogous to the Paso Robles soils on the Columbia Hills in Gusev Crater (*Yen et al.*, 2008), that were episodically transported and incorporated into the surficial material of RAVE.

6.4.6 Climate

Glacial hypotheses are underpinned by the Martian climate cycle which is in turn significantly affected by the obliquity cycle. While the temporally chaotic nature of Martian obliquity prevents precise retrograde modeling to Hesperian and older eras, variations within the last tens of Ma relevant to our investigation of RAVE (Section 6.4.4) may be modeled quite precisely (*Laskar et al.*, 2004). Such modeling indicates that obliquities of 42° and higher were more likely than the current value, with the most recent such occurrence ≈ 5 Ma ago (*Laskar et al.*, 2004, Section 3.2.1, 3.2.2, Fig 9, 10a). Assuming an atmospheric volatile budget including polar volatiles similar to that of current Mars, *Forget et al.* (2006, p. 370) model global circulation to estimate that $20\,\mu$m – $50\,\mu$m scale $H_2O_{(s)}$ (cf. $6\,\mu$m – $8\,\mu$m in current Tharsis clouds) would precipitate at column rates of 30 mm/a–70 mm/a. Such high rates of precipitation would be capable of generating hundreds of meters thick glaciers within a few ka (*Forget et al.*, 2006, p. 370). Global Circulation Models (GCMs) would be consistent with the hypothesized relict glaciers particularly since the predicted precipitation is localized over them (*Forget et al.*, 2006, p. 370). Given these retrograde predictions of high precipitation rates, it is quite likely that regionally pervasive ground ice would have accumulated throughout RAVE in addition to the spatially local-

ized glaciers.

In conjunction with high precipitation, instances of higher obliquity on Mars would have caused net deposition of atmospheric dust throughout RAVE and the broader Tharsis region (Figure 6.11) as predicted by GCMs (*Haberle et al.*, 2006, Para. 14). Along with dust deposition, high precipitation may have contributed to glaciation, aqueous chemical processes, and the formation of complex surficial bedforms such as those potentially buried beneath a veneer of dust that we discussed in Section 6.4.3. Such formation would have been facilitated by a significantly denser atmosphere lowering the threshold speeds for entrainment and saltation of particles (*Greeley et al.*, 1976) - even if the current polar deposits were the sole sources of CO_2 - under higher obliquities as well (*Manning et al.*, 2006).

The current 25° Martian obliquity does not lead to high precipitation within or in the neighborhood of RAVE. Nevertheless, present atmospheric conditions entail perennial $H_2O_{(s)}$ cloud cover over the SW flank of Arsia Mons (*Noe Dobrea and Bell*, 2005), orographic $H_2O_{(s)}$ clouds over neighboring Olympus, Pavonis, and Ascraeus summits (*Benson et al.*, 2006), ground H_2O fog (*Feldman et al.*, 2005, para 27), and GCM prediction of light $H_2O_{(s)}$ precipitation (*Feldman et al.*, 2005, Fig 5). Consistent with the persistence of regional E to W winds (e.g., *Benson et al.*, 2006, Section 3.2), the $H_2O_{(s)}$ clouds are distributed W-NW over Olympus, Ascraeus, and Pavonis Mons showing interannual and seasonal variability (cloud activity between L_s = 0, Northern spring, and L_s = 220, before winter, with peak area near L_s = 100 just after summer solstice) (e.g., *Benson et al.*, 2006, Section 3.2). The collective effect of these conditions, though probably insufficient to generate pervasive aqueous solutions within the surficial material of

RAVE, may nevertheless be sufficient to create occasional concentrated brines.

Could the limited activity of any concentrated brines be affected by the precipitation or formation of $CO_{2\,(s)}$ under current conditions? Precipitation is unlikely as $CO_{2\,(s)}$ clouds are limited to the mesosphere in the midlatitudes (*Montmessin et al.*, 2006). We obtained seasonal pressure and temperature estimates from the Martian Climate Database (`http://www-mars.lmd.jussieu.fr/mars/access.html`) as developed by *Forget et al.* (2007) and *Spiga et al.* (2007) to evaluate the possibility of CO_2 frost. Seasonal frost appears to be unlikely because the temperature at which CO_2 would condense (≈ 142 K in the Arsia Mons Caldera and ≈ 146 K in the region as a function of surface pressure (e.g., *Hourdin et al.*, 1995; *Mellon et al.*, 2000; *Wing and Austin*, 2006, Eq 2; Table 1; Eq 4, respectively)) is lower than average seasonal temperatures in this area (≈ 186 K in the caldera and ≈ 198 K elsewhere). Additionally, non-polar $CO_{2\,(s)}$ deposits observed to date have all been south of $\approx -33°$ (*Schorghofer and Edgett*, 2006). Nevertheless, diurnal CO_2 frost may form at the lowest observed overnight temperatures in RAVE, since apparent "nightside" thermal inertia in some locations is less than the threshold $56\,\mathrm{J\,m^{-2}\,K^{-1}\,s^{-0.5}}$ above which CO_2 frost is unlikely to form (*Putzig and Mellon*, 2007, Fig 8).

In contrast to the net deposition of atmospheric dust over Tharsis at higher obliquities, GCMs predict a somewhat complicated dust exchange between the surface and atmosphere under the current obliquity. The flanks of the Tharsis volcanoes, of Olympus Mons, and the broader Tharsis low thermal inertia region are net deflation areas at about $1\,\mu\mathrm{m\,a^{-1}}$ (*Kahre et al.*, 2006, Para. 46), while RAVE is mostly a net deposition area (*Kahre et al.*, 2006, Para. 44, Fig 7). Based on results at 22.5 ka and 72.5 ka, GCMs also predict these conditions to prevail

over the orbital precession cycle on the order of 50 ka (*Haberle et al.*, 2006). These inferences are directly relevant to the dust veneer within RAVE in terms of particle sizes, since 1 μm – 10 μm (*Kahre et al.*, 2006, Para. 21) dust used in the GCMs is consistent with the 3 μm atmospheric dust (e.g., *Lemmon et al.*, 2004) and the $< 40\,\mu$m surficial material (Section 6.4.2).

In summary, the climatic conditions during the late Amazonian are likely to have produced complex eolian and aqueous processes. Overall, the eolian processes have led to net dust deposition on most RAVE surfaces, with perhaps some of the dust derived regionally via deflation from the flanks of nearby volcanoes and surroundings. While localized H_2O-glaciers and regionally pervasive ground ice may have persisted before 5 Ma, the recent climate has been mostly arid though moderated by ground fog and local frost.

6.4.7 Synopsis of Overviews

The preceding overviews of geology (Section 6.4.4), thermally-derived attributes (Section 6.3.3), surficial morphology at high resolution (Section 6.4.3), ground ice/glacial conditions (Section 6.4.5), and climatic conditions (Section 6.4.6) over RAVE are consistent with hardpan/duricrust bedforms that may be a meter or two thick overlain by a veneer of dust. Such bedforms could form in any one of several different ways: fine material that originated as atmospheric dust subject to cyclical deflation and deposition, though mostly deposition, over obliquity cycles; basaltic ash and chemically/mechanically altered scoriaceous deposits on the flanks of nearby volcanoes transported by regional winds; lag deposits from the sublimation of relict glacial ice and dust matrices; remnants

of regionally expansive ash fall from basaltic plinian eruptions in Tharsis; or combinations thereof.

Our overview does not effectively constrain the composition of the material cementing the bedforms, or the processes that formed them. In fact, a broad range of processes could yield the indurating salts, such as leaching alteration of dust by low-pH brines derived from volcanic degassing (i.e., acid-fogs); eolian deflation of salts that were generated under hydrothermal acid-fog conditions on the flanks of volcanoes and their subsequent deposition in RAVE; significant concentrations of salt in atmospheric dust; local production of salts via aqueous processes facilitated by buried ground ice, relict glaciers, dehydration of sulfates (e.g., *Tosca et al.*, 2008, Fig. 18), or a combination thereof as H_2O sources; and local production of salts in isochemical alteration of basaltic lapilli deposited from plinian eruptions.

Clearly, additional information is needed to elucidate and evaluate candidate processes for the origin of RAVE. To this end, we discuss chemical considerations in the succeeding sections.

6.5 Origin of RAVE: What is the Bulk Component?

The chemical constraints on the bedform material and cementation processes that we just discussed can be established by considering the distribution of GS-derived elemental mass fractions within RAVE. The first order chemical properties are obviously those of Cl enrichment and Fe and Si depletion relative to the global average. Tentatively, this may reflect a mass dilution effect since Cl can be a proxy for salts, at least on Earth, and shows a statistically significant

anticorrelation with both thermal inertia and Si mass fractions at global scales (*Keller et al.*, 2006b, and Tables 5.2 and 5.3). However, this possibility is considerably weakened by the potential dominance of sulfates, rather than halides, under Martian low-pH aqueous conditions (e.g., *Tosca et al.*, 2005, p. 129) and the lack of a strong correlation of Cl with potential cations at either Meridiani (*Clark et al.*, 2005, sec 4.2.3, 4.2.4) or Gusev (*Clark et al.*, 2007a). It is also possible that a significant fraction of the Cl substitutes into sulfate or mixed anion salts rather than forming pure chlorides. While halides have been identified tentatively with TIR spectra (*Osterloo et al.*, 2008, Fig 2), their distribution appears decoupled from and their spatial extent minute relative to the GS Cl-enriched regions.

Since the primary chemical signature of RAVE does not lead us conclusively to either minerals or chemical processes, we compare elemental mass fraction ratios within RAVE with those for the Rest Of Mars (ROM) and for several types of material that have been analyzed in situ. We retain the ROM distributions as points of reference in comparisons involving all other types. The in situ types we use are those classified as "soils" at both MER sites, including surface dust; the rocks at both MER sites; and the Shergottite-Nakhlite-Chassignite (SNC) meteorites. To ease detailed comparisons, we divide each type of material into the classes and subclasses defined by the MER team.

The primary reasons we use ratios of mass fractions in lieu of the mass fractions themselves are to circumvent any systematic differences between the GS and MER Alpha Particle X-ray Spectrometer (APXS) data (e.g., Chapter 2), and the effectiveness of ratios when comparing different material as developed by Pearce (e.g., *Winter*, 2001, p. 180). To facilitate comparisons with other chem-

ical analyses in the literature, such as Total Alkali Silica (TAS) diagrams (*Bas*, 2000), we use SiO_2 (renormalized to an H_2O-free composition for the GS) as the abscissa in our comparative plots. Unfortunately, robust comparisons are currently limited to CaO, Cl, FeO, and K_2O as the ordinates. We do not compare Al_2O_3 since its GS-derived values are being refined, H_2O as it has only been estimated indirectly by the MER mission, and Th as it is undetectable by the MER APXS. The lack of robust S estimates with the GS and Th estimates with the APXS are particularly challenging, since both elements are important when evaluating the possibility of aqueous processes (e.g., *Taylor et al.*, 2006a).

We begin our comparisons of elemental ratio distributions with the soils of Mars. Since soil and dust are loaded terms, we limit ourselves to the abiogenic definition of soil by *Banin* (2005), and our definition of dust on the basis of particle size (Section 6.4.2), which are also consistent with the terminology used by the MER team.

6.5.1 Soils of Mars

The soil classes that we use, the sols on which they were sampled by the APXS, and the literature upon which the sample selection is based - including the work by Ming et al. (2008, submitted, Geochemical Properties of Rocks and Soils in Gusev crater, Mars: Results of the Alpha Particle X-ray Spectrometer from Cumberland Ridge to Home Plate, submitted to the J. Geophys. Res., `http://www.astro.cornell.edu/team/Ming_JGR05_08SpiritAPXSmerged.pdf`) - are listed in Table 6.9. It is important to note that the chemical differences among some of these classes,

Table 6.9: Soil classes used, the sols on which they were sampled by the APXS, and legend key for Figures 6.31– 6.34. Symbolic superscripts identify the references that we used to associate the particular samples with a given class as: (unmarked)*Yen et al.* (2005, Table 1), ($*$)*Morris et al.* (2006, Fig 1, Table 1), ($\diamond$)*Morris et al.* (2006, Table 4), and ($\wp$)Ming et al. (2008, submitted, Tables 3 and 6). Gusev samples are prefixed "G", Meridiani samples "M." The trench samples that helped to validate GS estimates (ξ)(Table 2.3), average Laguna-class soil ($\wp$)(Ming et al., 2008, submitted, Table 6), average Panda class soil at Gusev ($\diamond$)(*Morris et al.*, 2006, Table 9), average Panda class soil at Meridiani ($\diamond$)(*Morris et al.*, 2006, Table 9), and average Pathfinder soil ($\aleph$)(*Foley et al.*, 2003, Table 7) are included for completeness. Continued in Table 6.10.

Soil class	Legend key	APXS sampling sol
Berry class, Mooseberry subclass	BMSoil	$^{\diamond}$M80, $^{\diamond}$M91, $^{\diamond}$M100, $^{\diamond}$M416, $^{\diamond}$M420,$^{\diamond}$M420B, $^{\diamond}$M443
Berry class, Nougate subclass	BNSoil	$^{\diamond}$M023, $^{\diamond}$M090, $^{\diamond}$M369, $^{\diamond}$M509
Eileen Dean class	ESoil	$^{\wp}$G1239, $^{\wp}$G1246

such as surface dust (*Yen et al.*, 2005) and Laguna Class - Panda Subclass soil, are subtle (e.g., *Gellert et al.*, 2006, sec 11.2 – 11.4). Nevertheless, the classification appears reasonable given its utilization of the combined constraints from Mössbauer spectra, Miniature Thermal Emission Spectrometer (Mini-TES) spectra, and MI textural information, as has been used successfully for rocks (e.g., *McSween et al.*, 2008). Pending an update to the PDS files for Gusev `http://pds-geosciences.wustl.edu/mer/mer1_mer2-m-apxs-5-oxide-sci-v1/merap_2xxx/data/apxs_oxides_mer2.csv` and Meridiani `http://pds-geosciences.wustl.edu/mer/mer1_`

Table 6.10: Soil classes used, legend key for Figures 6.31– 6.34, and the sols on which they were sampled by the APXS continued from Table 6.9. Continued in Table 6.11.

Soil class	Legend key	APXS sampling sol
Gertrude Weise class	GSoil	℘G1190, ℘G1194, ℘G1199
Laguna class, Boroughs subclass	LBSoil	◦G113, ◦G114, ◦G140, ◦G141
Laguna class, Doubloon subclass	LDSoil	℘G502, ℘G611
Laguna class, Liberty subclass	LLSoil	∗G47, ∗G135, ∗G280, ∗G315, ∗G428, ∗G477, ℘G814, ℘G847, ℘G831, ℘G1017, ◦M123, ◦M368
Laguna class, Panda subclass	LPSoil	∗G43, ∗G49, ∗G50, ∗G74A, ∗G158, ∗G167, ∗G342, ∗G457, ℘G709, ℘G710, ◦M11, ◦M166, ◦M237A, ◦M237B, ◦M249
MER sufacE dusT (MERET)	Dust	G14, G65, G71, G126, ℘G823, ℘G1352, M25, M60, M90, M123
Paso Robles class	PSoil	∗G401, ∗G427, ℘G723, ℘G1013, ℘G1098
GS validation trenches	GRSSoil	ξG049, ξG050, ξG115, ξM081, ξM368

Table 6.11: Soil classes used, legend key for Figures 6.31– 6.34, and the sols on which they were sampled by the APXS continued from Table 6.10.

Soil class	Legend key	APXS sampling sol
Averages	LPPFSoil	♀Laguna, ♢GPanda, ♢MPanda, ♿Pathfinder

mer2-m-apxs-5-oxide-sci-v1/merap_2xxx/data/apxs_oxides_mer1.csv we obtained the data for sols 14−−1512 (Gusev) and sols 11−−1481 (Meridiani) from Ralf Gellert (05 May 2008, personal communication).

We make two key observations after considering all in situ soil classes, including the trench samples that were used to validate the GS estimates and average Pathfinder soil: (1) The absence of a consistent overlap with any class (or even with a single sample) across the four ratios highlights the chemical uniqueness of RAVE; and (2) The most consistent differences of oxide : SiO_2 ratios with RAVE counterparts are shown by MER surfacE dusT (MERET). Figures 6.31– 6.34 emphasize this consistency by juxtaposing the comparison of all classes with one of only MERET and ROM. In theory, the sol 1352 capture magnet dust sample that we include as a datum of MERET would have represented the composition of atmospheric dust. However, as discussed by Ming et al. (2008, submitted, Sec 9 Table 6), the capture magnet preferentially sequesters the titanomagnetite component of atmospheric dust, the sample may be insufficiently thick for accurate APXS analysis, and the bulk of the material may in fact be similar to Laguna class soil. Consistent with these issues, the capture magnet sample remains the outlier in MERET data across all four ratio types (Figures 6.31- 6.34) and we do not consider it further in our work.

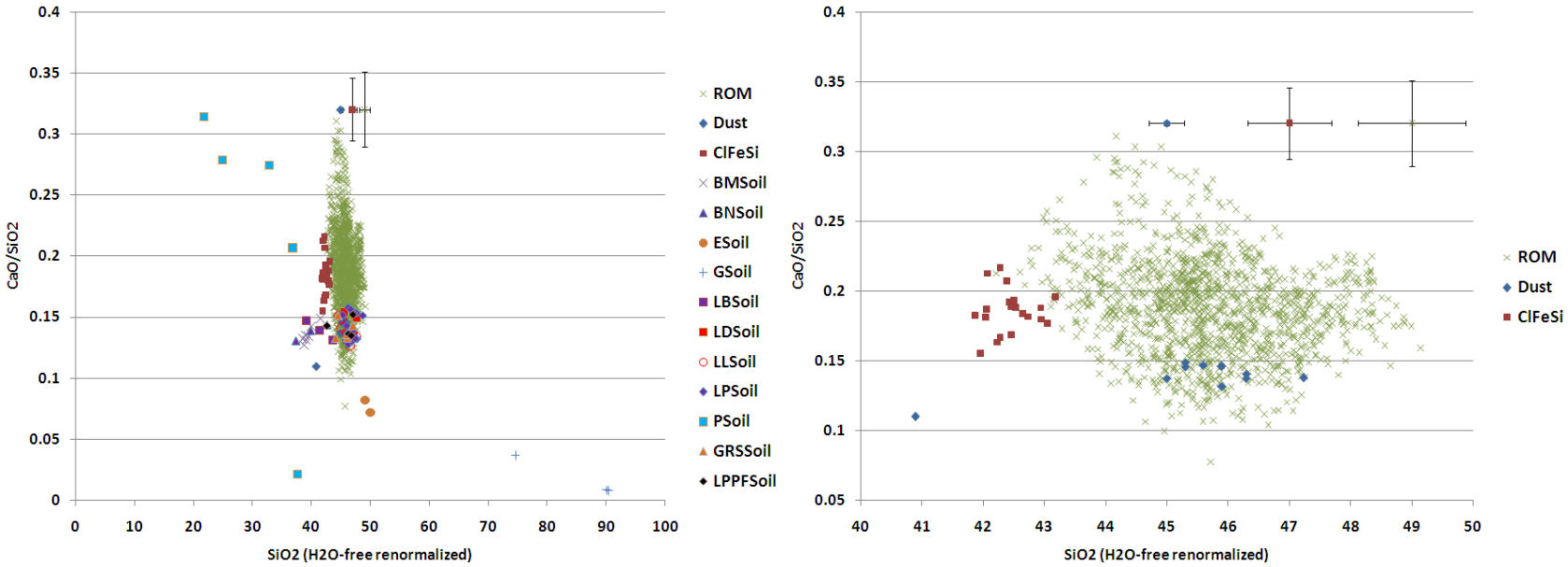

Figure 6.31: Scatter plot of CaO:SiO_2 mass fraction ratios versus the SiO_2 mass fraction for all soil classes at the MER sites, RAVE (legend: ClFeSi), and ROM as listed in Table 6.9. Scatter plot on the right highlights RAVE and MERET. Sample error bars are shown for RAVE, MERET, and ROM computed as the root mean square of numerical uncertainties. Plots of the other oxides shown in Figures 6.32– 6.34.

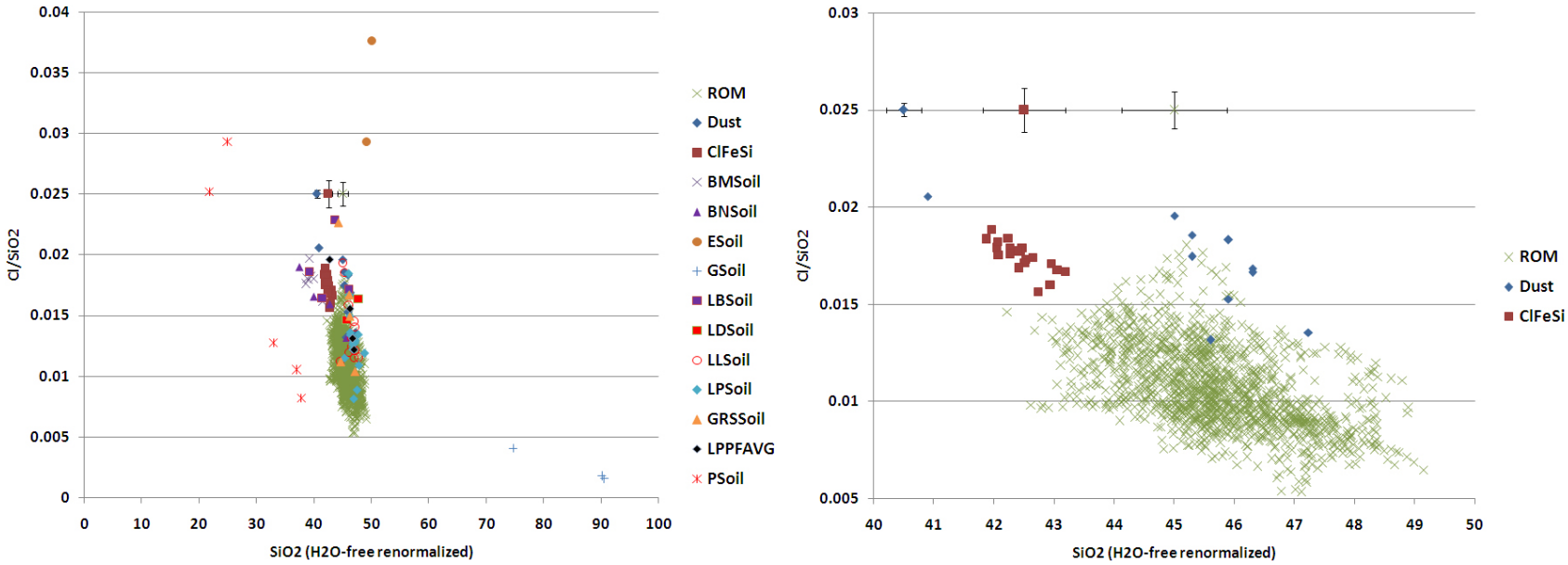

Figure 6.32: Scatter plot of Cl:SiO_2 mass fraction ratios versus the SiO_2 mass fraction for all soil classes at the MER sites, RAVE (legend: ClFeSi), and ROM as described in Figure 6.31.

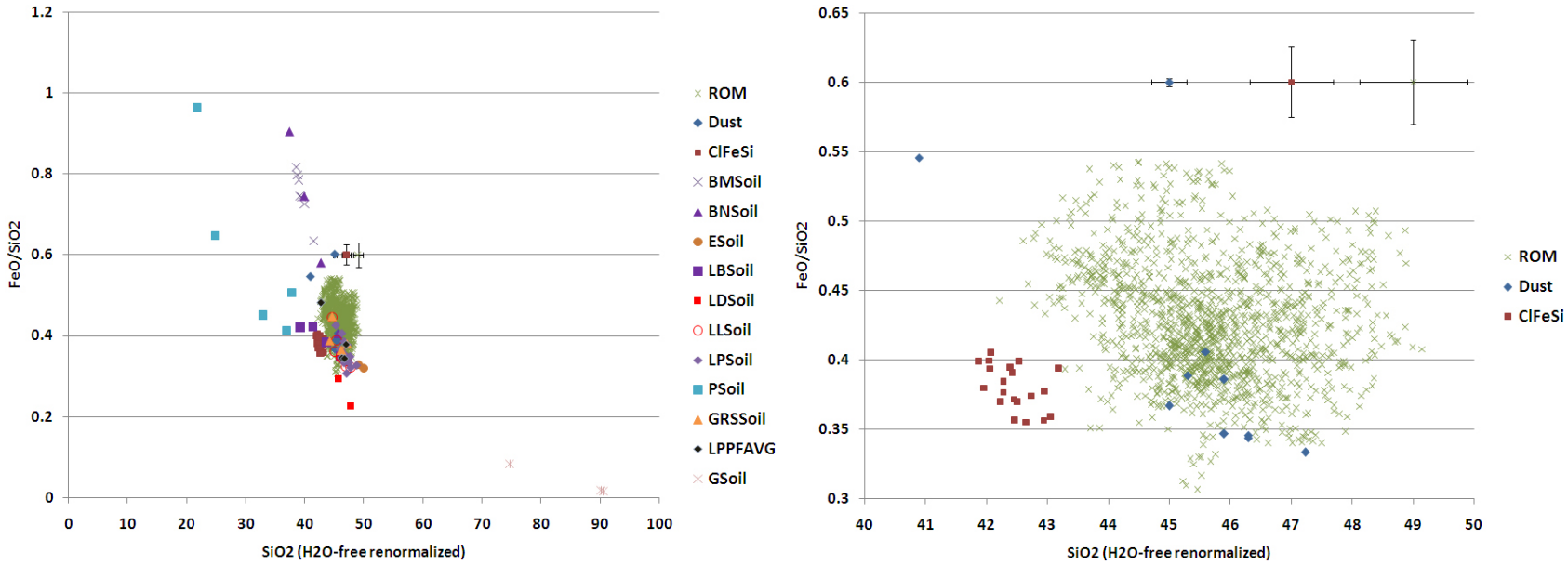

Figure 6.33: Scatter plot of FeO:SiO_2 mass fraction ratios versus the SiO_2 mass fraction for all soil classes at the MER sites, RAVE (legend: ClFeSi), and ROM as described in Figure 6.31.

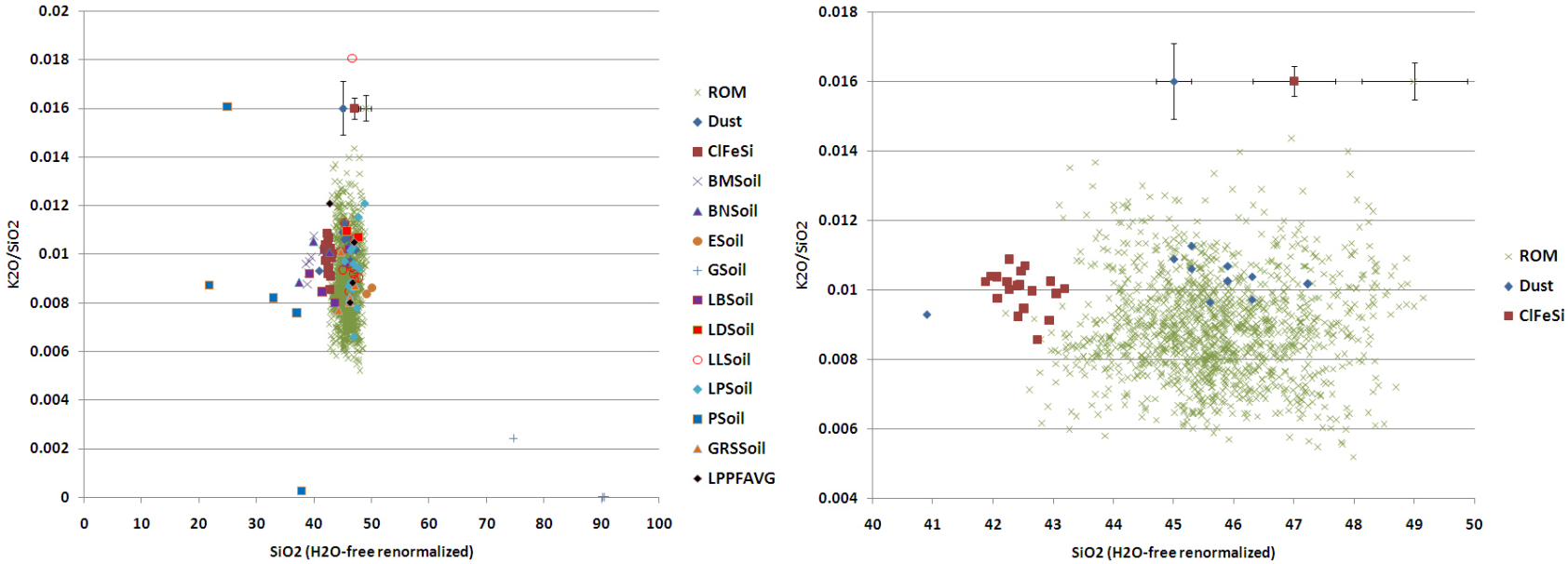

Figure 6.34: Scatter plot of K_2O:SiO_2 mass fraction ratios versus the SiO_2 mass fraction for all soil classes at the MER sites, RAVE (legend: ClFeSi), and ROM as described in Figure 6.31.

Figure 6.35: Modified box plots comparing the RAVE distribution to the ROM distribution for each element, and for ratios of particular elements of interest. Section 6.5.1 summarizes the features of the plot and the significance of the error bars.

An additional observation from Figure 6.32 is that, while strikingly enriched in Cl relative to the ROM, RAVE's Cl mass fractions are generally less than those of MERET. This yields the similar Cl/SiO_2 ratio between the two, which, along with the similar FeO/SiO_2 (Figure 6.33) and K_2O/SiO_2 (Figure 6.34) ratios and depletion of SiO_2 in RAVE would be consistent with a simple mass dilution effect on MERET as discussed in detail below. Since the GS-derived S map is still tentative, we are unable to investigate whether sulfates could be a diluting agent. Nevertheless, the significantly higher CaO/SiO_2 ratio in RAVE (Figure 6.31) could act as a proxy for sulfates, such as $CaSO_4 \cdot H_2O$ (gypsum) or $CaSO_4$ (anhydrite). Hydrated salts would also explain the slight enrichment of H_2O in RAVE relative to the ROM that is evident in Figure 6.35. These observations help to constrain our conjectures on the origin of RAVE in Section 6.7.

That an analog of MER soils could be a key chemical component of RAVE is reinforced by the RAVE oxide ratios lying within the extremes of soil classes

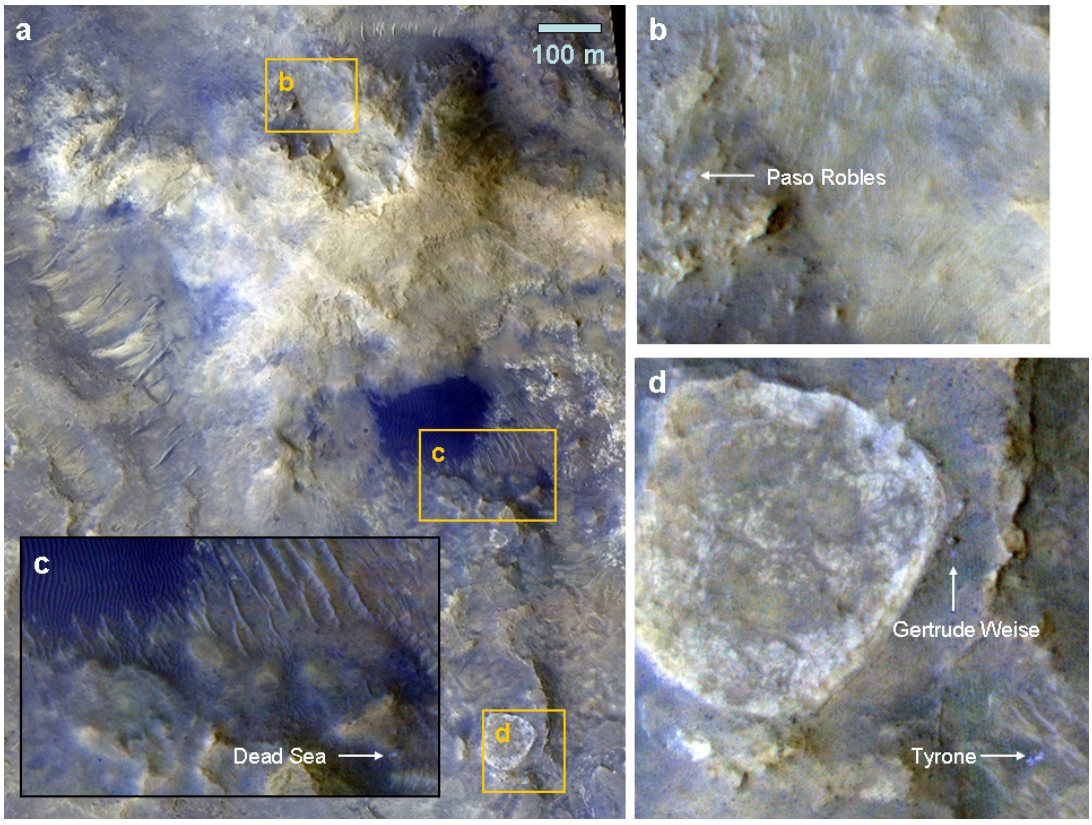

Figure 6.36: Paso Robles and Gertrude Weise samples visible from orbit as excerpts from HiRISE infrared-red-bluegreen enhanced color image PSP_003834_1650. As discussed in Section 6.5.1, their visibility in disturbed surfaces across a range of locations is consistent with a subsurface, perhaps even spatially widespread, presence.

(Figure 6.31), such as Paso Robles of a potentially hydrothermal origin (e.g., *Yen et al.*, 2008) and Berry dominated by hematite spherules of aqueous origin (e.g., *Morris et al.*, 2006). RAVE also appears roughly intermediate in composition relative to MERET and sulfate-rich Paso Robles soil for the case of FeO/SiO_2 and CaO/SiO_2. While such extreme soils with substantially higher CaO content than RAVE is reassuring for a dust-salt mixing model, the spatially isolated in situ detection and significant chemical variability (e.g., K_2O/SiO_2) of Paso Robles type soils precludes additional inferences. Nevertheless, as shown in Figure 6.36, the

presence of this soil class across a range of elevations (e.g., *Yen et al.*, 2008, Section 2, Para. 73), detection only in excavated surfaces (e.g., *Yen et al.*, 2008, Para. 4), and the presence of hydrous Fe^{3+}-sulfates that would dehydrate rapidly in the current atmosphere (e.g., *Lane et al.*, 2008, Section "Discussion" Para. 3) suggest that the Paso Robles class may be spatially more extensive beneath a veneer of other soils (e.g., *Lane et al.*, 2008, last para.).

We explore the feasibility of a MERET and salt mixing model further with first order estimates of the mass fraction of salts in a mixture that would yield the typical (median) mass fraction of FeO, Cl, K_2O, and SiO_2 within RAVE. With mass balance as the sole constraint, the mass fraction of salt in the mixture would vary between 5 % and 15 %, with the best agreement across elements for surface dust samples that appear to be composed of the finest material in Microscopic Imager (MI) images (e.g., sol 60 at Meridiani). Across all samples, the mass fraction of $CaSO_4$ only needs to be 3 %–5 % to account for the enrichment of Ca in RAVE relative to surface dust. That would amount to physically feasible bounds of 20 %–100 % of the diluting salt, with the rest unconstrained. For comparison, the areal fraction of cementing salts in the surface of White Rock duricrust, which we mentioned as a possible analog to the RAVE bedforms in Section 6.4.3, is estimated to be less than 15 % (*Ruff et al.*, 2001, Sec. 3 Para. 1).

A possible alternative RAVE composition to MERET is the ROM itself. Given the large number of ROM data, we may supplement the qualitative information in the ratio scatter plots (Figures 6.31– 6.34) with a more quantitative comparison of distributions using modified box plots as discussed in Section 3.4.1. In essence, we compare the low values within RAVE with the high values of ROM (25th percentile of RAVE divided by the 75th percentile of ROM), high values

of RAVE with low values of ROM (75th percentile of RAVE divided by the 25th percentile of ROM), and typical RAVE with typical ROM (median RAVE by median ROM). We estimate error bars conservatively as the per bin RMS uncertainty of RAVE and ROM propagated for the ratio of medians. The resulting plots are shown in Figure 6.35.

The qualitative comparison between RAVE and ROM (Figures 6.31– 6.34) suggests that CaO/SiO_2 and K_2O/SiO_2 are similar, while the RAVE FeO/SiO_2 values are significantly low. Even more striking, though already discussed in the delineation of RAVE, is the remarkably low SiO_2 mass fractions and remarkably high Cl mass fractions in RAVE relative to ROM. These observations are consistent with the quantitative comparisons (Figure 6.35) suggesting a typical (median) enrichment of Cl by about 50 %, depletion of Si by about 8 %, and depletion of the Fe/Si ratio by $\approx$ 10 %.

As discussed earlier, the enrichment of Cl and depletion of Si could be attributed to mass dilution by salts, much as we inferred for MERET in the case of Ca and Si. However, cations for potential halides are poorly constrained as the enrichment of K is tentative and Ca is, if anything, depleted (Figure 6.35). In addition, as discussed initially and elaborated further in Section 6.6.1, sulfates, not halides, are expected to be the typical salts in Martian surficial material. The biggest challenge of all to a salt dilution model of a ROM composition is the lower Fe/Si ratio in RAVE. While the preferential leaching of Fe under low-pH conditions (Section 6.6.2) is a possible resolution, the similarity of K/Th between RAVE and ROM (Figure 6.35) remains difficult to explain under any pH (*Taylor et al.*, 2006a). Lastly, ROM is chemically, geologically and mineralogically heterogeneous. It seems unlikely that such a heterogeneous surface could be

the source for the remarkably coherent chemical signature within RAVE and its neighborhood. Given these reasons we do not consider ROM to be a viable alternative to MERET either in a mass dilution scenario or in a chemical alteration scenario.

In summary, our comparison of the chemical distribution within RAVE with the various in situ soils of Mars and ROM hints that MERET (and Laguna class soil) may be a reasonable analog to the bulk material of RAVE. Dilution of such a composition by salts ($< 15\,\%$) with a significant Ca-cation component would yield the RAVE composition to first order. Such salts may also be hydrated, given the typical enrichment of H_2O in RAVE relative to ROM by $\approx 10\,\%$ (Section 6.7). If instead ROM were the primary source material, two key disparities that are somewhat difficult to resolve would arise: a lower Fe/Si ratio and a similar K/Th ratio (Figure 6.35). Therefore, we pursue the MERET analog in our conjectures on the origin of RAVE (Section 6.7), but first we also consider the in situ rocks observed by the MER mission and SNC meteorites as potential bulk candidates.

6.5.2 MER Rocks

The rock classes that we use, the sols on which they were sampled by the APXS, and the literature upon which the sample selection is based are listed in Table 6.12. The compositional consistency across Eagle, Fram, and Endurance craters (*Clark et al.*, 2005, sec 4.1) supports the use of seven stratigraphic layers (*Clark et al.*, 2005, Fig 2, Table 4) of the Burns class (*Morris et al.*, 2006, Table 4) to represent the typical compositional variations of outcrops across Meridiani.

Table 6.12: Rock classes used, legend key for Figure 6.37, and the sols on which they were sampled by the APXS. The symbolic superscripts identify the work that helped to associate the particular samples with a given class as: (+)*Clark et al.* (2007b, Table 1), (ψ)*Clark et al.* (2005, Fig 2, Table 4,5), ($*$)*Morris et al.* (2006, Fig 1, Table 1), ($\diamond$)*Morris et al.* (2006, Table 4), ($\wp$)Ming et al. (2008, submitted, Table 1, 1b, 2), (ζ)*McSween et al.* (2008, Table 1). Samples were limited to those that were either brushed or abraded to avoid surficial contamination and alteration effects, which excluded Everett; Fuzzy Smith; Good Question; Halley; Independence class, Assemblee subclass; and Other class, Joshua subclass rock types. Gusev samples are prefixed "G," Meridiani samples "M." Continued in Table 6.13.

Rock class	Legend	APXS sampling sol
Algonquin class	Algon	$^{\zeta}$G660, $^{\zeta}$G675, $^{\zeta}$G688, $^{\zeta}$G700
Adirondack class	Adiro	$^{\zeta}$G34, $^{\zeta}$G60, $^{\zeta}$G86, $^{\zeta}$G100, $^{\zeta}$G1341
Backstay class	Back	$^{\zeta}$G511
Barnhill class, Barnhill subclass	BaBa	$^{\wp}$G754, $^{\wp}$G763, $^{\wp}$G764
Barnhill class, Pesapallo subclass	BaPe	$^{\wp}$G1206, $^{\wp}$G1209, $^{\wp}$G1211, $^{\wp}$G1216
Burns class	Burns	$^{\diamond\psi}$M139, $^{\diamond\psi}$M145, $^{\diamond\psi}$M147, $^{\diamond\psi}$M149, $^{\diamond\psi}$M153, $^{\diamond\psi}$M155, $^{\diamond\psi}$M162, $^{\diamond\psi}$M178, $^{\diamond\psi}$M180, $^{\diamond\psi}$M184
Clovis class, Clovis subclass	ClCl	*G216, *G225, *G231, *G291, *G300, *G304

Table 6.13: Rock classes used, legend key for Figure 6.37, and the sols on which they were sampled by the APXS continued from Table 6.12.

Rock class	Legend	APXS sampling sol
Descarte class	Desc	℘G553
Elizabeth Mahon class, Elizabeth Mahon subclass	ElEl	℘G1216, ℘G1226
Elizabeth Mahon class, Innocent Bystander subclass	ElIn	℘G1251, ℘G1252
Independence class, Independence subclass	InIn	℘+G429B, ℘+G542, ℘+G533
Irvine class	Irvi	ζG600, ζG1055
Peace class	Peac	*G374, *G377, *G380, *G385B
Montalva class	Mont	℘G1072, ℘G1079
Other class, Pot of Gold subclass	OtPo	*G172
Torquas class	Torq	℘G1143
Watchtower class, Watchtower subclass	WaWa	*℘G416, *℘G417, *℘G496, *℘G499
Watchtower class, Keel subclass	WaKe	℘G646
Wishstone class	Wish	ζG335, ζG357

We use ten corresponding samples as well as a potential precursor composition (*Clark et al.*, 2005, Table 5) in our comparisons. It is important to note that the MER rock classes are chemically quite distinct (e.g., *Squyres et al.*, 2006a,c) unlike the soil classes. This is reinforced by the principal component analysis of APXS data for rocks as well (e.g., Tréguier et al., 2008, Overview of Mars surface geochemical diversity through APXS data multidimensional analysis: First attempt at modeling rock alteration, submitted to the J. Geophys. Res.).

Our ratio scatter plots of rock classes in Figures 6.37 and 6.38 do not show the consistent differences that were apparent for the case of MERET (Figures 6.31– 6.34). For example, a cursory look suggests that Adirondack class with its lower Cl/SiO_2 and K_2O/SiO_2 ratios could be diluted by KCl to give the composition of RAVE. However, FeO/SiO_2 of the Adirondack class is at the high end of RAVE, leading to issues similar to that for ROM in Section 6.5.1. Unlike for soils, the CaO/SiO_2 in RAVE also appears elevated relative to most rocks - including the sedimentary Burns formation - to the point of making the region an outlier.

While complex alteration processes in conjunction with mass dilution by salts may be contrived to infer a genetic association of RAVE with some igneous rocks, we do not find any parallels to the simpler possibilities that exist in the case of soils. We may have perhaps anticipated this given the dominance of fine material over rocks in the near surface of RAVE (Section 6.4.3). If a rock analog is sought in spite of these issues, the classes to show the most consistent differences would be the Adirondack class (picrobasalt-basalt in the TAS diagram (*McSween et al.*, 2006, Fig 7)) and the Barnhill-Pesapallo class of putative pyroclasts (Ming et al., 2008, submitted). We consider whether SNC meteorites

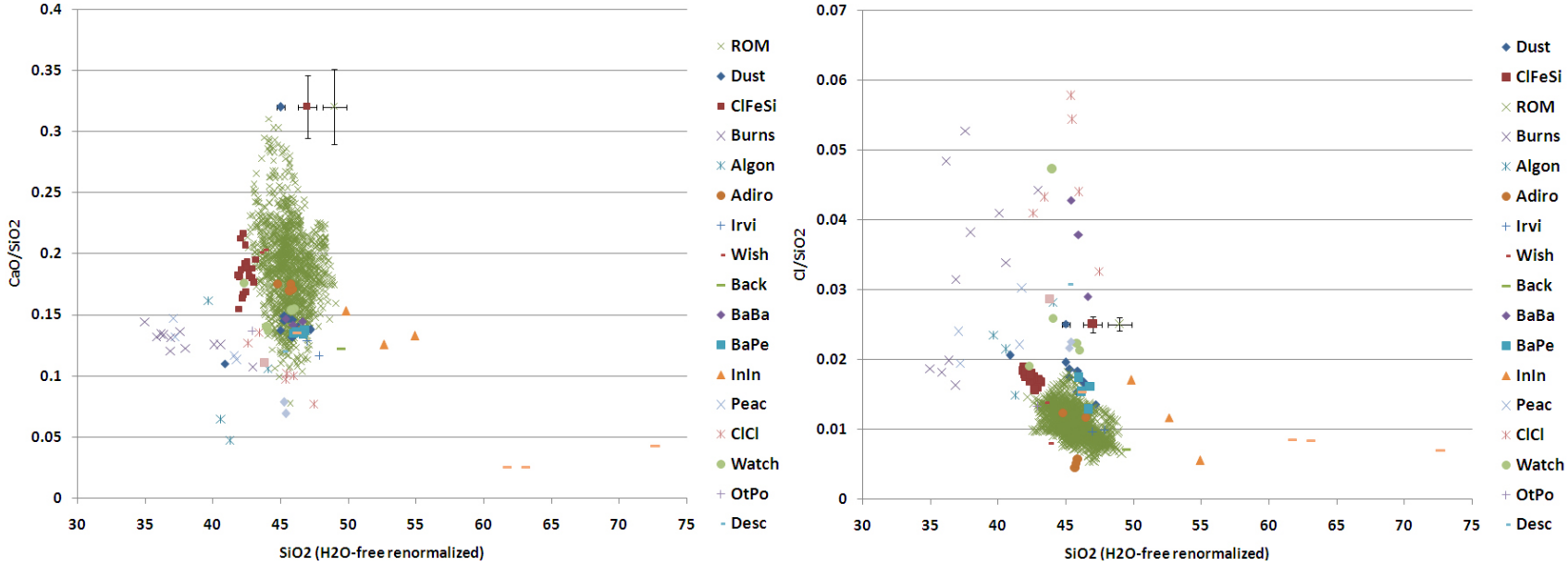

Figure 6.37: Scatter plots of oxide:SiO_2 mass fraction ratios versus the SiO_2 mass fraction for rock classes at the MER sites and RAVE (legend: ClFeSi) with ROM and MERET (legend: dust) included for reference and continued in Figure 6.38. Legends are identified in Table 6.12. Unlike MERET (Figures 6.31– 6.34), the rock classes do not show consistent differences with RAVE.

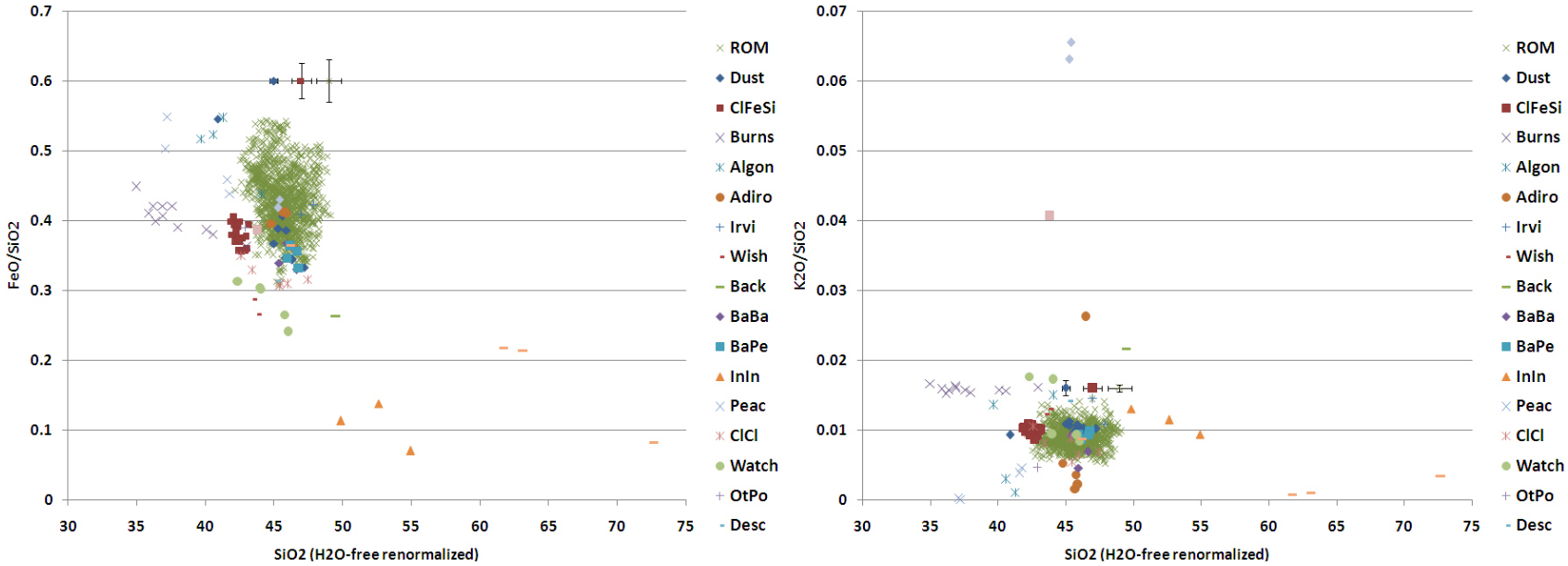

Figure 6.38: Scatter plots of oxide to SiO_2 mass fraction ratios versus the SiO_2 mass fraction for rock classes at the MER sites continued from Figure 6.37.

could be better analogs in the next section.

6.5.3 SNC Meteorites

We use the summary tabulation of chemical compositions of the Martian Meteorite Compendium (`http://curator.jsc.nasa.gov/antmet/mmc/index.cfm`) by Charles Meyer, limiting ourselves to the samples for which bulk compositions have been reported. The corresponding source files are listed in Table 6.14. As expected of minor elements in igneous material, meteoritic bulk compositions have far too low Cl/SiO_2. In addition, the SNC meteorites - possibly sourced from a depleted mantle (e.g., *Taylor et al.*, 2006b, Sec. 5, 7.2) - have very low K_2O/SiO_2 ratios (Figures 6.39 and 6.40) for a mix with salt to be plausible, unless mineral assemblages present in alteration veins (*Rao et al.*, 2005, 2008) were considered representative of the bulk.

Even if we disregard Cl as a mobile component and K in SNCs as unrepresentative of the crust (*Taylor et al.*, 2006b), a simple scenario of diluting the substantially higher mass fraction of SiO_2 in the majority of SNCs by salts would be difficult. Others such as Lherzolites, that have SiO_2 content comparable with RAVE, have higher FeO/SiO_2 ratios posing the same challenges as for ROM (Section 6.5.1). Alternatively, the igneous evolution of possible SNC parent magmas may possibly yield the Fe and Si mass fractions observed in RAVE, as has been considered by El Maarry et al. (2008, Gamma-ray constraints on the chemical composition of the Martian surface in the Tharsis region: A signature of partial melting of the mantle?, submitted to the J. Volcanol. Geoth. Res.).

We feel that of all three candidate material types just discussed, MER soils

Table 6.14: SNC classes, corresponding legend in Figure 6.39, and file names and tables of bulk compositions in the Martian Meteorite Compendium by Charles Meyer. For example, the URL for the file "any.pdf" would be `http://curator.jsc.nasa.gov/antmet/mmc/any.pdf` The last column also includes an abbreviated reference to analysts who determined the composition. Continued in Table 6.15.

SNC group	Legend	Sample	Source
Basaltic Shergottite	BS	EETA79001_A	79001.pdf; Lithology A, p. 11/26; Burghele83
		EETA79001_B	79001.pdf; Lithology B, p. 12/26; Burghele83
		Los Angeles	XVLosAngeles03.pdf; p. 5/5; Ruben2000
		QUE94201	que94201.pdf; p. 5/13; Warren1999
		RBT04262	RBT04261.pdf; p. 3/4; Anand2008
		Shergotty	que94201.pdf; p. 7/12; Laul1986
		Zagami	Zagami.pdf; p. 5/11; Lodders1998

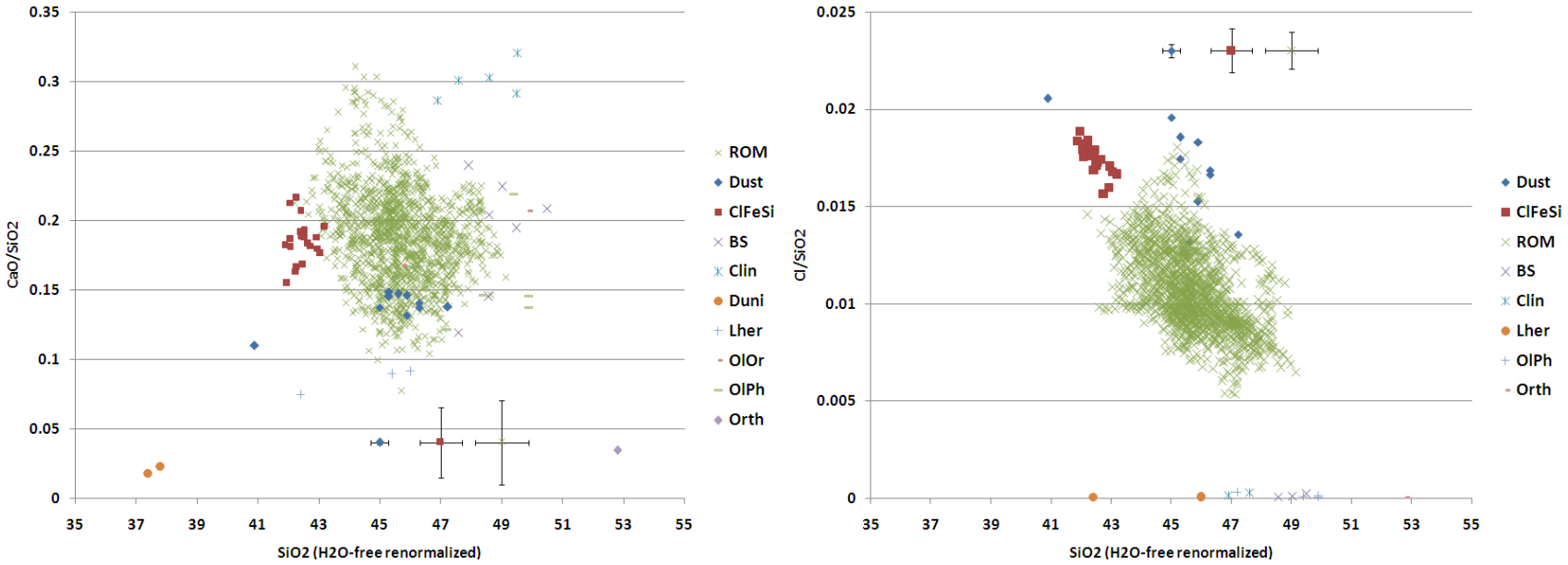

Figure 6.39: Scatter plots of oxide:SiO_2 mass fraction ratios versus the SiO_2 mass fraction for SNC meteorite classes and RAVE (legend: ClFeSi), with ROM and MERET (legend: Dust) included for reference, continued in Figure 6.40. Legends are identified and data sources listed in Tables 6.14– 6.17. Unlike MERET (Figures 6.31– 6.34), the SNCs do not show consistent differences with RAVE.

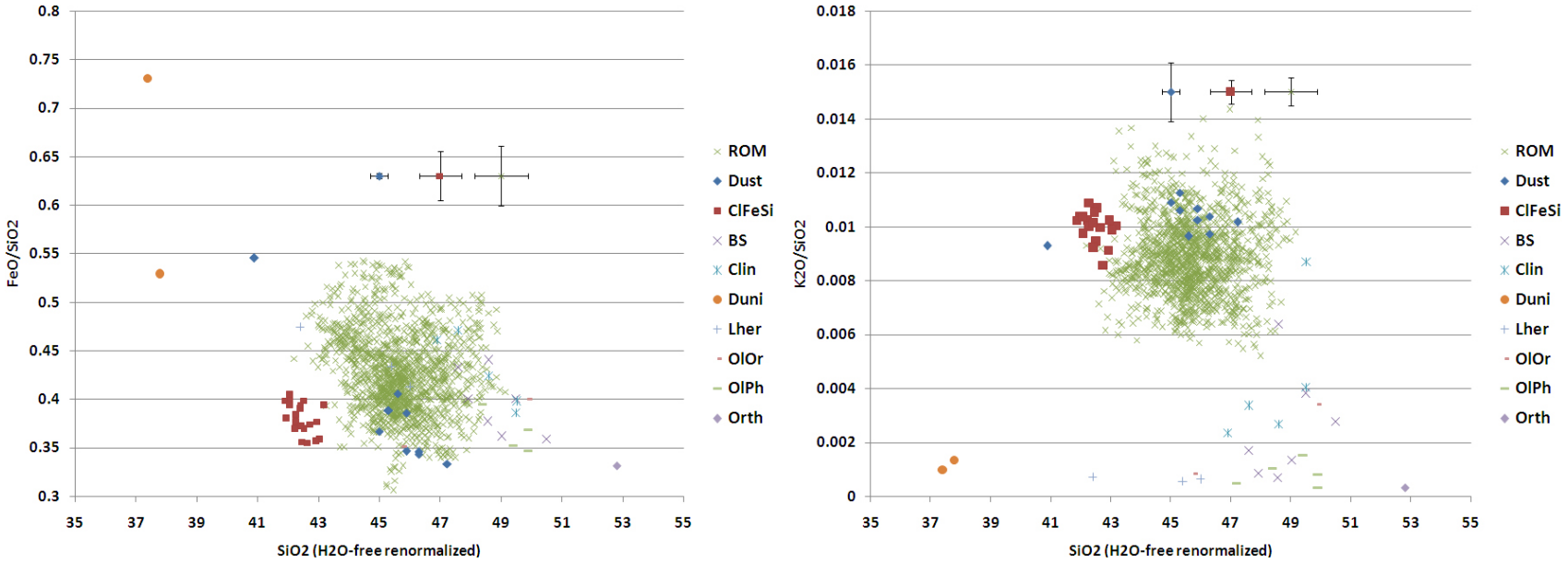

Figure 6.40: Scatter plots of oxide to SiO_2 mass fraction ratios versus the SiO_2 mass fraction for SNC classes continued from Figure 6.39.

Table 6.15: SNC classes, corresponding legend in Figure 6.39, and file names and tables of bulk compositions in the Martian Meteorite Compendium by Charles Meyer continued from Table 6.14. Continued in Table 6.16.

SNC group	Legend	Sample	Source
Clinopyroxenite (Nakhlite)	C	Governador	GovVal.pdf; p. 4/5; Burragato1975
		Lafayette	Lafay.pdf; p. 5/9; Lodders1998
		MIL03346	MIL03346e.pdf; p. 6/10; Barret2006
		Nakhla	Nakhla.pdf; p. 9/14; Lodders1998
		Y000593	XXII_Y000593.pdf; p. 5/5; Oura2003

in general and MERET in particular would be the optimal analog for the bulk component of RAVE, given consistent chemical differences, morphology particularly involving fine particle sizes at GS sampling depths (Sections 6.4.2, 6.4.1, and 6.4.3), and the relative simplicity of processes that need to be invoked.

6.6 Origin of RAVE: What is the Minor Component?

On the basis of scatter plot comparisons of elemental ratios between RAVE and each of ROM, Martian in situ soils, in situ rocks observed by the MER mission, and SNC meteorites in the preceding sections, we concluded that the most reasonable chemical analog for the bulk component of RAVE would be MERET.

Table 6.16: SNC classes, corresponding legend in Figure 6.39, and file names and tables of bulk compositions in the Martian Meteorite Compendium by Charles Meyer continued from Table 6.15. Continued in Table 6.17.

SNC group	Legend	Sample	Source
Dunitic shergottite	D	Chassigny	Chassig.pdf; p. 7/8; Lodders1998
		NWA2737	*Beck et al.* (2006, Table 2 FeO computed and normalized to 100.15 %)
Lherzolitic shergottite	L	ALH77005	*Lodders* (1998, Table 4, Cl from Table 3)
		LEW88516	*Lodders* (1998, Table 4, Cl from Table 3)
		Y793605	*Lodders* (1998, Table 4)
Orthopyroxenite	O	ALH84001	*Lodders* (1998, Table 4, Cl from Table 3)
Olivine-Orthopyroxene shergottite	OO	DarAlGani476	XIV-Dar%20al%20Gani.pdf; p. 5/6; Zipfel2000
		Dho378	dho378.pdf; p. 3/4; Ikeda2006

Table 6.17: SNC classes, corresponding legend in Figure 6.39, and file names and tables of bulk compositions in the Martian Meteorite Compendium by Charles Meyer continued from Table 6.16.

SNC group	Legend	Sample	Source
Olivine-phyric shergottite	OP	Dhofar019	XVII-%20Dhofar.pdf; p. 5/5; Taylor2002
		EETA79001_A	*Lodders* (1998, Table 4, Cl from Table 3)
		EETA79001_B	*Lodders* (1998, Table 4, Cl from Table 3)
		SayhAlUhaymir005	*Dreibus et al.* (2000, Table 1)
		Y980459	XXVII_Y980459.pdf; p. 4/4; Shirai2004

The bulk analog also requires a minor component of mass dilution. As summarized in Section 6.4.7 and reiterated in Section 6.5, the surficial properties are consistent with a salty cementation matrix as the diluting component. The diluted nature of RAVE relative to our analog(s) also requires that any chemical processes involved in the origin of the minor salt component not be isochemical within the GS sampling depths.

6.6.1 Could it be Sulfate(s)?

The higher CaO/SiO_2 ratio in RAVE relative to MERET and the $\approx 10\,\%$ enrichment of median H_2O mass fraction in RAVE relative to that of ROM (Figure 6.35) hint that a hydrated Ca-bearing salt may be a significant part of the cementing salts. In fact, our first order estimate in Section 6.5.1 indicated that this may exceed 20 % of the unknown salt, if the extra Ca were in the form of anhydrite. Sulfate could also be a reasonable anion for the rest of the salt mixture due to several reasons.

First, sulfates have been detected remotely on the surface as summarized by *Chevrier and Mathé* (2007, Section 2.4 Para. 2) and *Gendrin et al.* (2005). Such identifications include Gypsum-bearing outcrop surfaces and one dune field (Olympia Undae), the latter of substantial spatial extent (*Fishbaugh et al.*, 2007, Para. 6). All surface missions have detected sulfates in situ: Viking, Pathfinder, and MER (*Chevrier and Mathé*, 2007, Section 2.4 Para. 2). More specifically, Meridiani is a site of sulfate-rich outcrops (*Clark et al.*, 2005, Fig 12). Mineral modeling for the Meridiani outcrops suggest $\approx 7\,\%$ $CaSO_4$ (e.g., *Clark et al.*, 2005, Fig 12), with similar/greater enrichments in Boroughs soil within $\approx 10\,\mathrm{cm}$ depth (*Haskin et al.*, 2005), Clovis outcrop, Peace outcrop, and Paso Robles soil (*Ming et al.*, 2006, Table 5). S enrichment can also be associated with surface dust (e.g., *Knoll et al.*, 2008, Para. 9).

Second, the identification of sulfates in significant amounts across widely separated localities is consistent with the higher concentration of volatile elements in bulk Mars relative to Earth (*Dreibus and Wanke*, 1985). In fact, mass-independent depletion of ^{33}S in SNC meteorites suggests sustained S cycling between the atmosphere and the crust (*Farquhar et al.*, 2000) making sulfate anions

globally available for surficial processes over geologic time even in the absence of sustained volcanic exhalations. Furthermore, *Halevy et al.* (2007) estimate (volcanic - primarily Tharsis) S outgassing to be roughly twice that of Earth and suggest the control of aqueous conditions on early Mars by S-driven chemical pathways leading to the widespread formation of sulfites, which would cause a surficial prevalence of sulfates under the geologically more recent oxidizing atmosphere.

Third, mineralogic modeling of TES spectra using the methodology developed by *Cooper and Mustard* (2002) provides tentative evidence of cemented sulfates on the flanks of nearby Olympus Mons (10° N of the RAVE perimeter) and Ascreaus Mons (10° E) (*Cooper and Mustard*, 2001). It is possible that more definitive observations in these localities with TIR have been prevented by issues such as fine-particle volume scattering/non-linear mixing (e.g., *Christensen et al.*, 2001), detection difficulties when particle sizes are below $\approx 100\,\mu$m (*Poulet et al.*, 2007, sec 4.3.4), low surface temperatures, and spectral similarities between surface particles and atmospheric dust.

6.6.2 How would Sulfates Form?

Given the collective reasons to favor sulfates as cementation agents and key minor components within RAVE, an evaluation of chemical processes that form sulfates locally may help us identify reasonable conjectures for the genetic processes of RAVE. Experimental alteration of Hawaiian (plagioclase feldspar rich) basaltic tephra and (olivine-rich) sands by S-rich acidic vapors under hydrothermal conditions (145 °C) - simulating an acid fog scenario with very low wa-

ter/rock ratios - causes the isochemical precipitation of sulfates, primarily Mg and Ca sulfates, and the formation of amorphous silica (*Golden et al.*, 2005, Section 5.1, Para. 46). In contrast, high water : rock ratios under high temperature acid-fog conditions would cause significant leaching of cations from the host material (sand and tephra) (*Golden et al.*, 2005, Para. 30). Leaching is more likely for tephra than for sand (*Golden et al.*, 2005, Para. 31 Table 2). Of the Fe^{3+} sulfates that form under these conditions, jarosite is usually the only one to remain in the residue (*Golden et al.*, 2005, Table 2).

The results of hydrothermal high water : rock acid-fog experiments are consistent with low temperature counterparts that *Tosca et al.* (2004) conducted with synthetic Martian basalts, as well as the theoretical analyses by Tréguier et al. (2008, submitted). In particular, Fe, Mg, and Ca cations are released into solution (*Tosca et al.*, 2004) with subsequent precipitation of sulfates at low pH (1 – 3), with modeled solubilities increasing in the order Ca < Fe < Mg (*Tosca et al.*, 2005, p. 124 last para., p. 130 top left, Figs. 3–8). As expected, the sole exception is Jarosite which precipitates first.

McAdam et al. (2008, p. 93 last para) consider the possibility that the snow, ice, and dust deposition under higher obliquities that we discussed in Section 6.4.6 may have effectively scavenged acidic aerosols from volcanic exhalations. If so, the resulting ground ice (that may have been pervasive across RAVE) could have easily facilitated low pH alteration of fine material and rocks by acidic thin brine films, more effectively than by acid-fog alone (*McAdam et al.*, 2008, p. 93 last para).

Even in the absence of acid-fog related aerosols, *Chevrier and Mathé* (2007, Section 2.4) hypothesize that chemical alteration mediated by thin films of wa-

ter could yield sulfates isochemically as long as sulfide-bearing minerals (e.g., pyrrhotite) and suitable cation (e.g., Ca) bearing minerals (e.g., diopside) are available. However, aqueous conditions with high water : rock ratios (*Chevrier and Mathé*, 2007, Fig 8) are probably necessary to generate sulfate deposits on the scale of the Olympia Undae dune formation regardless of whether they formed by precipitation from percolating groundwaters (*Fishbaugh et al.*, 2007, Para. 32, 33) or some other mechanism. If deposited in place, the required Ca could still be locally derived from high-Ca pyroxenes or calcic-plagioclase feldspars (*Fishbaugh et al.*, 2007, Section 3.2.2), of which the former is also more likely to dissolve under low-pH conditions (*McAdam et al.*, 2008, p. 93 top right).

Perhaps more feasible at the large spatial scale of RAVE would be mediation of low-pH chemical processes in fine material by a sustained S-cycle between the atmosphere and the near surface of Mars (Section 6.6.1). For example, as *Tosca et al.* (2008) discuss in the Meridiani context, oxidation and dehydration processes involving hydrous Fe-sulfates may help to sustain low-pH brine films in Martian dust/soil. The acid-fog driven processes that we discussed at the beginning of this section could then occur even without volcanic exhalations.

Assuming that sulfate-rich brine films were to form by processes just described, in which direction are they likely to migrate within fine material deposits? Upward migration driven by a groundwater supply has been inferred on the basis of variations in Al, Ca, Mg, Cl, Br, and S at $\approx 10\,\mathrm{cm}$ depths (e.g., *Gellert et al.*, 2006; *Haskin et al.*, 2005, Gel06 sec 11.4 Has05 p 68 right col). However, at sites considered by some to be terrestrial analogs for Martian soil formation, such as Antarctica and the Atacama desert, upward migration of brines driven by groundwater is rare (*Amundson et al.*, 2008, p. 16 top). Accordingly,

Amundson et al. (2008, p. 15 line 19 - p. 16) suggest that brine formation by atmospherically derived solutes followed by downward migration may be a more likely scenario and consistent with the salt enrichment in the walls of $\approx 10\,\mathrm{cm}$ deep excavations at Gusev.

6.7 Synthesizing the Origin of RAVE

First order estimates of volume and mass may help develop a sense of scale for the salts and fine material involved in the formation of RAVE. RAVE has a surface area of roughly $2. \times 10^6\,\mathrm{km}^2$, approximating that of the Medusae Fossae Formation (MFF) (*Bradley et al.*, 2002, Section 7). Assuming a 2 m depth (Section 6.4.3), $1.2 \times 10^3\,\mathrm{kg\,m}^{-3}$ bulk density (Section 6.4.1), and 12.5 % mass fraction of salt (Section 6.5.1) yields a total $6. \times 10^{14}\,\mathrm{kg}$ mass of salts, roughly equivalent to a $2. \times 10^2\,\mathrm{km}^3$ volume if it were a mixture of gypsum (30 % mass fraction) and kieserite (70 %). The total mass of salt would exceed that of gypsum at Olympia Undae by a factor of 10, the volume by a factor of 8, and the area by a factor of 100 according to the Olympia Undae mass, volume, and area estimates by *Fishbaugh et al.* (2007, Para. 50, 51).

While the total volume of RAVE is smaller than what (*Bradley et al.*, 2002, Section 7) estimate for the MFF by a factor of 10^3, RAVE is still enormous by terrestrial standards at roughly 20 % of the land area of the USA. Terrestrial analogs even at the scale of Olympia Undae are rare, with the White Sands dune formation only $7 \times 10^2\,\mathrm{km}^2$ in extent *Fishbaugh et al.* (2007, Para. 4). Sulfate deposits associated with volcanism, such as the Julcani (Peru) and Creede (CO) formations (e.g., *Rye*, 2005) are even less than $1 \times 10^2\,\mathrm{km}^2$ in extent. These bulk comparisons

suggest that the chemical processes that helped to form the cementation salts in RAVE are likely to have been regional, rather than local, in scale.

6.7.1 General Inferences

While our chemical observations are currently too limited to fully constrain potential formation scenarios for RAVE, the preceding discussions may be used to guide a few conjectures. These generally share the same inference on the production of bedforms and the veneer of dust: Surficial salts in association with fine material were mobilized by thin films of water within RAVE during typical 42° and higher obliquities that last occurred ≈ 5 Ma ago (Section 6.4.6). The evaporation of resulting brine films aggregated fine particles to sufficiently large sizes to saltate (Section 6.4.3), particularly under denser atmospheres at higher obliquities (Section 6.4.6). Regional eolian turbulence, driven in part by katabatic winds at nearby volcanoes, formed the complex bedforms from the aggregated particles (Section 6.4.3).

However, cementation by salts over time indurated most of the bedforms to the point of hardpan to duricrust about 2 m thick in places, while others were either inactivated by ongoing air fall dust or are still evolving albeit at slower rates than can be observed over the lifetime of current missions (Section 6.4.3). The present centimeter scale veneer of dust (Section 6.4.2 and 6.4.3) has accumulated mostly under recent low-obliquity hyper-arid conditions (Section 6.4.6) that do not mobilize salts as effectively.

Most of the conjectures also rely on the chemically and physically reasonable assumption that the bulk of RAVE as seen by the GS is constituted of

indurated fine material (Section 6.4.3 and 6.4.7) with a composition similar to MERET (Section 6.5.1). The minor (mass fraction typically $< 15\,\%$) salt component that helped to form the bedforms via aggregation and indurated them subsequently is taken to be mostly sulfates with a significant mass fraction of Ca (Section 6.6.1). The scenarios differ from each other in terms of two key issues: (1) The primary source of the sulfates; and (2) The processes that produced them.

6.7.2 Scenario 1: Atmospheric Dust with Sulfates

Our simplest conjecture is that atmospheric dust, the deposition of which persisted across much of the region through obliquity cycles (Section 6.4.6), is compositionally similar to MER surface dust diluted by Ca-sulfate rich salts. The sulfates have been deflated and transported from the numerous, albeit localized, sulfate deposits on the planet (Section 6.6.1). An alternative atmospheric dust composition in this scenario would be in relation to the ROM, enriched in Cl, depleted in Si, and in Fe/Si. Either alternative under this conjecture would address the chemical (Section 6.5) and bulk properties of RAVE. However, both are inconsistent with the failure to detect significant sulfate concentrations in atmospheric dust via TIR spectral deconvolution (e.g., *Hamilton et al.*, 2005, Para. 41, 42). In either case, source localities for the sulfates that dilute the MERET would be mostly low-elevation regions with the nearest such deposit no closer than Valles Marineris more than a thousand kilometers away. The ROM alternative lacks any known examples, be it atmospheric or surficial. Therefore, this conjecture feels particularly contrived, and we consider it unlikely.

6.7.3 Scenario 2: Airfall Dust, Ground Ice, and Widespread Acid Fog

Our second conjecture invokes the chemical alteration of air fall dust by the activity of thin films of brine under higher obliquities, sustained mostly by regional scale ground H_2O ice more than 5 Ma ago (Section 6.4.6) with a minor contribution from long-term deep-seated interactions with relict H_2O glaciers that formed as recently as 65 Ma ago on the Arsia Mons flanks (Section 6.4.5). The low-to-moderate pH alteration mediated by this sustained source of groundwater formed regionally widespread sulfate salts that migrated to the surface by evaporative wicking-up effects (Section 6.6.2).

Alternatively, sulfates may have formed via the chemical alteration of air fall dust by regional scale acid fog (*McAdam et al.*, 2008, p. 93 right, bottom). The process may have been accelerated by the scavenging of acidic aerosols by H_2O snow at higher obliquities (Section 6.6.2). In either case, salts that had precipitated nearest to the surface mixed with continuing air fall dust that was chemically similar to MERET, eventually accumulating the meter-scale beds that we now see. In both cases the Ca cations would originate by leaching from the earliest dust deposits by the processes described in Section 6.6.2.

This conjecture, while invoking one additional step - the formation of salts driven by regional scale groundwater, acid fog, dehydration/oxidation of salts, or a combination thereof - relative to the simplest model (Section 6.7.2) avoids its compositional pitfalls. Much like the first, the regional scale of the second conjecture also accounts for the necessary bulk. A drawback to this scenario is that chemical alteration mediated by thin films of water and/or acid fog at

low temperature may require longer time scales than afforded by the < 65 Ma geologic age (Section 6.4.5) of RAVE. In addition, it is poorly known whether regional scale acid fogs ever formed on Mars and whether regional scale salt precipitation could occur via upward migration of brine films (Section 6.6.2). Except for these concerns, the second scenario appears viable.

6.7.4 Scenario 3: Basaltic Plinian Deposits and Acid Fog

Our third conjecture utilizes the location of RAVE surrounded by some of the largest volcanic edifices on the planet (Section 6.4.4). We propose that a few basaltic plinian eruptions or numerous fire fountain and strombolian eruptions during the late Amazonian deposited massive beds of unconsolidated material including reticulite, lapilli, and scoriaceous ash both East and West of the Tharsis construct (Section 6.4.4). The dominant wind direction westward from Tharsis (e.g., *Benson et al.*, 2006, Sec. 3.2) drove acid fog alteration under hydrothermal conditions (Section 6.6.2) forming sulfate deposits in southwestern near surfaces. These were reworked mechanically by eolian activity and mixed with ongoing air fall dust of a MERET composition.

Under this supposition, the chemical signature of RAVE would be best conserved if the pyroclastics had a composition similar to the Barnhill class, Pesapallo subclass (putative) pyroclastic rocks (Section 6.5.2 and Ming et al., 2008, submitted, Section 6.6.2) on SE Home Plate in the Columbia Hills of Gusev Crater (*Squyres et al.*, 2007). Like the first two, the third conjecture also satisfies bulk and chemical constraints. However, the concomitant basaltic plinian eruptions would have been at a scale much larger than their terrestrial analogs,

such as the 1886 CE Tarawera and 122 BCE Etna eruptions (*Houghton*, 2004). Furthermore, evidence for geologically recent explosive volcanism of such a magnitude is tenuous at best (Section 6.4.4). In the absence of stronger geomorphic evidence, our third surmise is probably untenable.

6.7.5 Scenario 4: Sulfates from the Flanks of Volcanoes

Our fourth, and last, conjecture invokes smaller magnitude volcanism than the third. The volcanism would have been comparable to Hawaiian type fire fountains or strombolian eruptions depositing large beds of scoriaceous ash and lapilli on the flanks of the Tharsis volcanoes perhaps as recently as 100 Ma ago (Section 6.4.4). These were exposed to local acid fog under hydrothermal conditions (Section 6.6.2) akin to those inferred for the Paso Robles soils in general and Tyrone Berkner Island/Tyrone Mount Darwin in particular (*Yen et al.*, 2008, Fig 14, Section 4.5, Para. 42). Although the scale of acid fog processes observed in the Kau desert downwind from the Kilauea caldera (*Schiffman et al.*, 2006) is orders of magnitude smaller than RAVE, they may be analogs for the chemical and mineralogical changes observed.

Resulting sulfate beds - particularly easily friable sulfates such as gypsum (e.g., *Fishbaugh et al.*, 2007, Para. 4) - would have been preferentially deflated under katabatic winds, a net deflation environment, and prevailing east-to-west winds, and deposited in the intervening topographic lows that include our region, perhaps throughout the last 0.1 Ma (Section 6.4.6). Meanwhile, ongoing air fall dust deposition, chemically similar to MERET, has produced the bulk component.

Both the strength and weakness of this last surmise is the source of sulfates - strength as it provides a regional source that is known to be undergoing deflation under the current obliquity, weakness as it invokes an eolian delivery method requiring preferential deflation of sulfates. An additional concern is with regard to bulk, as the original sulfate deposits need to be localized on the flanks of volcanoes. First order calculations assuming the volcanoes to be right cones suggest that if the sulfates accounted for no more than 5 % of the total surface area of flanks, the deposits would have been thicker than 10 m. At the other extreme of occupying the complete surface area, they would be at least 0.5 m thick. Obviously, the pyroclastic beds within which these sulfates would have been dispersed would need to be much thicker, perhaps by an order of magnitude. While these are not unphysical values, they nevertheless pose a considerable challenge for this conjecture. suggest that if the sulfates accounted for no more than 5 % of the total surface area of flanks, the deposits would have been thicker than 10 m. At the other extreme of occupying the complete surface area, they would be at least 0.5 m thick. Obviously, the pyroclastic beds within which these sulfates would have been dispersed would need to be much thicker, perhaps by an order of magnitude. While these are not unphysical values, they nevertheless pose a considerable challenge for this conjecture.

6.7.6 Favored Scenarios

In summary, we find the first and third surmises to be much less likely than the second and fourth. However, the second may require regional scale ground ice and/or acid fog. The evidence of such ice deposits in the past consists almost entirely of geomorphic similarities to the polar layered deposits and equivocal

inference of an ice-dust matrix at depth on the basis of radar loss tangents in nearby regions (Section 6.4.1). Furthermore, any extant ground ice is likely to be buried deeper than the GS can sense given the absence of a striking enrichment of H_2O within RAVE. The fourth conjecture is somewhat complicated by the requirement for preferential deflation and transport of sulfates, and weakened by bulk constraints. Nevertheless, both scenarios are reasonable educated guesses upon which to base further investigations of this region that is striking not only chemically, but also in radar stealth properties, unusual bedforms, and proximity to some of the largest volcanic edifices on the planet.

6.8 Conclusions

The Chemically Striking Regions (CSRs) that we have delineated on Mars may provide significant insight into surficial processes on the planet, and perhaps even into deep seated igneous processes in areas such as Elysium and low albedo surfaces in the North. They also show that the near surface of contiguous geologic units, such as the MFF, may nevertheless be chemically heterogeneous. The CSRs represent the synthesis of all chemical maps that have been finalized with the GS data, and supplement region delineations with Principal Component-based cluster analyses of the companion papers. More important, they demonstrate that the intensity and areal extent of chemical differentiation in the Martian surface is sufficient to guide future explorations and comparisons with other datasets.

We have demonstrated the synergy of the CSRs and other datasets with a case study involving the one region of the planet, RAVE, that is enriched in Cl

and depleted in both Fe and Si. The strong spatial overlap of RAVE with an area of Stealth in radar reflectivity as observed from Earth validates the complementary nature of Martian remote sensing observations. Meanwhile, the chemical constraints that we were able to establish with MER datasets demonstrate the utility of combining remote sensing and in situ data. Thermally derived attributes, observation of morphology with HiRISE, and climate modeling enabled us to further constrain potential formation scenarios of RAVE. While additional chemical and/or mineralogic information may be needed to fully constrain the processes that formed RAVE, we favor two of our four surmises, which may help guide future investigations. The refinement of GS-derived Al and S maps, as well as upcoming analyses of chemical layering with the NS data (*Diez et al.*, 2008) may be particularly useful in this regard.

CHAPTER 7

A VOYAGE COMPLETED

In the preceding chapters, we explored the surface of Mars with the Mars Odyssey GS complemented by an array of instruments. We began by examining whether the GS data were representative of the surface, and discovered that they were, indeed. In the process, we also observed that serious sampling issues in three dimensions had to be kept in mind whenever comparisons or extrapolations were made between the GS and in situ data sets. With the caveats laid bare, we proceeded to develop a statistical framework that would act as a reality check to our interpretations in the rest of the narrative. Exploring regions of Mars highlighted mineralogically by means of infrared spectra, we used the GS to constrain their compositions more thoroughly and the interpretations more robustly. Our final exercise, using the GS to identify regions of interest to be examined with other instruments, highlighted the utility of chemical information of the surface even when limited to a few elements. It also demonstrated that the GS can be as promising in characterizing the surface of Mars with γ photons as its predecessors have been with infrared light.

Even within the limited scope of our voyage on this planet, we are left with more queries than answers: What exactly, drives the spatial association of K and Th with surface type 2 mineralogy? Was any one geochemical process dominant in the formation of RAVE? What causes the chemical heterogeneities between eastern and western sections of the MFF? Beyond what we considered directly, lie numerous other questions, including: What limited CSRs to a few locations on the planet? What led to the association of many northern CSRs with the planetary dichotomy? What are the geological implications of the compositional

uniqueness to Elysium lava flows?

Such outstanding questions can help guide future exploration of the red planet: The one terrestrial planet of the solar system that was scarred by floods of mythological proportions, yet failed to become the veritable Eden that Earth has been for life and humanity for more than 1 Ga. It is my expectation that our geochemically-oriented explorations and discoveries would help define the path along which extraterrestrial life in the solar system may be found, or its rarity may be determined. I have been fortunate to experience an Odyssey that would have been fantasy a mere hundred years ago - It is my hope that the quests of future generations would be beyond my wildest dreams for humanity as a space-faring species!

APPENDIX A

TERMINOLOGY LIST

The following list contains key terms, symbols, acronyms, and notation that have been used throughout Chapter 4 in roughly alphabetic order. Where appropriate, corresponding sections and equations are identified.

1. $\hat{\cdot}$: Notation; Indicates an estimated parameter or sampled variable.
2. boldface font: Terminology; Indicates matrix of parameters or variables.
3. α: Parameter; Section 4.3.1; Identical to $1 - \tau$.
4. b_j: Parameter; Section 4.2; Equations 4.1, 4.4, 4.9, 4.13; Regression coefficient.
5. φ_i: Parameter; Section 4.2.2; Latitude of i^{th} bin's centroid.
6. d: Parameter; Section 4.4.3; Equation 4.27; Durbin-Watson test.
7. $\hat{e}_i$: Variable; Section 4.2; Residual.
8. $\hat{\mathbf{E}}$: Matrix; Sections 4.2.1, 4.2.2; Equations 4.6, 4.11, 4.15; Variance-covariance of $\mathbf{b}$.
9. HLR: Technique; Section 4.3.2; Heteroscedastic Linear Regression.
10. HRLR: Technique; Section 4.2.1; Heteroscedastic Response Linear Regression.
11. IID: Terminology; Section 4.2; Independent and Identically Distributed.
12. $k - 1$: Variable; Section 4.2; Number of predictors.
13. λ_i: Parameter; Section 4.2.2; Longitude of i^{th} bin's centroid.
14. N: Parameter; Section 4.1; Number of observed data.

15. OLR: Technique; Section 4.2.1; Ordinary Linear Regression.
16. p_j: Parameter; Section 4.3; Probability estimate for j^{th} predictor and the key parameter in hierarchical modeling.
17. p_R: Parameter; Section 4.3.1; Probability of R^2.
18. θ_b: Parameter; Section 4.2.2; Spatial separation beyond which spatial autocorrelation is insignificant.
19. r_j: Parameter; Sections 4.2.1, 4.3; Equations 4.8; Partial correlation coefficient for j^{th} predictors.
20. R: Parameter; Section 4.1; Multiple correlation coefficient.
21. R^2: Parameter; Section 4.1, 4.3.1; Equations 4.18, 4.19; Squared multiple correlation coefficient, i.e., coefficient of determination.
22. R^2_{df}: Parameter; Section 4.3.1; Equation 4.22; R^2 adjusted for the degrees of freedom.
23. R^2_0: Parameter; Section 4.3.1; Equation 4.23; Expected R^2 when sampling an uncorrelated population.
24. $\hat{\sigma}$: Parameter; Sections 4.2.1, 4.2.2; Equations 4.5, 4.10, 4.13; Estimated standard deviation.
25. $\hat{\sigma_{y,i}}$: Variable; Section 4.1; Standard error of i_{th} response.
26. SWLR: Technique; Section 4.2.2; Spatially Weighted Linear Regression.
27. τ: Parameter; Section 4.3.1; Statistical confidence fraction.
28. t_j: Parameter; Section 4.2.1; Equation 4.7; Confidence test parameter for j^{th} predictor.
29. t_R: Parameter; Section 4.3.1; Equation 4.24; Confidence test parameter for R^2.

30. $w_{i,j}$: Parameter; Section 4.2.2; Equation 4.16; Weight for spatial proximity between i^{th} and j^{th} bins and the i^{th} row, j^{th} column element of **W** matrix.

31. $X_{i,j}$: Variable; Section 4.2; i^{th} value of the j^{th} predictor.

32. $\psi(\theta)$: Parameter; Section 4.2.2; Equation 4.17; Similarity of attributes at θ angular separation.

33. $\hat{y}_i$: Variable matrix; Section 4.2; Equation 4.1; Modeled response.

APPENDIX B

SOFTWARE FUNCTION MODULES

We list some functions and procedures that relate sections of Chapter 4 to commercial mathematical software. The list includes the names of function modules, some of which are distributed in special packages (indicated in parenthesis). Descriptions of these functions is beyond the scope of this work, but available in software documentation. "-" indicates that a function module is unavailable for the particular task.

1. Section 4.1

   (a) Bivariate correlation with IDL: correlate; with R: cor (stats); with MatLab: corr; with Mathematica: Correlation.

2. Section 4.2

   (a) Ordinary Linear Regression (OLR) with IDL: imsl_regressors (Analyst); with R: lm (stats), glm (stats); with MatLab: regress ; with Mathematica: Regress.

   (b) Variance-covariance matrix with IDL: imsl_covariances (Analyst); with R: var (stats), cov.wt (stats), vcov (stats); with MatLab: cov; with Mathematica: Covariance.

   (c) Semi-variogram with IDL: -; with R: Variogram (nlme); with MatLab: -; with Mathematica: -.

3. Section 4.3

   (a) F-Distribution with IDL: f_pdf; with R: pf; with MatLab: fpdf; with Mathematica: FRatioPValue.

(b) χ^2 merit function minimization with IDL: imsl_chisqtest (Analyst); with R: chisq.test (stats); with MatLab: - ; with Mathematica: NMinimize.

(c) Normal distribution with IDL: gauss_pdf; with R: pnorm (stats); with MatLab: gausswin; with Mathematica: NormalPValue, NormalCI.

(d) Student's distribution with IDL: t_pdf; with R: pt (stats); with MatLab: tpdf; with Mathematica: StudentTPValue, StudentTCI.

4. Section 4.4

(a) Standardization with IDL: standardize; with R: scale (base); with MatLab: - ; with Mathematica: -.

(b) Cumulative distribution function with IDL: binomial; with R: ecdf (stats); with MatLab: normpdf; with Mathematica: Quantile and InverseCDF functions for the inverse cumulative distribution.

(c) Pseudorandom generator with IDL: randomu with normal keyword; with R: rnorm; with MatLab: random; with Mathematica: Random with NormalDistribution as an input.

(d) Spatial autocorrelation using Moran's formula with IDL: imsl_auto correlation (Analyst) with se_option=2; with R: -; with MatLab: -; with Mathematica: -.

BIBLIOGRAPHY

Almeida, M. P., E. J. R. Parteli, J. S. Andrade, Jr., and H. J. Herrmann (2008), Giant saltation on Mars, *P. Natl. Acad. Sci. USA*, *105*(17), 6222–6226, doi:10.1073/pnas.0800202105.

Amundson, R., S. Ewing, W. Dietrich, B. Sutter, J. Owen, O. Chadwick, K. Nishizumi, M. Walvoord, and C. McKay (2008), On the in situ aqueous alteration of soils on mars, *Geochim. Cosmochim. Acta*, p. in press, doi:10.1016/j.gca.2008.04.038.

Anderson, D. M., and A. R. Tice (1979), The analysis of water in the Martian regolith, *J. Mol. Evol.*, *14*, 33–38, doi:10.1007/BF01732365.

Arfken, G. B., and H. J. Weber (2005), *Mathematical Methods For Physicists*, 6 ed., 1200 pp., Elsevier Academic Press, Burlington, MA.

Arvidson, R. E., I. Seelos, F. P., K. S. Deal, W. C. Koeppen, N. O. Snider, J. M. Kieniewicz, B. M. Hynek, M. T. Mellon, and J. B. Garvin (2003), Mantled and exhumed terrains in Terra Meridiani, Mars, *J. Geophys. Res.*, *108*(E12), 8073, doi:10.1029/2002JE001982.

Arvidson, R. E., et al. (2004a), Localization and physical properties experiments conducted by Spirit at Gusev crater, *Science*, *305*(5685), 821–824, doi:10.1126/science.1099922.

Arvidson, R. E., et al. (2004b), Localization and physical property experiments conducted by Opportunity at Meridiani Planum, *Science*, *306*(5702), 1730–1733, doi:10.1126/science.1104211.

Arvidson, R. E., et al. (2006), Overview of the Spirit Mars Exploration Rover

Mission to Gusev Crater: Landing site to Backstay Rock in the Columbia hills, *J. Geophys. Res. Planets*, *111*, doi:10.1029/2005JE002499.

Baker, V. R., R. G. Strom, V. C. Gulick, J. S. Kargel, G. Komatsu, and V. S. Kale (1991), Ancient oceans, ice sheets and the hydrological cycle on Mars, *Nature*, *352*(6336), 589–594, doi:10.1038/352589a0.

Baker, V. R., S. Maruyama, and J. M. Dohm (2002), A theory for the geological evolution of Mars and related synthesis (GEOMARS), *Meteorit. Planet. Sci.*, *33*, Abstract 1586.

Balanda, K. P., and H. L. MacGillivray (1988), Kurtosis: A critical review, *Am. Stat.*, *42*(2), 111–119, doi:10.2307/2684482.

Bandfield, J. L., V. E. Hamilton, and P. R. Christensen (2000), A global view of Martian surface compositions from MGS-TES, *Science*, *287*(5458), 1626–1630, doi:10.1126/science.287.5458.1626.

Banin, A. (2005), Planetary science - The enigma of the Martian soil, *Science*, *309*(5736), 888–890, doi:10.1126/science.1112794.

Banin, A., B. C. Clark, and H. Wänke (1992), *Mars*, chap. 18, pp. 594–625, University of Arizona Press.

Bas, M. J. L. (2000), Iugs reclassification of the high-Mg and picritic volcanic rocks, *J. Petrology*, *41*(10), 1467–1470.

Basilevsky, A. T., and V. M. Linkin (1996), Lunar rover sample return: Lunokhod/Luna heritage and perspectives, *Adv. Space Res.*, *18*(11), 83–83, doi:10.1016/0273-1177(96)00106-8.

Basilevsky, A. T., C. P. Florensky, and L. B. Ronca (1977), Possible lunar outcrop - study of lunokhod-2 data, *The Moon*, *17*(1), 19–28, doi:10.1007/BF00566850.

Beck, P., et al. (2006), Petrography and geochemistry of the chassignite Northwest Africa 2737 (NWA 2737), *Geochim. Cosmochim. Acta*, *70*, 2127–2139, doi:10.1016/j.gca.2006.01.016.

Bell, J. F., J. Joseph, J. N. Sohl-Dickstein, H. M. Arneson, M. J. Johnson, M. T. Lemmon, and D. Savransky (2006a), In-flight calibration and performance of the Mars Exploration Rover Panoramic Camera (Pancam) instruments, *J. Geophys. Res. Planets*, *111*(E2), E02S03, doi:10.1029/2005JE002444.

Bell, J. F., D. Savransky, and M. J. Wolff (2006b), Chromaticity of the Martian sky as observed by the Mars Exploration Rover Pancam instruments, *J. Geophys. Res. Planets*, *111*(E12), E12S05, doi:10.1029/2006JE002687.

Bell, J. F., et al. (2003), Mars Exploration Rover Athena Panoramic Camera (Pancam) investigation, *J. Geophys. Res. Planets*, *108*(E12), 8063, doi:10.1029/2003JE002070.

Bell, J. F., et al. (2004), Pancam multispectral imaging results from the Opportunity Rover at Meridiani planum, *Science*, *306*, 1703–1709, doi:10.1126/science.1105245.

Benson, J. L., P. B. James, B. A. Cantor, and R. Remigio (2006), Interannual variability of water ice clouds over major martian volcanoes observed by MOC, *Icarus*, *184*(2), 365–371, doi:10.1016/j.icarus.2006.03.014.

Bevington, P. R., and D. K. Robinson (2003), *Data Reduction and Error Analysis for the Physical Sciences*, 3 ed., 336 pp., McGraw Hill, New York, NY.

Bibring, J. P., S. W. Squyres, and R. E. Arvidson (2006a), Merging views on Mars, *Science*, *313*(5795), 1899–1901, doi:10.1126/science.1132311.

Bibring, J. P., et al. (2005), Mars surface diversity as revealed by the OMEGA/Mars Express observations, *Science*, *307*(5715), 1576–1581, doi:10.1126/science.1108806.

Bibring, J. P., et al. (2006b), Global mineralogical and aqueous mars history derived from OMEGA/Mars express data, *Science*, *312*(5772), 400–404, doi:10.1126/science.1122659.

Bivand, R. (1980), A Monte Carlo study of correlation coefficient estimation with spatially autocorrelated observations, *Quaestiones Geographicae*, *6*, 5–10.

Blalock, H. M., Jr. (1964), *Causal Inferences in Nonexperimental Research*, University of North Carolina, Durham, NC.

Bleacher, J. E., R. Greeley, D. A. Williams, S. C. Werner, E. Hauber, and G. Neukum (2007), Olympus Mons, Mars: Inferred changes in late Amazonian aged effusive activity from lava flow mapping of Mars Express High Resolution Stereo Camera data, *J. Geophys. Res. Planets*, *112*, E04,003, doi:10.1029/2006JE002826.

Borg, L. E., and D. S. Draper (2003), A petrogenetic model for the origin and compositional variation of the martian basaltic meteorites, *Meteorit. Planet. Sci.*, *38*(12), 1713–1731.

Borg, L. E., L. E. Nyquist, H. Weissman, C.-Y. Shih, and Y. Reese (2003), The age of Dar al Gani 476 and the differentiation history of the martian meteorites inferred from their radiogenic isotopic systematics, *Geochim. Cosmochim. Acta*, *67*(18), 3519–3536, doi:10.1016/S0016-7037(03)00094-2.

Bourke, M. C., K. S. Edgett, and B. A. Cantor (2008), Recent aeolian dune change on Mars, *Geomorphology*, *94*(1-2), 247–255, doi:10.1016/j.geomorph.2007.05.012.

Boynton, W. V., et al. (1992), Science applications of the Mars-Observer Gamma-Ray Spectrometer, *J. Geophys. Res. Planets*, *97*(E5), 7681–7698.

Boynton, W. V., et al. (2004), The Mars Odyssey Gamma-Ray Spectrometer instrument suite, *Space Sci. Rev.*, *110*(1-2), 37–83, doi:10.1023/B:SPAC.0000021007.76126.15.

Boynton, W. V., et al. (2007), Concentration of H, Si, Cl, K, Fe, and Th in the low- and mid-latitude regions of Mars, *J. Geophys. Res. Planets*, *112*, 12–+, doi:10.1029/2007JE002887.

Bradley, B., S. Sakimoto, H. Frey, and J. Zimbelman (2002), Medusae Fossae Formation: New perspectives from Mars Global Surveyor, *J. Geophys. Res. Planets*, *107*(E8), 5058, doi:10.1029/2001JE001537.

Brandon, A. D., R. J. Walker, J. W. Morgan, and G. G. Goles (2000), Re–Os isotopic evidence for early differentiation of the Martian mantle, *Geochim. Cosmochim. Acta*, *64*(23), 4083–4095, doi:10.1016/S0016-7037(00)00482-8.

Brenan, J. M., H. F. Shaw, F. J. Ryerson, and D. L. Phinney (1995), Mineral-aqueous fluid partitioning of trace elements at 900 celsius and 2.0 GPa: Constraints on the trace element chemistry of mantle and deep crustal fluids, *Geochim. Cosmochim. Acta*, *59*(16), 3331–3350, doi:10.1016/0016-7037(95)00215-L.

Bridges, N. T., P. E. Geissler, A. S. McEwen, B. J. Thomson, F. C. Chuang, K. E. Herkenhoff, L. P. Keszthelyi, and S. Martinez-Alonso (2007), Windy Mars:

A dynamic planet as seen by the HiRISE camera, *Geophys. Res. Lett.*, *34*(23), L23,205, doi:10.1029/2007GL031445.

Bridges, N. T., E. Gorbaty, R. A. Beyer, S. Byrne, B. J. Thomson, J. Wray, and Hirise Team (2008), Low Thermal Inertia and High Elevation Bedforms as Seen by the HiRISE Camera, in *39th Lunar and Planetary Science Conference*, *Lunar and Planetary Inst. Technical Report*, vol. 39, p. Abstract 2108.

Brückner, J., M. Koerfer, H. Wänke, A. N. F. Schroeder, D. Filges, P. Dragovitsch, P. A. J. Englert, R. Starr, and J. I. Trombka (1991), Proton-induced radiation damage in germanium detectors, *IEEE Trans. Nucl. Sci.*, *38*(2), 209–217, doi: 10.1109/23.289298.

Brückner, J., G. Dreibus, R. Rieder, and H. Wänke (2003), Refined data of Alpha Proton X-ray Spectrometer analyses of soils and rocks at the Mars Pathfinder site: Implications for surface chemistry, *J. Geophys. Res. Planets*, *108*(E12), 8094, doi:10.1029/2003JE002060.

Bugayevskiy, L. M., and J. Snyder (1995), *Map Projections*, 248 pp., Taylor & Francis, Philadelphia, PA.

Cabrol, N. A., J. D. Farmer, E. A. Grin, L. Richter, L. Soderblom, R. Li, K. Herkenhoff, G. A. Landis, and R. E. Arvidson (2006), Aqueous processes at Gusev crater inferred from physical properties of rocks and soils along the Spirit traverse, *J. Geophys. Res. Planets*, *111*(E2), E02S20, doi:10.1029/2005JE002490.

Cabrol, N. A., et al. (2003), Exploring Gusev Crater with Spirit: Review of science objectives and testable hypotheses, *J. Geophys. Res. Planets*, *108*(E12), 8076, doi:10.1029/2002JE002026.

Cantor, B. A. (2007), Present-Day Martian Weather - 5 Mars Years of Observations by MGS-MOC and MRO-MARCI, *LPI Contributions*, *1353*, 3063–+.

Cantor, B. A., K. M. Kanak, and K. S. Edgett (2006), Mars Orbiter Camera observations of Martian dust devils and their tracks (September 1997 to January 2006) and evaluation of theoretical vortex models, *J. Geophys. Res. Planets*, *111*(E12), E12,002, doi:10.1029/2006JE002700.

Carter, L. M., et al. (2008), SHARAD Sounding Radar Observations of the Medusae Fossae Formation, Mars, in *39th Lunar and Planetary Science Conference*, *Lunar and Planetary Inst. Technical Report*, vol. 39, p. Abstract 1721.

Chakravarti, I. M., R. G. Laha, and J. Roy (1967), *Handbook of methods of applied statistics: Techniques of computation, descriptive methods, and stistical inference*, *Wiley series in probability and mathematical statistics*, vol. 1, John Wiley and Sons.

Chevrier, V., and P. E. Mathé (2007), Mineralogy and evolution of the surface of Mars: A review, *Plant. Space Sci.*, *55*, 289–314, doi:10.1016/j.pss.2006.05.039.

Christensen, P., et al. (2004), The Thermal Emission Imaging System (THEMIS) for the Mars 2001 Odyssey Mission, *Space Sci. Rev.*, *110*(1-2), 85–130, doi:10.1023/B:SPAC.0000021008.16305.94.

Christensen, P. R. (1986), The spatial–distribution of rocks on Mars, *Icarus*, *68*(2), 217–238, doi:10.1016/0019-1035(86)90020-5.

Christensen, P. R. (1988), Global albedo variations on Mars–implications for active aeolian transport, deposition, and erosion, *J. Geophys. Res. B Solid Earth Planets*, *93*(B7), 7611–7624.

Christensen, P. R., and M. C. Malin (1988), High resolution thermal imaging of Mars, *Lunar Planet. Sci.*, *19*, 180–181.

Christensen, P. R., and S. W. Ruff (2004), Formation of the hematite–bearing unit in Meridiani Planum: Evidence for deposition in standing water, *J. Geophys. Res. Planets*, *109*(E8), E08,003, doi:10.1029/2003JE002233.

Christensen, P. R., et al. (2001), Mars Global Surveyor Thermal Emission Spectrometer experiment: Investigation description and surface science results, *J. Geophys. Res. Planets*, *106*(E10), 23,823–23,871, doi:10.1029/2000JE001370.

Christensen, P. R., et al. (2003), Morphology and composition of the surface of Mars: Mars Odyssey THEMIS results, *Science*, *300*(5628), 2056–2061, doi:10.1126/science.1080885.

Christensen, P. R., et al. (2005), The igneous diversity of Mars: Evidence for magmatic evolution analogous to Earth, *Lunar Planet. Sci.*, *36*, abstract 1273.

Clark, B. C., A. K. Baird, R. J. Weldon, D. M. Tsusaki, L. Schnabel, and M. P. Candelaria (1982), Chemical composition of Martian fines, *J. Geophys. Res.*, *87*, 10,059–10,067.

Clark, B. C., R. Gellert, A. Yen, and Athena Science Team (2007a), The Gusev Geochemical Zoo: Compositional Diversity of Rocks and Sediments, from Subclass to Superclass, with Indicators for Aqueous Activity, *LPI Contributions*, *1353*, 3232–+.

Clark, B. C., et al. (2005), Chemistry and mineralogy of outrcrops at Meridiani Planum, *Earth Planet. Sci. Lett.*, *240*(1), 73–94, doi:10.1016/j.epsl.2005.09.040.

Clark, B. C., et al. (2007b), Evidence for montmorillonite or its compositional equivalent in Columbia Hills, Mars, *J. Geophys. Res. Planets*, *112*, E06S01, doi:10.1029/2006JE002756.

Clark, B. C., III, et al. (1977), The viking x ray fluorescence experiment - analytical methods and early results, *J. Geophys. Res.*, *82*, 4577–4594.

Claudin, P., and B. Andreotti (2006), A scaling law for aeolian dunes on Mars, Venus, Earth, and for subaqueous ripples, *Earth Planet. Sci. Lett.*, *252*(1-2), 30–44, doi:10.1016/j.epsl.2006.09.004.

Clifford, P., S. Richardson, and D. Hémon (1989), Assessing the significance of the correlation between two spatial processes, *Biometrics*, *45*(1), 123–134.

Cohen, J., and P. Cohen (1983), *Applied Multiple Regression/Correlation Analysis for the Behavioral Sciences*, 2 ed., L. Erlbaum Associates, Hillsdale, N.J.

Connerney, J. E. P., et al. (1999), Magnetic lineations in the ancient crust of Mars, *Science*, *284*(5415), 794–798, doi:10.1126/science.284.5415.794.

Cooper, C. D., and J. F. Mustard (2001), TES Observations of the Global Distribution of Sulfate on Mars, in *Lunar and Planetary Institute Conference Abstracts*, *Lunar and Planetary Inst. Technical Report*, vol. 32, pp. 2048–+.

Cooper, C. D., and J. F. Mustard (2002), Spectroscopy of Loose and Cemented Sulfate-Bearing Soils: Implications for Duricrust on Mars, *Icarus*, *158*, 42–55, doi:10.1006/icar.2002.6874.

Crumpler, L. S., et al. (2005), Mars Exploration Rover Geologic traverse by the Spirit rover in the Plains of Gusev Crater, mars, *Geology*, *33*(10), 809–812, doi:10.1130/G21673.1.

Cucinotta, F. A., M.-H. Kim, S. I. Schneider, and D. M. Hassler (2007), Description of light ion production cross sections and fluxes on the Mars surface using the QMSFRG model, *Radiat. Environ. Biophys.*, *Proceedings of the 4th IWSRR*, doi:10.1007/s00411-007-0099-y.

Daux, V., J. L. Crovisier, C. Hemond, and J. C. Petit (1994), Geochemical evolution of basaltic rocks subjected to weathering: Fate of the major elements, rare earth elements, and thorium, *Geochim. Cosmochim. Acta*, *58*(22), 4941–4954, doi:10.1016/0016-7037(94)90223-2.

Davis, J. A. (1985), *The logic of causal order*, no. 07-055 in Quantitative Applications in the Social Sciences, 71 pp., Sage, Thousand Oaks, CA.

DeGroot, M. H., and M. J. Schervish (2001), *Probability and Statistics*, 3 ed., Addison Wesley.

Diez, B., S. Maurice, O. Gasnault, C. D'Uston, W. C. Feldman, D. Baratoux, and N. Mangold (2008), Mars Odyssey GRS Results at the Cerberus Plains, in *Lunar and Planetary Institute Conference Abstracts*, *Lunar and Planetary Institute Conference Abstracts*, vol. 39, pp. 1642–+.

Dodge, Y., and V. Rousson (1999), The complications of the fourth central moment, *Am. Stat.*, *53*(3), 267–269, doi:10.2307/2686108.

Dohm, J., S. Maruyama, V. Baker, R. Anderson, and J. Ferris (2002), Evolution and traits of tharsis superplume in mars, in *Superplume International Workshop Abstracts with Programs*, pp. 406–410, Tokyo.

Dohm, J. M., et al. (2001a), Latent outflow activity for western Tharsis, Mars: Significant flood record exposed, *J. Geophys. Res. Planets*, *106*(E6), 12,301–12,314, doi:10.1029/2000JE001352.

Dohm, J. M., et al. (2001b), Ancient drainage basin of the Tharsis region, Mars: Potential source for outflow channel systems and putative oceans or paleolakes, *J. Geophys. Res. Planets*, *106*(E12), 32,943–32,958, doi:10.1029/2000JE001468.

Dohm, J. M., et al. (2008), Recent geological and hydrological activity on Mars: The Tharsis/Elysium corridor, *Plant. Space Sci.*, *56*, 985–1013, doi:10.1016/j.pss.2008.01.001.

Doreian, P. (1980), Linear models with spatially distributed data: Spatial disturbances of spatial effects?, *Socio. Meth. Res.*, *9*(1), 29–60.

Dreibus, G., and H. Wanke (1985), Mars, a volatile-rich planet, *Meteoritics*, *20*, 367–381.

Dreibus, G., E. Jagoutz, B. Spettel, and H. Wänke (1996), Posphate–mobilization on Mars? implication from leach experiments on SNCs, *Lunar Planet. Sci.*, *27*, 323–324.

Dreibus, G., B. Spettel, R. Haubold, K. P. Jochum, H. Palme, D. Wolf, and J. Zipfel (2000), Chemistry of a New Shergottite: Sayh Al Uhaymir 005, *Meteorit. Planet. Sci.*, *35*, Supplement A49.

Drever, J. I. (1997), *Geochemistry of Natural Waters: Surface and Groundwater Environments*, 3 ed., Prentice Hall, Upper Saddle River, N.J.

Durkin, P. (2008), *Oxford English Dictionary Online*, 2^{nd} 1989 ed., Oxford University Press.

Dutilleul, P., P. Clifford, S. Richardson, and D. Hémon (1993), Modifying the t test for assessing the correlation between two spatial processes, *Biometrics*, *49*(1), 305–314.

Easton, V. J., and J. H. McColl (1997), Statistics glossary, *Tech. Rep. 1.1*, Statistical Education through Problem Solving Consortium (STEPS), UK.

Edgett, K., B. Butler, J. Zimbelman, and V. Hamilton (1997), Geologic context of the Mars radar "Stealth" region in southwestern Tharsis, *J. Geophys. Res. Planets*, *102*(E9), 21,545–21,567, doi:10.1029/97JE01685.

Edgett, K. S. (1997), Aeolian dunes as evidence for explosive volcanism in the Tharsis region of Mars, *Icarus*, *130*(1), 96–114, doi:10.1006/icar.1997.5806.

Edgett, K. S. (2005), The sedimentary rocks of Sinus Meridiani: Five key observations from data acquired by the Mars Global Surveyor and Mars Odyssey orbiters, *Mars*, *1*, 5–58, doi:10.1555/mars.2005.0002.

Elkins-Tanton, L. T., P. C. Hess, and E. M. Parmentier (2005a), Possible formation of ancient crust on Mars through magma ocean processes, *J. Geophys. Res.*, *110*(E12), E12S01, doi:10.1029/2005JE002480.

Elkins-Tanton, L. T., S. E. Zaranek, E. M. Parmentier, and P. C. Hess (2005b), Early magnetic field and magmatic activity on Mars from magma ocean overturn, *Earth Planet. Sci. Lett.*, *236*(1-2), 1–12, doi:10.1016/j.epsl.2005.04.044.

Elphic, R. C., W. C. Feldman, T. H. Prettyman, R. L. Tokar, D. J. Lawrence, J. W. Head, III, and S. Maurice (2005), Mars Odyssey Neutron Spectrometer Water-Equivalent Hydrogen: Comparison with Glacial Landforms on Tharsis, in *36th Annual Lunar and Planetary Science Conference*, *Lunar and Planetary Inst. Technical Report*, vol. 36, edited by S. Mackwell and E. Stansbery, p. Abstract 1805.

Evans, L. G., R. C. Reedy, R. D. Starr, K. E. Kerry, and W. V. Boynton (2006), Analysis of gamma-ray spectra measured by Mars Odyssey, *J. Geophys. Res.*, *111*, E03S04, doi:10.1029/2005JE002657, [printed 112(E3), 2007].

Fairén, A. G., and J. M. Dohm (2004), Age and origin of the lowlands of Mars, *Icarus*, *168*(2), 277–284, doi:10.1016/j.icarus.2003.11.025.

Fairén, A. G., J. Ruiz, and F. Anguita (2002), An origin for the linear magnetic anomalies on mars through accretion of terranes: Implications for dynamo timing, *Icarus*, *160*(1), 220–223, doi:10.1006/icar.2002.6942.

Fairén, A. G., J. M. Dohm, V. R. Baker, M. A. de Pablo, J. Ruiz, J. C. Ferris, and R. C. Anderson (2003), Episodic flood inundations of the northern plains of Mars, *Icarus*, *165*(1), 53–67, doi:10.1016/S0019-1035(03)00144-1.

Fairén, A. G., D. C. Fernández-Remolar, J. M. Dohm, V. R. Baker, and R. Amils (2004), Inhibition of carbonate synthesis in acidic oceans on early Mars, *Nature*, *431*(7007), 423–426, doi:10.1038/nature02911.

Farquhar, J., J. Savarino, T. L. Jackson, and M. H. Thiemens (2000), Evidence of atmospheric sulphur in the martian regolith from sulphur isotopes in meteorites, *Nature*, *404*(6773), 50–52, doi:10.1038/35003517.

Farrand, W. H., J. F. Bell, J. R. Johnson, S. W. Squyres, J. Soderblom, and D. W. Ming (2006), Spectral variability among rocks in visible and near-infrared multispectral Pancam data collected at Gusev crater: Examinations using spectral mixture analysis and related techniques, *J. Geophys. Res. Planets*, *111*(E2), E02S15, doi:10.1029/2005JE002495.

Feldman, W. C., et al. (2005), Topographic control of hydrogen deposits at low latitudes to midlatitudes of mars, *J. Geophys. Res. Planets*, *110*(E11), E11,009, doi:10.1029/2005JE002452.

Fergason, R. L., P. R. Christensen, J. F. Bell, M. P. Golombek, K. E. Herkenhoff, and H. H. Kieffer (2006a), Physical properties of the Mars Exploration Rover

landing sites as inferred from Mini-TES-derived thermal inertia, *J. Geophys. Res. Planets*, *111*(E2), E02S21, doi:10.1029/2005JE002583.

Fergason, R. L., P. R. Christensen, and H. H. Kieffer (2006b), High-resolution thermal inertia derived from the Thermal Emission Imaging System (THEMIS): Thermal model and applications, *J. Geophys. Res. Planets*, *111*(E12), E12,004, doi:10.1029/2006JE002735.

Fishbaugh, K. E., F. Poulet, V. Chevrier, Y. Langevin, and J.-P. Bibring (2007), On the origin of gypsum in the Mars north polar region, *J. Geophys. Res. Planets*, *112*(E7), E07,002, doi:10.1029/2006JE002862.

Foley, C. N., T. E. Economou, R. N. Clayton, and W. Dietrich (2003), Calibration of the Mars Pathfinder alpha proton X-ray spectrometer, *J. Geophys. Res. Planets*, *108*(E12), 8096, doi:10.1029/2002JE002019.

Forget, F., R. Haberle, F. Montmessin, B. Levrard, and J. Heads (2006), Formation of glaciers on Mars by atmospheric precipitation at high obliquity, *Science*, *311*(5759), 368–371, doi:10.1126/science.1120335.

Forget, F., et al. (2007), The New (Version 4.2) Mars Climate Database, *LPI Contributions*, *1353*, 3098–+.

Gaddis, l., P. Mouginis-Mark, R. Singer, and V. Kaupp (1989), Geologic analyses of shuttle imaging radar (sir-b) data of kilauea volcano, hawaii, *Geol. Soc. Am. Bull.*, *101*(3), 317–332, doi:10.1130/0016-7606(1989)101⟨0317:GAOSIR⟩2.3.CO;2.

Gasnault, O., et al. (2002), Statistical analysis of thorium and fast neutron data at the lunar surface, *J. Geophys. Res. Planets*, *107*(E10), 5072, doi:10.1029/2000JE001461.

Gellert, R., et al. (2004), Chemistry of rocks and soils in gusev crater from the alpha particle x-ray spectrometer., *Science*, *305*(5685), 829–832, doi:10.1126/science.1099913.

Gellert, R., et al. (2006), Alpha Particle X-Ray Spectrometer (APXS): Results from Gusev crater and calibration report, *J. Geophys. Res.*, *111*(E2), E02S05, doi:10.1029/2005JE002555.

Gendrin, A., et al. (2005), Sulfates in Martian Layered Terrains: The OMEGA/Mars Express View, *Science*, *307*, 1587–1591, doi:10.1126/science.1109087.

Göbel, E., I. M. Mills, and A. J. Wallard (Eds.) (2006), *The International System of Units (SI)*, 8 ed., 130-135 pp., Bureau Inernational des Poids et Mesures, Paris, France.

Golden, D. C., D. W. Ming, R. V. Morris, and S. A. Mertzman (2005), Laboratory-simulated acid-sulfate weathering of basaltic materials: Implications for formation of sulfates at Meridiani Planum and Gusev crater, Mars, *J. Geophys. Res. Planets*, *110*, E12S07, doi:10.1029/2005JE002451.

Golombek, M. P., R. A. Cook, H. J. Moore, and T. J. Parker (1997), Selection of the Mars Pathfinder landing site, *J. Geophys. Res. Planets*, *102*(E2), 3967–3988, doi:10.1029/96JE03318.

Golombek, M. P., et al. (1999), Overview of the Mars Pathfinder mission: Launch through landing, surface operations, data sets, and science results, *J. Geophys. Res.*, *104*(E4), 8523–8554, doi:10.1029/98JE02554.

Golombek, M. P., et al. (2003), Selection of the Mars Exploration Rover landing sites, *J. Geophys. Res.*, *108*(E12), 8072, doi:10.1029/2003JE002074.

Golombek, M. P., et al. (2005), Assessment of Mars Exploration Rover landing site predictions, *Nature*, *436*(7047), 44–48, doi:10.1038/nature03600.

Golombek, M. P., et al. (2006), Geology of the Gusev cratered plains from the Spirit rover transverse, *J. Geophys. Res. Planets*, *111*(E2), E02S07, doi:10.1029/2005JE002503.

Grant, J. A., et al. (2004), Surficial deposits at Gusev crater along Spirit rover traverses, *Science*, *305*(5685), 807–810, doi:10.1126/science.1099849.

Greeley, R., and J. E. Guest (1987), Geologic map of the eastern equatorial region of Mars, 1:15000000, U.S. Geol. Surv. Misc. Invest. Ser., Map I-1802-A.

Greeley, R., R. Leach, B. White, J. Iversen, and J. Pollack (1976), Mars - Wind friction speeds for particle movement, *Geophys. Res. Lett.*, *3*, 417–420, doi:10.1029/GL003i008p00417.

Greeley, R., et al. (2005), Martian variable features: New insight from the Mars Express Orbiter and the Mars Exploration Rover spirit, *J. Geophys. Res. Planets*, *110*(E6), E06,002, doi:10.1029/2005JE002403.

Grotzinger, J. P., et al. (2005), Stratigraphy and sedimentology of a dry to wet eolian depositional system, Burns formation, Meridiani Planum, mars, *Earth Planet. Sci. Lett.*, *240*(1), 11–72, doi:10.1016/j.epsl.2005.09.039.

Grove, T. L., S. W. Parman, S. A. Bowring, R. C. Price, and M. B. Baker (2002), The role of an H_2O–rich fluid component in the generation of primitive basaltic andesites and andesites from the Mt. Shasta region, N California, *Contrib. Mineral. Petrol.*, *142*(4), 375–396.

Grove, T. L., L. T. Elkins-Tanton, S. W. Parman, N. Chatterjee, O. Müntener, and G. A. Gaetani (2003), Fractional crystallization and mantle–melting controls

on calc–alkaline differentiation trends, *Contrib. Mineral. Petrol.*, *145*(5), 515–533, doi:10.1007/s00410-003-0448-z.

Haberle, R. M., M. A. Kahre, J. R. Murphy, P. R. Christensen, and R. Greeley (2006), Role of dust devils and orbital precession in closing the Martian dust cycle, *Geophys. Res. Lett.*, *33*, L19S04, doi:10.1029/2006GL026188.

Hahn, B. C., et al. (2007), Mars Odyssey Gamma Ray Spectrometer elemental abundances and apparent relative surface age: Implications for Martian crustal evolution, *J. Geophys. Res. Planets*, *112*(E3), E03S11, doi:10.1029/2006JE002821.

Haining, R. (2003), *Spatial Data Analysis: Theory and Practice*, Cambridge University Press.

Halevy, I., M. T. Zuber, and D. P. Schrag (2007), A Sulfur Dioxide Climate Feedback on Early Mars, *Science*, *318*, 1903–1907, doi:10.1126/science.1147039.

Hamilton, V. E., H. Y. McSween, and B. Hapke (2005), Mineralogy of Martian atmospheric dust inferred from thermal infrared spectra of aerosols, *J. Geophys. Res. Planets*, *110*, E12,006, doi:10.1029/2005JE002501.

Harmon, J., R. Arvidson, E. Guinness, B. Campbell, and M. Slade (1999), Mars mapping with delay-Doppler radar, *J. Geophys. Res. Planets*, *104*(E6), 14,065–14,089, doi:10.1029/1998JE900042.

Hartmann, W. K., J. Anguita, M. A. de la Casa, D. C. Berman, and E. V. Ryan (2001), Martian cratering 7: The role of impact gardening, *Icarus*, *149*(1), 37–53, doi:10.1006/icar.2000.6532.

Haskin, L. A., et al. (2005), Water alteration of rocks and soils on Mars at

the Spirit rover site in Gusev crater., *Nature*, *436*(7047), 66–69, doi:10.1038/nature03640.

Hassler, D. M., et al. (2006), The radiation assessment detector (RAD) on the Mars Science Laboratory (MSL), in *36th COSPAR Scientific Assembly*, abstract 2720.

Hawkesworth, C., S. Turner, D. Peate, F. McDermott, and P. van Calsteren (1997), Elemental U and Th variations in island arc rocks: Implications for U–series isotopes, *Chem. Geol.*, *139*(1-4), 207–221, doi:10.1016/S0009-2541(97)00036-3.

Head, J. W., et al. (2005), Tropical to mid-latitude snow and ice accumulation, flow and glaciation on Mars, *Nature*, *434*, 346–351, doi:10.1038/nature03359.

Helsel, D. R., and R. M. Hirsch (2002), *Statistical Methods in Water Resources*, Techniques of Water-Resources Investigations of the United States Geological Survey, USGS.

Herd, C. D. K. (2003), The oxygen fugacity of olivine-phyric martian basalts and the components within the mantle and crust of mars, *Meteorit. Planet. Sci.*, *38*(12), 1793–1805.

Herkenhoff, K. E., et al. (2006), Overview of the Microscopic Imager Investigation during Spirit's first 450 sols in Gusev crater, *J. Geophys. Res. Planets*, *111*(E2), E02S04, doi:10.1029/2005JE002574.

Hiesinger, H., J. W. Head, and G. Neukum (2007), Young lava flows on the eastern flank of Ascraeus Mons: Rheological properties derived from High Resolution Stereo Camera (HRSC) images and Mars Orbiter Laser Altimeter (MOLA) data, *J. Geophys. Res. Planets*, *112*, E05,011, doi:10.1029/2006JE002717.

Honnorez, J. J. (1981), The aging of the oceanic crust at low temperature, in *The Oceanic Lithosphere*, *The Sea*, vol. 7, edited by C. Emiliani, pp. 525–587, John Wiley & Sons Inc., New York, NY.

Houghton, B. (2004), The influence of conduit processes on changes in style of basaltic Plinian eruptions: Tarawera 1886 and Etna 122 BC, *J. Volcanol. Geoth. Res.*, *137*, 1–3, doi:10.1016/j.jvolgeores.2004.05.009.

Hourdin, F., F. Forget, and O. Talagrand (1995), The sensitivity of the Martian surface pressure and atmospheric mass budget to various parameters: A comparison between numerical simulations and Viking observations, *J. Geophys. Res.*, *100*, 5501–5523, doi:10.1029/94JE03079.

Hurowitz, J. A., S. M. McLennan, N. J. Tosca, R. E. Arvidson, J. R. Michalski, D. W. Ming, C. Schröder, and S. W. Squyres (2006), In situ and experimental evidence for acidic weathering of rocks and soils on Mars, *J. Geophys. Res. Planets*, *111*(E2), E02S19, doi:10.1029/2005JE002515.

Hynek, B. M., R. J. Phillips, and R. E. Arvidson (2003), Explosive volcanism in the Tharsis region: Global evidence in the Martian geologic record, *J. Geophys. Res. Planets*, *108*, 5111–+, doi:10.1029/2003JE002062.

Ivanov, A., D. Muhleman, and A. Vasavada (1998), Microwave thermal mapping of the Stealth region on Mars, *Icarus*, *133*(2), 163–173, doi:10.1006/icar.1998.5921.

Jerolmack, D. J., D. Mohrig, J. P. Grotzinger, D. A. Fike, and W. A. Watters (2006), Spatial grain size sorting in eolian ripples and estimation of wind conditions on planetary surfaces: Application to Meridiani Planum, Mars, *J. Geophys. Res. Planets*, *111*(E5), E12S02, doi:10.1029/2005JE002544.

Joanes, D. N., and C. A. Gill (1998), Comparing measures of sample skewness and kurtosis, *The Statistician*, *47*(1), 183–189, doi:10.1111/1467-9884.00122.

Jochum, K. P., and S. P. Verma (1996), Extreme enrichment of Sb, Tl and other trace elements in altered MORB, *Chem. Geol.*, *130*(3-4), 289–299, doi:10.1016/0009-2541(96)00014-9.

Johnson, J. R., J. F. Bell, E. Cloutis, M. Staid, W. H. Farrand, T. McCoy, M. Rice, A. Wang, and A. Yen (2007), Mineralogic constraints on sulfur-rich soils from Pancam spectra at Gusev crater, Mars, *Geophys. Res. Lett.*, *34*, L13,202, doi:10.1029/2007GL029894.

Jolliff, B. L., and S. M. McLennan (2006), Evidence for water at meridiani, *Elements*, *2*, 163–167.

Jones, J. P., III, and E. Casetti (Eds.) (1992), *Applications of the expansion method*, 375 pp., Routledge, New York, NY, iSBN 0415034949.

Kadish, S. J., J. W. Head, N. G. Barlow, and D. R. Marchant (2008), Martian pedestal craters: Marginal sublimation pits implicate a climate-related formation mechanism, *Geophys. Res. Lett.*, p. in press, doi:10.1029/2008GL034990.

Kahre, M. A., J. R. Murphy, and R. M. Haberle (2006), Modeling the Martian dust cycle and surface dust reservoirs with the NASA Ames general circulation model, *J. Geophys. Res. Planets*, *111*, E06,008, doi:10.1029/2005JE002588.

Karunatillake, S., S. Squyres, J. Taylor, O. Gasnault, S. McLennan, and W. V. Boynton (2007), The mars odyssey gamma ray spectrometer reveals chemically striking regions on mars, in *7th International Conference on Mars*, p. Abstract 3190, Lunar and Planetary Institute.

Karunatillake, S., et al. (2006), Composition of northern low albedo regions of Mars: Insights from the Mars Odyssey Gamma Ray Spectrometer, *J. Geophys. Res. Planets*, *111*(E3), E03S05, doi:10.1029/2006JE002675.

Kato, M., S. Sasaki, K. Tanaka, Y. Iijima, and Y. Takizawa (2007), The japanese lunar mission selene: Science goals and present status, *Adv. Space Res.*, *in press*, doi:10.1016/j.asr.2007.03.049.

Keller, J. M., W. V. Boynton, R. M. S. Williams, S. Karunatillake, and GRS science team (2006a), Analysis of layering at Mars near-surface using attenuation of chlorine gamma rays, in *37th Annual Lunar and Planetary Science Conference*, vol. 37, edited by S. Mackwell and E. Stansbery, p. 2343, Lunar and Planetary Institute, League City, TX.

Keller, J. M., et al. (2006b), Equatorial and mid-latitude distribution of chlorine measured by Mars Odyssey GRS, *J. Geophys. Res.*, *111*, E03S08, doi:10.1029/2006JE002679, [printed 112(E3), 2007].

Keszthelyi, L., and W. L. Jaeger (2008), HiRISE Observations of the Medusae Fossae Formation, in *39th Lunar and Planetary Science Conference*, Lunar and Planetary Inst. Technical Report, p. Abstract 2420.

Keszthelyi, L., W. Jaeger, A. McEwen, L. Tornabene, R. A. Beyer, C. Dundas, and M. Milazzo (2008), High Resolution Imaging Science Experiment (HiRISE) images of volcanic terrains from the first 6 months of the Mars Reconnaissance Orbiter Primary Science Phase, *J. Geophys. Res. Planets*, *113*, E04,005, doi:10.1029/2007JE002968.

Kieffer, H. H., B. M. Jakosky, C. W. Snyder, and M. S. Matthews (Eds.) (1992), *Mars*, University of Arizona Press.

Kim, K. J., W. V. Boynton, M. Finch, R. M. S. Williams, R. C. Reedy, and D. M. Drake (2006a), Effects of rocks on neutron and gamma-ray production in Martian surface soil, in *37th Annual Lunar and Planetary Science Conference*, vol. 37, p. Abstract 2356, Lunar and Planetary Institute.

Kim, K. J., D. M. Drake, R. C. Reedy, R. M. S. Williams, and W. V. Boynton (2006b), Theoretical fluxes of gamma rays from the Martian surface, *J. Geophys. Res.*, *111*, E03S09, doi:10.1029/2005JE002655, [printed 112(E3), 2007].

Klingelhöfer, G., et al. (2004), Jarosite and hematite at Meridiani Planum from Opportunity's Mössbauer Spectrometer., *Science*, *306*(5702), 1740–1745, doi:10.1126/science.1104653.

Knoll, A. H., et al. (2008), Veneers, rinds, and fracture fills: Relatively late alteration of sedimentary rocks at Meridiani Planum, Mars, *J. Geophys. Res. Planets*, *113*, E06S16, doi:10.1029/2007JE002949.

Kobayashi, M., et al. (2005), Germanium detector with Stirling cryocooler for lunar gamma-ray spectroscopy, *Nucl. Instrum. Meth. Phys. Res. Sec. A*, *548*(3), 401–410, doi:10.1016/j.nima.2005.03.170.

Konopliv, A., C. Yoder, E. Standish, D. Yuan, and W. Sjogren (2006), A global solution for the Mars static and seasonal gravity, Mars orientation, Phobos and Deimos masses, and Mars ephemeris, *Icarus*, *182*(1), 23–50, doi:10.1016/j.icarus.2005.12.025.

Lane, M. D., J. L. Bishop, M. D. Dyar, M. Parente, P. L. King, and B. C. Hyde (2007), Identifying the phosphate and ferric sulfate minerals in the Paso Robles soils (Gusev crater, Mars) using an integrated spectral approach, in *Lunar and Planetary Institute Conference Abstracts*, abstract 2176.

Lane, M. D., J. L. Bishop, M. D. Dyar, P. L. King, M. Parente, and B. C. Hyde (2008), Mineralogy of the Paso Robles soils on mars, *Am. Mineral.*, *93*(5-6), 728–739, doi:10.2138/am.2008.2757.

Laskar, J., A. Correia, M. Gastineau, F. Joutel, B. Levrard, and P. Robutel (2004), Long term evolution and chaotic diffusion of the insolation quantities of Mars, *Icarus*, *170*(2), 343–364, doi:10.1016/j.icarus.2004.04.005.

Lemmon, M. T., et al. (2004), Atmospheric Imaging Results from the Mars Exploration Rovers: Spirit and Opportunity, *Science*, *306*, 1753–1756, doi: 10.1126/science.1104474.

Lodders, K. (1998), A survey of SNC meteorite whole-rock compositions, *Meteorit. Planet. Sci.*, *33*, Supplement 183–190.

Loss, R. D. (2003), Atomic weights of the elements 2001 (IUPAC technical report), *Pure Appl. Chem.*, *75*(8), 1107–1122.

Mandel, J. (1964), *The Satistical Analysis of Experimental Data*, 410 pp., Interscience, National Burea of Standards, Washington, D.C.

Manning, C., C. McKay, and K. Zahnle (2006), Thick and thin models of the evolution of carbon dioxide on Mars, *Icarus*, *180*(1), 38–59, doi:10.1016/j.icarus.2005.08.014.

Masarik, J., and R. C. Reedy (1996), Gamma ray production and transport in mars, *J. Geophys. Res. Planets*, *101*(E8), 18,891–18,912, doi:10.1029/96JE01563.

Mascagni, M., W. C. Rinaman, M. Sousa, and M. T. Strauss (2002), *Probability and Statistics*, chap. 7, pp. 615–727, 31 ed., Chapman and Hall/CRC.

Mayo, A. P., W. T. Blackshear, R. H. Tolson, W. H. Michael, G. M. Kelly, J. P. Brenkle, and T. A. Komarek (1977), Lander locations, Mars physical ephemeris, and solar system parameters-determination from Viking lander tracking data, *J. Geophys. Res.*, *82*, 4297–4303.

McAdam, A. C., M. Y. Zolotov, T. G. Sharp, and L. A. Leshin (2008), Preferential low-pH dissolution of pyroxene in plagioclase-pyroxene mixtures: Implications for martian surface materials, *Icarus*, *196*, 90–96, doi:10.1016/j.icarus.2008.01.008.

McEwen, A., B. Preblich, E. Turtle, N. Artemieva, M. Golombek, M. Hurst, R. Kirk, D. Burr, and P. Christensen (2005), The rayed crater Zunil and interpretations of small impact craters on Mars, *Icarus*, *176*(2), 351–381, doi:10.1016/j.icarus.2005.02.009.

McEwen, A. S., et al. (2007), Mars Reconnaissance Orbiter's High Resolution Imaging Science Experiment (HiRISE), *J. Geophys. Res. Planets*, *112*(E5), E05S02, doi:{10.1029/2005JE002605}.

McGovern, P. J., J. R. Smith, J. K. Morgan, and M. H. Bulmer (2004), Olympus Mons aureole deposits: New evidence for a flank failure origin, *J. Geophys. Res. Planets*, *109*, E08,008, doi:10.1029/2004JE002258.

McLennan, S. M. (2003), Sedimentary silica on Mars, *Geology*, *31*(4), 315–318, doi:10.1130/0091-7613(2003)031⟨0315:SSOM⟩2.0.CO;2.

McLennan, S. M., et al. (2005), Provenance and diagenesis of the evaporite–bearing Burns formation, Meridiani Planum, Mars, *Earth Planet. Sci. Lett.*, *240*(1), 95–121, doi:10.1016/j.epsl.2005.09.041.

McNutt, J., Ralph L., S. C. Solomon, R. E. Gold, J. C. Leary, and the MESSENGER Team (2006), The MESSENGER mission to Mercury: Development history and early mission status, *Adv. Space Res.*, *38*(4), 564–571, doi: 10.1016/j.asr.2005.05.044.

McSween, H. Y., T. L. Grove, and M. B. Wyatt (2003), Constraints on the composition and petrogenesis of the Martian crust, *J. Geophys. Res. Planets*, *108*(E12), 5135, doi:10.1029/2003JE002175.

McSween, H. Y., et al. (2004), Basaltic rocks analyzed by the Spirit rover in Gusev crater, *Science*, *305*(5685), 842–845, doi:10.1126/science.3050842.

McSween, H. Y., et al. (2006), Alkaline volcanic rocks from the Columbia Hills, Gusev crater, Mars, *J. Geophys. Res. Planets*, *111*, E09S91, doi:10.1029/2006JE002698.

McSween, H. Y., et al. (2008), Mineralogy of volcanic rocks in Gusev Crater, Mars: Reconciling Mössbauer, Alpha Particle X-Ray Spectrometer, and Miniature Thermal Emission Spectrometer spectra, *J. Geophys. Res. Planets*, *113*, E06S04, doi:10.1029/2007JE002970.

McSween, J., H. Y. (2002), The rocks of Mars, from far and near, *Meteorit. Planet. Sci.*, *37*(1), 7–25.

McSween, J., H. Y., and K. Keil (2000), Mixing relationships in the Martian regolith and the composition of globally homogeneous dust, *Geochim. Cosmochim. Acta*, *64*(12), 2155–2166, doi:10.1016/S0016-7037(99)00401-9.

McSween, J., Harry Y. (1994), What we have learned about Mars from SNC meteorites, *Meteoritics*, *29*, 757–779.

McSween, Y., et al. (2006), Characterization and petrologic interpretation of olivine-rich basalts at Gusev Crater, mars, *J. Geophys. Res. Planets*, *111*(E2), E02S10, doi:10.1029/2005JE002477.

Mellon, M. T., B. M. Jakosky, H. H. Kieffer, and P. R. Christensen (2000), High-Resolution Thermal Inertia Mapping from the Mars Global Surveyor Thermal Emission Spectrometer, *Icarus*, *148*, 437–455, doi:10.1006/icar.2000.6503.

Merrison, J. P., H. P. Gunnlaugsson, P. Nornberg, A. E. Jensen, and K. R. Rasmussen (2007), Determination of the wind induced detachment threshold for granular material on Mars using wind tunnel simulations, *Icarus*, *191*(2), 568–580, doi:10.1016/j.icarus.2007.04.035.

Metzger, A. E., and D. M. Drake (1990), Identification of lunar rock types and search for polar ice by gamma ray spectroscopy, *J. Geophys. Res.*, *95*, 449–460.

Mills, I., T. Cvitaš, K. Homann, N. Kallay, and K. Kuchitsu (Eds.) (1993), *Quantities, Units and Symbols in Physical Chemistry (IUPAC, Physical Chemistry Division)*, Commission on Physicochemical Symbols, Terminology and Units, 2 ed., 5,44,47,59-62,77,83 pp., Blackwell Science, Malden, MA.

Ming, D. W., et al. (2006), Geochemical and mineralogical indicators for aqueous processes in the Columbia Hills of Gusev crater, mars, *J. Geophys. Res. Planets*, *111*(E2), E02S12, doi:10.1029/2005JE002560.

Minitti, M. E., and M. J. Rutherford (2000), Genesis of the Mars Pathfinder "sulfur–free" rock from SNC parental liquids, *Geochim. Cosmochim. Acta*, *64*(14), 2535–2547, doi:10.1016/S0016-7037(00)00366-5.

Minitti, M. E., J. F. Mustard, and M. J. Rutherford (2002), Effects of glass content

and oxidation on the spectra of SNC-like basalts: Applications to Mars remote sensing, *J. Geophys. Res.*, *107*(E5), 5030, doi:10.1029/2001JE001518.

Montmessin, F., et al. (2006), Subvisible CO_2 ice clouds detected in the mesosphere of mars, *Icarus*, *183*, 403–410, doi:10.1016/j.icarus.2006.03.015.

Moore, H. J., and B. M. Jakosky (1989), Viking landing sites, remote-sensing observations, and physical-properties of martian surface materials, *Icarus*, *81*(1), 164–184, doi:10.1016/0019-1035(89)90132-2.

Moore, H. J., and J. Keller (1991), Surface–material maps of Viking landing sites on Mars, in *Planetary Geology and Geophysics Program Report*, vol. 2005, edited by T. A. Maxwell, pp. 160–162, NASA.

Moore, H. J., R. E. Hutton, R. F. Scott, C. R. Spitzer, and R. W. Shorthill (1977), Surface materials of Viking landing sites, *J. Geophys. Res.*, *82*, 4497–4523.

Morgan, J. K., and P. J. McGovern (2005), Discrete element simulations of gravitational volcanic deformation: 1. Deformation structures and geometries, *Journal of Geophysical Research (Solid Earth)*, *110*, B05,402, doi:10.1029/2004JB003252.

Morris, R. V., et al. (2004), Mineralogy at Gusev crater from the Mössbauer spectrometer on the Spirit Rover, *Science*, *305*(5685), 833–836, doi:10.1126/science.1100020.

Morris, R. V., et al. (2006), Mössbauer mineralogy of rock, soil, and dust at Gusev crater, Mars: Spirit's journey through weakly altered olivine basalt on the plains and pervasively altered basalt in the Columbia hills, *J. Geophys. Res. Planets*, *111*(E2), E02S13, doi:10.1029/2005JE002584.

Morris, R. V., et al. (2006), Mössbauer mineralogy of rock, soil, and dust at Meridiani Planum, Mars: Opportunity's journey across sulfate-rich outcrop, basaltic sand and dust, and hematite lag deposits, *J. Geophys. Res. Planets*, *111*, E12S15, doi:10.1029/2006JE002791.

Mouginis-Mark, P. J. (2002), Prodigious ash deposits near the summit of Arsia Mons volcano, Mars, *Geophys. Res. Lett.*, *29*(16), 1768, doi:10.1029/2002GL015296.

Mustard, J. F., and C. D. Cooper (2005), Joint analysis of ISM and TES spectra: The utility of multiple wavelength regimes for Martian surface studies, *J. Geophys. Res. Planets*, *110*(E5), E05,012, doi:10.1029/2004JE002355.

Nesbitt, H. W., and G. Markovics (1997), Weathering of granodioritic crust, long–term storage of elements in weathering profiles, and petrogenesis of siliciclastic sediments, *Geochim. Cosmochim. Acta*, *61*(8), 1653–1670, doi:10.1016/S0016-7037(97)00031-8.

Nesbitt, H. W., and R. E. Wilson (1992), Recent chemical–weathering of basalts, *Am. J. Sci.*, *292*(10), 740–777.

Neukum, G., et al. (2004), Recent and episodic volcanic and glacial activity on Mars revealed by the High Resolution Stereo Camera, *Nature*, *432*(7020), 971–979, doi:10.1038/nature03231.

Newsom, H. E., et al. (2007), Geochemistry of Martian soil and bedrock in mantled and less mantled terrains with gamma ray data from Mars Odyssey, *J. Geophys. Res. Planets*, *112*, E03S12, doi:10.1029/2005JE002597.

Nimmo, F., and D. J. Stevenson (2000), Influence of early plate tectonics on the

thermal evolution and magnetic field of Mars, *J. Geophys. Res. Planets*, *105*(E5), 11,969–11,979, doi:10.1029/1999JE001216.

Noe Dobrea, E. Z., and J. F. Bell (2005), TES spectroscopic identification of a region of persistent water ice clouds on the flanks of Arsia Mons Volcano, Mars, *J. Geophys. Res. Planets*, *110*, E05,002, doi:10.1029/2003JE002221.

Nowicki, S. A., and P. R. Christensen (2007), Rock abundance on Mars from the Thermal Emission spectrometer, *J. Geophys. Res. Planets*, *112*(E5), E05007, doi:10.1029/2006JE002798.

Olhoeft, G. R., and G. R. Johnson (1989), *Practical Handbook of Physical Properties of Rocks and Minerals*, chap. Densities of rocks and minerals, pp. 139–175, 1 ed., Chemical Rubber Company.

Osterloo, M. M., V. E. Hamilton, J. L. Bandfield, T. D. Glotch, A. M. Baldridge, P. R. Christensen, L. L. Tornabene, and F. S. Anderson (2008), Chloride-Bearing Materials in the Southern Highlands of Mars, *Science*, *319*, 1651–1654, doi:10.1126/science.1150690.

Pain, C. F., J. D. A. Clarke, and M. Thomas (2007), Inversion of relief on Mars, *Icarus*, *190*(2), 478–491, doi:10.1016/j.icarus.2007.03.017.

Patino, L. C., M. A. Velbel, J. R. Price, and J. A. Wade (2003), Trace element mobility during spheroidal weathering of basalts and andesites in Hawaii and Guatemala, *Chem. Geol.*, *202*(3-4), 343–364, doi:10.1016/j.chemgeo.2003.01.002.

Pelkey, S. M., et al. (2007), CRISM multispectral summary products: Parameterizing mineral diversity on Mars from reflectance, *J. Geophys. Res. Planets*, *112*(E8), E08S14, doi:10.1029/2006JE002831.

Picardi, G., et al. (2005), Radar soundings of the subsurface of Mars, *Science*, *310*(5756), 1925–1928, doi:10.1126/science.1122165.

Pirard, B., C. d'Uston, S. Maurice, and O. Gasnault (2005), Performance limits on new generation scintillators for planetary gamma-ray spectroscopy, in *36th Annual Lunar and Planetary Science Conference*, edited by S. Mackwell and E. Stansbury, p. 2187.

Pitas, I. (2000), *Digital image processing algorithms and applications*, Wiley, New York.

Plescia, J. B. (1994), Geology of the small Tharsis Volcanos - Jovis-Tholus, Ulysses-Patera, Biblis-Patera, Mars, *Icarus*, *111*(1), 246–269, doi:10.1006/icar.1994.1144.

Poulet, F., C. Gomez, J.-P. Bibring, Y. Langevin, B. Gondet, P. Pinet, G. Belluci, and J. Mustard (2007), Martian surface mineralogy from Observatoire pour la Minéralogie, l'Eau, les Glaces et l'Activité on board the Mars Express spacecraft (OMEGA/MEx): Global mineral maps, *J. Geophys. Res. Planets*, *112*, E08S02, doi:10.1029/2006JE002840.

Press, S. J. (1982), *Applied Multivariate Analysis: Using Bayesian and Frequentist Methods of Inference*, 2 ed., R.E. Krieger Pub. Co.

Press, W. H., S. A. Teukolsky, W. T. Vetterling, and B. P. Flannery (2002), *Numerical Recipes in C the Art of Scientific Computing*, 2 ed., Cambridge University Press.

Press, W. H., S. A. Teukolsky, W. T. Vetterling, and B. P. Flannery (2007), *Numerical Recipes in C the Art of Scientific Computing*, 3 ed., Cambridge University Press.

Putzig, N. E., and M. T. Mellon (2007), Apparent thermal inertia and the surface heterogeneity of Mars, *Icarus*, *191*(1), 68–94, doi:10.1016/j.icarus.2007.05.013.

Putzig, N. E., M. T. Mellon, K. A. Kretke, and R. E. Arvidson (2005), Global thermal inertia and surface properties of Mars from the MGS mapping mission, *Icarus*, *173*(2), 325–341, doi:10.1016/j.icarus.2004.08.017.

Rao, M. N., S. R. Sutton, D. S. McKay, and G. Dreibus (2005), Clues to Martian brines based on halogens in salts from nakhlites and MER samples, *J. Geophys. Res. Planets*, *110*, E12S06, doi:10.1029/2005JE002470.

Rao, M. N., L. E. Nyquist, S. J. Wentworth, S. R. Sutton, and D. H. Garrison (2008), The nature of Martian fluids based on mobile element studies in salt-assemblages from Martian meteorites, *J. Geophys. Res. Planets*, *113*, E06,002, doi:10.1029/2007JE002958.

Rawlings, J. O., S. G. Pantula, and D. A. Dickey (1998), *Applied Regression Analysis: A Research Tool*, Springer texts in statistics, 2 ed., Springer, New York.

Rieder, R., H. Wänke, T. Economou, and A. Turkevich (1997), Determination of the chemical composition of Martian soil and rocks: The alpha proton X ray spectrometer, *J. Geophys. Res. Planets*, *102*(E2), 4027–4044, doi:10.1029/96JE03918.

Rieder, R., R. Gellert, J. Bruckner, G. Klingelhofer, G. Dreibus, A. Yen, and S. W. Squyres (2003), The new Athena Alpha Particle X–ray Spectrometer for the Mars Exploration Rovers, *J. Geophys. Res. Planets*, *108*(E12), 8066, doi:10.1029/2003JE002150.

Rieder, R., et al. (2004), Chemistry of rocks and soils at Meridiani Planum from

the Alpha Particle X–ray Spectrometer, *Science*, *306*(5702), 1746–1749, doi:10.1126/science.1104358.

Rogers, A. D. (2005), Spatial and stratigraphic variations in Martain surface mineralogy determined from orbital thermal infrared data: Implications for upper crustal evolution and alteration, Dissertation, Arizona State University.

Rogers, A. D., and P. R. Christensen (2007), Surface mineralogy of Martian low-albedo regions from MGS-TES data: Implications for upper crustal evolution and surface alteration, *J. Geophys. Res. Planets*, *112*(E1), doi:10.1029/2006JE002727.

Rogers, A. D., J. L. Bandfield, and P. R. Christensen (2007a), Global spectral classification of Martian low-albedo regions with Mars Global Surveyor Thermal Emission Spectrometer (MGS-TES) data, *J. Geophys. Res. Planets*, *112*(E2), E02,004, doi:10.1029/2006JE002726.

Rogers, A. D., P. R. Christensen, and J. L. Bandfield (2007b), Global compositional heterogeneity on the Martian surface and key geologic interpretations using MGS-TES and complementary data sets, in 7^{th} *International Conference on Mars*, p. Abstract 3303.

Rudnick, R. L. (1995), Making continental crust, *Nature*, *378*(6557), 571–578, doi:10.1038/378571a0.

Ruff, S., et al. (2001), Mars' "White Rock" feature lacks evidence of an aqueous origin: Results from Mars Global Surveyor, *J. Geophys. Res. Planets*, *106*(E10), 23,921–23,927, doi:10.1029/2000JE001329.

Ruff, S. W. (2003), Basaltic andesite or weathered basalt: A new assessment,

in *Sixth International Conference on Mars*, Abstract 3258, Lunar and Planetary Institute, Pasadena, California.

Ruff, S. W., and P. R. Christensen (2007), Basaltic andesite, altered basalt, and a TES-based search for smectite clay minerals on Mars, *Geophys. Res. Lett.*, *34*, L10,204, doi:10.1029/2007GL029602.

Russell, P. S., and J. W. Head (2007), The Martian hydrologic system: Multiple recharge centers at large volcanic provinces and the contribution of snowmelt to outflow channel activity, *Plant. Space Sci.*, *55*, 315–332, doi:10.1016/j.pss.2006.03.010.

Rye, R. O. (2005), A review of the stable-isotope geochemistry of sulfate minerals in selected igneous environments and related hydrothermal systems, *Chem. Geol.*, *215*(1-4), 5–36, doi:10.1016/j.chemgeo.2004.06.034.

Schatz, V., H. Tsoar, K. Edgett, E. Parteli, and H. Herrmann (2006), Evidence for indurated sand dunes in the Martian north polar region, *J. Geophys. Res. Planets*, *111*(E4), E04,006, doi:10.1029/2005JE002514.

Schiffman, P., R. Zierenberg, N. Marks, J. L. Bishop, and M. Darby Dyar (2006), Acid-fog deposition at Kilauea volcano: A possible mechanism for the formation of siliceous-sulfate rock coatings on Mars, *Geology*, *34*, 921–924, doi:10.1130/G22620A.1.

Schorghofer, N., and K. S. Edgett (2006), Seasonal surface frost at low latitudes on Mars, *Icarus*, *180*, 321–334, doi:10.1016/j.icarus.2005.08.022.

Schultz, P. H. (2007), Planetary science - Hidden Mars, *Science*, *318*(5853), 1080–1081, doi:10.1126/science.1151412.

Scott, D., and J. M. Dohm (1997), *Encyclopedia of Planetary Sciences*, chap. Mars: Structural Geology and Tectonics, pp. 461–463, University of Arizona Press.

Scott, D. H., and K. L. Tanaka (1986), Geologic map of the western equatorial region of Mars, 1:15000000, U.S. Geol. Surv. Misc. Invest. Ser., Map I-1802-A.

Shean, D. E., J. W. Head, J. L. Fastook, and D. R. Marchant (2007), Recent glaciation at high elevations on Arsia Mons, Mars: Implications for the formation and evolution of large tropical mountain glaciers, *J. Geophys. Res. Planets*, *112*, E03,004, doi:10.1029/2006JE002761.

Sheather, S. J., and M. C. Jones (1991), A reliable data-based bandwidth selection method for kernel density estimation, *J. Roy. Stat. Soc. B Met.*, *53*, 683–690.

Shkuratov, Y. G., V. G. Kaydash, D. G. Stankevich, L. V. Starukhina, P. C. Pinet, S. D. Chevrel, and Y. H. Daydou (2005), Derivation of elemental abundance maps at intermediate resolution from optical interpolation of lunar prospector gamma-ray spectrometer data, *Planetary Space Science*, *53*(12), 1287–1301, doi:10.1016/j.pss.2005.07.001.

Skinner Jr., J. A., T. M. Hare, and K. L. Tanaka (2006), Digital renovation of the atlas of mars 1:15,000,000-scale global geologic series maps, in *37th Lunar and Planetary Science Conference*, p. Abstract 2331.

Sleep, N. H. (1994), Martian plate tectonics, *J. Geophys. Res. Planets*, *99*(E3), 5639–5655, doi:10.1029/94JE00216.

Snyder, J. P. (1987), *Map projections–a working manual*, Washington.

Soderblom, L. A., et al. (2004), Soils of Eagle crater and Meridiani Planum at the Opportunity Rover landing site, *Science*, *306*(5702), 1723–1726, doi:10.1126/science.1105127.

Solomon, S. C., R. L. McNutt, R. E. Gold, and D. L. Domingue (2007), Messenger - Mission overview, *Space Sci. Rev.*, *131*(1-4), 3–39, doi:10.1007/s11214-007-9247-6.

Spiga, A., et al. (2007), Remote sensing of surface pressure on Mars with the Mars Express/OMEGA spectrometer: 2. Meteorological maps, *J. Geophys. Res. Planets*, *112*, E08S16, doi:10.1029/2006JE002870.

Squyres, S. W., and L. G. Evans (1992), Effects of material mixing on planetary gamma–ray spectroscopy, *J. Geophys. Res. Planets*, *97*(E9), 14,701–14,715.

Squyres, S. W., et al. (2004a), The opportunity rover's athena science investigation at meridiani planum, mars., *Science*, *306*(5702), 1698–1703, doi:10.1126/science.1106171.

Squyres, S. W., et al. (2004b), The spirit rover's athena science investigation at gusev crater, mars., *Science*, *305*(5685), 794–799, doi:10.1126/science.1100194.

Squyres, S. W., et al. (2006a), Rocks of the Columbia hills, *J. Geophys. Res. Planets*, *111*(E2), E02S11, doi:10.1029/2005JE002562.

Squyres, S. W., et al. (2006b), Planetary science: Bedrock formation at Meridiani Planum, *Nature*, *443*(7107), E1, doi:10.1038/nature05212.

Squyres, S. W., et al. (2006c), Two years at Meridiani Planum: Results from the Opportunity rover, *Science*, *313*(5792), 1403–1407, doi:10.1126/science.1130890.

Squyres, S. W., et al. (2007), Pyroclastic activity at Home Plate in Gusev Crater, Mars, *Science*, *316*(5825), 738–742, doi:10.1126/science.1139045.

Staudigel, H., T. Plank, B. White, and H.-U. Schmincke (1996), Geochemical fluxes during seafloor alteration of the basaltic upper crust: DSDP sites 417 and 418, in *Subduction: Top to Bottom, Geophysical Monograph*, vol. 96, edited by G. E. Bebout, D. Scholl, S. Kirby, and J. Platt, pp. 19–38, American Geophysical Union, Washington, D.C.

Stephens, M. A. (1970), Use of the kolmogorov-smirnov, cramer-von mises and related statistics without extensive tables, *J. Roy. Stat. Soc. B Met.*, *32*(1), 115–122.

Stolper, E., and S. Newman (1994), The role of water in the petrogenesis of Mariana trough magmas, *Earth Planet. Sci. Lett.*, *121*(3-4), 293–325, doi: 10.1016/0012-821X(94)90074-4.

Stuart, A., J. K. Ord, and S. Arnold (1999), *Kendall's Advanced Theory of Statistics*, vol. 2A, 6 ed., 885 pp., Oxford University Press, New York, NY.

Sullivan, R., et al. (2005), Aeolian processes at the Mars Exploration Rover Meridiani Planum landing site, *Nature*, *436*(7047), 58–61, doi:10.1038/nature03641.

Sullivan, R., et al. (2008), Wind-driven particle mobility on Mars: Insights from Mars Exploration Rover observations at "El Dorado" and surroundings at Gusev Crater, *J. Geophys. Res. Planets*, *113*, E06S07, doi:10.1029/2008JE003101.

Tanaka, K. L. (1985), Ice-lubricated gravity spreading of the Olympus Mons aureole deposits, *Icarus*, *62*, 191–206, doi:10.1016/0019-1035(85)90117-4.

Tanaka, K. L., M. Chapman, and D. H. Scott (1992), Geologic map of the Elysium region of Mars, U.S. Geol. Surv. Misc. Invest. Ser., Map I-2147.

Tanaka, K. L., J. A. Skinner, T. M. Hare, T. Joyal, and A. Wenker (2003), Resurfacing history of the northern plains of Mars based on geologic mapping of Mars Global Surveyor data, *J. Geophys. Res. Planets*, *108*(E4), 8043, doi: 10.1029/2002JE001908.

Tanaka, K. L., J. Skinner, J. A., and T. M. Hare (2005), Geologic map of the northern plains of Mars, 1:15000000, U.S. Geol. Surv. Misc. Invest. Ser., Map 2888.

Taylor, G. J., et al. (2006a), Variations in K/Th on Mars, *J. Geophys. Res.*, *111*, E03S06, doi:10.1029/2006JE002676, [printed 112(E3), 2007].

Taylor, G. J., et al. (2006b), Bulk composition and early differentiation of Mars, *J. Geophys. Res.*, *111*, E03S10, doi:10.1029/2005JE002645, [printed 112(E3), 2007].

Taylor, J. R. (1982), *An Introduction to Error Analysis*, 270 pp., University Science Books.

Taylor, S. R., and S. M. McLennan (1985), *The Continental Crust: Its Composition and Evolution*, Blackwell Science, Oxford.

Thompson, T. W., B. A. Campbell, R. R. Ghent, B. R. Hawke, and D. W. Leverington (2006), Radar probing of planetary regoliths: An example from the northern rim of Imbrium basin, *J. Geophys. Res. Planets*, *111*(E6), E06S14, doi: 10.1029/2005JE002566.

Thornton, S. T., and J. B. Marion (2003), *Classical Dynamics of Particles and Systems*, 5 ed., Brooks Cole.

Tosca, N. J., S. M. McLennan, D. H. Lindsley, and M. A. A. Schoonen (2004), Acid-sulfate weathering of synthetic Martian basalt: The acid fog model revisited, *J. Geophys. Res. Planets*, *109*, E05,003, doi:10.1029/2003JE002218.

Tosca, N. J., S. M. McLennan, B. C. Clark, J. P. Grotzinger, J. A. Hurowitz, A. H. Knoll, C. Schröder, and S. W. Squyres (2005), Geochemical modeling of evaporation processes on mars: Insight from the sedimentary record at meridiani planum, *Earth Planet. Sci. Lett.*, *240*(1), 122, doi:10.1016/j.epsl.2005.09.042.

Tosca, N. J., S. M. McLennan, M. D. Dyar, E. C. Sklute, and F. M. Michel (2008), Fe oxidation processes at Meridiani Planum and implications for secondary Fe mineralogy on Mars, *J. Geophys. Res. Planets*, *113*, E05,005, doi:10.1029/2007JE003019.

Upton, G. J. G., and B. Fingleton (1985), *Spatial Data Analysis by Example: Point Pattern and Quantitative Data*, *Wiley series in probability and mathematical statistics*, vol. 1, J. Wiley, Chichester, New York.

Wang, A., J. F. Bell, and R. Li (2007), Salty soils at gusev crater as revealed by Mars Exploration Rover Spirit, in *Lunar and Planetary Institute Conference Abstracts*, abstract 1196.

Wang, A., et al. (2006), Sulfate deposition in subsurface regolith in Gusev crater, mars, *J. Geophys. Res. Planets*, *111*(E2), E02S17, doi:10.1029/2005JE002513.

Wänke, H., J. Brückner, G. Dreibus, R. Rieder, and I. Ryabchikov (2001), Chemical composition of rocks and soils at the Pathfinder site, *Space Sci. Rev.*, *96*(1-4), 317–330, doi:10.1023/A:1011961725645.

Watters, T. R., et al. (2007), Radar sounding of the Medusae Fossae Formation Mars: Equatorial ice or dry, low-density deposits?, *Science*, *318*(5853), 1125–1128, doi:10.1126/science.1148112.

Weitz, C. M., et al. (2006), Soil grain analyses at Meridiani Planum, mars, *J. Geophys. Res. Planets*, *111*(E12), E12S04, doi:10.1029/2005JE002541.

Whelley, P. L., and R. Greeley (2008), The distribution of dust devil activity on Mars, *J. Geophys. Res. Planets*, *113*, E07,002, doi:10.1029/2007JE002966.

Wilson, L., and J. W. Head (2007), Explosive volcanic eruptions on Mars: Tephra and accretionary lapilli formation, dispersal and recognition in the geologic record, *J. Volcanol. Geoth. Res.*, *163*, 83–97, doi:10.1016/j.jvolgeores.2007.03.007.

Wing, D. R., and G. L. Austin (2006), Description of the University of Auckland global Mars mesoscale meteorological model, *Icarus*, *185*, 370–382, doi:10.1016/j.icarus.2006.07.016.

Winter, J. D. (2001), *An Introduction to Igneous and Metamorphic Petrology*, Prentice Hall.

Wyatt, M. B. (2007), The chemically altered basaltic northern plains of Mars: TES, OMEGA, and GRS integrated data sets and conclusions, in 7^{th} *International Conference on Mars*, p. Abstract 3402.

Wyatt, M. B., and H. Y. McSween (2002), Spectral evidence for weathered basalt as an alternative to andesite in the northern lowlands of Mars, *Nature*, *417*(6886), 263–266, doi:10.1038/417263a.

Yen, A. S., et al. (2005), An integrated view of the chemistry and mineralogy of Martian soils., *Nature*, *436*(7047), 49–54, doi:10.1038/nature03637.

Yen, A. S., et al. (2008), Hydrothermal processes at Gusev Crater: An evaluation of Paso Robles class soils, *J. Geophys. Res. Planets*, *113*, E06S10, doi:10.1029/2007JE002978.

Young, H. D. (1962), *Statistical Treatment of Experimental Data*, 172 pp., McGraw-Hill.